



Universidade do Minho  
Escola de Engenharia

Flávia Vieira Barbosa Convection from Multiple Jets over a Complex Moving Surface

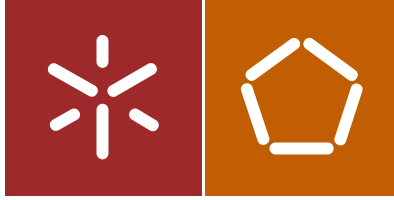
Flávia Vieira Barbosa

Convection from Multiple Jets over a Complex  
Moving Surface

UMinho | 2021

novembro de 2021





Universidade do Minho  
Escola de Engenharia

Flávia Vieira Barbosa

Convection from Multiple Jets over a Complex  
Moving Surface

Tese de Doutoramento  
Programa Doutoral em Líderes para Indústrias Tecnológicas

Trabalho realizado sob a orientação de  
Professor Doutor José Carlos Fernandes Teixeira  
Professora Doutora Senhorinha de Fátima Capela  
Fortunas Teixeira

## DIREITOS DE AUTOR E CONDIÇÕES DE UTILIZAÇÃO DO TRABALHO POR TERCEIROS

Este é um trabalho académico que pode ser utilizado por terceiros desde que respeitadas as regras e boas práticas internacionalmente aceites, no que concerne aos direitos de autor e direitos conexos.

Assim, o presente trabalho pode ser utilizado nos termos previstos na licença abaixo indicada.

Caso o utilizador necessite de permissão para poder fazer um uso do trabalho em condições não previstas no licenciamento indicado, deverá contactar o autor, através do RepositóriUM da Universidade do Minho.

*Licença concedida aos utilizadores deste trabalho*



Atribuição-NãoComercial  
CC BY-NC

<https://creativecommons.org/licenses/by-nc/4.0/>

## ACKNOWLEDGMENTS

Este documento reflete muitos anos de trabalho e dedicação, e a sua conclusão não teria sido possível sem o apoio de algumas pessoas e instituições. Antes de mais, quero agradecer ao meu orientador, Professor José Carlos Teixeira, por todo o apoio prestado desde a licenciatura até ao doutoramento. Por confiar no meu trabalho e por estar sempre presente para dar os impulsos necessários para que a investigação fosse conduzida com sucesso. À Professora Senhorinha Teixeira, pelos comentários construtivos, conselhos e partilha de informação relevante para que a tese fosse levada a bom porto. Agradeço ainda ao Professor Pierre Lermusiaux do MIT por me ter acolhido e dado uma oportunidade de viver uma das melhores experiências da minha vida. Um agradecimento especial ao Professor Sérgio Sousa pelo seu apoio incansável no desenvolvimento do DoE. Ao Eng. Carlos Costa, pelo apoio prestado, pelos conhecimentos partilhados, e pelas longas semanas de trabalho em torno da instalação experimental e quantificação de incertezas. Ao Eng. Filipe Marques, por impulsionar o trabalho prático nas oficinas do DEM e pela partilha de experiências que me ajudou na tomada de decisões. Ao Eng. Nuno Pacheco, por estar sempre atento e disponível para ajudar nos trabalhos experimentais. Ao Wael por todo o apoio prestado nos trabalhos desenvolvidos no MSEAS e ao Abhinav pela partilha de conhecimentos do 2.29 FV.

Quero ainda agradecer à Fundação para a Ciência e Tecnologia (FCT) pela bolsa de doutoramento que me foi atribuída (PD/BD/128216/2016), sem a qual este trabalho não poderia ter sido realizado, e ao programa MIT Portugal pela oportunidade que me concedeu em realizar o programa doutoral LTI. Assim como ao METRICs pelo apoio na investigação e apresentação de trabalhos em conferências nacionais e internacionais e ao Departamento de Engenharia Mecânica da Universidade do Minho por me facultar condições para realizar o trabalho mas também por me ter convidado a lecionar.

Finalmente agradeço aos meus fortes pilares, à minha família e amigos pelo apoio ao longo desta caminhada. Começando pelo meu namorado, Orlando, por ser o meu porto seguro e nunca me deixar desanimar por mais ingreme que o caminho fosse. Aos meus amigos e parceiros Vítor e Filipe que estiveram sempre ao meu lado ao longo destes últimos anos, apoiando em tudo o que pudessem, transmitindo sempre boas energias. Ao João que me ajudou com o CFD e à Andreia Faria, minha parceira do PhD, que se tornaram grandes amigos neste percurso. Um agradecimento especial à Professora Cândida Vilarinho pelo carinho e apoio prestado ao longo da minha vida académica. Agradeço à minha irmã, Andréa, pelo carinho e por acreditar sempre em mim, e especialmente aos meus pais e avós, pelos valores que me transmitiram e por me incentivarem a seguir os meus sonhos e nunca desistir. Sem eles não seria quem sou hoje. Muito obrigada a todos.

## STATEMENT OF INTEGRITY

I hereby declare having conducted this academic work with integrity. I confirm that I have not used plagiarism or any form of undue use of information or falsification of results along the process leading to its elaboration.

I further declare that I have fully acknowledged the Code of Ethical Conduct of the University of Minho.

### Convecção por jatos múltiplos sobre uma superfície complexa em movimento

Os jatos múltiplos de ar são usados como processo de convecção forçada em diversas aplicações de engenharia, uma vez que garantem elevadas taxas de transferência de calor. Porém, a complexidade da física envolvida no impacto dos jatos sobre a superfície alvo em espaços confinados torna esta área de investigação desafiante. Em algumas indústrias, a complexidade do aquecimento e/ou arrefecimento aumenta com o uso de superfícies irregulares e em movimento, tal como no processo de soldadura por refluxo. Por forma a contribuir para a sua melhoria em ambiente industrial, este trabalho tem como objetivo o estudo experimental e numérico do impacto de jatos de ar sobre superfícies complexas em movimento. Uma instalação experimental foi desenvolvida para a medição da velocidade do escoamento usando um sistema 2D-PIV, e a transferência de calor sobre a superfície alvo é medida por um sensor de fluxo. Estas técnicas experimentais permitem a caracterização da dinâmica do escoamento de um e múltiplos jatos. Os resultados provam que a técnica PIV captura com rigor as estruturas complexas do escoamento, geradas em toda a zona de medição, para diferentes números de Reynolds. Para além disso, modelos numéricos foram desenvolvidos usando o *software* comercial ANSYS FLUENT para a simulação de jatos em diferentes regimes de escoamento, assim como uma ferramenta própria desenvolvida em MATLAB para a análise do escoamento de um jato laminar. A comparação com dados experimentais mostra que o FLUENT prevê com rigor as diferentes regiões do jato, as interações entre jatos, bem como a transferência de calor, sem comprometer a eficiência computacional, ao passo que a ferramenta MATLAB consegue prever os vórtices gerados em todo o domínio. De modo a otimizar o trabalho experimental, os ensaios são definidos usando um planeamento de experiências baseado no método de Taguchi. Este método mostra que o processo de convecção por jatos múltiplos é otimizado para elevados números de Reynolds, um espaçamento entre jatos e uma distância entre a placa de jatos e a superfície alvo igual a 3 e 2 vezes o diâmetro do jato, respetivamente. Por outro lado, os resultados mostram um aumento da transferência de calor em 25% na vizinhança do degrau localizado sobre a superfície, devido ao aumento da turbulência do fluido comparativamente com a superfície plana. Finalmente, os resultados experimentais e numéricos apresentam um aumento da taxa de transferência de calor com o movimento da placa, mesmo quando são aplicadas baixas velocidades. Correlações para a determinação do número de Nusselt médio são propostas para superfícies estáticas e dinâmicas, estando de acordo com a literatura.

**Palavras-chave:** Dinâmica de Fluidos Computacional; Impacto de jatos; Velocimetria por imagem de partículas; Planeamento de experiências; Transferência de calor.

## ABSTRACT

### Convection from multiple jets over a complex moving surface

Multiple air jet impingement is a complex heat transfer process widely used in several engineering applications since it allows high heat transfer rates. However, the complexity of the physics under multiple jets impinging a target surface in a confined space makes this research field highly challenging. In some industrial processes, the complexity of the cooling and/or heating is increased by non-flat and moving surfaces, which is the case of the reflow soldering process. To provide relevant insights for industries that apply multiple jet impingement in their processes, this work focuses on the experimental and numerical study of air jets impinging a complex moving surface. A purpose-built test facility has been commissioned to measure the flow field velocity using a 2D-PIV system, while the heat transfer over the target plate is collected using a heat flux sensor. These experimental techniques are used to characterize the jet flow dynamics of single and multiple air jets. The results demonstrate that the PIV is able to capture the complex flow structure generated all over the measurement region, for different Reynolds numbers. Moreover, numerical models were developed using the commercial software ANSYS FLUENT to simulate jets lying in all flow regimes, and an in-house MATLAB code to analyze a laminar single jet impingement. Comparisons with experimental data show that FLUENT predicts with accuracy the jet flow regions, jets interactions, and heat transfer, at low computational costs, while the MATLAB code is able to capture the large and small scales induced over the domain. To optimize the experimental work, the tests are defined using a Design of Experiments based on Taguchi's method. This study demonstrated that the multiple jet impingement process is optimized for high Reynolds numbers, a jet-to-jet spacing, and a nozzle-to-plate distance equal to 3 and 2 times the jet diameter, respectively. Furthermore, results show that the heat transfer increases 25 % in the vicinity of the step surface due to the increased flow turbulence induced by the step compared with a flat plate. Finally, both numerical and experimental results highlight an increase of the heat transfer rate with the plate motion, even for low target surface velocities. Correlations for the average Nusselt number are proposed for both static and moving plates and are in good agreement with the literature.

**Keywords:** Computational Fluid Dynamics, Design of Experiments, Heat Transfer, Jet Impingement, Particle Image Velocimetry.

# TABLE OF CONTENTS

ACKNOWLEDGMENTS.....	III
RESUMO .....	V
ABSTRACT .....	VI
TABLE OF CONTENTS .....	VII
LIST OF FIGURES.....	IX
LIST OF TABLES .....	XV
LIST OF ACRONYMS .....	XVII
LIST OF SYMBOLS.....	XIX
<b>1. INTRODUCTION.....</b>	<b>1</b>
1.1. Motivation .....	1
1.2. Scope and Objectives .....	4
1.3. Research Methodology .....	5
1.4. Thesis Outline .....	7
1.5. Scientific Contribution .....	9
<b>2. LITERATURE REVIEW .....</b>	<b>11</b>
2.1. Jet Impingement .....	11
2.2. Influence of Process Variables .....	15
2.3. Jet Impingement Modeling .....	39
<b>3. EXPERIMENTAL METHODS .....</b>	<b>45</b>
3.1. Experimental Procedure .....	45

3.2.	Measurement Techniques .....	50
3.3.	PIV Technique .....	69
<b>4.</b>	<b>NUMERICAL METHODS .....</b>	<b>97</b>
4.1.	Mathematical Modeling .....	97
4.2.	Numerical Softwares .....	105
4.3.	Jet Impingement Models .....	107
<b>5.</b>	<b>RESULTS AND DISCUSSION OF A SINGLE JET IMPINGEMENT .....</b>	<b>119</b>
5.1.	Test Conditions .....	119
5.2.	Laminar Single Jet Impingement.....	120
5.3.	Single Jet Impingement in a Transition Regime .....	141
<b>6.</b>	<b>RESULTS AND DISCUSSION OF A MULTIPLE JET IMPINGEMENT .....</b>	<b>151</b>
6.1.	Test Conditions: DoE Method.....	151
6.2.	Results and Discussion.....	156
6.3.	Non-flat Plate .....	176
6.4.	Numerical Validation .....	185
6.5.	Proposed Correlation.....	194
<b>7.</b>	<b>CONCLUSIONS AND FUTURE DEVELOPMENTS.....</b>	<b>201</b>
7.1.	Conclusions .....	201
7.2.	Future Developments .....	203
	<b>REFERENCES.....</b>	<b>205</b>

## LIST OF FIGURES

Figure 1. Typical reflow thermal profile [5].	1
Figure 2. Non-uniform thermal behavior due to the complexity of the PCB: (a) cooling; (b) heating [6].	2
Figure 3. Typical process variables identified in multiple jet impingement.	3
Figure 4. Flow regions of an impinging jet captured by the PIV system. Right-hand side: Averaged velocity field; Left-hand side: Instantaneous flow field.	12
Figure 5. Flow regions of a multiple jet impingement for $Re = 2,000$ , $S/D = 5.7$ and $H/D = 3$ : (a) orifice nozzle; (b) free jet; (c) separation flow; (d) stagnation point; (e) stagnation region; (f) wall jet region; (g) central jet; (h) adjacent jets; (i) fountain flow; (j) collision point; (k) upwash flow; (l) primary vortices; (m) separation point; (n) vortices.	14
Figure 6. Basic geometric parameters in jet impingement.	15
Figure 7. Crossflow schemes in multiple jet impingement (a) complete or maximum crossflow (b) partial or intermediate crossflow (c) minimum crossflow.	16
Figure 8. Influence of different crossflow schemes on the average Nusselt number for different nozzle-to-jet distances.	19
Figure 9. Jet pattern (a) inline; (b) staggered.	20
Figure 10. Influence of different jet pattern on the average Nusselt number for different Reynolds numbers, $H/D$ and $S/D$ .	21
Figure 11. Averaged Nusselt number in function of the streamwise direction at different $Re$ numbers, $S/D$ and $H/D$ spacing.	24
Figure 12. Average Nusselt number in function of the $H/D$ spacing.	27
Figure 13. Average Nusselt number variation in function of the Reynolds number for different jet-to-plate and jet-to-jet distances.	28
Figure 14. Ribs structure (a) Longitudinal ribs; (b) V ribs.	30
Figure 15. Micro pins structure.	31
Figure 16. Dimple configuration (adapted from [77]).	32
Figure 17. Experimental setup: (a) Test rig; (b) Setup structure; (c) Target plate; (d) System control.	46

Figure 18. Position of the heat flux and thermocouples over the target surface. $T_1$ , $T_2$ , and $T_3$ represent the thermocouples; $T_c$ is the thermocouple connected to the temperature controller. The heat flux, located at the center of the plate, has an integrated thermocouple, $T_{\text{heat flux}}$ , to measure the local temperature. ....	47
Figure 19. Target plate configurations: (a) Flat plate; (b) Non-flat plate. The scheme represents the location of the heat flux, at the center of the plate, and the numbers are the location of thermocouples over the surface for each configuration.....	48
Figure 20. Heat transfer coefficient variation with time for both static and moving target surfaces. ....	49
Figure 21. OMEGA® heat flux sensor HFS-4.....	51
Figure 22. Experimental setup for validation of the heat flux measured by the HFS-4.....	52
Figure 23. (a) Mica heater; (b) Type K thermocouple (c) Acquisition system NI 9213. ....	54
Figure 24. Temperature controller TC544A. ....	54
Figure 25. Velocity measurement at the inlet and outlet of the experimental setup. ....	55
Figure 26. Apparatus to measure the total pressure at the setup exit. ....	56
Figure 27. Fan frequency regulator Mitsubishi S500.....	56
Figure 28. Measurement of the total pressure at the nozzle's inlet (a) Photograph of the Pitot tube position in the setup; (b) Schematic position of the Pitot tube in relation to the nozzle. ....	57
Figure 29. Velocity field measured at the bottom of the acrylic tube, upstream of the nozzle plate: (a) 5 Hz; (b) 15 Hz. ....	59
Figure 30. Inlet and outlet flow rate in function of the fan frequency.....	59
Figure 31. Factors that influence the uncertainty of the heat transfer and velocity field measurements. ....	60
Figure 32. Time-averaged velocity profile for $H/D = 7$ distances at $Re = 2,000$ and $S/D = 5.7$ . ....	61
Figure 33. PIV system alignment using the Bushnell® laser.....	62
Figure 34. PIV measurement system.....	69
Figure 35. (a) PIV system; (b) measurement region. ....	71
Figure 36. Response in amplitude of olive oil droplets in air for different particles diameter. ....	74
Figure 37. Response in phase of olive oils in air at different particles diameter. ....	75
Figure 38. Concept Smoke Aerotech System.....	76
Figure 39. Experimental setup scheme for the measurement of the particle's diameter. ....	77
Figure 40. Geometry of the experiment.....	78
Figure 41. Photograph of the experimental setup. ....	78

Figure 42. Auto-ignition of the olive oil particles inside the vaporizer.....	80
Figure 43. Variation of the vaporizer temperature with time at 15 V. ....	81
Figure 44. Variation of the vaporizer temperature with time at 10 V. ....	81
Figure 45. Partial evaporation of the olive oil particles at 10 V. ....	83
Figure 46. Mean particle diameter variation with flow rate and heater voltage for 95 % confidence level. .....	83
Figure 47. Effect of seeding concentration on PIV measurements: (a) uniform; (b) high; (c) low. ....	85
Figure 48. PIV system calibration.....	86
Figure 49. Variation of the normalized velocity magnitude at the exit of the nozzle throughout all its diameter for different time between pulses. ....	87
Figure 50. Normalized velocity magnitude over the target plate at a different time between pulses (a) 800 $\mu$ s to 1300 $\mu$ s (b) 200 $\mu$ s to 700 $\mu$ s. ....	88
Figure 51. Normalized random error estimation for a different time between pulses at $Re = 420$ and $H/D = 7$ . ....	94
Figure 52. Normalized random error estimation for different Reynolds numbers for $H/D = 7$ . ....	95
Figure 53. Representation of a turbulent velocity field measurement. ....	98
Figure 54. Velocity profile over the target plate, at $y/D = 0.2$ , for different SST $k-\omega$ model approaches. .....	103
Figure 55. Velocity profile over the central jet axis ( $x/D = 0$ ) for different SST $k-\omega$ model approaches. .....	103
Figure 56. Velocity field for $S/D = 4$ , $H/D = 2$ , and $Re = 5,000$ : (a) without curvature correction; (b) with curvature correction. ....	104
Figure 57. Velocity profile over the target plate, at $y/D = 0.02$ , for $S/D = 4$ , $H/D = 2$ , and $Re = 5,000$ . .....	104
Figure 58. Problem statement of a single jet impingement. ....	108
Figure 59. Normalizes velocity profile, at $y/D = 0.02$ , over the surface for different grids. ....	114
Figure 60. Problem statement of a multiple jet impingement. ....	114
Figure 61. Numerical domain. ....	115
Figure 62. Variation of the average Nusselt number over the target plate ( $y/D = 0$ ) for different meshes. .....	117
Figure 63. Numerical domain to conduct the dynamic simulations. ....	118

Figure 64. Experimental setup for the study of a single jet impingement.....	119
Figure 65. Instantaneous flow profile of an isothermal air jet impinging a flat plate at $Re = 420$ and $H/D = 6$ .....	122
Figure 66. Normalized time-averaged velocity magnitude at $Re = 420$ (a) all the domain; (b) throughout and near the jet axis; (c) over the target plate.....	123
Figure 67. Normalized time-averaged velocity magnitude at $Re = 420$ (a) all the domain; (b) throughout and near the jet axis; (c) over the target plate.....	124
Figure 68. Instantaneous normalized velocity variation over the target plate ( $y/D = 0.02$ ) at $Re = 420$ : (a) FLUENT (b) 2.29 FV.....	130
Figure 69. Instantaneous normalized velocity variation along the jet axis at $Re = 420$ : (a) FLUENT; (b) 2.29 FV .....	132
Figure 70. Averaged Nusselt number over the target plate at $t = 1$ s ( $y/D = 0$ ). .....	133
Figure 71. Normalized velocity profile over the target plate ( $y/D = 0.02$ ) at $t = 1$ s and $Re = 420$ . ...	134
Figure 72. Instantaneous vorticity field at $Re = 420$ and $t = 0.6$ s: (a) 2.29 FV; (b) FLUENT. ....	135
Figure 73. Normalized velocity variation along the jet axis, at $t = 1$ s, $x/D = 0$ and $Re = 420$ (isothermal jet). .....	136
Figure 74. Normalized velocity profile over the target plate ( $y/D = 0.02$ ) at $t = 1$ s and $Re = 420$ (non-isothermal jet). .....	138
Figure 75. Normalized velocity variation along the jet axis, at $t = 1$ s, $x/D = 0$ , and $Re = 420$ (non-isothermal jet). .....	138
Figure 76. Instantaneous vorticity field at $t = 1$ s and $Re = 420$ predicted by 2.29 FV. ....	140
Figure 77. Jet velocity profile: (a) $H/D = 2$ ; (b) $H/D = 3$ ; (c) $H/D = 4$ ; (d) $H/D = 5$ ; (e) $H/D = 6$ . ...	142
Figure 78. Time-averaged velocity over the target surface ( $y/D = 0.15$ ) at different $H/D$ and $Re = 2,000$ . .....	144
Figure 79. Velocity field: (a) $H/D = 2$ ; (b) $H/D = 3$ ; (c) $H/D = 4$ ; (d) $H/D = 5$ . ....	146
Figure 80. Velocity near the target surface ( $y/D = 0.15$ ) at different $H/D$ and $Re = 2,000$ (SST $k-\omega$ turbulence model). .....	148
Figure 81. Variation of the normalized velocity through the jet axis ( $x/D = 0$ ). .....	149
Figure 82. Predicted vs measured Nusselt numbers for a static plate case. ....	158
Figure 83. Predicted vs measured Nusselt numbers for a moving plate case. ....	158
Figure 84. Effects of design parameters on Nusselt number for the static plate case.....	160

Figure 85. Effects of design parameters on Nusselt number for the moving plate case. ....	160
Figure 86. Jet's velocity field for different jet-to-jet spacing: (a) $S/D = 2$ ; (b) $S/D = 3$ ; (c) $S/D = 4$ ; (d) $S/D = 6$ . ....	162
Figure 87. Jet's velocity field for different nozzle-to-plate distances: (a) $H/D = 2$ ; (b) $H/D = 3$ ; (c) $H/D = 5$ ; (d) $H/D = 7$ . ....	164
Figure 88. Jet's velocity field at $S/D = 3$ , $H/D = 2$ for different jet patterns: (a) Inline; (b) Staggered; (c) Inline with motion. ....	166
Figure 89. Jet's velocity profile for $S/D = 4$ for different plate geometry: (a) Step plate $H/D = 5$ ; (b) Step plate $H/D = 7$ ; (c) Flat plate $H/D = 3$ . ....	167
Figure 90. Jet's velocity profile for different Reynolds numbers: (a) Test 1 - $Re = 2,000$ , $S/D = 2$ , $H/D = 2$ ; (b) Test 15 - $Re = 5,000$ , $S/D = 6$ , $H/D = 5$ . ....	168
Figure 91. Test 11: (a) Static plate; (b) Dynamic plate: $t = 0$ s; $t = 1.5$ s; $t = 5$ s; $t = 7.5$ s; ....	170
Figure 92. Test 9: (a) dynamic plate; (b) static plate. ....	171
Figure 93. Experimental setup for the study of multiple jet impingement. ....	177
Figure 94. Staggered multi-jets configuration impinging a flat and non-flat plate at $Re = 5,000$ , $H/D = 2$ , and $S/D = 3$ (a) Flat plate (b) Non-flat with 1 $D$ step (c) Non-flat with 2 $D$ step. ....	177
Figure 95. Velocity profile over the target plate ( $y/D = 0.15$ ) for different plates geometry at $Re = 5,000$ , $H/D = 2$ , and $S/D = 3$ . ....	180
Figure 96. Velocity profile over the jet axis ( $x/D = 0$ ): (a) Central jet; (b) Right adjacent jet. ....	182
Figure 97. Jets position in relation to the heat flux sensor. (a) Non-flat plate; (b) Flat plate. ....	183
Figure 98. Position of the heat flux sensor on the numerical domain. ....	186
Figure 99. Static case: (a) Experimental data; (b) Numerical data. ....	187
Figure 100. Moving case: (a) Experimental data; (b) Numerical data. ....	188
Figure 101. Nusselt number over the target plate ( $y/D = 0$ ) at the central row. ....	190
Figure 102. Turbulence intensity: (a) at the left-hand side jet (b) at the central jet. ....	192
Figure 103. Measured values vs predictions with the present correlation. ....	196
Figure 104. Variation of the Nusselt number in function of the Reynolds number ( $2,000 \leq Re \leq 5,000$ ). ....	196
Figure 105. Variation of the Nusselt number in function of the Reynolds number ( $6,000 \leq Re \leq 15,000$ ). ....	197
Figure 106. Measured values vs predictions with the present correlation. ....	198

Figure 107. Variation of the Nusselt number in function of the Reynolds number for  $H/D = 2$  and  $S/D = 3$ .  
..... 198

Figure 108. Variation of the Nusselt number in function of the Reynolds number for  $H/D = 6$  and  $S/D = 6$ .  
..... 199

## LIST OF TABLES

Table 1. Correlations for average Nusselt number. ....	36
Table 2. Turbulence models applied in jet impingement simulations. ....	43
Table 3. Averaged heat flux and temperature measurements. ....	52
Table 4. Analytical results of heat flux over the plate. ....	53
Table 5. Reynolds number obtained by the total pressure measurements. ....	58
Table 6. Systematic uncertainties. ....	66
Table 7. Systematic uncertainties. ....	67
Table 8. Virgin olive oil properties. ....	79
Table 9. Variation of the mean vaporizer temperature in function of the heater voltage and the flow rate in steady-state conditions. ....	82
Table 10. Velocity and Reynolds number at the exit of the orifice nozzle measured indirectly using the Pitot tube and directly by PIV. ....	92
Table 11. Optimized time between pulses for different Reynolds numbers. ....	94
Table 12. Air Properties at 22 °C. ....	110
Table 13. Simulation data information. ....	110
Table 14. Mesh Properties. ....	113
Table 15. Air Properties at 25 °C. ....	116
Table 16. Properties of the three grids analyzed. ....	116
Table 17. Comparison between the experimental heat transfer values and data presented in the literature. ....	127
Table 18. Instantaneous velocity profile at Re = 420 obtained by FLUENT and 2.29 FV. ....	128
Table 19. Average Nusselt number obtained experimentally and numerically. ....	140
Table 20. Selected factors and their levels. ....	154
Table 21. Design Orthogonal Array generated using Minitab™. ....	156
Table 22. Nusselt number obtained from the static and moving plate experiments. ....	157
Table 23. ANOVA results for Signal-to-Noise ratios for the static plate case. ....	172

Table 24. ANOVA results for Signal-to-Noise ratios for the moving plate case. ....	172
Table 25. ANOVA results for Signal-to-Noise ratios for the static plate case. ....	174
Table 26. ANOVA results for Signal-to-Noise ratios for the moving plate case. ....	174
Table 27. Confirmation test results.....	175
Table 28. Average Nusselt number measurements.....	184
Table 29. Average Nusselt number over the static plate. ....	186
Table 30. Average Nusselt number over the moving plate. ....	187

## LIST OF ACRONYMS

ANOVA	Analysis of Variance
CAGR	Compound Annual Growth Rate
CCD	Charge Coupled Device
CD-SR	Convergent-Divergent Ribs
CDS	Central Difference Scheme
CFD	Computational Fluid Dynamics
CFL	Courant-Friedrichs-Lewy
DNS	Direct Numerical Simulation
DoE	Design of Experiments
DoF	Degree of Freedom
EDAM	Engineering Design and Advanced Manufacturing
EVM	Eddy Viscosity Models
FCT	Fundação para a Ciência e Tecnologia
FV	Finite Volume
GCI	Grid Convergence Index
HFS	Heat Flux Sensor
IA	Interrogation Area
LES	Large Eddy Simulation
LIF	Laser-Induced Fluorescent
LTI	Leaders for Technical Industries
MIT	Massachusetts Institute of Technology
MSEAS	Multidisciplinary simulation, Estimation, and Assimilation Systems

N-S	Navier-Stokes Equations
OA	Orthogonal Array
PCB	Printed Circuit Boards
PIV	Particle Image Velocimetry
RNG	Re-Normalisation Group
RSM	Reynolds Stress equation Model
SMD	Sauter Mean Diameter
SMT	Surface Mount Technology
SST	Shear Stress Transport
TFO	Transitional Flow Option
TVD	Total Variation Diminishing
UW	Upwind scheme
V-SR	V-Shaped Ribs
2D	2-Dimensional
3D	3-Dimensional

## LIST OF SYMBOLS

### Latin Symbols

Symbol	Unit (SI)	Description
$A_f$	-	Non-dimensional area
$A$	(m)	Area
$B$	-	Systematic uncertainty
$C$	-	Physical advection speed
$d$	(m)	Dimple depth
$d_i$	(m)	Mean diameter of the size band
$d_{off}$	(m)	Offset distance
$D$	(m)	Diameter
$e$	(m)	Height of rib
$F$	-	Variance ratio
$g$	(m/s <sup>2</sup> )	Gravitational acceleration
$G$	(kg/s)	Mass flow rate
$G_k$	(kg/m <sup>3</sup> ·s <sup>3</sup> )	Generation of $k$
$G_\omega$	(kg/m <sup>3</sup> ·s <sup>2</sup> )	Generation of $\omega$
Gr	-	Grashof number
$h$	(W/m <sup>2</sup> K)	Heat transfer coefficient
$\bar{h}$	(W/m <sup>2</sup> K)	Average heat transfer coefficient

$H$	(m)	Nozzle-to-plate distance
$I$	(%)	Turbulence intensity
$k$	(m <sup>2</sup> /s <sup>2</sup> ); (W/m·K)	Turbulent kinetic energy; Thermal conductivity
$k_p$	-	Expansion factor
$l$	(m)	Characteristic length
$L$	(m)	Length
$L_j$	(m)	Estimated seeding particle diameter
Ma	-	Mach number
$n$	-	Refractive index; Number of test repetitions
$N$	-	Samples number
Nu	-	Nusselt number
$\overline{Nu}$	-	Average Nusselt number
$p$	(Pa)	Pressure
$p_i$	-	Sensitivity coefficient
$P$	(Pa)	Pseudo-pressure
Pr	-	Prandtl number
$q$	(W/m <sup>2</sup> ); -	Heat flux; order of the method
$\bar{q}$	(W/m <sup>2</sup> )	Average heat flux
$Q$	(W)	Heat transfer rate
$r$	(m)	Radial distance
Ra	-	Rayleigh number
Re	-	Reynolds number
Ri	-	Richardson number

$S$	(m)	Jet-to-jet spacing
$SS$	-	Sum of squares
$SS'$	-	Pure sum of squares
$S_c$	-	Scale factor
$S_{eff}$	-	Seebeck coefficient
$S_q$	( $\mu\text{V}/\text{W}/\text{m}^2$ )	Sensor sensitivity
$S_t$	(1/s)	Modulus of the mean rate-of-strain tensor
$S_x, S_y$	(m)	Streamwise pitch, Spanwise pitch
$S_\phi$	( $\text{W}/\text{m}^3$ )	Source term
$t$	(s)	Time
$T$	( $^\circ\text{C}$ )	Temperature
$T^*$	(dependent variable)	Grand total of all results
$u$	(dependent variable)	Uncertainty
$u_{95}$	(dependent variable)	Uncertainty for 95 % confidence
$U$	(m/s)	Velocity
$U'$	(m/s)	Velocity fluctuation
$\bar{U}$	(m/s)	Average velocity
$U_\tau$	(m/s)	Shear velocity
$V$	( $\text{m}^3$ ); -	Volume; Variance
$\dot{V}$	( $\text{m}^3/\text{s}$ )	Volumetric flow rate
$V_i$	( $\text{m}^3$ )	Relative volume
$V_s$	-	Surface-to-jet velocity
$y^+$	-	Dimensionless distance of the first node to the wall

$Y_i$	(dependent variable)	Quality characteristic
$Y_k$	(kg/m·s <sup>3</sup> )	Dissipation of $k$
$Y_{opt}$	(dependent variable)	Estimated performance at optimum condition
$Y_\omega$	(kg/m <sup>3</sup> ·s <sup>2</sup> )	Dissipation of $\omega$
$x, y, z$	-	Cartesian coordinates
$u, v, w$	(m/s)	Velocity according to the cartesian coordinates

## Greek Symbols

Symbol	Unit (SI)	Description
$\alpha$	-	Slip correction adjustment factor
$\beta$	-	Response phase
$\beta^*$	(1/°C)	Coefficient of volume expansion
$\gamma$	-	Intermittency factor
$\Gamma_k$	(kg/m·s)	Effective diffusivity of $k$
$\Gamma_\omega$	(kg/m·s)	Effective diffusivity of $\omega$
$\Delta t$	(s)	Time between laser pulses
$\Delta V$	(V)	Output voltage
$\Delta x$	(m)	Absolute distance of the first grid cell to the wall
$\Delta x_p$	(pix)	Particle displacement
$\Delta \delta$	(m)	Thickness
$\varepsilon$	(m <sup>2</sup> /s <sup>3</sup> )	Turbulent dissipation rate
$\eta$	-	Amplitude ratio
$\theta$	(°)	Angle with the jet impinging point

$\kappa$	(m <sup>2</sup> /s)	Thermal diffusivity
$\mu$	(Pa/s)	Dynamic viscosity
$\mu_t$	(Pa/s)	Turbulent dynamic viscosity
$\nu$	(m <sup>2</sup> /s)	Kinematic viscosity
$\nu_t$	(m <sup>2</sup> /s)	Turbulent kinematic viscosity
$\zeta$	(dependent variable)	Error
$\rho$	(kg/m <sup>3</sup> )	Density
$\sigma$	-	Standard deviation
$\sigma_{\bar{x}}$	-	Random uncertainty
$\sigma_{\bar{x}R}$	-	Resultant random uncertainty
$\sigma_{\bar{x}U,V}$	(m)	Displacement random uncertainty
$\sigma_{\omega}, \sigma_k$	-	Turbulent Prandtl number
$\tau_{ij}$	(Pa)	Reynolds stress tensor
$\phi$	(dependent variable)	Scalar quantity
$\omega$	(1/s)	Specific dissipation rate
$\Omega$	(1/s)	Angular frequency

## Subscripts

---

$\infty$	Ambient air
$c_f$	Crossflow
$c_e$	Cell
$d$	Dimple

---

<i>e</i>	Experimental
<i>f</i>	Fluid
<i>fa</i>	Face
<i>in</i>	Inline
<i>int</i>	Intermediate
<i>j</i>	Jet
<i>max</i>	Maximum
<i>min</i>	Minimum
<i>p</i>	Particle
<i>pic</i>	Piccolo tube
<i>pre</i>	Predicted
<i>s</i>	Surface
<i>t</i>	Turbulent
<i>t-f</i>	Thin-film
<i>w</i>	Wall
<i>w-adj</i>	Fluid adjacent to the wall

# 1. INTRODUCTION

## 1.1. Motivation

The growing consumption of electronic products has led to a fast increase in the demands of Printed Circuit Boards (PCB). According to [1], the PCB market is expected to reach a CAGR (Compound Annual Growth Rate) of 3 % during the forecast period 2021-2027. The market value in 2020 was estimated to USD 60 billion and it is projected to be worth USD 75 billion by 2027. The expansion of the electronic products market has led to an increase in the complexity of PCBs.

The method to produce PCBs is called surface mount technology (SMT) and it consists of the deposition of the solder paste onto the pads of the PCB, known as a stencil printing process, followed by the placement of the components on the pasted pads [2]. To attach the electronic components to the PCB, the reflow soldering process is applied [3]. Reflow soldering consists of heating the entire assembly to a temperature beyond the melting point of the solder paste which wets the contact surfaces and forms the joint [4]. After the heating, PCB's passes through a cooling process, through forced convection, before it enters a final cooling stage by natural convection to ensure the connection between the board and the electronic components, as can be observed in Figure 1. However, due to the increased complexity of the PCB's, complicated thermal responses occur.

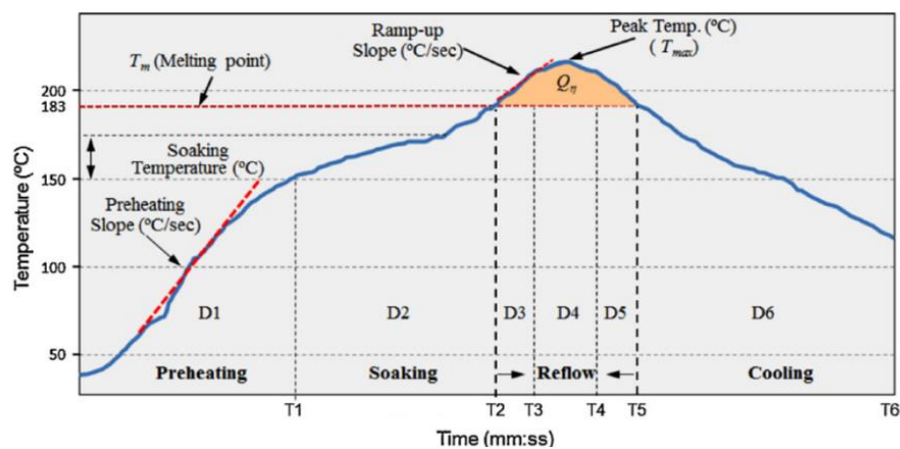
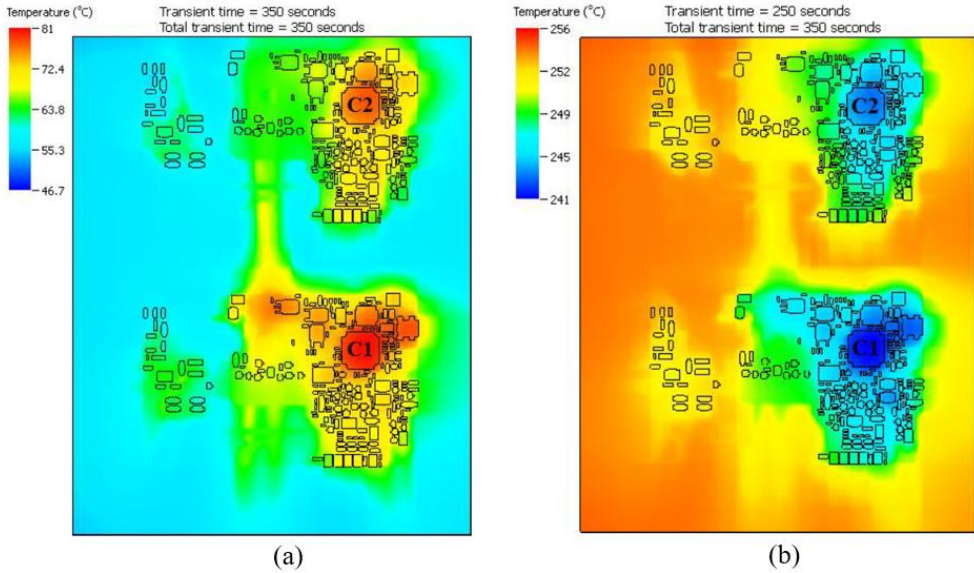


Figure 1. Typical reflow thermal profile [5].

Reflow soldering is commonly achieved using an oven that contains several independently controllable heating and cooling zones, as expressed in Figure 1. The heat transfer is governed by the convective process [2], ensured by the multiple air jet impingement technologies. The cooling [Figure 1 (a)] and heating [Figure 1 (b)] performance of convective reflow ovens mainly depends on the heat transfer coefficient which is influenced by several variables [4]. However, during the reflow soldering process, it was observed that inhomogeneous thermal distribution emerges around and within the components [3], as it can be observed in Figure 2. This complex thermal behavior is due to the variability of the dimensions and the high thermal capacity of the electronic components, leading to soldering failures such as cold or/and hot spots, overheated joints, and insufficient wetting [5]. In practice, defective products require additional repairs and reworking that can cause a loss of productivity of roughly 30 - 50 % of the total manufacturing costs [6]. To enhance the convective heat transfer, minimizing the defects that result from multiple air jet impingement, studies have been conducted in order to increase the heat transfer rate uniformity and to improve the coverage of the impinging surface. However, the total control of all the variables identified in jet impingement is still one of the remarkable issues for the thermal design of this process [7]. In that sense, to understand all these parameters and to ensure a good performance of the reflow soldering process, a detailed analysis of the multiple air jet impingement process is mandatory.



**Figure 2.** Non-uniform thermal behavior due to the complexity of the PCB: (a) cooling; (b) heating [6].

Multiple air jet impingement consists of directing a jet flow through several nozzles with a specific shape and configuration over a target surface [8], as demonstrated in Figure 3. The complexity of the impinging surface depends on the application. In the case of the reflow soldering, beyond the variation of shapes and sizes of the components that cover the surface, its motion is another important factor. In this

configuration, back and forward steps are identified which increases the complexity of the study of the heat transfer behavior in the vicinity of these surface transitions. Regarding the variables identified in the multiple jet impingement, that influence the heat transfer performance of the process, they can be divided into geometrical variables and flow properties, besides the surface geometry and motion [9]. Focusing on reflow soldering, the variables identified are the following: jets configuration (inline or staggered), nozzle shape (circular, triangular, etc.), jet-to-jet spacing ( $S_x$  and  $S_y$ ), and nozzle-to-plate spacing ( $H$ ). About flow properties, the most important parameter is the Reynolds number which depends on the jet flow density and viscosity, which depend on jet temperature, velocity,  $U_j$ , and the nozzle diameter,  $D$ .

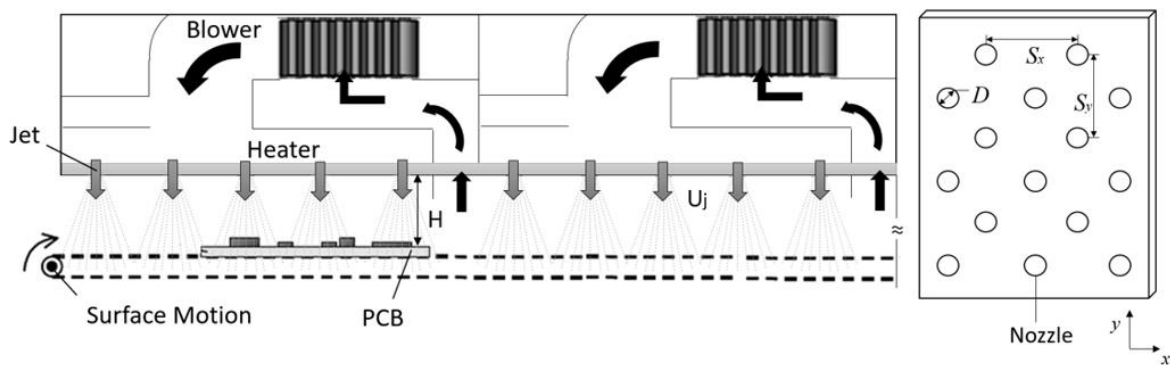


**Figure 3.** Typical process variables identified in multiple jet impingement.

In some industrial processes that use multiple air jets, the variables are established through empiricism and “trial and error” procedures, which involve huge costs that can no longer be supported due to the increasing market competitiveness. To overcome this situation, a full understanding and definition of this complex heat transfer process need to be conducted. To enhance the heat transfer over the target plate, reducing time and costs, it is fundamental to define accurately all the parameters in order to perform an optimized design with a higher degree of control. In this stage, the introduction of computational tools is an important aspect since problems can be identified at an early stage of the project. To determine the convective conditions that allow to simulate the process with accuracy, it is necessary to perform experimental tests. Through these experiments, it is possible to determine the influence of the process variables on heat transfer performance. The flow characterization and the monitorization of the heat transfer over the target plate are the two main goals of the experimental analysis, providing relevant inputs to be implemented in the numerical model. The numerical results allow the optimization of the process before the development of expensive physical tests, reducing the company’s budgetary impact.

Considering the interest of the multiple jet impingement field, this PhD thesis focuses on the study of the non-isothermal jet interaction with non-flat surfaces moving perpendicularly to the jet’s axes. This

investigation enables the definition of more realistic boundary conditions and turbulence models for the thermal simulation of multiple air jet impingement. It is intended that the results obtained from the experimental and numerical studies contribute to the enhancement of industrial processes that use multiple jet impingement. This knowledge will contribute to fully understand and define the process in order to reduce the problems and defects related to the non-uniformity of the heat transfer.

## 1.2. Scope and Objectives

The present PhD thesis has been developed under the Leaders for Technical Industries (LTI) PhD program. LTI within the Engineering Design and Advanced Manufacturing (EDAM) focus on multidisciplinary research problems, lying within an Engineering Systems framework. EDAM, created in 2006, is part of the MIT Portugal program which is a Fundação para a Ciência e Tecnologia (FCT) initiative built under a strategic partnership with Portuguese institutions, the MIT, and partners from industries and governments. The main objectives of EDAM are the development of a new educational paradigm in Europe with high-quality research and the promotion of a new entrepreneurial attitude towards knowledge-based manufacturing and competitive products. With this approach, EDAM pretends to develop human resources and knowledge integrated communities capable to lead an innovative manufacturing industry worldwide. Being the leadership one of the visions of EDAM, LTI PhD was designed to create leaders for technically advanced industries. The focus of LTI is to generate new scientific knowledge and new engineering solutions, in order to create and capture value in the highly competitive industrial sector. Always having in mind the industrial environment, this program is based on product and process innovation, taking into account complex decision-making, economics, management, and social aspects. Due to the relevance and differentiating factors of this PhD program, the thesis proposal needs to follow the LTI and EDAM philosophies.

Therefore, this PhD thesis is based on the experimental and numerical analysis of a multiple jet impingement system. This is a complex process widely implemented in several engineering applications and industrial processes, such as reflow soldering, drying of textile, cooling of turbojet engine blades, and fusion reactors [10]. These applications require high average heat transfer coefficients and the uniformity of the heat transfer over the impinging surface in order to enhance the process and to avoid local hot and/or cold spots. Considering the complexity of the multiple jet impingement, the design and management of this process are of paramount importance. In that sense, this project aims to reduce the industrial paradigms around the multiple air jet impingement specifically implemented in the reflow soldering process, giving scientific explanations to the phenomena identified in the process, being possible

to anticipate errors and defects that can occur during the impingement over a complex target surface. In addition, the combination between the experimental work and the numerical simulation tools is expected to reduce time and costs, leading to the improvement of the process.

Taking these ideas into consideration, the main goal of this work is to understand the flow interaction between impinging jets and a non-flat and moving surface. This will enable a more accurate definition of the convective boundary conditions that control the multiple air jet impingement process. Due to experimental limitations, the focus of this work is on the cooling of hot static and dynamic target plates by multiple air jets at ambient temperature. The specific milestones under this project include:

1. Design and construction of the test facility which includes the cooling system, plenum, nozzle orifices, and target surfaces;
2. Analysis of the flow field near the target surface in isothermal and non-isothermal conditions by using a 2D Particle Image Velocimetry (PIV) technique. This investigation takes into account the jet distribution, flow conditions, and surface pattern;
3. Determination of the average heat transfer over flat and non-flat target surfaces;
4. Definition of the numerical modeling of the test facility and validation of the turbulence model;
5. Evaluation of the influence of the moving surface and surface patterns and calculation of the average heat transfer coefficients;
6. Definition of the optimized configuration that enhances the heat transfer over the static and dynamic target surface.

Considering the motivation and the research objectives under this PhD thesis, two principal research questions arise:

- ✓ How does the flow interaction between impinging jets and a moving non-flat surface (specifically a stairway surface) behave?
- ✓ How is it possible to predict the behavior of the interaction between impinging jets and a moving non-flat surface in an industrial process?

### 1.3. Research Methodology

To successfully accomplish the aims proposed in this PhD thesis, the research follows two methodologies: experimentation and numerical simulation. Each method pretends to answer a specific research question. The experimental work focuses on providing an answer to the question *“How does the flow interaction between impinging jets and a moving non-flat surface (specifically a stairway surface)*

*behave?”*; while numerical simulation focuses on “*How it is possible to predict the behavior of the interaction between impinging jets and a moving non-flat surface in an industrial process?*”.

Even if these methodologies are complementary, each one can be, in the beginning, conducted separately. After the complete definition of the numerical modeling of the multiple jet impingement system, some experimental results can be introduced in the numerical model to enhance the accuracy of the simulations. The analysis of both numerical and experimental results allows to define the heat transfer of multiple jet impingement over a complex moving surface. In the end, the knowledge acquired throughout the experimental and numerical studies allows to optimize the multiple air jet impingement process, which can be implemented in the reflow soldering, in order to reduce product defect and to increase the process performance.

To determine the convective conditions that allow to simulate the multiple air jet impingement process with accuracy, it is necessary, first, to perform experimental tests. Through these experiments, it is possible to characterize all the variables involved in this forced convection process, from the flow characterization to the analysis of the geometrical properties between the jets and the target surface. This laboratory research is conducted on a purpose-built test facility that has been commissioned, using a PIV system. This technique is highly suited to measure the velocity field of flows, providing detailed information about the flow behavior over the target surface, but also to identify the phenomenon that occurs in the vicinity of surface transition (such as back steps and forward steps). To determine the heat transfer coefficients over the target plate, a heat flux sensor and thermocouples are applied on the impinging plate. However, to reduce time and costs related to the experimental tests, it is important to perform a Design of Experiments (DoE), which allows to reduce the number of tests, focusing on the parameters that have a greater influence on the process performance [11]. Taguchi’s method allows the optimization of the process through the selection of the most suitable parameter values. Therefore, this DoE method is applied in this work.

The results obtained from these experiments allow to apply more realistic boundary conditions to the numerical simulation and the accuracy of the numerical model is validated by the experimental data. To develop the numerical simulation of the process, several studies such as [12]–[15], use the CFD (Computational Fluid Dynamics) software ANSYS FLUENT, specially designed to predict the flow behavior. This is an important tool to solve engineering problems since there is an increasing demand for precision in the least time possible to reduce production costs. Considering these advantages, numerical simulation has been a tool widely implemented in jet impingement studies. The fast advancement of computational resources and numerical algorithms has led to an improvement in the accuracy of the models used to

study impinging flows and heat transfer. Most industrial applications that use jet impingement are governed by turbulent flows which is the case of reflow soldering. Nevertheless, these flows represent a great challenge to predict the behavior of jets with accuracy. To validate the turbulence model, proving its reliability, the results obtained numerically need to be compared with the experimental data. However, even if several numerical works have been conducted in multiple jet impingement, a lack of experimental studies that support the numerical modeling of multiple jets impinging on a complex moving surface was identified. This leads to an uncertainty of the results obtained numerically which is not acceptable in an industrial context. In that sense, this PhD thesis pretends to develop a reliable and accurate numerical model of this process which will take into consideration all the variables applied in the process but also the complex geometry of the target surface.

## 1.4. Thesis Outline

This work focuses on the experimental and numerical analysis of multiple air jets impinging on a complex moving surface. Within this general objective, the present thesis is organized into seven chapters.

The second chapter presents the literature review under the topic of this PhD thesis. The physical concepts under single and multiple air jet impingement are discussed, followed by the influence of the process variables on both jet flow dynamics and heat transfer performance. The correlation for the average Nusselt number for both single and multiple jet impingement is provided. Finally, the different methods applied for the numerical modeling of single and multiple jet impingement are presented. Although this work focuses on a multiple air jet impingement process, the single jet impingement must be fully understood to be able to interpret the physical concept under multiple jet interactions. Thus, the single jet is also explored in this work.

Chapter three discusses the experimental methodology followed in this thesis. The purpose-built experimental setup is presented, and its operation is discussed. Furthermore, the experimental techniques used in this work are detailed. Due to its complexity, the PIV technique has a sub-chapter entirely dedicated to it, in which the study of the seeding particles, which plays an important role in the accuracy of the PIV measurement, is presented. Considering the relevance of the source of errors on the measurement's accuracy, a section regarding this topic was created, as well as a section for data reduction and uncertainty estimation of the measured variables.

Chapter four is dedicated to the numerical methodology implemented in this project. The main concepts are discussed, from the governing equations to the turbulence model applied. Two numerical techniques are explored in this thesis. A Direct Numerical Simulation (DNS) is conducted for the study of

a laminar single jet flow, using a MATLAB framework implemented by the MSEAS group at MIT, followed by RANS (Reynolds Averaged Navier-Stokes Equations) for the study of the jet flow in transition and turbulence regimes, using the ANSYS FLUENT software. All the details regarding the numerical domain, boundary conditions, and mesh sensitivity analysis are presented in this chapter.

The results are divided into two chapters, five and six. Chapter 5 concerns the study of a single jet in a laminar and transition regime. This chapter is relevant since it makes the bridge between the relevant physical concepts concerning the jet flow dynamics and the main goal of this work, the study of the convection of multiple jets over a complex moving surface. The flow dynamics analysis of isothermal and non-isothermal jets impinging a flat plate is discussed. The experimental results are used to validate two numerical techniques implemented in Chapter four. Considering that the nozzle-to-plate distance ratio ( $H/D$ ) is one of the most relevant process variables identified in jet impingement, the study of the effect of  $H/D$  on the flow dynamics of a jet in the transition regime is provided.

Chapter six is the focus of the research since the experimental and numerical results of the multiple air jet impingement over a complex moving surface are presented. The presentation of the DoE methodology is the starting point of this chapter, from which a matrix of experiments is presented. This matrix sets the pattern to conduct both velocity field and heat transfer measurements. The heat flux measurements allow to define the effect of each control variable on the average heat transfer performance, and the jet's flow velocity profiles obtained by the PIV measurements analyze the effect of these variables on the jet's flow dynamics and provide the physical insight of the flow dynamics to understand the cause-effect diagrams and ANOVA (Analysis of Variance) analysis. From this study, an optimized configuration is obtained, and a numerical model is developed. The experimental data are used to validate the optimized numerical modeling of multiple air jets impinging a complex moving surface. At the end of this chapter, correlations for both static and dynamic plates impinged by multiple air jets are proposed.

Finally, in chapter seven, the most relevant conclusions of the present work are outlined. Based on the experimental and numerical work, different research lines are proposed for future investigation in this field.

## 1.5. Scientific Contribution

Jet impingement is widely implemented in a variety of engineering applications and industrial processes, essentially in thermal equipment for heating, cooling, and drying and, as such, this process has been extensively investigated [10]. This technology received considerable attention due to its inherent characteristics of high performance for heat transfer enhancement in thermal equipment, providing very high rates of heat transfer, which lead to rapid cooling and heating in specific heat transfer areas [16] [17].

Even if several works have been published in this area, it is observed a lack of studies in multiple jet impingement that involves target surface motion and the influence of different geometries over the impinging surface, such as electronic components with different sizes and shapes. Until now, no study addresses the average heat transfer in the vicinity of surface transitions (such as back steps and forward steps) coupled with surface motion. In that sense, this PhD thesis focus on the study of the non-isothermal jet interaction with non-flat surfaces moving perpendicularly to the jet axis. This investigation enables the definition of more realistic boundary conditions and turbulence models for the thermal simulation of multiple air jet impingement. To achieve, with success, the objectives previously stated, this project follows an experimental and numerical approach. The results are expected to contribute to the enhancement of scientific knowledge and industrial processes that use multiple air jet impingement, in order to optimize the engineering applications and to reduce the problems and defects related to non-uniform heat transfer.

The project thesis involves proficiency in several areas, from the design and construction of a setup and experimentation using a PIV system to the effective learning and application of theoretical concepts in jet impingement, heat transfer, and numerical modeling. The innovation and added values of this thesis are reinforced by the LTI PhD program partnership since the numerical models developed during the project are improved through the collaboration of MIT. This is an ambitious project that intends to provide relevant answers to the reflow soldering process, but which can be extended to other applications that use multiple jet impingement. In that sense, the LTI provided relevant methodologies necessary to combine the research and advanced processes in order to obtain results worthy to be implemented in technically advanced industries.

This page was intentionally left in blank.

## 2. LITERATURE REVIEW

Impinging jets have been extensively studied due to their wide applicability in engineering applications, where high heat transfer rates are required. However, the complexity of this flow continues to encourage researchers to provide scientifically-based solutions to the industry in order to reduce product defects and increase heat transfer performance. Jet impingement can be performed by single or multiple jets. While single jets have a localized high heat transfer rate, multiple jets produce a more uniform cooling and heating, which can be a great advantage in some applications [18]. In a multi-jet configuration, the individual jets can be substantially affected by different interactions that increase the complexity of the flow. In addition, the jet impingement process involves several variables which increase these flow interactions, from the jet flow parameters (velocity and temperature) to the target surface and process geometry (nozzle-to-plate distance, ribs, etc.).

To fully characterize the flow field and heat transfer of a jet impingement process, several studies have been conducted. In that sense, this chapter focuses on the flow characterization of single and multiple jet impingement systems as well as the analysis of the influence of the process variables on the heat transfer efficiency over the target plate. Considering the fast advancement of numerical tools and their increasing implementation to predict the fluid flow structure and heat transfer of single and multiple jet impingement, this chapter analyzes different numerical and experimental works that have been conducted in this field and presents the relevant concepts and phenomena.

### 2.1. Jet Impingement

Jet impingement is a complex heat transfer process that involves flow interactions between the jets and the target surface. To be able to analyze accurately all the phenomena that occur during the jet impingement, it is important to understand the underlying physics of single and multiple jets.

### 2.1.1. Jet Flow Characterization

In jet impingement, fluid passes through a nozzle and flows into a domain with ambient fluid in rest, and progresses in direction to the target plate. Once the flow reaches the surface, strong flow interactions occur over the wall, and high heat transfer rates are obtained, ensuring an effective cooling or heating of the impinging plate. From the nozzle to the target plate, different regions can be identified. This work was first conducted by Martin [19], who presented relevant insights in this field and divided the jet impingement regions into the free jet, the stagnation zone, and the wall jet. Between the free jet and the stagnation regions, Viskanta [20] identified the decaying region and subdivided it into two zones, the initial “developing zone” and the “fully developed zone”. These primary studies are the basis for the development of a jet flow configuration known until then and presented in Figure 4.

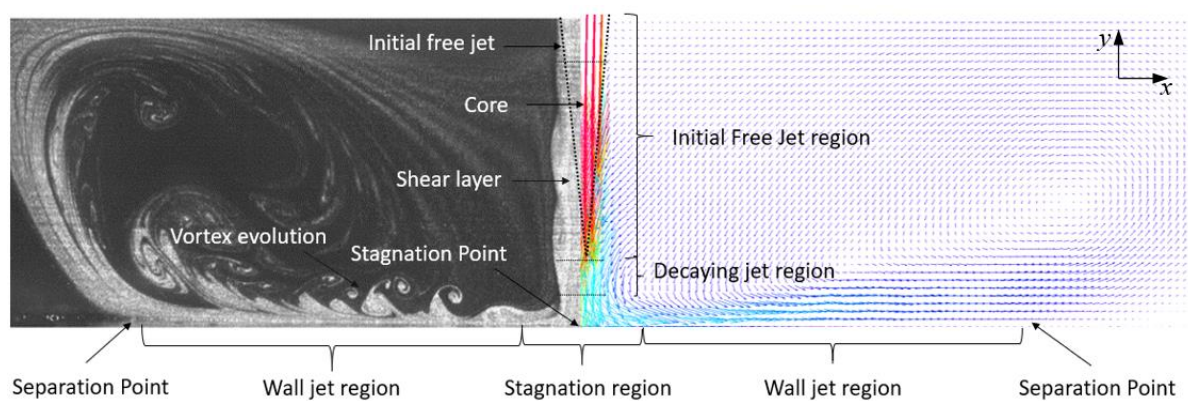


**Figure 4.** Flow regions of an impinging jet captured by the PIV system. Right-hand side: Averaged velocity field; Left-hand side: Instantaneous flow field.

The free jet region is generated at the nozzle exit, being characterized by its maximum velocity. As the jet flows through the nozzle, it produces a near flat-topped velocity profile, dominated by axial velocity. Once the jet flow starts to mix with the ambient fluid, a shear flow generated at its edges is the primary source of turbulence characterized by entrainment of mass, momentum, and energy [20]. This entrainment generates several effects such as jet expansion, a nonuniform radial velocity profile within the jet, the increase of the overall mass flow rate, and jet temperature change before the impingement over the target surface. As the jet develops in direction of the impinging plate, the shear layer grows. If the jet velocity is high, i.e.  $Re > 1,000$ , the destabilizing effects of the shear forces overcome the stabilizing effect of fluid viscosity/momentum diffusion and Kelvin-Helmholtz instabilities are induced [21]. These instabilities increase the flow entrainment and form large-scale eddies along the sides of the jet. The length scale of the large-scale eddies correlates with the jet diameter. This structure is preserved

until eddies break up into smaller ones or when an interaction with other downstream flows occurs [22]. The strong interactions between the jet flow and the surrounding fluid induce a decrease in velocity as the flow gets closer to the target plate. The point where the maximum velocity decays 5 % defines the end of the potential core [23]. As depicted in Figure 4, the end of the core region represents the beginning of the decaying region, characterized by the decay of the axial velocity caused by large shear stress at the jet boundary [20, 21]. Viskanta [20] subdivided the decaying region into the “developing zone” and the “developed zone”, characterized by a bell-shape that can be described approximately by a Gaussian distribution. As the flow gets closer to the wall, it loses axial velocity and turns, generating a stagnation region in which the velocity is near zero [24]. In the stagnation region, the flow is characterized by higher static pressure on and above the wall, the eddies are stretched and distorted and the flow is gradually reoriented to be roughly parallel with the wall [25], inducing the wall upstream effect [21]. According to Katti & Prabhu [9] the stagnation region occurs at a nozzle-to-plate distance ratio ( $H/D$ ) below the unity.

The last zone, called the wall jet region, occurs once the jet impacts the target surface. After the contact with the plate, the flow is divided into two streams moving in opposite radial directions along the surface, being observed a change of the flow direction from axial (vertical axis  $y$ ) to radial (longitudinal axis  $x$ ) direction. As the flow impinges the wall, its kinetic energy decreases rapidly and is converted into a corresponding rise in pressure energy which generates an accelerated streamwise flow in radial direction [26]. A boundary layer is formed, showing a constant thickness, typically lower than 1 % of the jet diameter [19], and grows until maximum levels of turbulence are reached, away from the jet axis [9, 22]. Higher heat transfer coefficients are identified in the vicinity of the stagnation region, where the boundary layer is thinner. As the boundary layer gets thicker, turbulence increases due to turbulent fluctuations in velocity and pressure gradient which produce a reversal of the local flow along the wall and promote the formation of secondary vortices [24]. These vortices cause local rises in heat and mass transfer [22]. The separation of the flow occurs where the boundary layer leaves the surface of the plate [8].

### 2.1.2. Multiple Jet Impingement

In several applications such as reflow soldering, textile drying, and cooling of turbojet blades, high average heat transfer coefficients and the uniformity of the heat transfer over the impinging surface are required to improve the performance of the process and to avoid local hot (or cold) spots. These applications require large areas, and therefore, a single jet system is not efficient, being the multi-jet configuration more appropriate.

Regarding the flow as arrays of impinging jets, the same three regions identified in single jet impingement are recognized: free jet, stagnation zone, and wall jet [19]. However, as mentioned above, in a multiple jet configuration, the individual jets are substantially affected by three types of interactions that do not occur in a single jet impingement: the jet interference between adjacent jets prior to the impingement over the target surface; the jet-to-jet interaction among the adjacent jets after the impingement over the surface; and the interactions due to jet-induced crossflow [7]. Figure 5 represents the main regions identified in a multiple jet impingement process.

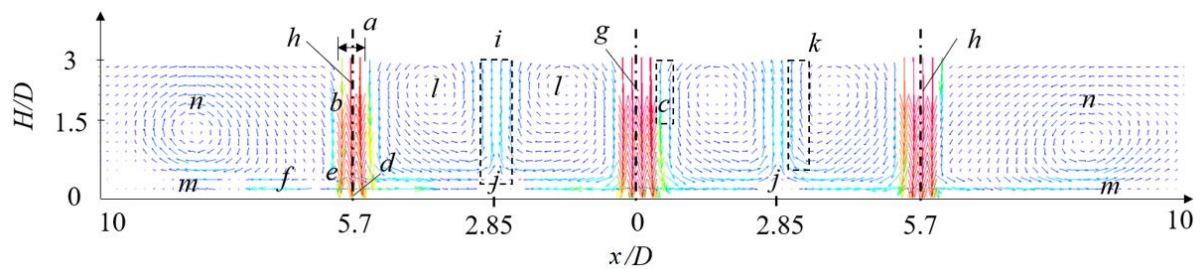


**Figure 5.** Flow regions of a multiple jet impingement for  $Re = 2,000$ ,  $S/D = 5.7$  and  $H/D = 3$ : (a) orifice nozzle; (b) free jet; (c) separation flow; (d) stagnation point; (e) stagnation region; (f) wall jet region; (g) central jet; (h) adjacent jets; (i) fountain flow; (j) collision point; (k) upwash flow; (l) primary vortices; (m) separation point; (n) vortices.

The flow exits the orifice nozzles [Figure 5 (a)] with a mostly flat velocity profile at a maximum value [21]. As the flow moves downstream, it progresses through a free jet region [Figure 5 (b)] in which jets and the surrounding air start to mix, leading to some flow separation [Figure 5 (c)] identified at the sides of the jets. Jets transfer momentum and entrain surrounding flow, leading to an increase of the jet's mass flow and a decrease of their energy and, consequently, a decrease of the velocity magnitude along jets periphery is observed [20] [27]. As the jets approach the target plate, the axial velocity decreases, reaching the stagnation point [Figure 5 (d)], and the flow is diverted radially. This is the stagnation region [Figure 5 (e)], characterized by a constant thin boundary layer [21]. After the impingement, the jets turn and the flow moves parallel to the target wall, entraining surrounding flow, growing in thickness, and decreasing in velocity magnitude. This is the wall jet region [Figure 5 (f)]. In this specific zone, [27] observed that the impinging surface starts to obstruct the flow leading to a deflection of jets into the wall-parallel direction. The remaining part of the spent fluid flows in direction of the outlet, generating a self-induced crossflow. This crossflow interaction can cause an asymmetric jet flow field, disruptions to other wall jets, movement of the stagnation points, thicker boundary layers, and a reduction of the average heat transfer rates [21]. The collision between the wall jets of the central jet [Figure 5 (g)] and adjacent jets [Figure 5 (h)] generate a fountain flow region [Figure 5 (i)], clearly identified on both sides of the central jet. The collision between

the two wall jets originates a second stagnation region at the collision point [Figure 5 (j)], and the rotation of the flow. Here, upwash flows [Figure 5 (k)] are induced, leading to an increase of the axial velocity in the jets shear layers and to a generation of recirculation regions on both sides of the central jet, identified by Caliskan et al. [28] as primary vortices [Figure 5 (l)]. These large primary vortices interfere with the flow development of the adjacent jets. While in the central jet the vortex ring is closed, the vortex flow of the jets located around it are pushed outwards.

The separation of the jet's flow from the wall occurs where the boundary layer detaches the surface of the target plate. The position of the separation point [Figure 5 (m)] moves away from the centerline of the jet with increasing the Reynolds number [24]. Looking at the vortices generated at the boundaries of the side jets [Figure 5 (n)], it seems that the separation point occurs at a higher distance from the jet axis, minimizing the interference of these vortices with the jet flow.

Considering that the behavior of the heat transfer in multiple jet impingement is highly influenced by the geometric variables and flow properties, but also by the roughness of the impinging surface, all these process variables need to be very well understood to enhance the heat transfer performance. In that sense, they will be referred to in the following section.

## 2.2. Influence of Process Variables

Although heat transfer by jet impingement is highly effective and easily controllable by changing the flow rate [29], it is highly heterogeneous and associated with complex interactions between a wide variety of parameters [30]. Therefore, a wrong combination between them can result in a decrease in heat transfer rates over the target plate. In that sense, these process variables are discussed in this section and Figure 6 identifies the terminology used.

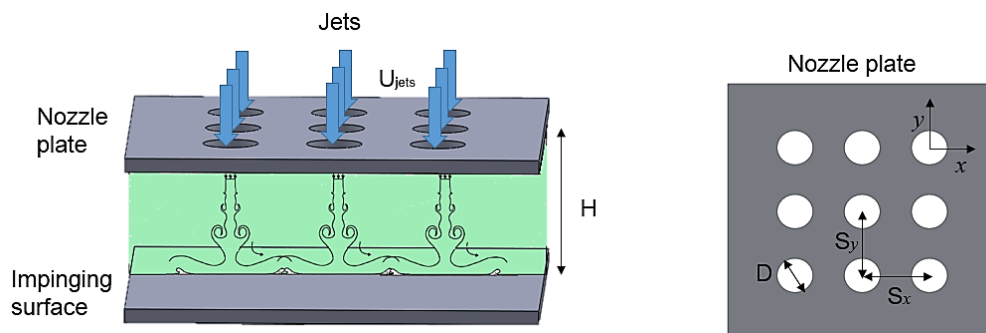


**Figure 6.** Basic geometric parameters in jet impingement.

The jet-to-jet spacing for regular arrangements ( $S_x = S_y = S$ ) and the nozzle-to-plate distances ( $H$ ) are usually expressed non-dimensionally by the dimensionless ratios  $S/D$  and  $H/D$ . While the first one represents the separation distance between two jets over the corresponding nozzle diameter, the second one refers to the distance between the nozzle and the target plates, divided by the nozzle diameter. In that sense, these ratios will be mentioned in the literature review.

Considering that the configuration of the exhaust section plays an important role in multiple-jet impingement systems since it highly influences all the other process variables, crossflow will be presented first.

### 2.2.1. Crossflow

Crossflow, defined as the flow that exits through the sides of the target surface (on a perpendicular direction to the jet impingement), can be generated by external flow or accumulated spent jet flow [31]. In multiple jet impingement, a crossflow arises essentially from the spent air of the accumulated jets, meaning that the flow and heat transfer of adjacent jets are influenced by this phenomenon [32]. However, crossflow can also appear from a free stream type flow, as it happens in the mid-chord region of gas turbine airfoils, which means that an external flow approaches the impinging jets from upstream. Considering that the crossflow due to spent air of the jets is the most common in cooling and heating of large areas, the literature review will focus on this crossflow type.

In a jet array configuration, the strength of the crossflow is defined by the exhaust configuration of the system and by the direction of the spent air flow. In that sense, the crossflow can be defined by three different schemes in multi-jet systems, as it can be observed in Figure 7: maximum, partial or intermediate, and minimum. The maximum or complete crossflow requires the confinement of the flow in one direction only. Consequently, the intermediate or partial crossflow is related to the confinement in two directions and the minimum crossflow to no restriction of the spent air away from the heat transfer surface [20].

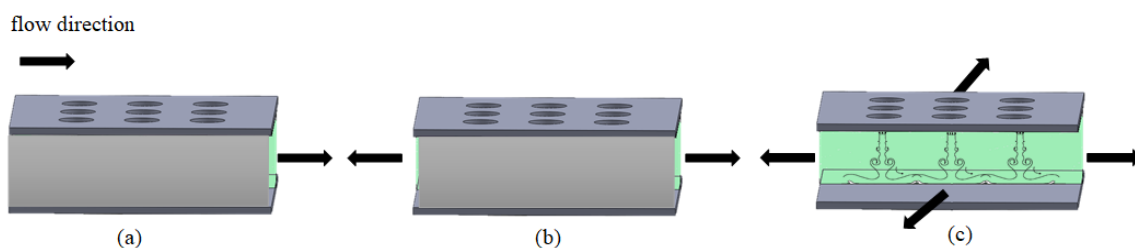


**Figure 7.** Crossflow schemes in multiple jet impingement (a) complete or maximum crossflow (b) partial or intermediate crossflow (c) minimum crossflow.

Considering the importance of the crossflow in jet impingement, this parameter needs to be fully understood and controlled to enhance the heat transfer performance. According to Viskanta [20], the heat transfer coefficient decreases with crossflow in a multiple jet array, since spent air from upstream jets interferes with the downstream jets and may worsen the heat transfer performance. Considering the complexity of multiple jet impingement due to the jet's interactions, several experiments were performed in order to understand the influence of crossflow on heat transfer and jets flow dynamics. In that sense, many researchers analyzed the effect of crossflow considering different geometrical variables (jet-to-jet spacing, nozzle-to-plate distance, surface roughness, etc.) and jet flow properties (temperature and Reynolds number).

Lee et al. [33] analyzed the effect of maximum crossflow, nozzle-to-plate distance ratio ( $H/D$ ), and jet-to-jet spacing ratio ( $S/D$ ) in a jet array and stated that the local Nusselt number is increased for  $S/D = 5D$  and  $1.5 < H/D < 3$  with streamwise development due to a significant accumulation of crossflow. This leads to an increase of the local shear stress and local turbulent transport downstream the impingement which is intensified by the confinement of the jets. These conclusions are also supported by the numerical analysis performed by [34] and [35] using Large Eddy Simulation (LES). Otero-Pérez et al. [34] mentioned that the maximum Nusselt number decreases linearly as a function of the jet-to-jet spacing, and according to Penumadu & Rao [35] the degrading effect of crossflow is more pronounced for the last jets of the array than for the first ones. It seems that the total vorticity magnitude of the first jets of an array exhibits a curly structure; however, for the last jets, this structure is lost due to the crossflow effects, affecting significantly the downstream jets. The degradation of the curly structure due to the increased crossflow was also predicted by [36], using the SST  $k-\omega$  turbulence model. These conclusions are obtained for maximum crossflow. For minimum crossflow, it is expected that the central jet of an array is less affected by the crossflow compared with the jets located close to the outlets, as observed by [37]. Li et al. [38] analyzed in detail the influence of the nozzle-to-plate spacing and found that lower  $H/D$  values (between 0.75 and 1.2) enhance the crossflow momentum and the interaction between downstream jets, increasing the local turbulence transport. This results in an increase of heat transfer coefficients due to an overall displacement of the jet core which increases the local turbulence transport, while at higher nozzle-to-plate distances ( $H/D > 3$ ), the effect is reversed. According to Florschuetz et al. [39] and Barata [40], this reduction of the cooling effectiveness of downstream jets, at  $H/D > 3$ , is due to the strong crossflow produced by the upstream jets and the diffusion/deflection of the downstream jets by this intense crossflow. While for highly confined spaces, the crossflow accumulation of jet flows increases the mixing caused by strong flow interactions, for less confined spaces, the individual

effect of each jet is more pronounced, and the crossflow induced by upstream jets diminishes the local heat transfer of downstream jets. Wae-Hayee et al. [31] demonstrated that a moderate crossflow velocity increases the peak value of the heat transfer of jet impingement due to the interaction between the crossflow with jets, increasing the turbulence of the jet upstream the impingement. However, high crossflow velocity decreases the peak value of the heat transfer due to the low momentum of the jet upstream of the impingement, which is in accordance with [34]. Recently, Lo & Liu [41] experimentally investigate the effect of crossflow and target plate geometry on heat transfer and found that intermediate crossflow is more effective than maximum configuration for both half-smooth and half-rough target surfaces.

To understand the effects of minimum, intermediate and maximum crossflow in a jet array, Obot & Trabold [42] performed an interesting work ( $1,000 < \text{Re} < 21,000$ ). Through their analysis, they concluded that the heat transfer is enhanced by a minimum crossflow. The heat transfer average decreases in the case of intermediate and maximum crossflow, being that a greater number of jets and the increase of  $H/D$  lead to a more pronounced degradation of the heat transfer. These results are in accordance with the numerical study developed by Brakmann et al. [43] for both flat and pin fin target surfaces. Furthermore, Xing et al. [44] concluded that the heat transfer is enhanced by the minimum crossflow and small nozzle-to-plate distances for both flat and dimple target surfaces. This conclusion is in agreement with the previous discussion. Figure 8 demonstrates the results obtained by Xing et al [44] and Obot & Trabold [42] for different crossflow schemes. As it can be observed, independently of the Reynolds number or target plate geometry, the minimum crossflow leads to higher average Nusselt numbers. In addition, the effect of crossflow configuration on heat transfer is more pronounced for low jet-to-jet spacing ( $S/D = 4$  and  $5$ ), compared with higher values ( $S/D = 10$ ). This difference is mainly due to the fact that at  $S/D = 10$ , the jets present a flow behavior similar to a single jet and therefore, the interactions induced by jet-induced crossflow are reduced.

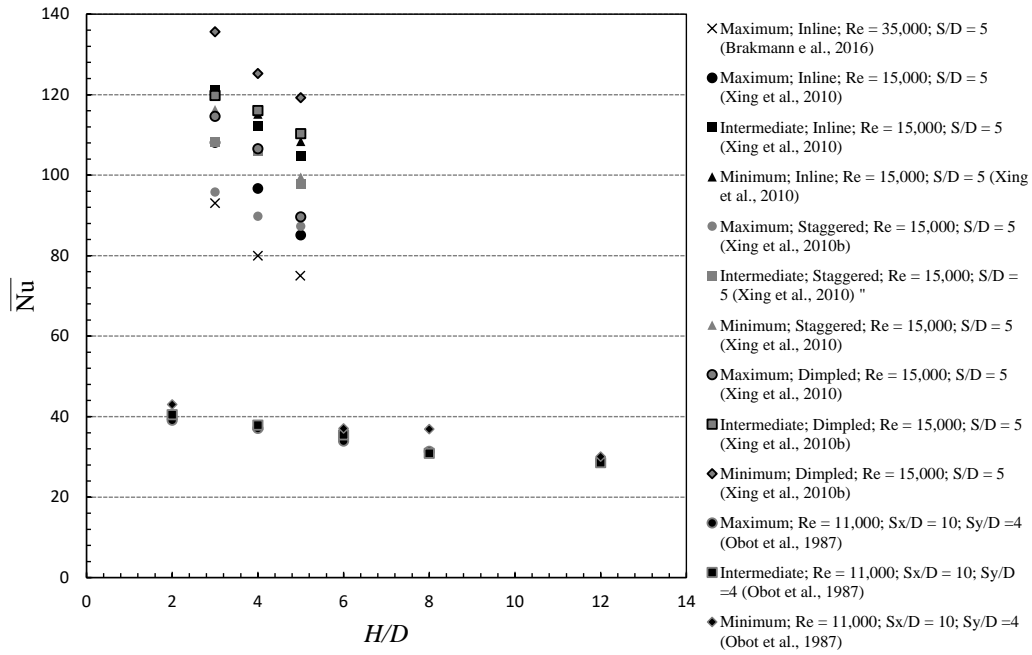


**Figure 8.** Influence of different crossflow schemes on the average Nusselt number for different nozzle-to-jet distances.

The crossflow can also be analyzed by the distribution of the cross-to-jet mass ratio, which represents the ratio between the mass flow rate of crossflow ( $G_{cf}$ ) and the mass flow rate of a single jet ( $G_j$ ). Li et al. [45] observed that the  $G_{cf}/G_j$  ratio is independent of the average Reynolds number. Terzis [46] added that, in the absence of crossflow ( $G_{cf}/G_j = 0$ ), the primary Nusselt number peaks are essentially induced by the vertical component of the velocity, while the secondary peaks emerge in a region where both velocity components are reduced. For low crossflow momentums ( $G_{cf}/G_j < 0.3$ ), upstream vortices are generated, enhancing the heat transfer coefficients. At higher crossflow momentums ( $G_{cf}/G_j > 0.4$ ), the streamwise velocity component is responsible for the convective heat transfer pattern, since in this case, jets clog the incoming crossflow promoting the convection. Harrington et al. [47] analyzed  $G_{cf}/G_j$  ratio for both plane and curvature surfaces and found no significant differences between these two cases.

### 2.2.2. Jet pattern

In multiple jet impingement, two jets configurations are possible, inline [Figure 9 (a)] and staggered arrays [Figure 9 (b)]. One of the first significant studies conducted to understand the influence of the jet pattern was presented by Florschuetz et al. [39]. These researchers analyzed the differences between inline and staggered jets configurations, mentioning that minor differences in average heat transfer were observed. However, these differences become significant for closely spaced arrays ( $H/D = 2$  and  $3$ ), large

jet separation distance ( $S/D > 5$ ), and increased crossflow. For such conditions, the inline array performs better in terms of average heat transfer rates [39, 48].

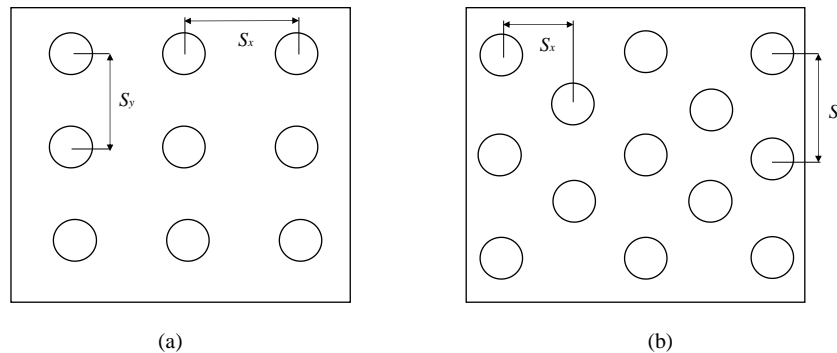


**Figure 9.** Jet pattern (a) inline; (b) staggered.

These observations are in accordance with [31, 44, 49] and are mostly supported by the fact that in a staggered configuration, the oncoming crossflow generated by the upstream jets affects the jets directly, leading to stronger diffusion of the flow and consequently to a decrease of the heat transfer rates. Xing et al. [44] observed that for different crossflow schemes, the inline pattern presents always higher heat transfer coefficients than the staggered one for different  $H/D$ , excepted for  $H/D = 5$  at maximum crossflow. It seems that in inline arrays, the downstream jets are protected by upstream jets, and the effect of the crossflow is reduced. However, other studies [7, 50, 51] found that the heat transfer over the target surface is slightly enhanced by the staggered configuration compared with the inline array. It seems that combining the staggered configuration with the confinement induces stronger interference of upstream jet-induced crossflow on downstream jets, slightly increasing the heat transfer over the impinging surface. This effect was also demonstrated numerically by [52], who found that staggered arrangements enhance the mixing and increase the flow velocity near the target plate, mainly due to the recirculation region induced between the adjacent jets. Pachpute & Premachandran [53] analyzed the effect of the jet pattern on cylinder cooling and found that for small jets spacing ( $S/D = 1.4$ ) and nozzle-to-plate distances ( $H/D = 2$ ), the staggered array enhances the cooling. However, the average Nusselt number of the staggered configuration is lower than inline for  $6 < H/D < 12$ . Moreover, according to the experimental work conducted by [50], it seems that higher Reynolds numbers increase the difference between the effects of inline and staggered arrangements.

From these studies, it is clear that the staggered arrangement increases the crossflow compared with the inline pattern. However, as previously mentioned, the degrading or improving effect of the crossflow on heat transfer depends on other variables such as  $H/D$ . While in highly confined spaces the crossflow

enhances the heat transfer due to the increased mixing between the jet flow and the ambient fluid, for high  $H/D$  values, since the jets have a lower momentum, the crossflow mainly reduces the heat transfer rates[31]. Therefore, it seems that for  $H/D > 3$  the inline arrangement performs better than the staggered one. Moreover, it seems that the difference between these two configurations increases with the Reynolds number. To clearly understand the relation between these variables ( $H/D$  and  $Re$ ) and the jet pattern, relevant experimental results are plotted in Figure 10.

First, it is clear that the lower the Reynolds number, the smaller, the difference between the two arrangements. However, the results obtained by [39] and [50], for low Reynolds number and  $H/D = 1$ , show that the staggered configuration induces higher heat transfer rates in the first jets of the row than the inline configuration, but the reverse is observed for the last jets of the row. Even if in both inline and staggered configurations the average Nusselt number decreases along the downstream direction, it is slightly higher in the case of the inline configuration. As the Reynolds number increases, the heat transfer rate also increases, and the staggered configuration seems to outperform the inline array. Looking at the results presented by [7], it seems that the heat transfer enhancement induced by the staggered configuration for  $S/D = 5$  is kept from the first to the last jet of the row while at  $S/D = 3$ , inline configuration presents better values from the 5<sup>th</sup> jet of the row. The protecting effect from the crossflow by the inline array is more evident for low  $S/D$  values, which seems to be in agreement with the other studies [39] and [50].

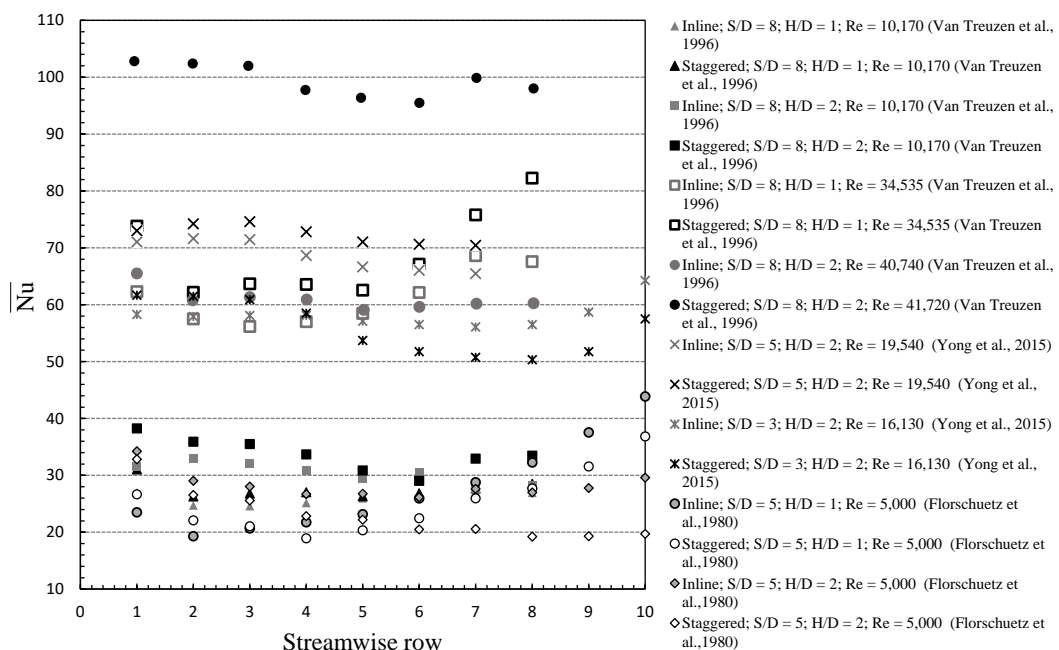


Figure 10. Influence of different jet pattern on the average Nusselt number for different Reynolds numbers,  $H/D$  and  $S/D$ .

In summary, this analysis shows that the effect of the jet pattern in heat transfer depends mainly on the jet-to-jet spacing and the nozzle-to-plate distance. Comparing the results presented by [7, 39, 43, 44, 50, 51, 53], it seems that for  $S/D \geq 3$  and  $H/D = 2$ , the staggered pattern enhances the heat transfer compared with inline arrays, due to stronger jet's interactions. While, for  $S/D < 3$  and  $H/D \geq 3$ , the degrading effects of crossflow are intensified, reducing the heat transfer over the surface. Therefore, in this specific case, an inline configuration increases the heat transfer rate due to the protecting effect of upstream jets on downstream jets from crossflow. This means that equilibrium must be found between the effect of the different variables on crossflow, in order to ensure that the turbulence intensity induced inside the confined space promotes the heat transfer and does not degrade it.

### 2.2.3. Jet-to-Jet Spacing

In multiple jet impingement, jet-to-jet spacing is a parameter extremely important since it influences the jet's interaction upstream the impingement of the target surface. Two jet-to-jet spacing configurations are possible, irregular arrangements, in which the spanwise ( $S_y$ ) and streamwise ( $S_x$ ) distances are different and regular arrangements, where  $S_x = S_y = S$ . Due to the added complexity of irregular arrangements, regular ones have been studied more frequently [54].

The jet-to-jet interaction is mainly caused by the upwash flows, already presented in Figure 5 (k), resulting from the collision of wall jets. Therefore, the interactions between jets before and after the impingement are intensified at low  $S/D$ , as confirmed in several studies [7, 27, 48, 55–60]. At the collision point, midway two jets, Figure 5 (j), a second heat transfer peak arises due to their strong interaction. Buchlin [61] explained that this phenomenon occurs due to the increase of the pressure gradient when two jets approach each other, inducing a thickening of the boundary layer which generates a flow separation, giving rise to a complex three-dimensional vortex. The remaining part of the spent fluid leaves the configuration, generating a self-induced crossflow which can cause an asymmetric jet flow field, disturbs other wall jets, moves stagnation points, thickens boundary layers, reducing the average heat transfer rates over the plate [21].

San & Lai [62] observed that, for small  $S/D$ , the interference between two adjacent jets occurs before the impingement due to the shear layer expansion, which weakens the jet strength, minimizing the heat transfer. In addition, Ichikawa et al. [29] verified that a small  $S/D$  ratio leads to an intensification of the effect of the interaction between adjacent jets and the velocity dispersion after the vortex roll-up affects the jet directly. Recently, Li et al. [38] and Chen et al. [63] found that higher  $S/D$  values reduce the heat transfer mainly due to inadequate surface coverage. These observations are in agreement with [48].

Considering the complex flow dynamics induced by jet interactions in multiple jet impingement, several studies focused on the analysis of the jet-to-jet spacing that enhances the average heat transfer rates. Metzger et al. [64] determined that the heat transfer is higher for configurations with  $S/D < 10$  in both streamwise and spanwise directions. Buchlin [61] observed that increasing the distance from the jet axis, the velocity dispersion increases at  $S/D = 4$  and  $S/D = 6$  due to the influence of vortex breakdown which induces large velocity dispersions [65]. From their analysis, San & Lai [62] concluded that the optimum jet-to-jet-spacing, considering a Reynolds number between 10,000 and 30,000, is 8 for a nozzle-to-plate distance equal to 2, 12 if  $H/D$  is equal to 3, and 6 for  $H/D$  equal to 5. Goodro et al. [66] observed that for a streamwise and spanwise distance equal to  $12 D$ , the jets show the behavior of an individual jet. However, decreasing the distance to  $8 D$ , the influence of the adjacent jets is strong, inducing crossflow and interactions. In that sense, the averaged Nusselt number is higher for a jet spacing of  $8 D$  than for  $12 D$  at the same conditions, as it can be observed in Figure 11. In its turn, Yong et al. [7] mentioned that for  $S/D = 3$  the highest heat transfer is observed at the same Reynolds number (16,130). However, considering the same mass flow rate of coolant per unit area of cooled surface, it seems that  $S/D = 5$  increases the heat transfer performance ( $Re = 19,540$ ), which is in agreement with [67]. Comparing  $S/D = 3$  with  $S/D = 2$ , the authors mentioned that at  $S = 2 D$ , due to the strong interactions between adjacent jets, the jet impingement behaves like a channel flow. This effect induces the jet's flow deflection prior to the impingement that weakens the normal penetration of the jets and decreases the jet's momentum, reducing the heat transfer. At  $S = 3 D$ , the increase of the Nusselt number shows that the interaction between jets prior to the impingement is weaker when compared with  $S = 2 D$ , allowing the wall jet to develop over the surface, leading to an increase of the local heat transfer. Overall, higher jet-to-jet spacing values ( $S/D > 3$ ) result in less effective surface coverage, leading to a decrease in local heat transfer.

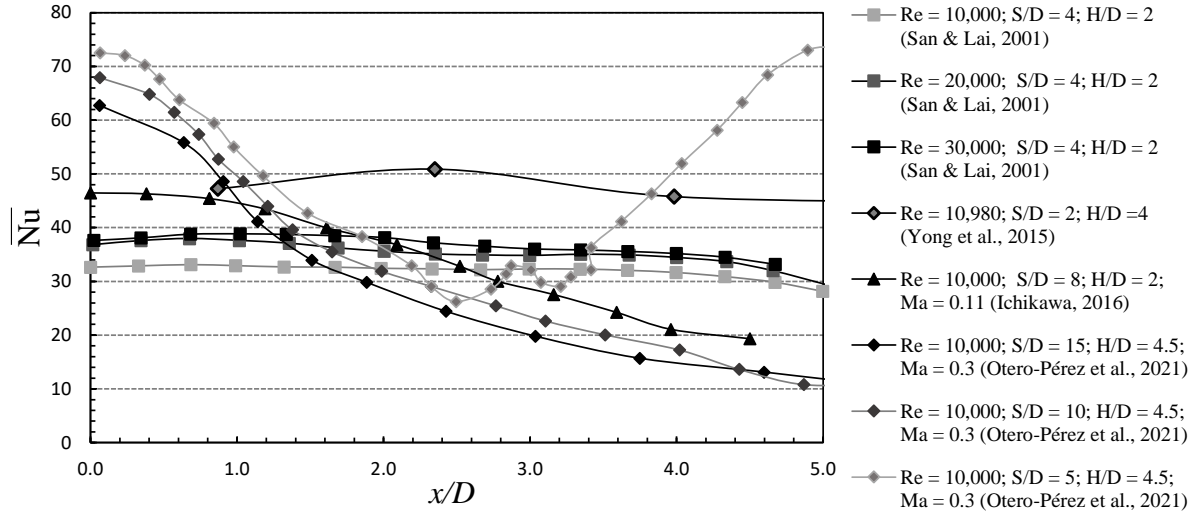


**Figure 11.** Averaged Nusselt number in function of the streamwise direction at different  $Re$  numbers,  $S/D$  and  $H/D$  spacing.

Based on numerical results, Badra et al. [55] concluded that the interaction between jets occurs at  $S/D < 10$ . Jet's interference is intensified at  $S/D = 2$ , resulting in heat transfer enhancement. However, for  $S/D > 10$ , this interaction disappears, and the two adjacent jets behave as a single jet with a symmetric profile is observed in both jets. Through a LES simulation, Draksler et al. [27] mentioned that  $S/D = 2$  allows that the individual jet of a multiple jet array preserves some of the typical characteristics of a single jet, enabling at the same time the development of jets interactions. Barbosa et al. [56] found through RANS simulation that the size of recirculation flow between two jets increases with the separation ( $S/D > 4$ ), leading to a deviation of the secondary stagnation point. This is not observed for  $S/D = 2$  and 3 and so, higher heat transfer rates are obtained for these two cases. Recently, Otero-Pérez et al. [34] perform a parametric study on turbulent multi-jet impingement cooling using LES for  $H/D = 4.5$ ,  $Re = 10,000$ ,  $Ma = 0.3$ , and different jet-to-jet distances ( $S/D = 5, 10, \text{ and } 15$ ). Their results demonstrate that as  $S/D$  increases the Nusselt number decreases. In addition, at the midpoint between two adjacent jets, they observed that the heat transfer is dominated by the interaction of two developing boundary layers induced by the wall jets. Regarding the central jet, the Nusselt number peak decreases with the increasing the  $S/D$  ratio. Compared with a single jet, the results show that the cooling effect is slightly reduced due to flow recirculation induced by the wall jets collision which increases the temperature in the vicinity of the central jet. However, the surface coverage is increased, leading to an increase of the average heat transfer over the surface. Regarding a moving target plate, results obtained by [68] and [69] demonstrate that the Nusselt number decreases with the increase of  $S/D$ , as for the static plate case.

Through the analysis of the literature, summarized in Figure 11, it seems that experimental and numerical results agree that the higher the  $S$  the less effective the surface coverage, leading to a decrease in local heat transfer. A large distance between jets reduces the interaction between the wall jets and weakens the jets induced crossflow, reducing the turbulence and consequently the local and average Nusselt number. This is clearly observed in Figure 11, comparing the results obtained by Yong et al. [7] for  $S/D = 2$  with those presented by San & Lai [62] and Otero-Perez et al. [34], for a Reynolds number close to 10,000. In addition, Figure 11 shows that higher Reynolds and Mach numbers increase the heat transfer for the same  $S/D$  conditions and that the  $H/D$  is another parameter that plays an important role in the heat transfer efficiency. Therefore,  $H/D$  is analyzed in detail in the next section.

#### 2.2.4. Nozzle-to-Plate Distance

Amongst the different process variables, nozzle-to-plate distance ( $H$ ) is considered one of the most important geometrical parameters in jet impingement due to its strong influence on heat transfer performance. As stated by [45], the effect of  $H/D$  is the result of the interaction between jet momentum and locally generated crossflow. In that sense, for both single and multiple jets, confined jets (low  $H/D$  values) induce higher heat transfer rates, as mentioned by several authors [9, 48, 64, 70, 71].

Garimella & Schroeder [72] demonstrated experimentally that a decrease in  $H/D$  leads to an increase of the heat transfer coefficients, due to higher levels of turbulence intensity induced in the confined space, increasing this effect at higher Reynolds numbers. Reodikar et al. [73] observed that the Nusselt number distribution is more uniform for lower  $H/D$  values, due to the uniform velocity profile in the potential core region of the jet. This is valid for both single and multiple jet impingement as recently demonstrated by [37]. The jet's flow structure obtained by PIV analysis shows a thicker wall jet for lower  $H/D$  induced by stronger interactions between jets and the surrounding air in a confined space. Increasing the  $H/D$  value, larger primary vortices are generated. These large but weak vortices interfere with the flow development of the adjacent jets and reduce the heat transfer in the vicinity of the target surface. These observations are supported by Ichikawa et al. [29], who determined, through PIV, that a small impinging distance increases the jet's momentum around the impingement, leading to a bigger and stronger roll-up structure of the vortex. Ozmen & Ipek [74] found a significant increase of the pressure near the stagnation points at low  $H/D$  followed by a pressure decrease as the flow accelerates along the target surface. Furthermore, they identified that the primary stagnation Nusselt numbers and heat transfer ratios increase with the decrease of  $H/D$  and the pressure's peak at the jet's stagnation point decreases with increasing this distance. Shariatmadar et al. [75] stated that large  $H/D$  decreases the heat transfer performance due to

a decrease of jet's momentum before the contact with the surface. Considering a target surface with roughness (in this case micro pin fins), the study performed by Brakmann et al. [43] showed that the Nusselt number decreases with increasing the nozzle-to-plate distance, being more pronounced in this target surface than in flat plate. These observations are supported both experimentally and numerically by Tepe et al. [76]. Even when inclined nozzles are applied, the trend is still the same: smaller  $H/D$  increases the averaged Nusselt number over the wall. However, studies conducted by [39, 44, 45] show that at  $0 \leq H/D \leq 1.2$  the heat transfer is lower than at  $H/D = 2$ . According to [45], as the flow accelerates in direction to the outlet, the pattern of the Nusselt number is shifted from a circular shape to a horseshoe vortex shape distribution. A large discrepancy is observed between the local jet momentum of the upstream jets and downstream jets, being the first ones lower than the second ones. This induces lower average heat transfer rates, and it is called crossflow-dominated impingement flow.

To determine the value of the nozzle-to-plate distance, that enhances the heat transfer, several studies were conducted. Xing & Weigand [44] analyzed experimentally multiple jets impinging on a flat and dimpled surface with different crossflow schemes and Reynolds numbers ranging between 15,000 and 35,000. They observed that heat transfer performance is enhanced at  $H/D = 3$  and minimum crossflow, on both flat and dimpled plates [77]. Caliskan et al. [28] studied experimentally and numerically the effect of  $H/D$  over a flat and non-flat surface and found that the heat transfer performance at  $Re = 10,000$  is higher for  $H/D = 2$ . Yong et al. [7] analyzed the convective heat transfer for multiple air jets in a semi-confined channel for a Reynolds number between 5,000 and 25,000 and observed that the strong interference between adjacent jets at  $H/D = 2$  increases the heat transfer over the target surface. Li et al. [45] determined the effect of  $H/D$  on the cooling performance of a jet array ( $5,000 < Re < 25,000$ ) and showed that the Nusselt number is increased by the increase of the  $H/D$ , reaching a peak value at around  $H/D = 2$ . These results are in agreement with several numerical and experimental studies [28, 29, 45, 60, 78–80]. This enhanced efficiency is enlightened by the generation of strong vortices in a confined space, while larger distances reduce both crossflow and jet's momentum, decreasing the heat transfer over the target surface [51].

These studies demonstrated that the heat transfer over an impinging surface is enhanced when  $H/D = 2$ . As it can be observed in Figure 12, regardless of the experimental conditions, such as jet pattern,  $S/D$  spacing, Reynolds number, and surface roughness, the Nusselt number decreases with the increase of  $H/D$  in multi-jet configurations. This decrease seems to be more pronounced for higher Reynolds numbers and complex surfaces.

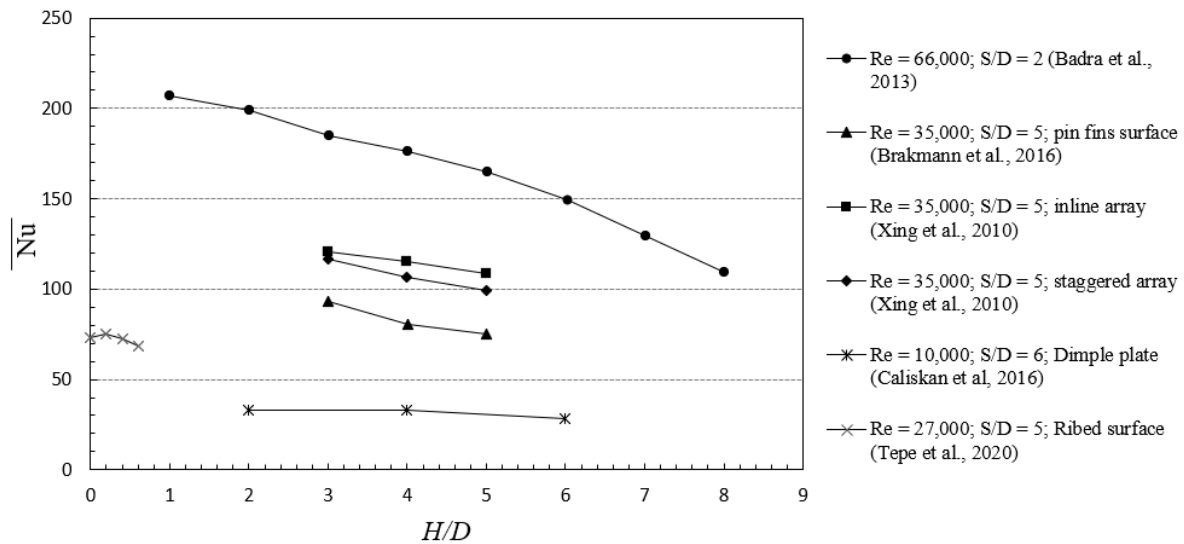


Figure 12. Average Nusselt number in function of the  $H/D$  spacing.

### 2.2.5. Jet Velocity

The jet velocity, as defined by the Reynolds number, is crucial in jet impingement processes since it strongly influences the local, line-averaged, and area-averaged Nusselt number [66]. Each study uses a specific range of Reynolds numbers, some authors decided to perform their studies on laminar flows others in turbulent ones. Air jets exhibit a typical laminar flow at  $Re < 1,000$ , becoming fully turbulent at  $Re > 3,000$ . In that sense, the transition region occurs at  $1000 < Re < 3,000$  [21]. Through the analysis of the research performed in jet impingement, most of the studies focus on turbulent flows since turbulence induces higher heat and mass transfer rates. Due to this fact, a typical gas jet installation for heat transfer works at a Reynolds number ranging between 4,000 and 80,000 [21].

According to the researches conducted for a single and multiple jet impingement, a higher Reynolds number increases the local heat transfer coefficient throughout the target surface [38, 53, 77, 79, 81–85]. High Reynolds number increases the flow turbulence which promotes the mixing between the jet's flow and the surrounding air, increasing the heat transfer. According to Jensen & Walther [82], high turbulence levels are generated near the stagnation point for high jet Reynolds numbers, increasing the heat transfer rates. Shariatmadar et al. [75] mentioned that at lower Reynolds numbers a decrease of the local Nusselt number over the target plate is observed since the strength of the jet momentum is not enough to reach the surface uniformly. Chandramohan et al. [79] complemented the idea stating that at a particular Reynolds number, as the nozzle-to-plate distance increases, the jet flow can mix and becomes wavier leading to a decrease of the heat transfer coefficient. Li et al. [38] detected that the flow structure is qualitatively similar at different Reynolds numbers and by increasing this parameter five times (5,000

to 25,000) an increase of the Nusselt number by a factor of 3.5 is observed. This is in agreement with Park et al. [81] who mentioned that regardless of the Reynolds number used, the qualitative distribution of the local Nusselt number induced by each jet is similar. In terms of cooling efficiency optimization, it seems that it is more efficient to increase the Nusselt number through the increase of the Reynolds number and the non-dimensional area ( $A_f = \text{total nozzle exit area}/\text{total target area}$ ). These results are in agreement with several studies which perform an analysis of the effect of different process variables on heat transfer [59, 60, 79, 86].

Figure 13 summarizes the results obtained by several authors, showing clearly that the average Nusselt number increases with increasing the Reynolds number regardless of the nozzle-to-plate and jet-to-jet distances, supporting the discussion previously presented.

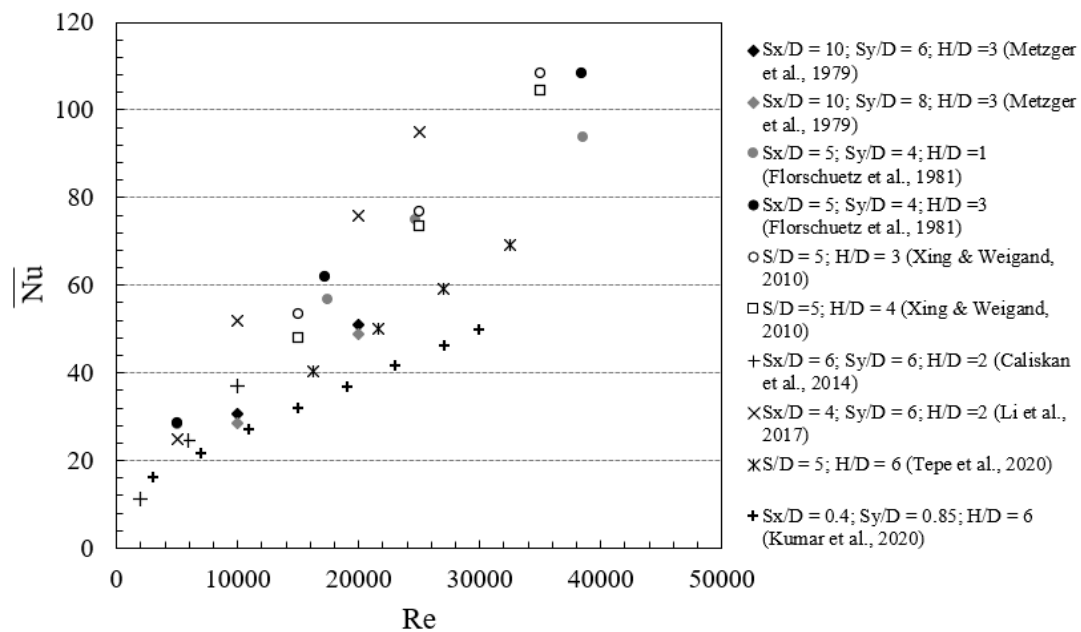


**Figure 13.** Average Nusselt number variation in function of the Reynolds number for different jet-to-plate and jet-to-jet distances.

## 2.2.6. Target Plate Geometry

One of the biggest challenges of the multiple jet impingement is the difficulty to obtain uniform temperatures over the impinging surface. If the complexity of the surface is increased, more hot/cold spots can appear, leading to product defects. In order to understand the influence of the target plate geometry on heat transfer performance, several studies have been conducted. Different geometries can

be considered, from ribs and pin fins to dimples. Since their effect on heat transfer is different, they are presented separately.

#### a) Ribs

Ribs, depicted in Figure 14, are applied over impinging surfaces to increase the turbulence and the effective surface area [21]. In order to understand the effect of ribs on heat transfer performance, several studies have been conducted. Spring et al. [87] combined experimental and numerical investigation of turbulent flows ( $Re = 35,000$ ) and determined that ribs did not improve the heat transfer coefficients in inline arrays configurations, while for staggered jet pattern, an enhancement is observed. This is explained by the fact that ribs help to minimize the strong degrading effects of the crossflow. The analysis of the pressure loss shows that ribs do not increase the pressure drop, since a reduction of the mixing and turbulence induced by the interaction between the crossflow and the jet flow is observed. This is in accordance with Andrews et al. [88]. The last authors added that ribs do not contribute to an improvement of the surface average heat transfer compared with a flat plate. The main effect of ribs is to change the axial dependence of the heat transfer on the crossflow. In the absence of crossflow, ribs reduce turbulence over the surface, removing the aerodynamics interactions between jets on the target surface. As concluded by Andrews et al. [88], smooth ribs with co-flow improve the heat transfer compared with slotted ribs configuration since secondary flows in the channels between the ribs are induced. Regarding ribs shape, Annerfeldt et al. [89] mentioned that triangle-shaped, wing-shaped, cylindrical, and rectangular elements enhance the Nusselt number by a factor from 1 to 1.3 for cooling application and recommended the use of rectangular ribs or cylinders. Further, Caliskan & Baskaya [90] investigated the heat transfer in an inline impingement jet array on smooth and rib-roughened surfaces according to two configurations: V-shaped ribs (V-SR) and convergent-divergent ribs (CD-SR). Through their analysis, they concluded that both configurations increase the heat transfer coefficient over the surface from 4 % to 26.6 % when compared with a flat plate. Their results show that V-SR configuration presents a higher average heat transfer than CD-SR since this structure generates vortices that increase the mixing of the flow, enhancing the heat transfer. V-SR disturbs the boundary layer induced by jet impingement inside the rib cavity, which creates a higher turbulence, especially at  $H/D = 2$ . Alenezi et al. [91] and Tepe et al. [76] highlight the importance of the rib height since too height rib can induce lower heat transfer rate compared with flat plates. In height ribs, the flow must travel a longer distance between the wall and the upper edge of the rib before the re-attachment. In that sense, it seems that a rib height that matches with the boundary layer thickness, and located between the stagnation region and

the wall jet region, enhances the local heat transfer mainly due to the increased turbulence induced by the flow recirculation upstream and downstream the rib [91]. Shukla [92] analyzed the effect of ribs using different RANS models and found that a detached rib configuration enhances the heat transfer rates compared to attached ribs due to flow acceleration in the space between the plate and the rib.

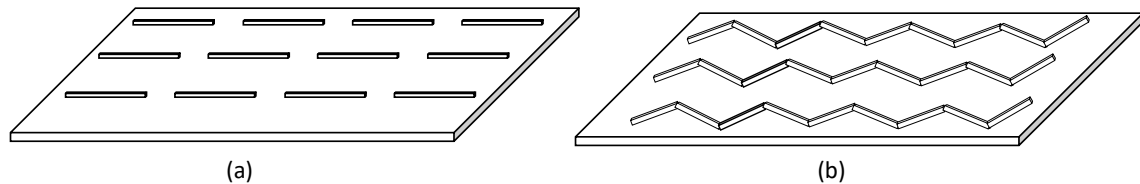


**Figure 14.** Ribs structure (a) Longitudinal ribs; (b) V ribs.

#### **b) Small-scale pin fins roughness**

Brakmann et al. [43] analyzed the influence of micro cube-shaped pins (Figure 15) on the target surface ( $15,000 < Re < 35,000$ ) and concluded that pin fins increase the target area by 150 % in comparison with a flat plate. This increases the convective heat transfer between 135 % and 142 %. In terms of the flow field, the airflow that goes through a pin is separated, creating a vortex on the downstream side of the pin. This leads to a decrease in heat transfer and an increase in pressure loss in this zone. Furthermore, Ligrani et al. [93] studied the influence of small-scale cylinders in the target plate and observed that the increase of the height of small cylinders leads to an increase of the local mixing, vorticity, turbulent thermal transport, and thermal resistance, generating a substantial thermal insulation barrier. These elements increase the target area by 47 % for a height of  $0.125 D$ , 71 % for  $0.188 D$  and 94 % in the case of  $0.250 D$ . Buzzard et al. [84] proved that, for  $Re$  ranging between 900 and 11,000, the average Nusselt number is increased by small rectangle roughness height, since the increase of the height leads to an increase of the local vorticity and larger amounts of mixing. In addition, for laminar flows, plates with small roughness alone present higher Nusselt numbers than plates with a combination of small and large roughness. However, the inverse situation is observed when the flow is turbulent. According to Ren et al. [94], this is due to two reasons: firstly, in turbulent flows, the combination of large and small pins increases the mixing of the flow, increasing the convective heat transfer at the surface; secondly, in laminar flows, the extra material provided by large rectangles generates an insulating effect. Regarding the effective surface area, Ren et al. [94] registered that small rectangle roughness alone increases this area by 60 % and 120 % compared with the smooth target surface. However, for the combination between large and small rectangles, this increase varies between 105 % and 160 %. In

addition, these authors mentioned that the combination of large and small triangle roughness presents little advantages compared with small triangle roughness alone. This is explained by the fact that small triangle roughness arises the Nusselt number due to their sharper corners that generate a more turbulent mixing, increasing the vorticity within the flow. This configuration induces a higher averaged Nusselt number and higher surface convective heat transfer rates compared with small rectangle roughness elements (at the same height and Reynolds number). The combination of large rectangles and small triangles roughness induces higher average Nusselt numbers than small triangle or rectangle roughness alone, leading to an increase of the effective surface area between 92 % and 132 % compared with a smooth target surface.

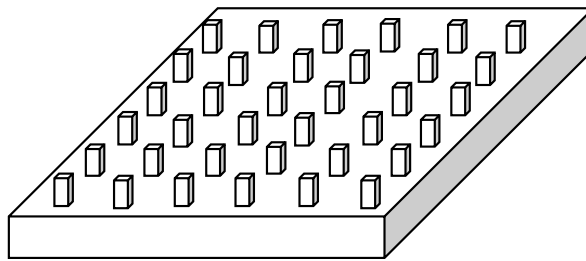


Figure 15. Micro pins structure.

### c) Dimples, grooves, and protrusions

Xing & Weigand [77] proved that the application of dimples (Figure 16) over the target plate leads to an increase of 26.4 % of the effective surface area compared with a flat plate. Regarding the crossflow scheme, an increase of 6.2 % of the heat transfer coefficient is recorded for a maximum crossflow. This phenomenon is explained by the fact that dimples enhance the heat transfer of the channel flow. For medium crossflow, dimples worsen the heat transfer coefficient by 10 % since the recirculation flow generated inside the dimples cannot escape fast from them. This value is improved by the minimum crossflow scheme (for  $H/D = 3$  and  $Re = 35,000$ ) in 12.3 %, essentially due to the full usage of the dimple edge to make the boundary layer thinner and to increase the crossflow velocity. Kanokjaruvijit & Martinez-Botas [95] observed that at  $H/D \leq 2$ , the dimples did not improve the heat transfer compared with the flat plate due to the occurrence of strong recirculation. Nevertheless, considering a higher  $H/D$  value, dimples lead to an improvement of the heat transfer. They also concluded that a small dimple curvature ( $D/D_d = 0.25$ , where  $D$  is the jet diameter and  $D_d$  the dimple diameter) leads to a lower heat transfer value when compared with a flat plate while higher values (0.50 and 1.15) improve the heat transfer. Moreover, a shallow dimple ( $d/D_d = 0.15$ , where  $d$  is the dimple depth measured from edge to

bottom of dimple) increases the heat transfer by 48 % while deep ones induce an improvement of 23.4 % compared with a flat plate. Ortega-Casanova & Granados-Ortiz [96] performed a numerical study to analyze the influence of dimples and bumps and compared the data with experimental results. They analyzed two regions separately, the stagnation point and the whole plate. In the former region, it was observed that heat transfer can be increased by dimples. In the second region, bumps provide higher heat transfer coefficients than flat plates. They also mentioned that for large nozzle-to-plate distance, target surfaces with geometrical variations do not present any benefits in increasing the heat transfer performance when compared with flat plates, excepted for dimpled plates at the stagnation point.

Later, Jing et al. [97] numerically found that the local heat transfer is improved near the dimple/protrusion surface while the averaged Nusselt number over the surface deteriorates. In addition, the authors show that the triangular rib-protrusion arrangements generate strong vortices which worsen the flow structure. Yuan-Hsiang & Yao-Hsien [41] experimentally investigated the heat transfer distribution from multiple jets impinging target plates with different roughness, at  $2,500 < Re < 7,700$ , and found that the change in surface geometry broke the flow development and enhance the flow mixing. Their study demonstrates that partially rough surfaces increase the heat transfer by 50 % for the case of longitudinal grooves. A recent research conducted by Nagesha et al. [98] at  $10,000 < Re < 27,500$  mentions that the heat transfer enhancement in rough target surfaces is due to area increase and to turbulence enhancement. However, this enhancement depends on the target shape. For example, while multi-protrusions increase the turbulence generation, this increase is not observed in V-grooves due essentially to the air trapped inside the cavities.

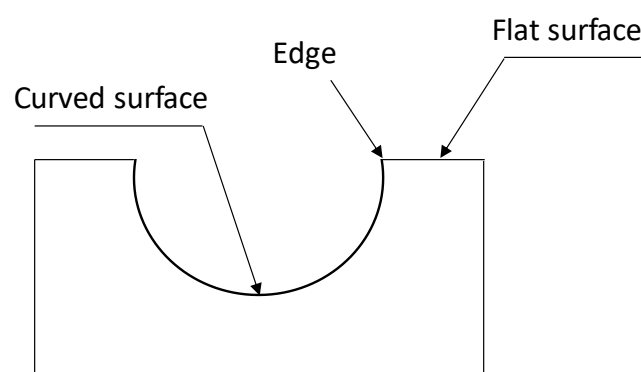


**Figure 16.** Dimple configuration (adapted from [77]).

### 2.2.7. Target Plate Motion

Several industrial applications require moving target surfaces, such as reflow soldering, drying, and food processing [99]. However, the complexity of the flow field is highly increased by a moving surface. As the flow analysis is very challenging, and several studies have been conducted. However, few experimental works are found in the literature.

Raju & Schundler [100] determined experimentally the heat transfer between a single air jet and a continuously moving surface, considering different jet velocities,  $4 < U_j < 40$  m/s, and target surface velocity motion,  $0.15 < U_s < 5.5$  m/s. They found that the maximum heat transfer coefficients are about 1.5 to 2.0 times higher than those obtained on a stationary surface. Senter & Sollic [101] analyzed a turbulent slot air jet impinging a moving flat plate at  $Re = 5,300, 8,000, \text{ and } 10,600$ , using a Particle Image Velocimetry (PIV) measurement technique. Varying the surface-to-jet velocity ratios ( $V_s = U_s/U_j = 0, 0.25, 0.5, \text{ and } 1$ ), they found a slight modification of the flow field for a surface-to-jet velocity ratio equal to 0.25, while at higher ratios the flow field is highly affected. Or et al. [102] compared both stationary and moving surfaces impinged by a circular jet using PIV and Laser-Induced Fluorescent (LIF) techniques. Their results show a reduction of the jet potential core length in a moving environment, mainly due to the strong turbulence generated by the plate motion. Mobtil et al. [103] designed an experimental method with an inverse technique to determine the heat flux distribution on a moving wall induced by a single air jet. They tested different  $V_s$  (0, 0.29, 0.57, 1.15) and found that even for high  $V_s$  the estimation of the heat flux distribution using their new method is accurate. Barbosa et al. [104] analyzed the effect of isothermal multiple jets ( $Re = 690 \text{ and } 1380$ ) impinging on a moving flat plate using a 2D-PIV technique and found that, even for low velocity ratios  $V_s = 0.0006 \text{ and } 0.0012$ , the jets are deflected by the plate motion. The thickness of the boundary layer increase in direction of the motion and the jets-induced crossflow is intensified. Compared with single jets, it seems that the effect of the plate motion is intensified in multiple jet impingement since the air movement in the vicinity of the target plate intensifies the jet's interactions, and the jets induced crossflow increases the complexity of the flow. Therefore, increased mixing is expected to occur, leading to higher average heat transfer.

Although the experimental analysis of air jets impinging a moving plate is scarce, several numerical works have been conducted. Regarding a single jet impingement, Chattopadhyay et al. [105] performed a numerical study of an unconfined slot jet using the LES model. Their results indicate that total heat transfer is reduced with increasing the plate velocity. At a velocity ratio,  $V_s$ , higher than 0.5 the reduction of the heat transfer can be more than 40 %. Sharif & Banerjee [14] applied a  $k-\varepsilon$  turbulence model to

analyze the heat transfer due to confined slot-jet ( $Re = 5,000$  to  $20,000$ ) impinging on a hot moving plate ( $0 < V_s < 2$ ). The numerical results show that at low  $V_s$  the impinging effect of the jet controls the flow and heat transfer behavior while at high  $V_s$ , shear-driven flow gradually dominates the overall flow and thermal fields. The jets get distorted and skewed in the direction of the plate motion and the average Nusselt number increases. Aghahani et al. [106] analyzed the heat transfer of a turbulent jet impinging ( $3,000 < Re < 60,000$ ) a plate moving at a high velocity ratio ( $0 < V_s < 6$ ) using the  $v^2-f$  turbulence model. The authors found that the motion increases the average Nusselt number for  $V_s > 1.25$ . Furthermore, these high velocity ratios limit the impact of the jet on the plate and therefore, no stagnation point is formed, and flow is similar to Couette flow. Achari & Das [107] applied the Yang-Shih version of the low Reynolds number  $k-\varepsilon$  turbulence model to study a turbulent slot jet ( $Re = 15,000$ ) impinging a moving plate. Their results demonstrated that the magnitude of the skewness of the flow field increases with a high surface-to-jet velocity ratio and the stagnation pressure seems to decrease with increasing the plate velocity beyond  $V_s = 0.75$ . Rahimi & Soran [108] studied the effect of a laminar slot jet ( $Re = 500$ ) impinging on a moving plate on heat transfer and compared the results with a moving nozzle. The results demonstrated that as the velocity ratio increases, the flow field is gradually dominated by the shear-driven flow. Regarding the average Nusselt number, it seems to decrease as the velocity ratio increases, declining more rapidly for the case of a moving nozzle.

Working with multiple jets, Badra et al. [55] applied the SST  $k-\omega$  and the  $v^2-f$  turbulence models and a sliding mesh method to determine the effect of an array of air jet ( $5,000 < Re < 30,000$ ) and considered that the relative velocity between the plate and its surroundings is equal to the plate velocity. The results obtained from their simulation show that as the plate approaches the leading jet, sharper temperature gradients are observed at its center point due to the high temperature difference between the jet and the plate. Aldabbagh & Mohamad [68] analyzed numerically the effect of a laminar air jet array ( $100 < Re < 400$ ) impinging on a moving plate ( $0.25 < V_s < 1.0$ ) using a three-dimensional laminar flow model. They found an increase in the average Nusselt number with the surface velocity ratio. It seems that at  $V_s > 0$ , the movement of the plate acts as a crossflow effect over the first jets column, generating horse-shoe vortices around them. The increase of the velocity increases this crossflow effect which results in the absence of ground vortex formation in front of the second and third columns of the jet array. Further studies were conducted by Kadiyala & Chattopadhyay [109] who applied the SST  $k-\omega$  model to numerically simulate the effect of an array of jets impinging a moving plate ( $100 < Re < 5,000$ ) and the velocity ratio considered varies between 0 and 6 and  $H/D = 2$ . Their results highlight that the Nusselt number only presents a higher value than the stationary case for non-dimensional surface velocity,  $V_s$ ,

ranging between 4 and 6. This increased heat transfer is mainly due to the stretching of the vortices along the direction of the motion. Increasing the Reynolds number, the surface velocity that increases the Nusselt number is equal to 6. Liu et al. [110] implemented a  $k-\varepsilon$  model to predict a three-dimensional multiple jet impingement using different jet geometries. A static plate is compared with a plate moving at 0.02 m/s and the results show an improvement of the cooling rate for the case of the moving plate impinged by V-shaped slot jets. Chitsazan & Glasmacher [111] analyzed the influence of the nozzle-to-plate distance ( $0.5 < H/D < 6$ ), jet-to-jet spacing ( $4 < S/D < 10$ ), jets angle ( $45^\circ$  to  $90^\circ$ ), and velocity ratio ( $0 < V_s < 1$ ) on heat transfer performance. The results demonstrated that interactions between jets are intensified for small  $H/D$  and high  $V_s$ . However, high jet inclinations decrease the heat transfer. Shah [69] applied the SST  $k-\omega$  model to compare the heat transfer over a moving plate impinged by a single and multiple jets for different  $V_s$  (0.25 to 2),  $S/D$  ( $2D$ ,  $4D$ , and  $6D$ ),  $H/D = 6$  and  $Re = 26,000$ . They found that while for a single jet the average Nusselt number remains almost constant for  $0 < V_s < 0.75$  and increases drastically for  $V_s > 0.75$ , in multiple jet impingement it increases smoothly with  $V_s$ .

### 2.2.8. Correlations for average Nusselt Number

The main objective of the study of multiple jet systems, from a practical point of view, is to develop a correlation for both average and local Nusselt numbers, to determine, with accuracy, the heat transfer performance of a specific industrial process. However, correlations to find a reasonable empirical correlation in multiple jet impingement requires the consideration of many additional factors, such as Reynolds number, jet pattern, nozzle-to-plate distances, jet-to-jet spacings, crossflow, jet velocity, open area, among others.

Considering the huge variety of parameters that need to be considered in multiple jet impingement studies, several correlations were developed, always taking into consideration a limited range of values for each parameter. However, correlations for single jet impingement are the basis for jet impingement studies, therefore they are also presented in this section. The selection of these correlations was based on the range of parameters that are of interest in this study.

Table 1 summarizes the relevant empirical correlations determined by experimental work for both single and multiple jet impingement. As it can be observed, some coefficients are determined by graphical analysis and therefore, the results obtained by the authors must be analyzed and adapted for each case study.

Table 1. Correlations for average Nusselt number.

Reference	Average Nusselt number ( $\overline{Nu}$ )	Limitations	Comments
<b>Single Jet Impingement</b>			
Huang [112]	$\overline{Nu} = 0.022 Re^{0.87} Pr^{0.33}$	$1,000 \leq Re \leq 10,000$ ; $1 \leq H/D \leq 10$ ; $0 \leq r/D \leq 20$ .	Single round nozzle
Gardon & Akfirat [113]	$\overline{Nu} = 0.78 Re^{0.55}$	$Re > 2,000$ ; $H/D > 12$ ; $1 \leq r/D \leq 24$ .	Single round nozzle
Martin [19]	$\overline{Nu} = Pr^{0.42} \frac{D}{r} \frac{1 - 1.1(D/r)}{1 + 0.1(H/D - 6)D/r} 1.36 Re^{0.574}$	$2,000 \leq Re \leq 30,000$ ; $2 \leq H/D \leq 12$ ; $0.004 \leq A_f \leq 0.04$ ; $2.5 \leq r/D \leq 7.5$ .	Single round nozzle
Tawfek [114]	$\overline{Nu} = 0.453 Pr^{1/3} Re^{0.691} (H/D)^{-0.22} (r/D)^{-0.38}$	$3,400 \leq Re \leq 41,000$ ; $6 \leq H/D \leq 58$ ; $2 \leq r/D \leq 30$ .	Single round nozzle
Lytle & Webb [115]	$\overline{Nu}_{out\ to\ r/D=1} = 0.424 Re^{0.57} (H/D)^{-0.33}$ $\overline{Nu}_{out\ to\ r/D=2} = 0.150 Re^{0.67} (H/D)^{-0.36}$	$3,600 \leq Re \leq 27,600$ ; $0.1 \leq H/D \leq 1$ .	Single round nozzle
Wen & Jang [116]	$\overline{Nu} = 0.442 Pr^{1/3} Re^{0.696} (H/D)^{-0.20} (r/D)^{-0.41}$	$750 \leq Re \leq 27,000$ ; $3 \leq H/D \leq 16$ ; $0 \leq r/D \leq 7.14$ .	Single round nozzle
<b>Multiple Jet Impingement</b>			
Gardon & Cobonpue [117]	$\overline{Nu} = 0.299 Re^{0.625} A_f^{0.1875}$	$1,000 \leq Re \leq 130,000$ ; $1 \leq H/D$ ; $0.0077 \leq A_f \leq 0.049$ .	Regular inline array; Minimum crossflow.

**Table 1.** Correlations for average Nusselt number (cont.).

Kercher & Tabakoff [118]	$\overline{Nu} = \phi_1 \phi_2 Re^m Pr^{1/3} (H/D)^{0.091}$ Graphical evaluation of coefficients $\phi_1$ , $\phi_2$ and $m$ in paper	$300 \leq Re \leq 30,000;$ $1 \leq H/D \leq 4.8;$ $0.005 \leq A_f \leq 0.08.$	Regular inline arrays.
Martin [19]	$\overline{Nu} = Pr^{0.42} \left[ 1 + \left( \frac{H/D}{0.6/\sqrt{A_f}} \right)^6 \right]^{-0.05} \left[ \frac{2\sqrt{A_f} (1 - 2.2\sqrt{A_f})}{1 + 0.2((H/D) - 6)\sqrt{A_f}} \right] 0.5 Re^{2/3}$	$2,000 \leq Re \leq 100,000;$ $2 \leq H/D \leq 12.$	Regular arrays; Round nozzles.
Florschuetz et al. [48]	$\overline{Nu} = A Re^m \{1 - B[(H/D)(U_{cf}/U_j)]^n\} Pr^{1/3}$ Coefficient $A$ , $B$ , $m$ , and $n$ are defined in the paper.	$2,500 \leq Re \leq 70,000;$ $1 \leq H/D \leq 3;$ $5 \leq S_x \leq 15$ inline; $5 \leq S_x \leq 10$ stag; $4 \leq S_y \leq 8$ inline; $0.625 \leq S_y \leq 3.75$ stag; $0 \leq U_{cf}/U_j \leq 0.8.$	General correlation flow.
Behbahani & Goldstein [119]	$\overline{Nu} = a Re^{0.78} (S/D)^{-n}$ Coefficients $a$ and $n$ are defined in the paper.	$5,000 \leq Re \leq 15,000;$ $2 \leq H/D \leq 5;$ $0.0123 \leq A_f \leq 0.049.$	Regular staggered arrays; Maximum crossflow.
Obot & Trabold [42]	$\overline{Nu}_{\min cf} = 0.863 Re^{0.8} (H/D)^a A_f^{0.815}$ $\overline{Nu}_{\text{int } cf} = 0.484 Re^{0.8} (H/D)^a A_f^{0.676}$ $\overline{Nu}_{\max cf} = 0.328 Re^{0.8} (H/D)^a A_f^{0.595}$	$1,000 \leq Re \leq 21,000;$ $2 \leq H/D \leq 16;$ $0.0098 \leq A_f \leq 0.0352.$	Irregular inline array; Graphical evaluation of $a$ .
Huber & Viskanta [67]	$\overline{Nu} = 0.285 Re^{0.71} Pr^{0.33} (H/D)^{-0.123} (S/D)^{-0.725}$	$3,400 \leq Re \leq 20,500;$ $0.25 \leq H/D \leq 6;$ $4 \leq S \leq 8;$ $0.0123 \leq A_f \leq 0.0491.$	Regular arrays; Round nozzles.

**Table 1.** Correlations for average Nusselt number (cont.).

Garimella & Schroeder [72]	$\overline{\text{Nu}} = 0.127 \text{Re}^{0.693} \text{Pr}^{0.4} (H/D)^{-0.105}$	$5,000 \leq \text{Re} \leq 20,000.$	Regular inline array; Minimum crossflow.
Meola [120]	$\overline{\text{Nu}} = \frac{0.3 \text{Re}^{0.68} \text{Pr}^{0.42} (H/D)^{-0.3} A_f^{0.15}}{C_F^{-0.56}}$ Flow coefficient, $C_F$ , is defined in the paper.	$200 \leq \text{Re} \leq 100,000;$ $1.6 \leq H/D \leq 20;$ $0.0008 \leq A_f \leq 0.02$	General correlation flow.
Kanokjaruvijit & Martinez-Botas [95]	$\overline{\text{Nu}}_{\text{flat}} = 0.1543 \text{Re}_D^{0.69} (H/D)^{-0.49}$ $\overline{\text{Nu}}_{\text{on dimple}} = 0.1770 \text{Re}_D^{0.61} (H/D)^{-0.23} (d/D_d)^{-0.60} (D/D_d)^{0.85}$ $\overline{\text{Nu}}_{\text{on flat}} = 0.3472 \text{Re}_D^{0.50} (H/D)^{-0.16} (d/D_d)^{-0.64} (D/D_d)^{0.31}$	$5,000 \leq \text{Re} \leq 11,500;$ $1 \leq H/D \leq 12;$ $d/D_d = 0.15, 0.25, 0.29.$	Round nozzles inline array.
Caliskan & Baskaya [90]	$\overline{\text{Nu}} = 0.0687 \text{Re}^{0.697} (H/D)^{-0.11} (e/D)^{0.069}$	$2,000 \leq \text{Re} \leq 10,000;$ $2 \leq H/D \leq 12;$ $0.6 \leq e/D \leq 1.2.$	Round nozzles inline array impinging on a V-shaped ribs (V-SR) plate.
Chitsazan & Glasmacher [111]	$\overline{\text{Nu}} = 1.09 \text{Re}^{0.54} (S/D)^{-0.73} (1 + U_s / U_j)^{-0.85}$ $\overline{\text{Nu}} = 0.78 \text{Re}^{0.54} (S/D)^{-0.49} (\sin \theta)^{0.5}$ $\overline{\text{Nu}} = 0.85 \text{Re}^{0.49} (S/D)^{-0.46} \sin \theta$	$H/D \geq 2;$ Single row; $H/D < 2;$ Single row; Multiple rows.	Moving plate; Equidistant jets.
Pachpute & Premachandran. [53]	$\overline{\text{Nu}}_{\text{lin}} = a(H/D)^b (D/d)^{-0.1} (S/d_{\text{pic}})^{0.6} \text{Re}^{0.7}$ $\overline{\text{Nu}}_{\text{stag}} = a(H/D)^b (D/d)^{-0.1} (S/d_{\text{pic}})^{0.6} (d_{\text{off}}/d_{\text{pic}})^{-0.02} \text{Re}^{0.7}$	$5,000 \leq \text{Re} \leq 20,000;$ $5.5 \leq D/d \leq 17;$ $1.4 \leq S/d_{\text{pic}} \leq 2.9;$ $2 \leq H/D \leq 12.$	$a = 0.25$ and $b = -0.14$ $5,000 \leq \text{Re} \leq 15,000;$ $a = 0.27$ and $b = -0.14$ $15,000 \leq \text{Re} \leq 20,000.$ $a = 0.25$ and $b = -0.13$ $5,000 \leq \text{Re} \leq 15,000;$ $a = 0.3$ and $b = -0.2$ $15,000 \leq \text{Re} \leq 20,000.$

## 2.3. Jet Impingement Modeling

Numerical simulation has been a tool widely implemented in jet impingement studies, essentially due to cost savings resulting from the minimization of the experimental tests required to study and improve the process. The fast advancement of computational resources and numerical algorithms has led to an improvement in the accuracy of the models used to study impinging flow dynamics and heat transfer. Numerical modeling has been essentially used for device design, prediction, sensitivity analysis, and validation/verification. Most of the industrial applications that use jet impingement involve turbulent flows, however, they represent a great challenge to predict the behavior of jets with accuracy and rapidity.

Different numerical methods can be implemented to study turbulent single and multiple jets, such as Large Eddy Simulation (LES), Reynolds Averaged Navier-Stokes (RANS), or Direct Numerical Simulation (DNS), and the selection of the most appropriate method depends on the aim of the research work. If time-averaged quantities are suitable to characterize the flow, RANS must be applied since it is less expensive and therefore, widely used in practice. However, if fundamental research is required, DNS is the obvious choice, since Navier-Stokes (N-S) equations are fully solved. The use of LES in jet flow modeling has been an astute choice for fundamental investigation at higher Reynolds numbers since filtered N-S equations are solved, leading to lower computational costs compared to DNS.

### 2.3.1. DNS

DNS is the most physical exact approach since the N-S, continuity, and energy equations are fully solved using discrete units of time and space [21]. However, to fully resolve all the turbulent flow properties, an extremely small grid must be implemented in order to capture the microscopic turbulent length scale. This involves high computational costs and time which limits the applicability of DNS, special for the study of turbulent flows, and therefore, it is mainly applied for the study of flows with a low Reynolds number. Focusing on the numerical modeling of laminar air jet impingement, Chung & Luo [121] applied DNS to study the unsteady heat transfer caused by a confined impinging jet at Reynolds numbers between 300 and 1,000. Their results show that the vortices generated over the target plate induce an increase of the heat transfer and that higher Reynolds numbers promote the generation of secondary maximum Nusselt number. Chung et al. [122] performed DNS of unsteady jet impingement at low Reynolds number ( $Re = 300, 500, \text{ and } 1,000$ ) and analyzed the momentum and heat transfer. They used a high-order time-accurate finite differences method with non-reflecting boundary conditions to solve the N-S and energy equations. Numerical results show that primary vortices generated from the jet nozzle cause,

together with the wall shear layer, the unsteadiness of the impingement heat transfer over the target plate. Chattopadhyay [123] used an axisymmetric formulation with the SIMPLE algorithm to solve the governing equations used for the prediction of an annular impinging jet ( $250 < Re < 1,000$ ). Their predictions demonstrate that the heat transfer performance of annular jets is 20 % lower compared to circular jets. Jiang et al. [124] analyzed the unsteady flow and temperature of an impinging hot jet, at  $Re = 1,000$  and  $H/D = 6$ , using a spatial DNS based on high order finite difference numerical scheme and high-fidelity boundary-conditions. They concluded that external perturbations strongly affect the jet flow structures. However, the re-laminarization effect of the wall reduces these perturbations on the wall stresses and heat transfer characteristics of the jet. Lee et al. [125] applied a central differences scheme with second-order accuracy based on the finite volume (FV) method to investigate the unsteady 2D fluid flow and heat transfer of confined jets for Reynolds numbers between 50 and 500. Their results show that different characteristics in terms of pressure coefficient, skin friction coefficient, and Nusselt number are observed compared with the steady region.

### 2.3.2. LES

As a way to solve the limited applicability of the DNS method, LES simulation was developed. This method tracks flow properties with the full equations down to some user defined length scale, which is usually the grid spacing and uses additional sub-grid-scale equations to describe the flow structure at smaller scales [21]. Therefore, LES is applied for the analysis of complex physical phenomena which occur during the impingement, such as the flow dynamics and development of vortical structures. In this context, Hadžiabdić and Hanjalić [126] performed an interesting work using LES in order to analyze in the detail the vortical and turbulence structures induced by a round impinging jet ( $Re = 20,000$  and  $H = 2 D$ ). They concluded that LES data provided explanations of some phenomena detected experimentally in statistically averaged flow features, such as double peaks Nusselt numbers and the negative production of turbulence energy in the stagnation region. These observations are also supported by Uddin et al. [127] who added that LES is very sensitive to the quality of the grid in different regions of the jet impingement. Dairay et al. [128] analyzed a turbulent single jet ( $Re = 10,000$  and  $H = 2 D$ ) and found that LES leads to acceptable velocity statistics in comparison with DNS and experimental data. In addition, Dutta et al. [129] found that LES with the vortex method activated increases the efficiency of the jet impingement simulation. A study performed by Draksler et al. [27] demonstrated that LES generates accurate results, in good agreement with experimental data, allowing to understand the complex flow interaction between multiple jets and the target surface. However, LES is limited to a small

Re number for wall-bounded flows, which can be an important limitation in some applications. Penumadu & Rao [130] compared RANS and LES to model the heat transfer and pressure drop characteristics in multiple jet impingement systems ( $5,000 < Re < 90,000$ ) and found that LES provides deeper insight into the flow physics of multiple jet impingement. Recently, Otero-Pérez et al. [34] performed a parametric study on multiple jet impingement cooling ( $Re = 10,000$ ;  $H = 4.5 D$ ) using LES, validated by both experimental data and DNS, and found that the jet-to-jet spacing and crossflow highly affect the heat transfer.

### 2.3.3. RANS

As mentioned previously, even if DNS and LES provide deeper insights into the physics of single and multiple jet impingement flows, RANS has been widely implemented in industrial and academic research, since it provides fairly accurate results at low computational costs. However, the selection of the most appropriate RANS model to simulate numerically, with accuracy, this enhanced heat transfer process, has been the topic of several research projects.

Hofmann et al. [131] analyzed 13 turbulence models to determine which one better predicts the jet impingement process of a turbulent round jet ( $Re = 34,000$  and  $124,000$ ;  $H/D = 2.5$  and  $10$ ): standard  $k-\varepsilon$  model, RNG (Re-Normalisation Group)  $k-\varepsilon$  model, realizable  $k-\varepsilon$  model, Reynolds stress model, Low-Reynolds  $k-\varepsilon$  model (Launder-Sharma), Low-Reynolds  $k-\varepsilon$  model (Abid) Low-Reynolds  $k-\varepsilon$  model (Abe-Kondoh-Nagano), Standard  $k-\omega$  model, Shear Stress Transport (SST)  $k-\omega$  model and transitional flow option. To analyze and compare each model, the authors modeled a single jet impingement. Through this study, they concluded that nearly all the models predict well the wall jet heat transfer. However, they almost all fail in predicting the local heat transfer near the stagnation region. The SST  $k-\omega$  model, developed by Menter [132], with activated transitional flow option seems to be the model which ensures more accurate results. Ortega-Casanova & Granados-Ortiz [96] compared the efficiency of three turbulence models for the simulation of a single jet ( $7,000 < Re < 19,000$  and  $H/D = 5, 10, 30$ ): the SST  $k-\omega$  model, the Standard  $k-\omega$  and the Enhanced  $k-\varepsilon$  models. The authors agreed that SST  $k-\omega$  model is more accurate in single jet impingement modeling since it predicts the secondary maximum Nusselt number with accuracy. Zhou et al. [133] investigated the accuracy of the  $v^2-f$ , SST, RSM (Reynolds Stress equation Model), and RNG turbulence models for the modeling of a turbulent round jet ( $4,000 < Re < 12,000$ ) and concluded that  $v^2-f$  presents good predictions for the local Nu number, especially of the secondary Nusselt number peak, even if it over-predicts the Nusselt number in the stagnation region. The other models present a higher difference between their predictions and the

experimental data: 70 % in the stagnation region by RSM model, 10 % by RNG model, and 6 % by SST  $k-\omega$  model. Hatami et al. [134] also observed a higher deviation between the numerical and experimental results in the case of the SST  $k-\omega$  model (10 %) compared with the  $v^2-f$  model (2 %). These deviations were observed near the center of the heated surface for the prediction of the stagnation Nusselt number. These results are in agreement with [135].

Regarding the numerical analysis of multiple jet impingement, Zu et al. [136] compared different turbulence models with experimental data (standard  $k-\varepsilon$  model, realizable  $k-\varepsilon$  model, the standard  $k-\omega$  model, and the SST  $k-\omega$  model) and determined their accuracy for the modeling of two-line staggered and inline round jets. From the analysis, they found that the SST  $k-\omega$  model presents a better compromise between computational costs and accuracy. Wen et al. [137] modeled multiple round jets ( $Re = 35,000$ ) impinging on a flat plate and compared the SST  $k-\omega$  model with the Standard  $k-\omega$  model, the Realizable  $k-\varepsilon$  model, and the  $v^2-f$ . From the results, they concluded that comparing the prediction with experimental data, the SST  $k-\omega$  model presents a higher accuracy than the  $k-\omega$  and  $k-\varepsilon$  models. Additionally, even if  $v^2-f$  presents a good accuracy in predicting the stagnation zone, it requires a higher computational cost, making the SST  $k-\omega$  model a better choice. Badra et al. [138] compared the SST  $k-\omega$  model with  $v^2-f$  to determine the accuracy of the predictions obtained for the case of multiple jets impinging on a moving flat plate. The results show that both models are comparable in performance, although, SST  $k-\omega$  predictions of the stagnation Nusselt number are more accurate. Penumadu et Rao [35] analyzed a jet array ( $5,000 < Re < 90,000$ ) and compared the SST  $k-\omega$  with the standard  $k-\varepsilon$ . From the data analysis, they found that the heat transfer characteristics are better predicted by the SST  $k-\omega$  model essentially due to its ability to predict with accuracy regions with high pressure gradients. However, the simulation of the pressure drop is critical, the prediction deviations from the experimental data are around 50 %.

The main characteristics of the different numerical methods applied in jet impingement studies are summarized in Table 2. The literature review regarding the turbulence models applied for the numerical simulation of jet impingement shows that, according to several authors, the SST  $k-\omega$  model was revealed both accurate and computing time-saving in engineering applications. These advantages make this model a good choice for the numerical modeling of single and multiple jets impinging on static [15, 52, 76, 85, 139–141] and moving [109, 111, 138] plates.

**Table 2.** Turbulence models applied in jet impingement simulations.

Model	DNS	LES	RANS	
			Classical $k-\varepsilon$	$k-\omega$ models
			Standard $k-\varepsilon$ , RNG $k-\varepsilon$ , realizable $k-\varepsilon$ , RSM	Standard $k-\omega$ SST $k-\omega$ Transitional flow option (TFO)
<b>Equations</b>	Original N-S equations	Filtered N-S equations	Time-averaged N-S equations	
<b>Velocity field</b>	Three-dimensional and unsteady	Three-dimensional and unsteady	Steady/Unsteady	
<b>Modeling</b>	No modeling	Only small scales are modeled	All scales are modeled	
<b>Cost of computation</b>	Most expensive	Between DNS and RANS	Low (RSM is moderate)	Least expensive Moderate
<b>Accuracy</b>		Excellent	Poor	Poor except SST $k-\omega$ which is good
<b>Application</b>	Simple geometries at low Reynolds number	High potential for practical as well as fundamental use		Widely used in practice
<b>Studies</b>	[121]–[125], [142]–[146]	[27], [34], [35], [126]–[129], [147], [148]	[107], [131], [135], [149]–[152]	[15], [21], [52], [76], [85], [87], [111], [131], [135]–[137], [139]–[141], [153]–[155]
<b>Performance in jet impingement simulation</b>	Notable outcome on the local heat transfer upon changing the boundary condition at the impingement wall from a constant heat flux to a constant temperature.	Good prediction of the flow physics. However, the design of a practical impinging system at a small cost requires modeling of the near-wall region since LES is limited to a small Re number for wall-bounded flows.	Good prediction in the wall jet region but is not able to predict heat transfer in the low-turbulence region near the stagnation point.	Only the SST $k-\omega$ with TFO can predict correctly the laminar-turbulent transition and the local heat transfer coefficients at small $H/D$ spacing. At large $H/D$ distances, the standard $k-\omega$ model with TFO is most appropriate, however, it fails for small radial distances.

This page was intentionally left in blank.

## 3. EXPERIMENTAL METHODS

### 3.1. Experimental Procedure

The experimental procedure concerns the presentation of the experimental setup which was specially designed and constructed to conduct the heat transfer and PIV measurements. Each component was built to ensure the highest accuracy of the measurements, in that sense, the correct operation of the facility is crucial. Therefore, all the steps followed to conduct, with success, the experiments are detailed in this section.

#### 3.1.1. Experimental Setup

The experimental setup was specially built to perform the PIV and heat transfer measurements of multiple air jets impinging on static and moving hot flat plates. As it can be observed, the test rig presented in Figure 17 (a) can be divided into three main sections: the setup structure, shown in Figure 17 (b), the target plate, Figure 17 (c), and the system control, Figure 17 (d).

Starting with the setup structure, it consists of a centrifugal fan that blows the air into an acrylic plenum, which is an acrylic box with a section with larger dimensions compared with the exit of the fan, in order to stabilize the flow and to reduce the turbulence. The seeding particles are introduced inside this box, to ensure a uniform mixing with the air flow. The length of the acrylic plenum allows the flow to develop uniformly, upstream of the nozzle plate. A honeycomb structure is placed at the beginning of the tube, to promote the uniformization of the flow. At the bottom of this tube, a nozzle plate with a pattern of circular orifices is placed to generate the air jets. The number of nozzles was fixed according to the nozzle plate with the larger jet-to-jet spacing ( $S = 6 D$ ) to ensure a constant open area in all nozzle plates applied in this study. The seeded air flow goes through the circular nozzles, 5 mm in diameter, spaced by a jet-to-jet spacing normalized by the jet diameter ( $S/D$ ), which varies between 2 and 6, depending on the nozzle plate applied in the experiment. A normalized jet-to-plate distance ( $H/D$ ) is also defined in each experiment and can vary between 2 and 7. The measurement zone consists of the area between the nozzle plate and the target surface, which is surrounded by an acrylic box to minimize the interference

of the surrounding air. The transparency of this box is crucial to ensure the correct operation of the PIV measurement technique.

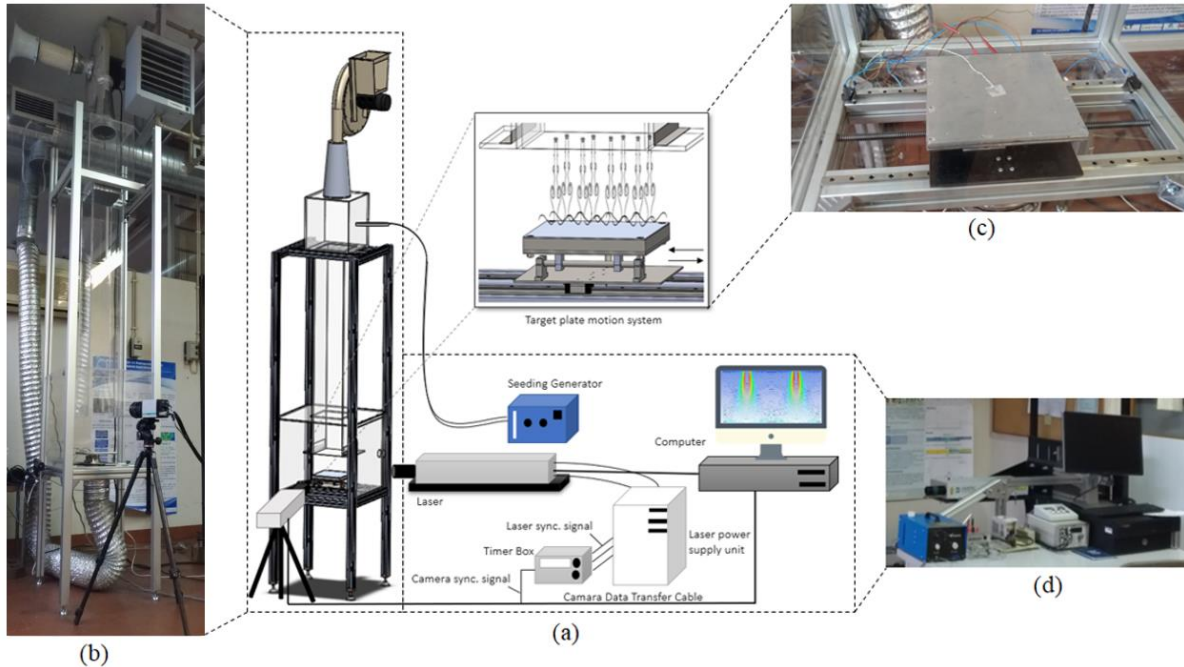


**Figure 17.** Experimental setup: (a) Test rig; (b) Setup structure; (c) Target plate; (d) System control.

The jets generated by the air flowing through the nozzle plate impinge an aluminum alloy target plate. This material was selected to ensure a uniform temperature distribution over the surface, Figure 17 (c). Since aluminum alloy presents a high thermal conductivity,  $k \approx 170 \text{ W/m}\cdot\text{K}$  [156], the contribution of the plate to the overall thermal resistance is expected to be reduced. To ensure the uniform heating of this plate, a 1000 W, 200× 200 mm mica heater is fixed between two support plates also made of aluminum alloy, as it can be observed in detail in Figure 18. The control of the target plate temperature is ensured by a thermocouple connected to a *Selec* TC544 temperature controller, as explained in more detail in the next section. To measure the convective heat transfer, an OMEGA® HFS-4 thin film heat flux sensor, rated at a maximum of 94,500 W/m<sup>2</sup>, is mounted at the center of the target surface. Thermocouples are also placed over the impinging plate to measure the local surface temperature, as depicted in Figure 18. Besides the representation of the thermocouples and the heat flux sensor positions over the target plate, the schematic shows the configuration of the plate with the mica heater inserted between the support plates; the plate motion, from the left to the right; and the air motion from the inlets to the outlets.

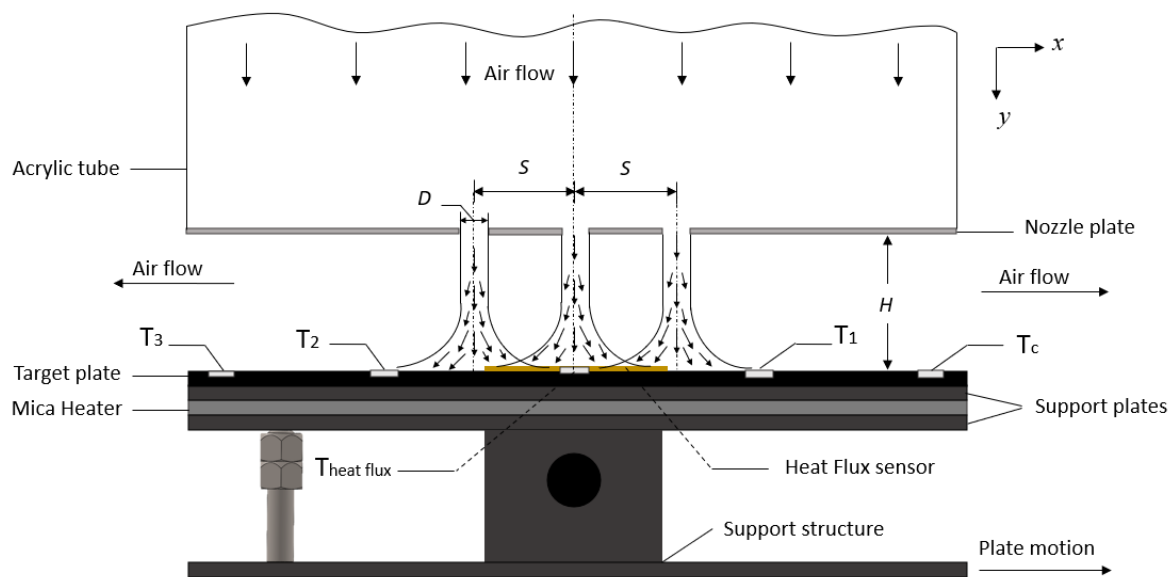


**Figure 18.** Position of the heat flux and thermocouples over the target surface.  $T_1$ ,  $T_2$ , and  $T_3$  represent the thermocouples;  $T_c$  is the thermocouple connected to the temperature controller. The heat flux, located at the center of the plate, has an integrated thermocouple,  $T_{\text{heat flux}}$ , to measure the local temperature.

The target surface has two configurations possible, flat and non-flat, as represented in Figure 19. The second one consists of a step surface with a high equal to  $2D$ . The plate is fixed to a motion mechanism, Figure 17 (b), which comprises a worm gear connected to a 24 V motor. The system allows the motion and variation of the target plate velocity and consists of two end course sensors, a speed controller, and an on-off switch. As presented in Figure 18, besides the plate motion, the variation of the angle of inclination of the target plate can also be controlled, using a screw and nuts system.

The system control table allows the control of all the sub-systems of the experimental setup. From the right to the left of Figure 17 (d), it is possible to identify: the computer which controls the 2D PIV system from Dantec™, through the Dynamic Studio software; the frequency regulator, which adjusts the air blown by the fan; the switch that allows to move the target plate from the right to the left and vice-versa; and the seeding generator Aerotech Concept™, through which it is possible to control the seeding concentration inside the test rig.

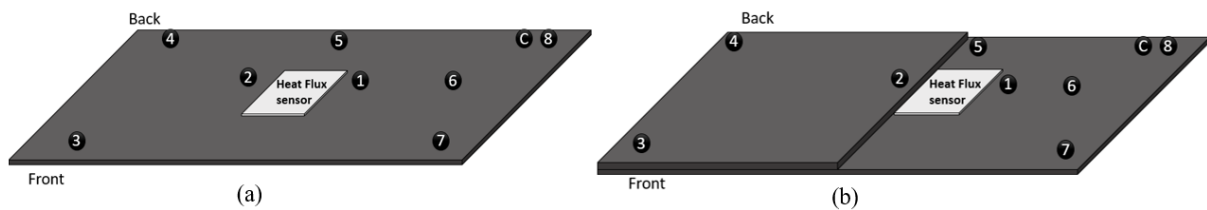


**Figure 19.** Target plate configurations: (a) Flat plate; (b) Non-flat plate. The scheme represents the location of the heat flux, at the center of the plate, and the numbers are the location of thermocouples over the surface for each configuration.

### 3.1.2. Operation of the Test Facility

The experiments are carried out at ambient temperature and relative humidity varying between 40 % and 60 %. In the cases where the target plate motion is analyzed, a constant velocity equal to 0.003 m/s is applied. This velocity range is relevant to the reflow soldering manufacturing process, which involves a low target plate velocity that provides accurate heating and cooling of the surface throughout the different zones of the thermal cycle.

To conduct the heat transfer measurements, the position of the heat flux sensor is crucial to ensure the reproducibility of the experiments. In this study, the OMEGA HF4 sensor is positioned at the center of the target plate. Relatively to the nozzle plate, the central nozzle is always positioned at the center of the heat flux sensor. To ensure the accuracy of the plate position, a Bushnell® laser level is used. The center of the heat flux in both  $x$  and  $z$  directions is identified on the plate and so, the laser sheet must cross both the center of the heat flux sensor and the center of the central nozzle.

Once the target plate is precisely positioned, the measurements start, and this happens from the moment the heater is powered on. A thermocouple linked to the plate is connected to a *Selec* TC544 temperature controller with an accuracy of 0.25 % of full-scale or  $\pm 1$  °C, which switches the heater, on an on/off basis, to ensure a surface temperature of 120 °C. This thermocouple is placed at such a distance that the effect of the jet flow on the reference temperature can be neglected. In that sense, the heat transfer coefficient is determined by the heat flux measured by the heat flux sensor and the temperature difference between the plate and jets. The jets are at ambient temperature, measured by a thermocouple placed inside the acrylic box, to reduce the effect of the hot plate on the jet's temperature measurements.

Both the heat flux and the temperature of the air jets and plate are recorded over a time span of 30 min. The stabilization of the plate temperature occurs at approximately 10 min from the beginning of the trial. At this moment, the plate temperature is considered constant and equal to 120 °C and the temperature of the jets is equal to the ambient temperature measured.

The experiments for the case of the moving target plate start after the end of the static tests. At this time, the temperature and heat flux are stabilized and the experimental conditions at time zero are the same as the static case. Therefore, the moving system is activated, and the plate starts its motion from the left to the right. During the movement, a spike in the heat transfer coefficient is observed, due to the increased flow velocity induced by the plate motion, as shown in Figure 20 at approximately 31 min. As the sensor moves downstream, away from the jets, the heat transfer coefficient decreases until the movement is completed. The comparison between the Nusselt numbers obtained in the static and dynamic conditions is performed between the values recorded after the heat transfer stabilization and the peaks reached during the plate motion. The experiments are repeated three times.

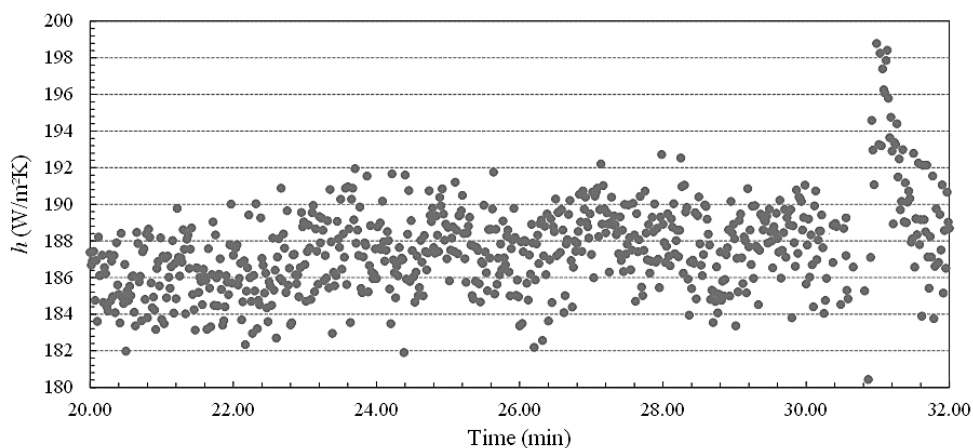


**Figure 20.** Heat transfer coefficient variation with time for both static and moving target surfaces.

Regarding the PIV measurements, a procedure is followed to ensure accurate measurements. The laser of the PIV system induces a light sheet in the  $xy$  plane which crosses the central jets. In that sense, it is important to ensure that the laser sheet is completely aligned with the system, ensuring an angle of 90° with the nozzle plate. Moreover, it is important to guarantee that the light sheet crosses the center of the central nozzles to be sure that the 2D jets profiles captured are representative of the full profile and no relevant information regarding the flow dynamics is missing. After the alignment of the laser, the camera must be positioned in order to capture the measurement window desired. Once again, the camera must be accurately positioned in order to avoid parallax problems and to be able to capture all the flow from the inlet to the outlets. After the correct positioning of all the equipment, the system can be turned

on. Before the seeding particles are introduced into the system, the calibration process must be completed. This will be discussed in the following section.

## 3.2. Measurement Techniques

### 3.2.1. Heat Transfer Measurement

To measure the average heat transfer, an OMEGA® HFS-4 thin-film heat flux sensor is mounted at the center of the target surface (Figure 21). This sensor contains an integral thermocouple for discrete temperature measurement needed to describe the heat flux. The difference in temperature across the thermal barrier is proportional to the heat flow through the sensor. Thin-film sensors present several advantages since, with a thickness of less than 10  $\mu\text{m}$ , they are thinner than wires and foils and have minimal impact on the physical and thermal characteristics of the supporting structures [157]. One of the most applied thin-film sensors for heat flux measurements is based on a thermopile formed around an electrically insulating layer [158]. This measurement technique consists of several thermocouple pairs connected between them in series. Through this configuration, the voltage of individual thermocouples adds up, increasing the output signal and its accuracy [159]. The resulting output signal is a voltage difference proportional to the heat flux through the sensor. To determine the heat flux, Fourier's law of thermal conduction is applied, expressed in Eq. (1). Through the thermocouples connected to the heat flux, the temperature difference,  $\Delta T$ , is determined across a known thickness,  $\Delta\delta$ , of material whose thermal conductivity,  $k_{t-f}$ , is also known, being possible to determine the heat flux,  $q$  [160]. Here, the thin-film has a thickness of 0.18 mm and the Kapton® thermal conductivity, given by the manufacturer, is 0.045 W/m·K.

$$q = -k_{t-f} \left( \frac{\Delta T}{\Delta\delta} \right) \quad (1)$$

Furthermore, the output voltage,  $\Delta V$ , from the sensor is given by Eq. (2), where  $N$  is the number of thermocouple pairs across the sensor,  $N = 112$  for HFS-4, and  $S_{eff}$  is the Seebeck coefficient, which depends on the thermocouple type.

$$\Delta V = N \cdot S_{eff} \cdot \Delta T \quad (2)$$

The sensor sensitivity equation, Eq. (3), shows that the heat flux through the sensor is directly proportional to the output voltage [161].

$$S_q = \frac{\Delta V}{q} \quad (3)$$

Combining Eq. (2) with Eq. (3)  $S_q$  can be obtained by Eq. (4) [158]:

$$S_q = \frac{N \cdot S_{eff} \cdot \Delta \delta}{k_{t,f}} \quad (4)$$

The information provided by the manufacturer shows that the output given by the heat flux sensor at 21.1 °C is equal to 2  $\mu\text{V}/(\text{W}/\text{m}^2)$ . Considering a correction factor that varies with the operating temperature, a value of 1.8  $\mu\text{V}/(\text{W}/\text{m}^2)$  is considered since the sensor will be exposed to temperatures close to 120 °C. Taking this information into account, the Seebeck coefficient can be determined by Eq. (4), being equal to 4.01  $\mu\text{V}/^\circ\text{C}$ . The heat flux sensor and the thermocouples are connected to a NI 9213 data acquisition system and the data processing is performed using *LabVIEW* based software.

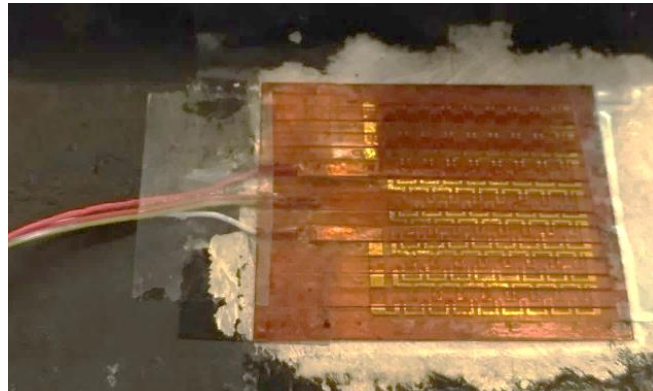


**Figure 21.** OMEGA® heat flux sensor HFS-4.

To determine if the heat flux sensor is properly calibrated, a confirmation test is conducted in order to validate the heat flux measured by the HFS-4. The experiment consists of measuring the heat flux over a copper plate heated by a stainless-steel hot plate. The heat flux sensor HFS-4 (1) is mounted over the target plate (2) as well as a type K thermocouple (3), as illustrated in Figure 22, while a second thermocouple measures the ambient air temperature. The copper plate is heated by a J.P Selecta® Agimatic-N magnetic stirrer with a stainless-steel hot plate. The temperature is controlled to ensure a uniform plate temperature of 55 °C. The thermocouple and heat flux sensor are connected to a NI 9213 data acquisition system and the data processing is performed using *LabVIEW* based software (5).

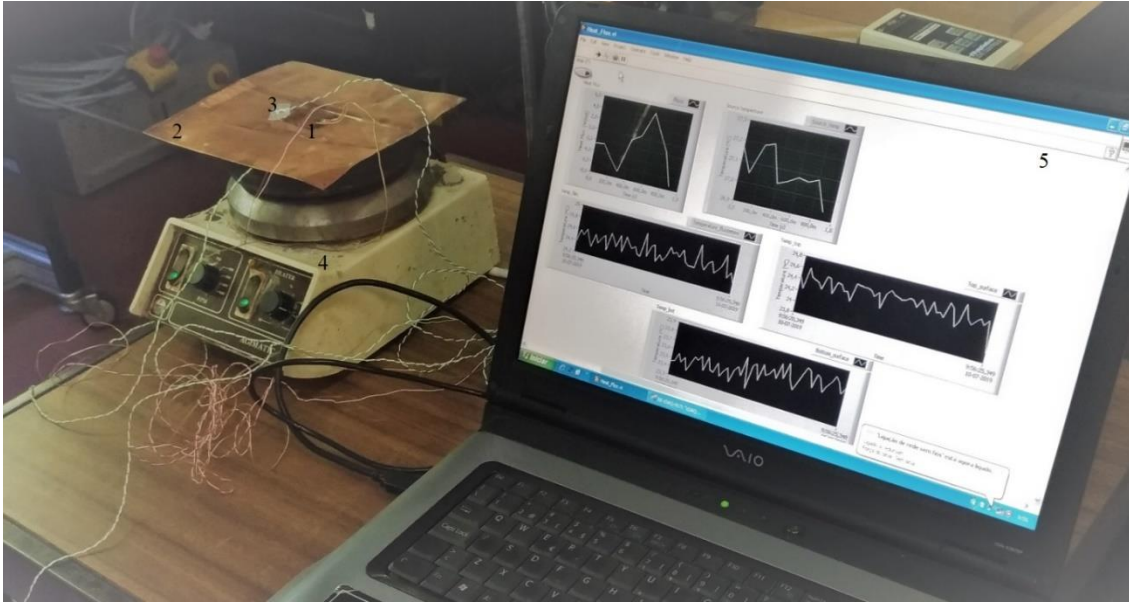


**Figure 22.** Experimental setup for validation of the heat flux measured by the HFS-4.

After the temperature stabilization, measurements are conducted over 128 s, recording a total of 1280 samples. The average heat flux and temperature data are expressed in Table 3, as well as the total uncertainty associated with the measurements.

**Table 3.** Averaged heat flux and temperature measurements.

Heat Flux (W/m <sup>2</sup> )	Plate temperature (°C)	Ambient air temperature (°C)
417.6(6) ± 2.91	54.5(5) ± 0.12	23.6(6) ± 0.16

() – uncertain digit

To validate the values measured by the heat flux sensor, the heat flux induced by natural convection is determined analytically. The heat flux is considered uniform over the copper plate and the thermal properties of the air are obtained at film temperature, i.e., approximately 40 °C.

The convective heat transfer rate is determined by Eq. (5):

$$Q = h A_w (T_w - T_\infty) \quad (5)$$

where,  $h$  represents the natural convective heat transfer coefficient between the plate and the surrounding fluid and it can be calculated by Eq. (6), in which,  $Nu$  represents the Nusselt number over the characteristic length  $l$  and  $k$  is the air thermal conductivity.

$$h = \frac{Nu \cdot k}{l} \quad (6)$$

According to [156], the Nusselt number over a heated horizontal surface exposed is correlated by Eq. (7) for a Rayleigh number (Ra) varying between  $10^4$  and  $10^7$ .

$$\text{Nu} = 0.59 \text{ Ra}^{1/4} \quad (7)$$

Since Ra is given in function of the Prandtl number (Pr) and the Grashof number (Gr) by Eq. (8) and considering Eq. (9) to calculate Gr, it is possible to obtain the natural convective heat transfer coefficient.

$$\text{Ra} = \text{Pr Gr} \quad (8)$$

$$\text{Gr} = \frac{g \beta^* (T_w - T_\infty) l^3}{\nu^2} \quad (9)$$

where  $\nu$  is the kinematic viscosity of the air flow,  $g$  the gravitational acceleration, and  $\beta^*$  the coefficient of volumetric expansion ( $1/T$  for ideal gases).

The air flow and geometrical properties used for the calculations are presented in Table 4, as well as the final results, expressed as input and output variables, respectively. Comparing the experimental results with the analytical ones, the estimated difference between both heat fluxes is approximately 10 % which is within the correlation (Eq. 7) accuracy. Other uncontrollable factors that occur during the experimental measurements also contribute to the difference. In that sense, this analysis validates the heat flux sensor measurements.

**Table 4.** Analytical results of heat flux over the plate.

Input variables		Output variables	
$\beta^*$	0.025 (1/°C)	Gr	$2.58 \times 10^6$
$\nu$	$1.702 \times 10^{-5}$ (m <sup>2</sup> /s)	Ra	$1.87 \times 10^6$
$k$	0.026 (W/m·K)	Nu	21.82
Pr	0.725	$h$	12.33 (W/m <sup>2</sup> K)
$l$	0.046 (m)	$q$	380.90 (W/m <sup>2</sup> )

### 3.2.2. Temperature

The experimental setup is designed to analyze the heat transfer and the flow behavior of multiple jets, at ambient temperature, impinging on a hot plate. To conduct this analysis, it is necessary to set up the temperature of the target plate. Considering the design and configuration presented in Figure 18, a flat mica resistance, shown in Figure 23 (a), with a power of 1,000 W and 200 × 200 mm in dimensions, allows the uniform heating of the surface. In order to record the surface temperature, type K thermocouples, Figure 23 (b), are mounted over the surface according to the configuration presented in Figure 19. This type allows a temperature reading between -199 °C and 999 °C which complies with the

requirements of the experiments since the temperatures vary between 20 °C and 120 °C. These thermocouples are connected to a NI 9213 data acquisition system, Figure 23 (c), with a measurement sensibility < 0.02 °C and a sample rate of 75 s<sup>-1</sup>. The thermocouple which controls the reference temperature is coupled to a temperature controller TC544A with a resolution of 0.1 °C (for thermocouples), Figure 24. However, due to the thermal inertia of the target plate, the plate takes time to achieve a uniform temperature. From experiments, the target plate takes 10 min to achieve an average temperature of 120 °C.

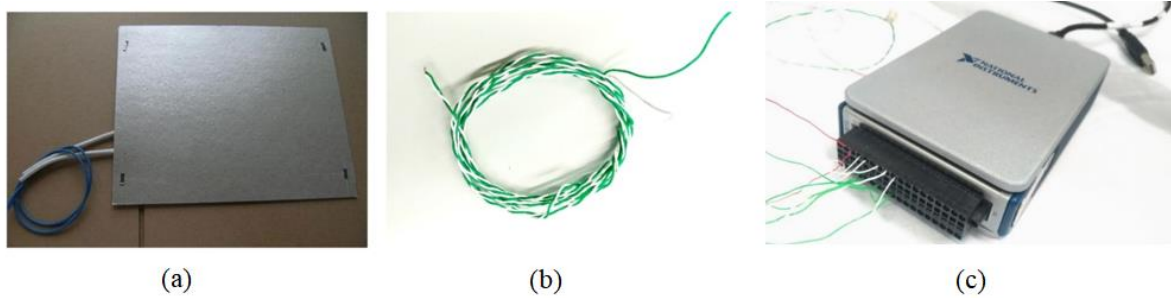


**Figure 23.** (a) Mica heater; (b) Type K thermocouple (c) Acquisition system NI 9213.

From the measurements of the temperatures over the target plate, it was observed a standard deviation of  $120 \pm 1$  °C between the thermocouples placed on the flat plate and  $120 \pm 2.5$  °C over the step plate. This higher difference is due to the temperature measured over the step plate. Considering that the step thickness is equal to  $2 D$ , the losses due to conduction are twice higher. However, since all the heat transfer measurements are conducted at the bottom of the step, this temperature difference will not interfere with the accuracy of the measurements performed by the heat flux sensor.



**Figure 24.** Temperature controller TC544A.

Besides the control of the plate temperature, it is also important to control the temperature of the jets, to ensure the reproducibility of the experiments. Since the jet flow corresponds to the air which is blown

by the fan from the ambient to the setup, the jet temperature corresponds to the ambient air temperature. To control the temperature, an air conditioning system installed in the laboratory is used, ensuring that the temperature variation does not exceed 1 °C throughout the experiments. Besides the thermocouple located in the stabilization chamber, a weather station (W.155 Weather station from Ventus, Denmark) with a resolution of 0.1 °C records the temperature variation of the ambient air.

### 3.2.3. Flow Rate

The precise control of the flow parameters throughout the experiments is crucial to ensure the accuracy of the measurements. In that sense, the flow rate is measured both at the inlet of the experimental setup and at the exit. The monitorization of the flow rate is also important to ensure that no leaks or air intakes interfere with the results. To conduct this analysis, a bell mouth of elliptical shape ( $\varnothing = 125$  mm) followed by a straight section for flow development, is mounted upstream of the air inlet of the ventilator, as presented in Figure 25.

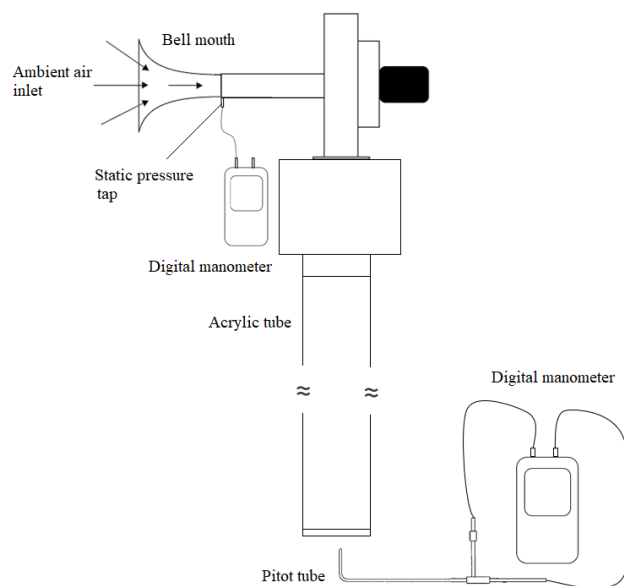


**Figure 25.** Velocity measurement at the inlet and outlet of the experimental setup.

A pressure tapping, located at the throat of the bell mouth, enables the static pressure measurement using the digital micromanometer Love Controls HM28 with a resolution of 1 Pa and a range of measurement from 0 to 7,000 Pa. To determine the dynamic pressure at the exit of the acrylic duct with a rectangular section (200 × 200 mm), a Pitot tube is used. Subtracting the value measured by both static and dynamic pressures to the atmospheric pressure, it is possible to obtain the theoretical average

velocity of the flow at the entrance and exit using a simplified Bernoulli equation (Eq. 10), in which  $\rho$  is assumed to be  $1.204 \text{ kg/m}^3$  (air density at  $20 \text{ }^\circ\text{C}$  [156]).

$$U = \sqrt{\frac{2 \Delta p}{\rho}} \quad (10)$$

The apparatus used to perform the measurements is presented in Figure 26 and consists of a Pitot tube fixed to a support instrument that ensures its correct positioning according.

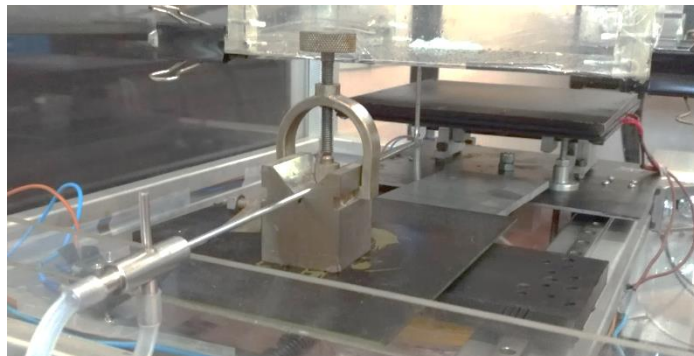


**Figure 26.** Apparatus to measure the total pressure at the setup exit.

The flow rate which supplies the experimental setup is controlled by a Mitsubishi S500 fan frequency regulator, presented in Figure 27, which allows the variation of the frequency from 0 to 50 Hz with a resolution equal to 0.1 Hz. Furthermore, to determine the flow rate, the velocity obtained by Eq. (10) is multiplied by the section area.



**Figure 27.** Fan frequency regulator Mitsubishi S500.

The variation of the flow rate at the exit and the entry of the experimental setup, without the nozzle plate, for different fan frequencies, was analyzed. The results show that within the operating flow rate (up to 15 Hz) the difference was below 7 %, which is acceptable.

To determine the flow rate at the nozzle's inlet, the same procedure is followed. First, the mean total pressure at the nozzle's inlet is measured at the nozzle of the central jet, and the adjacent jets, in a total of five measurement points. The analysis focuses on the center of the nozzle plate, due to the location of the heat flux sensor. However, as expected, the velocity decreases from the center to the tube walls, therefore the focus of the study is on the central region of the nozzle plate. Although the Pitot tube is a sensitive measurement device, to ensure accurate velocity values at the nozzle's inlet, some considerations must be taken into account. According to Klopfenstein [162], it is recommended to allocate the sensing tip of the Pitot tube at least one diameter downstream of the air exit of the measurement zone and point straight to the moving air stream, ensuring that the Pitot tube is parallel to the direction of the flow since its radial placement influences the accuracy of the flow calculations. Considering these recommendations, the Pitot tube is placed as presented schematically in Figure 28.

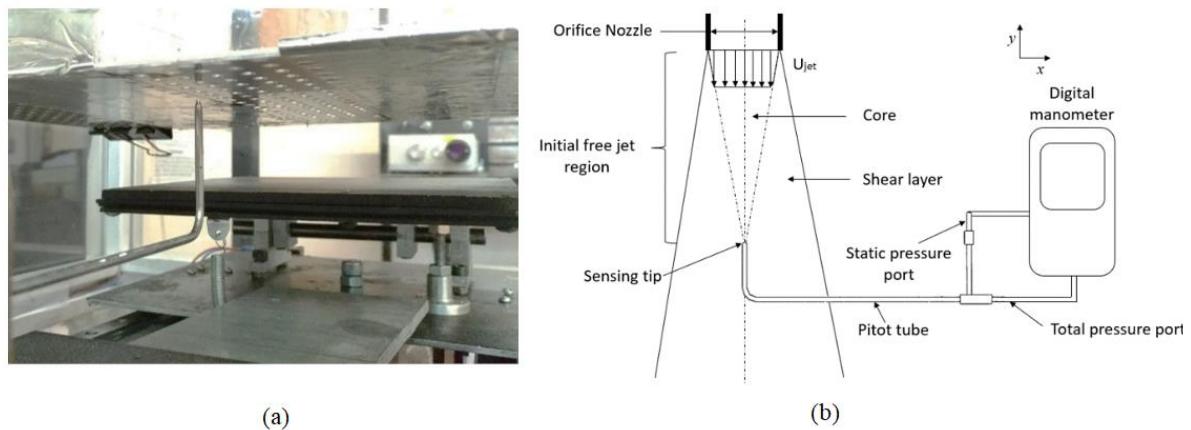


**Figure 28.** Measurement of the total pressure at the nozzle's inlet (a) Photograph of the Pitot tube position in the setup; (b) Schematic position of the Pitot tube in relation to the nozzle.

As the maximum velocity is recorded at the exit of the nozzle, this is the selected reference velocity. The control of the velocity is performed using the fan frequency regulator and the frequency range analyzed varies between 2.5 to 50 Hz. The direct measurement of the total mean pressure by the Pitot tube, expressed by the digital manometer, allows to determine the mean velocity using Eq. (10). From these measurements, the volumetric flow rate,  $\dot{V}$ , and Reynolds number are obtained by Eq. (11) and Eq. (12), respectively. The results are expressed in Table 5.

$$\dot{V} = U A_j \quad (11)$$

$$\text{Re} = \frac{\rho U D}{\mu} \quad (12)$$

where  $U$  is the jet velocity measured at the nozzle inlet,  $A_j$  is the cross-section area of the jet and  $D$  the jet's diameter, and  $\rho$  and  $\mu$  are the density and dynamic viscosity of the air flow.

**Table 5.** Reynolds number obtained by the total pressure measurements.

Fan Frequency (Hz)	Mean Dynamic Pressure (Pa)	Mean Jets Velocity (m/s)	Mean Flow rate (m <sup>3</sup> /s)	Mean Re
2.5(0) ± 0.06	2.(0) ± 0.3	1.(8) ± 0.2	3.(3)E-05 ± 8.2E-07	601.(2) ± 5.9
5.0(0) ± 0.06	15.(6) ± 3.1	5.(1) ± 0.6	1.(0)E-04 ± 3.8E-06	1,679.(2) ± 172.5
10.0(0) ± 0.06	70.(2) ± 6.5	10.(8) ± 1.0	2.(1)E-04 ± 7.5E-06	3,562.(1) ± 322.2
15.0(0) ± 0.06	150.(4) ± 8.6	15.(8) ± 1.0	3.(1)E-04 ± 9.2E-06	5,213.(9) ± 328.0
20.0(0) ± 0.06	256.(6) ± 7.0	20.(6) ± 0.6	4.(1)E-04 ± 9.9E-06	6,810.(3) ± 197.8
25.0(0) ± 0.06	373.(0) ± 8.5	24.(9) ± 0.6	4.(9)E-04 ± 1.2E-05	8,210.(9) ± 218.1
30.0(0) ± 0.06	490.(6) ± 10.3	28.(6) ± 0.7	5.(6)E-04 ± 1.4E-05	9,416.(7) ± 243.8
35.0(0) ± 0.06	601.(2) ± 24.5	31.(6) ± 1.7	6.(2)E-04 ± 1.7E-05	10,424.(3) ± 561.8
40.0(0) ± 0.06	687.(4) ± 22.0	33.(8) ± 1.4	6.(6)E-04 ± 1.7E-05	11,146.(5) ± 471.4
45.0(0) ± 0.06	757.(4) ± 25.5	35.(5) ± 1.6	6.(7)E-04 ± 1.9E-05	11,700.(3) ± 526.2
50.0(0) ± 0.06	800.(4) ± 38.0	36.(5) ± 2.3	7.(2)E-04 ± 2.1E-05	12,027.(9) ± 773.6

() – uncertain digit

The methodology followed to determine the uncertainty of the measurements is detailed in the next section. Looking at the results, it seems that for a frequency equal to 2.5 Hz, the flow is laminar, at 10 Hz is in a transition regime, while for a frequency above 10 Hz, the flow is turbulent. In this study, the focus is on flow which lies in the transition and turbulent regimes, therefore a Reynolds number near to 2,000 and 5,000 are selected. However, to fully understand the flow dynamics of the jet impingement a case study for a single laminar air jet is also considered.

From the analysis of the experimental setup, it is observed that the nozzle plate highly increases the head losses. To determine the effect of the head losses upstream of the nozzle plate, PIV measurements were conducted. The velocity field obtained is presented in Figure 29 for a fan frequency varying between 5 Hz and 15 Hz and shows that the head losses increase with the increase of the air flow velocity, as observed in Figure 29. Moreover, it is clear that as the fan frequency rises, the complexity of the flow highly increases upstream of the nozzle plate. However, the results demonstrate that the air flow is, in general, uniform at the center of the acrylic tube, and near to zero at the edges of the wall, as expected.

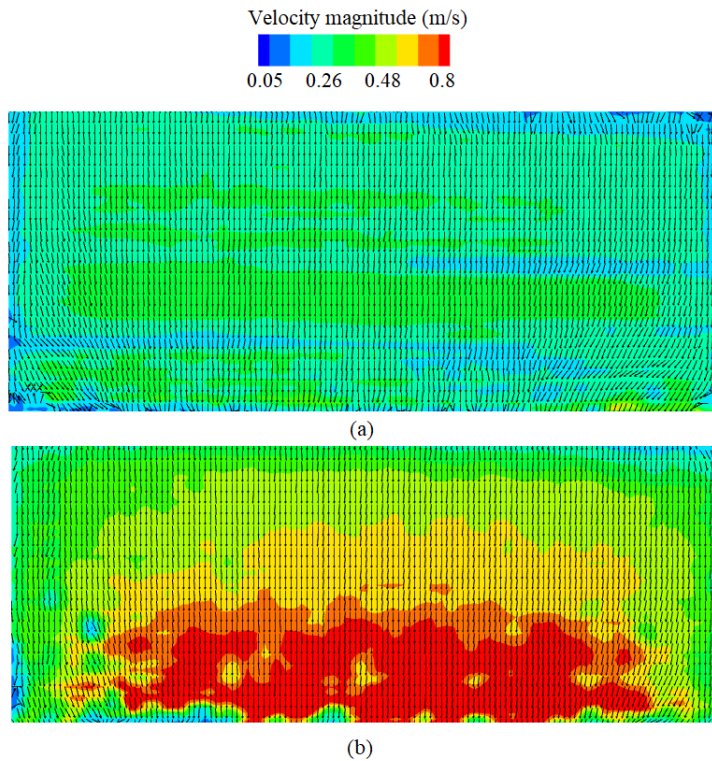


**Figure 29.** Velocity field measured at the bottom of the acrylic tube, upstream of the nozzle plate: (a) 5 Hz; (b) 15 Hz.

To understand the effect of the nozzle plate on the flow rate, this property was measured at the outlet of the setup with and without the nozzle plate. As shown in Figure 30, as the flow velocity increases, a slight difference is observed between the two cases. This difference can be explained by the fact that the Pitot tube is an intrusive method and considering the slight difference between the Pitot's head (3 mm) and the nozzle's diameter (5 mm), it is expected that high flow velocities induce higher measurement errors.

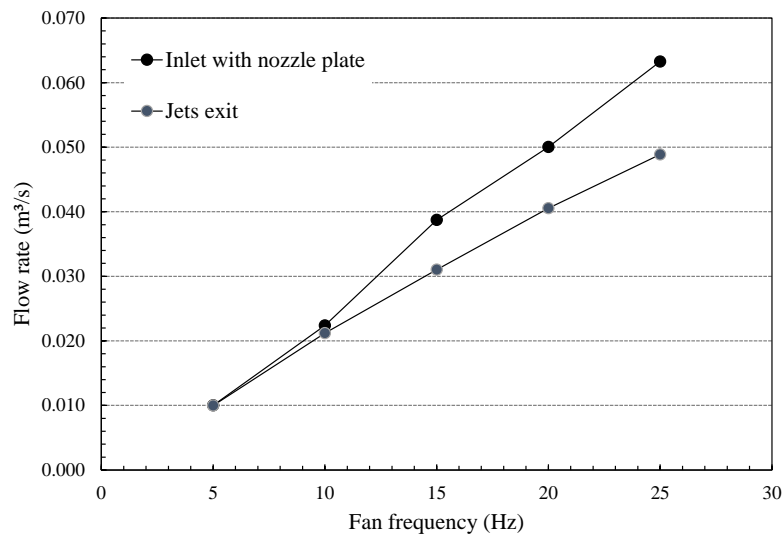


**Figure 30.** Inlet and outlet flow rate in function of the fan frequency.

### 3.2.4. Source of Errors

Several factors influence the measurements performed, inducing errors that can have two different components, random and systematic errors [163]. Therefore, every measurement is a combination of the true value and the total measurement error (random and systematic), being necessary to express the uncertainty in every measured value, i.e. the range within which lies the true value [164, 165]. To be able to estimate the uncertainties associated with the measurements, it is necessary to identify the contribution of each factor. The sources of error identified in the experimental apparatus are expressed by the Cause-and-Effect Diagram (or Ishikawa Diagram), illustrated in Figure 31.

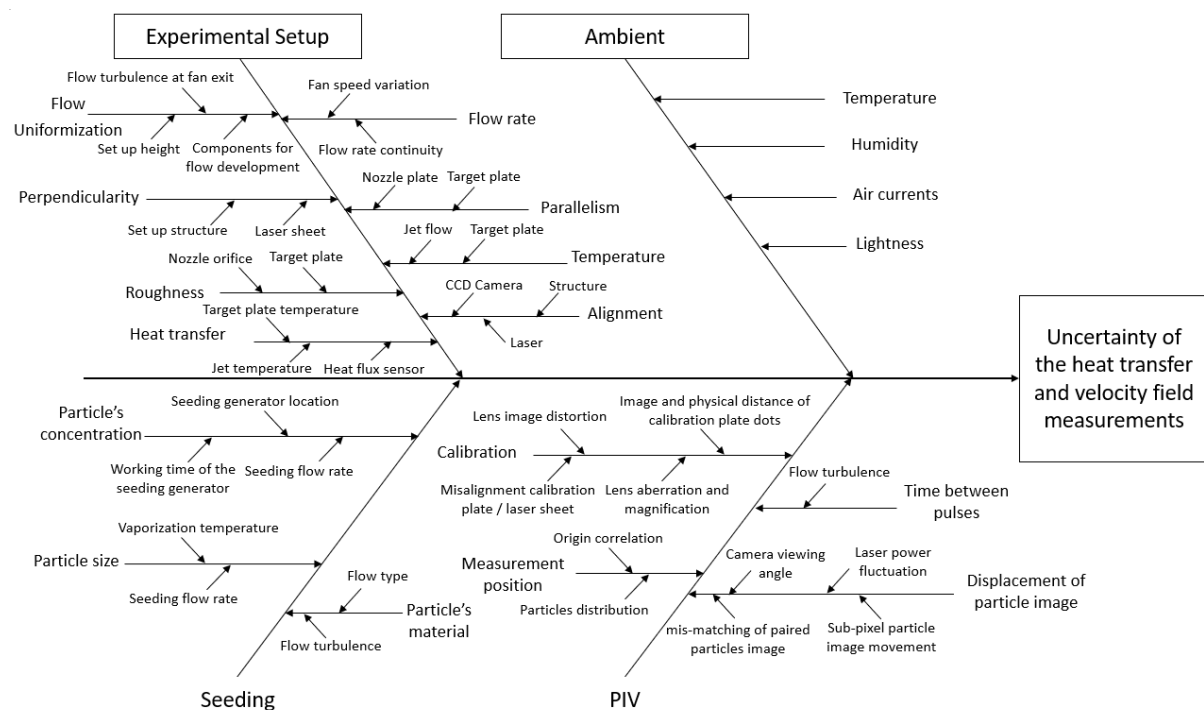


**Figure 31.** Factors that influence the uncertainty of the heat transfer and velocity field measurements.

Through this diagram, it is possible to identify the causes for the uncertainty associated with the velocity fields, measured through the PIV technique and heat transfer, measured by the heat flux sensor. The causes of the problem are divided into four main categories: Experimental setup, Ambient, Seeding, and PIV system. Each main category has specific causes that are expressed as branches in the Cause-and-Effect Diagram. Sub-causes are added in order to understand why a particular event occurred. To understand how the different causes, interfere with the problem statement, each category is discussed in detail below. However, the source of errors and uncertainty quantification related to the Seeding and PIV system is explored in the next section. Even if it is difficult to quantify the influence of each quantity,

i.e. the quantity that affects the relationship between the value provided by the measuring instrument and the result but does not affect the measured quantity directly [163], it is important to identify them and to act in order to minimize their effects on the measurements. Therefore, while the effect of some influence quantities is only discussed in this section, others must be considered on the uncertainty estimation of heat transfer and velocity measurements, thus, they are quantified in the following section: “3.2.5. Data Reduction and Uncertainty Estimation”.

#### a) Flow uniformization

The uniformization of the flow through the setup is important to ensure the reliability of the results. The same quantity of seeded flow must go through the different orifice nozzles. Furthermore, the same velocity must be recorded at the exit of the orifices. For that, it is necessary to minimize the turbulence of the flow at the exit of the fan as well as to ensure uniform distribution, upstream the nozzle plate. Through experimental analysis, it is observed that a large distance between the fan and the orifice nozzles must be ensured for proper flow development. In that sense, the full height of the laboratory is used for the setup design. To minimize the turbulence and increase the flow uniformity, a diffuser is placed at the exit of the fan, followed by a stabilization chamber with a larger cross section compared with the diffuser. The air enters into the acrylic tube, inside which a honeycomb structure is placed, to straighten the air flow. To validate that the uniformization of the flow is performed with success, the velocity vectors obtained by PIV at the exit of the nozzles are analyzed.

The experiments are conducted in a confined space at  $Re = 2,000$ . The jet-to-jet spacing ( $S/D$ ) is fixed at 5.7 while the nozzle-to-plate distance ( $H/D$ ) is equal to 7. The results presented in Figure 32 show a good uniformity of the flow through the different orifice nozzles, with the maximum velocity recorded at the exit of the orifice and decreasing with the decrease of the distance to the target plate. The symmetry of the vortices generated on both sides of the central jet, as well as on each side of the adjacent jets (in direction to the exhaust), also supports the idea of a proper uniformization of the flow.

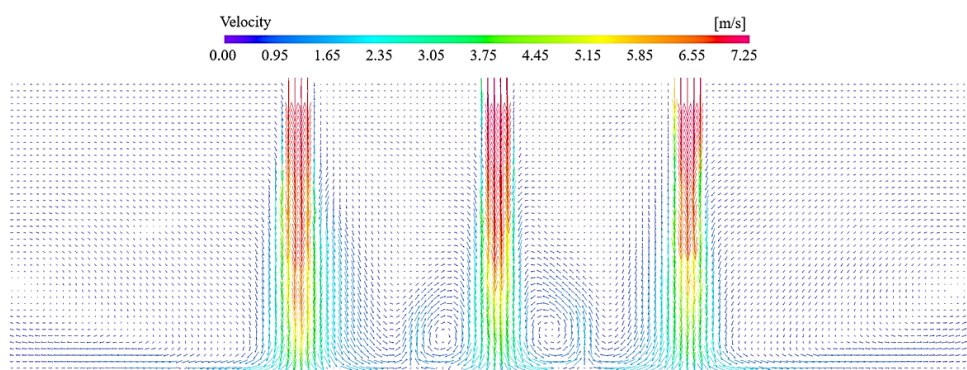


**Figure 32.** Time-averaged velocity profile for  $H/D = 7$  distances at  $Re = 2,000$  and  $S/D = 5.7$ .

## b) Alignment, perpendicularity, and parallelism

As previously mentioned, the alignment between the CCD (Charge Coupled Device) camera and the laser is crucial to minimize particle lag and out-of-plane velocity components. In that sense, a pivot point Bushnell® laser level is used for the perfect alignment between the laser and the experimental setup as well as the experimental setup, laser sheet, and the CCD camera, as observed in Figure 33.



**Figure 33.** PIV system alignment using the Bushnell® laser.

After the definition of the correct setting of the camera and the laser, their position must be fixed before starting the calibration. As mentioned by [166], to minimize errors, it is important to ensure that the calibration conditions are the same as the measurement conditions. Other important aspects are identified during the preparation of the experiments. First, it is verified that the nozzle plate and the target plate must be perfectly parallel to minimize flow deviation and asymmetry. To ensure this requirement, a torpedo level is used. This condition cannot be verified if the perpendicularity of the acrylic tube is not ensured. Furthermore, the perpendicularity between the setup and the laser must be verified, otherwise, undesired shadows can appear over the measurement region.

Problems related to the alignment between the laser, the camera, and the acrylic tube for jet impingement visualization are very common and difficult to be fully controlled. In that sense, they must be considered in the design of the setup and accurate measurement instruments must be used to minimize the effect of these factors on both jet flow profile and PIV images.

#### **d) Transparency and reflectivity**

As mentioned previously, to minimize the interference of the ambient on the measurement, an acrylic box is placed around the measurement region. The transparency of this box is of paramount importance since it must allow a clear passage of the laser beam to ensure an accurate illumination of the measurement region. However, it is necessary to account for the refraction of the light, since it can induce errors during the measurement of the seeding particles displacement [167]. In that sense, it is important to ensure that the materials used for flow visualization, i.e., test section walls and seeding particles, have closely matched refractive indices. According to [167] and considering that the laser emits light of a wavelength of 532 nm, the refractive index ( $n$ ) of the acrylic material is approximately 1.49. The refractive index of the seeding particles is addressed in section 3.3.3.

In addition, the images captured by the camera must be as clear as possible to reduce image distortion noise. However, transparency is not required in the background captured by the camera, i.e., behind the measurement zone, or in any wall that can induce reflections of the laser beam. That means that the acrylic box must have two transparent walls and the opposite walls must be painted in black (opaque). In addition, any part of the experimental setup which induces reflections that interfere negatively with the results is removed or painted in black [166].

#### **e) Roughness**

The orifice nozzles plate is manufactured by laser cutting. However, looking at preliminary results, it is observed that problems with jet symmetry occurred due to orifice roughness. To reduce the effect of the roughness on the air flow, the swarf around the orifice nozzles was removed. After this process, the mean roughness value is estimated to be equal to  $0.900 \pm 0.015 \mu\text{m}$  throughout the nozzle orifice, which seems to be satisfactory to ensure the flow symmetry. This parameter represents the arithmetical average of surface heights measured over the surface. The heights are averaged across microscopic peaks and valleys. Further studies must be conducted to analyze quantitatively the effect of orifice nozzle roughness on the jet impingement performance.

Regarding the target plate roughness, several studies are conducted [84, 93, 94, 98, 168] showing the influence of this parameter on the heat transfer performance of impinging jets. This parameter will be explored in future works.

#### **f) Heat transfer and temperature measurements**

As previously mentioned, the average heat transfer over the target plate is obtained by the heat flux measured by the heat flux sensor and the temperature measured by thermocouples. The uncertainty quantification of the heat transfer and temperature measurements are expressed in the next section.

#### **g) Ambient**

The experiments are affected by influence quantities related to ambient conditions, since the air passes over the bell mouth and enters the fan at a specific temperature and humidity. In that sense, if these two parameters vary during the test, this will interfere with the flow properties and consequently with the uncertainty of the results obtained. To control the temperature and humidity variation throughout the experiments, a weather station (W.155 Weather station from Ventus, Denmark) is used for monitorization. Moreover, as mentioned above, the air currents interfere with the jet flow. Even if this influence quantity is difficult to quantify, precautions must be taken to minimize its effects on the measurements. In this specific case, the acrylic box is the solution selected.

The ambient light is another influence quantity, which induces measurement errors, by adding undesired background illumination in the second frame of a cross-correlation camera [166]. If this factor cannot be avoided, filters can be tuned to the camera lens, as implemented in this experiment, or to the wavelength of the laser light source. Filters combined with a dark measurement room seem to be enough to minimize the influence over the measurements and are implemented in this work.

### **3.2.5. Data Reduction and Uncertainty Estimation**

Regarding the Experimental Setup, the systematic errors due to the orifice nozzle diameter and roughness can be easily determined. However, the flow uniformization, as well as the perpendicularity, parallelism, and alignment are difficult to estimate. As far as the effect of ambient variables is concerned, temperature and humidity are influence quantities used to define the air flow properties, such as  $\rho$  and  $\mu$ , that are used for the calculation of the Reynolds number and flow rate. Although air currents and ambient light are not accounted for the Reynolds number and velocity uncertainty quantification, precautions are taken to minimize their effects on the measurements.

The uncertainty quantification follows the ASME 98 [165]. This approach, which provides a meaningful estimative of measurement uncertainty and effects of these uncertainties on test results, is based on important assumptions: (1) The systematic sources of uncertainty result from the contribution of independent parameters, which are distributed separately throughout the measurement process,

affecting the final result; (2) The random sources of uncertainty are estimated as  $\sigma_{\bar{x}}$  (Eq. 13); (3) The systematic and random uncertainties of measurement are grouped in  $B$  and  $\sigma_{\bar{x}}$ , respectively; (4) The uncertainty estimated for 95 % confidence is obtained by Eq. (14), for an expansion factor,  $k_p$ , which varies in function of  $N$ .

$$\sigma_{\bar{x}} = k_p \frac{\sigma}{\sqrt{N}} \quad (13)$$

$$u_{95} = \sqrt{B^2 + \sigma_{\bar{x}}^2} \quad (14)$$

However, it is important to mention that the uncertainty analysis of the measurement requires a previous definition of the tests procedures and objectives, the control of the measurement system and test process, the application of appropriate calibration corrections, as well as the correct definition of instrument package and data reduction [165]. Considering the different approaches presented throughout this work, mainly related to the test procedure, measurement system, and calibration, it is clear that these assumptions are met in this case study showing that the uncertainty quantification using ASME 98 can be implemented.

#### a) Reynolds number

To estimate the uncertainty related to the Reynolds number, four main variables are identified:  $\rho$ ,  $\mu$ ,  $D$  and  $U$ , as expressed in Eq. (15). The nozzle orifice diameter ( $D$ ) is mainly affected by the systematic errors due to the caliper [ $D \pm 0.01$  (mm)]. The systematic uncertainty of this variable can be determined by their accuracy and follow a type B evaluation uncertainty with a rectangular distribution [169].  $\rho$  and  $\mu$  vary with the air temperature which is measured by the thermocouple located inside the stabilization chamber [ $T_j \pm 0.12$  (°C)]. The air velocity which supplies the experimental setup,  $U$ , is controlled by the fan frequency regulator. Since velocity is determined indirectly by the total pressure measured by Pitot tube or directly by PIV, the fan frequency is considered an influence quantity, meaning that it is not the measurand, which in this case is the velocity, but it affects the measurements [169]. Besides the systematic errors, the random errors, are estimated through the analysis of the results fluctuation after repeating the experiments several times. The larger the sample size, the lower the uncertainty.

$$\text{Re} = \frac{\rho U D}{\mu} \quad (15)$$

To obtain the Reynold number uncertainty, it is necessary to determine the propagation of the measurement uncertainty, since Re is not measured directly but depends on  $\rho$ ,  $U$ ,  $D$ , and  $\mu$ , as expressed in Eq. (16).

$$u_{Re} = \sqrt{\left(\frac{\partial Re}{\partial \rho} u_{\rho}\right)^2 + \left(\frac{\partial Re}{\partial U} u_U\right)^2 + \left(\frac{\partial Re}{\partial D} u_D\right)^2 + \left(\frac{\partial Nu}{\partial \mu} u_{\mu}\right)^2} \quad (16)$$

$U$  depends on  $\Delta p$  and  $\rho$ , meaning that the uncertainty of the measurements of these parameters is propagated to the result and must also be considered. The velocity uncertainty is obtained by Eq. (17). Regarding the systematic uncertainties, they are expressed in Table 6.

$$u_U = \sqrt{\left(\frac{\partial U}{\partial \Delta p} u_{\Delta p}\right)^2 + \left(\frac{\partial U}{\partial \rho} u_{\rho}\right)^2} \quad (17)$$

**Table 6.** Systematic uncertainties.

Source	Method of measurement	Uncertainty
Density	Tabled value [156]	$\pm 0.0005$ (kg/m <sup>3</sup> )
Dynamic Viscosity	Tabled value [156]	$\pm 5 \times 10^9$ (Pa·s)
Nozzle diameter	Caliper	$\pm 0.01$ (mm)
Pressure	Micromanometer	$\pm 0.3$ (Pa)

## b) Heat transfer

The average Nusselt number is calculated using Eq. (18), where  $\bar{h}$  is the average convective heat transfer coefficient,  $D$  is the nozzle diameter, and  $k$  the thermal conductivity of the jet's flow. While the nozzle diameter is a constant geometrical parameter that is directly measured and  $k$  is temperature-dependent that can be obtained directly from the measured air temperature,  $\bar{h}$  must be calculated.

$$\overline{Nu} = \frac{\bar{h} D}{k} \quad (18)$$

$\bar{h}$  is obtained by the average heat flux measured by the heat flux sensor ( $\bar{q}$ ), the plate temperature ( $T_w$ ) and the average jet's temperature ( $T_j$ ), as presented in Eq. (19) [170]:

$$\bar{h} = \frac{\bar{q}}{(T_w - T_j)} \quad (19)$$

As previously mentioned, the wall temperature is considered constant and equal to 120 °C. The jet is at ambient temperature, measured by a thermocouple placed inside the acrylic box. The air properties are determined at the jet exit temperature, following the perceptive presented by [67], i.e. the jet exit temperature can be used to define the Nu, because the jet temperature is considered equal to the ambient temperature and the Reynolds number is low enough to avoid significant compressibility effects, Mach number (Ma) is equal to 0.04.

As already stated, the systematic errors result from the combination of elemental systematic uncertainties. In this study, the systematic uncertainty related to the thermocouples for temperature measurement, heat flux sensor for heat flux measurement, and caliper for diameter measurements, must be considered. The standard uncertainty of these measurement instruments is determined by their accuracy and follows a type B evaluation uncertainty with a rectangular distribution [169], as presented in Table 7.

**Table 7.** Systematic uncertainties.

Source	Method of measurement	Uncertainty
Density	Tabled value [156]	$\pm 3 \times 10^{-6}$ (kg/m <sup>3</sup> )
Heat Flux	Heat flux sensor	$\pm 0.58$ (W/m <sup>2</sup> )
Nozzle diameter and heat flux sensor area	Caliper	$\pm 0.01$ (mm)
Target and jets temperature	Thermocouples type K	$\pm 0.12$ (°C)

Random errors,  $\sigma_{\bar{x}}$ , are assumed to be independent and normally distributed with zero mean and standard deviation,  $\sigma$ , [169] and are obtained by Eq. (13), presented in the previous section. Here, the total number of samples ( $N$ ) varies in the case of static and moving plates. For the first case, an  $N$  around 5,000 is applied, therefore the 95 % confidence level is achieved with an expansion factor equal to  $k_p = 2.57583$  [171]. The samples include the heat flux and temperature measurements collected during the stabilization period. For the moving plate, the data analyzed are those recorded at the peaks, which gives a total of 30 samples and a  $k_p$  for a 95 % confidence level equal to 2.75639.

To obtain the uncertainty of the Nusselt number, it is necessary to determine the propagation of measurement uncertainty, since Nu is not measured directly but depends on  $\bar{h}$ ,  $D$  and  $k$ , as expressed in Eq. (20).

$$u_{\overline{\text{Nu}}} = \sqrt{\left(\frac{\partial \text{Nu}}{\partial \bar{h}} u_{\bar{h}}\right)^2 + \left(\frac{\partial \text{Nu}}{\partial D} u_D\right)^2 + \left(\frac{\partial \text{Nu}}{\partial k} u_k\right)^2} \quad (20)$$

In its turn,  $\bar{h}$  depends on  $\bar{q}$ ,  $\overline{T_w}$  and  $\overline{T_j}$ , meaning that the uncertainty of measurements of these parameters is propagated to the result and must also be considered. The heat transfer coefficient uncertainty is obtained by Eq. (21).

$$u_{\bar{h}} = \sqrt{\left(\frac{\partial \bar{h}}{\partial \bar{q}} u_{\bar{q}}\right)^2 + \left(\frac{\partial \bar{h}}{\partial \Delta T} u_{\Delta T}\right)^2} \quad (21)$$

In addition, while  $\bar{q}$ ,  $\overline{T_w}$  and  $\overline{T_j}$ , are instantaneously recorded by the data acquisition system and analyzed following the method previously expressed;  $D$  results from the measurement of 10 orifices diameters of a nozzle plate. From the statistical analysis of the measurements obtained with the caliper, a mean equal to 4.92 mm is determined with an uncertainty of  $2.45 \times 10^{-2}$  mm. Regarding  $k$ , the theoretical values are obtained from the literature [156]. Since  $k$  varies linearly with temperature ( $20 \text{ }^\circ\text{C} < T_j < 35 \text{ }^\circ\text{C}$ ),  $k$  is calculated for each air jet temperature recorded by the thermocouple using Eq. (22).

$$k = 7 \times 10^{-5} T_j + 2.366 \times 10^{-2} \quad (22)$$

This shows that, since  $k$  is a variable that depends on  $T_j$ , the uncertainty of this parameter must also be propagated to the result. The thermal conductivity uncertainty is calculated through Eq. (23). These equations, (20), (21), and (23), follow the theoretical concepts expressed in [165] to determine the uncertainty of the Nusselt number values obtained in the experimental measurements.

$$u_k = \sqrt{\left(\frac{\partial k}{\partial \Delta T} u_{\Delta T}\right)^2} \quad (23)$$

$u_{\bar{q}}$ ,  $u_{\Delta T}$ ,  $u_{\bar{h}}$ ,  $u_D$ ,  $u_k$  (Eqs. 20, 21, and 23) represent the uncertainty of heat flux, temperature, heat transfer coefficient, diameter, and thermal conductivity respectively. Since the total uncertainty of the Nusselt number is given by both random and systematic errors the procedure must be applied for each error type. This means that,  $u_{\bar{q}}$ ,  $u_{\Delta T}$ ,  $u_D$ , are assumed as random uncertainties and calculated using Eq. (13), while for systematic uncertainties calculation,  $u_{\bar{q}}$ ,  $u_{\Delta T}$ ,  $u_D$  assume the values presented in Table 7.

### 3.3. PIV Technique

#### 3.3.1. Measurement Principles

PIV is a non-intrusive method that acquires a series of images of tracer particles in a fluid flow to measure instantaneous velocity fields [172]. As shown in Figure 34, the PIV system consists of a double pulse laser that passes a coherent light beam through a cylindrical lens, creating a laser sheet. This configuration illuminates a two dimensional plane across a seeded flow in two short pulses and a CCD camera records the illuminated images of the flow field [173]. An electronic synchronizer ensures the synchronization between the CCD camera, the two laser beams, and the frame grabber.

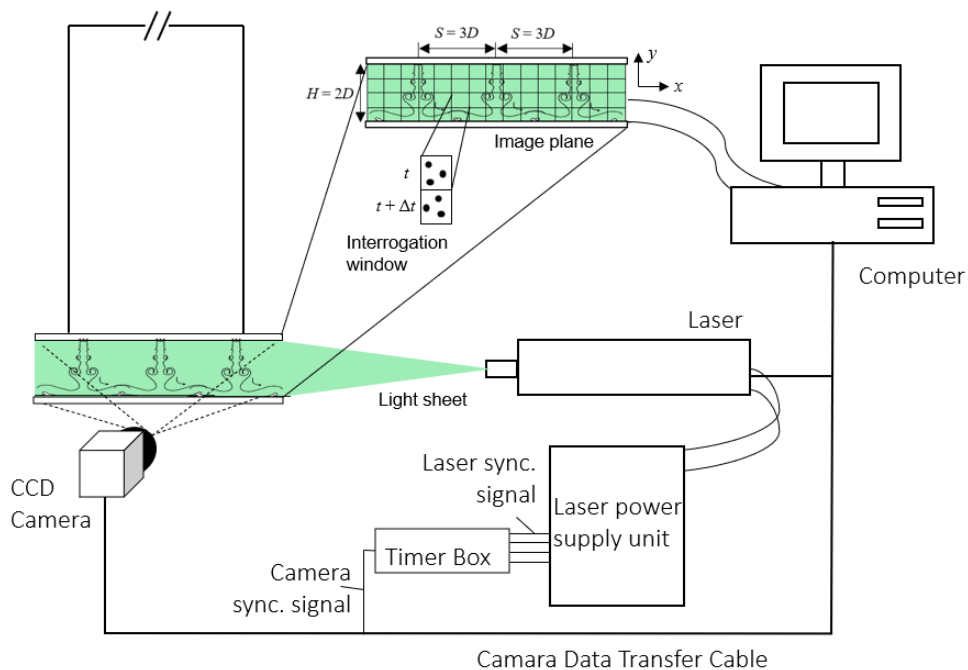


Figure 34. PIV measurement system.

The short time interval ( $\Delta t$ ) between the images allows the seeding particles to be displaced from one image to the next. Once the images have been acquired, they are processed into vector fields of the flow and divided into interrogation areas. From these interrogation areas velocity vectors are extracted for each region by performing mathematical correlation analysis on the cluster of the seeding particles within each area between the two frames. This produces a signal peak that identifies the particle displacement [174].

The accuracy of the velocity field measurements is limited by the ability of the scattering particles to follow the instantaneous motion of the continuous phase. A compromise between reducing the particle size to improve flow tracking and increasing the particle size to improve light scattering is, therefore,

necessary [175]. Gas flows are seeded with liquid droplets or with solid particles. For droplets, the techniques of atomization and condensation are feasible, whereas for solid particles atomization (solutions or suspensions of particles) and fluidization can be considered.

Considering the accuracy of this technique, PIV is highly suited to measure the flow velocity field, providing detailed information about the jet's flow dynamics. Therefore, it has been used in several jet impingement studies [8, 29, 176–180]. Using this method, it is intended to see, on a macro scale, the flow behavior over the target surface, but also to identify, on a micro-scale, the phenomenon that occurs in the vicinity of surface transition (such as back steps and forward steps). The PIV method also allows the measurement of the velocity distribution of the impinging jet flow, being possible to identify the jet's regions – the shear layer of the free jet, the stagnation zone, and the wall jet region – and the disturbances of its normal behavior when the fluid flows through the various surface irregularities, considering also the plate motion.

### 3.3.2. 2D-PIV System

The 2D-PIV system, presented in Figure 35 (a), used for the experimental measurements consists of a 145 mJ double-pulse Nd:YAG laser which generates a light sheet firing on the second harmonic, i.e. green 532 nm. A two-dimensional laser sheet is obtained by the two beams previously recombined on the same optical path by a polarized dichroic filter and expanded in one direction through a combination of spherical and cylindrical lenses [8]. This laser sheet illuminates the measurement region, shown in Figure 35 (b), from the exit of the nozzles to the target plate over the length of the test chamber. The light scattered by the seeding particles is captured by the HiSense Zyla CCD camera, positioned perpendicularly to the laser sheet. This camera is equipped with a 50 mm Zeiss lens with a pixel size of 6.5  $\mu\text{m}$  and a pixel resolution of 2560  $\times$  2160 (5.5 Megapixel).

The instantaneous motion of the air is obtained by the analysis of the two consecutive images, spaced by a short  $\Delta t$ , defined by the user as a function of the flow velocity. It is clear that, for seeded flows with a low velocity, the  $\Delta t$  must be large enough to capture the motion of the particle, while for high flow velocity,  $\Delta t$  should be small enough to be able to capture on time the required number of particles per interrogation area. Therefore, studies must be conducted to define the best compromise between  $\Delta t$  and the flow velocity. The data acquisition and processing of the images are performed by the software Dynamic Studio.

The adaptive correlation method is used to process the data. According to [181–183], this method achieves higher accuracy supplemented with high sub-pixel accuracy and adaptive deforming window

algorithm. This method applies a certain number of refinement steps to iteratively adjust the size and shape of the interrogation area (IA) and uses the information of the intermediary results between a larger and a smaller IA until the final IA is reached [181]. To achieve higher spatial resolution, a small IA size and a high overlap ratio are required. However, a compromise between higher quality images and computing time must be ensured. In this case, the interrogation area size is varied from  $128 \times 128$  pixels to  $32 \times 32$  pixels with 3 refinement steps and an overlap of 50 % in both horizontal and vertical directions. According to Cao et al. [182], these values lie between the typical values implemented for indoor airflow PIV applications.



**Figure 35.** (a) PIV system; (b) measurement region.

To conduct the measurements, three inputs can be introduced by the user to improve the accuracy of the measurements: the time between two laser pulses, i.e., the time difference between the two particle images,  $\Delta t$ ; the trigger rate, i.e., the sampling frequency of the PIV setup; and the number of images required for acquisition. The measurements are performed using a double frame mode through which the camera acquires one single frame for each trigger pulse. Considering that the time between each pulse defines the exposure time, the camera is triggered twice in double frame mode giving the double exposure [184]. Since the trigger rate is defined by the properties of the laser, it is kept constant and equal to the maximum frequency allowed by the system, i.e. 15 Hz.

Regarding the time between pulses, the definition of the appropriate value is more difficult to determine. According to Cao et al. [185], the pulse delay is defined by the separation of the particle images on the CCD camera which means that for cross-correlation, the separation of the particle images, in pixels, must be smaller than a quarter of the interrogation area (in pixels) and larger than the accuracy of the peak detection. The analysis of the most appropriate time between pulses for the measurements is presented in detail in section 3.3.4.

### 3.3.3. Seeding Particles

As mentioned previously, the seeding particles play an important role in the accuracy of the PIV measurement. According to [175], the tracer particles should not affect the dynamic of the flow neither changing their properties during the measurement nor interact with each other. Furthermore, they must be randomly and uniformly distributed across all the flow with a specific concentration in order to increase the accuracy of the measurements. However, achieving an optimum flow seeding is the most difficult part of the PIV experiments. According to [186], if the working fluid is air, the seeding needs to be entrained into the air upstream of the measurement region. However, the correct concentration of tracer particles is challenging, since besides ensuring a uniform distribution of the seeding across the test chamber, the deposition of the particles on walls is another factor difficult to overcome. Two problems arise from this deposition: first, the seeding system must insert more particles to compensate those adhering to the walls; second, window deposition is also a limiting factor, since the transparency is reduced, leading to a deformation of the image captured that generates measurement errors. This implies a continuous cleaning of the experimental setup walls.

In addition to the precise distribution of the seeding throughout the measurement region, the selection of the seeding particles for the accurate tracking of the working flow is crucial to obtain accurate measurements. According to [187], a compromise between reduced particle size and low inertia, to improve the flow tracking, and large particle size to improve the light scattering, ensuring its detection by the camera, must be ensured. Melling [175] mentioned that a particle's diameter between 2  $\mu\text{m}$  and 3  $\mu\text{m}$  is acceptable to track gas flows with a frequency response close to 1 kHz, while particles with 1  $\mu\text{m}$  are suitable for turbulent flows. Another aspect is related to the concentration of the particles since a reduced concentration leads to inaccurate measurements while too many particles induce medium opacity [186]. In that sense, a compromise between the dimension of the seeding particles and their concentration must be ensured to obtain accurate velocity fields. Due to the importance of the selection of tracer particles that are suitable for the tracking of the flow in the study and the entire test facility, a seeding characterization is performed and presented in this section.

#### a) Particles motion in air flow

The interaction between particles in a continuous flow can be expressed by Eq. (24), assuming that the particles are small compared with the length scale of the motion and that the Stokes regime is valid. This equation is known as the equation for the unsteady motion of a suspended sphere [188].

$$\frac{\pi}{6} d_p^3 \rho_p \frac{dU_p}{dt} = 3\pi\mu_f d_p U_R + \frac{\pi}{6} d_p^3 \rho_f \frac{dU_f}{dt} + \frac{1}{2} \frac{\pi}{6} d_p^3 \rho_f \frac{dU_R}{dt} + \frac{3}{2} d_p^2 \sqrt{\pi\rho_f\mu_f} \int_0^t \frac{dU_R}{dt'} \frac{dt'}{\sqrt{t-t'}} \quad (24)$$

where  $d_p$  is the particle diameter,  $\rho_f$  and  $\rho_p$  represent the fluid and particle density, respectively.  $U_f$  and  $U_p$  are the fluid and particle velocity, respectively, while  $U_R$  is the relative velocity ( $U_f - U_p$ ) and  $\mu_f$  the fluid viscosity. The first two terms represent the acceleration force and the viscous resistance according to Stokes' law which can be applied if the particle Reynolds number is lower than unity. That can be simplified using Eq. (25).

$$\frac{dU_p}{dt} + a_1 U_p = a_1 U_f + a_2 \frac{dU_f}{dt} + a_3 \int_0^t \frac{\frac{dU_f}{dt'} - \frac{dU_p}{dt'}}{\sqrt{t-t'}} dt' \quad (25)$$

where  $a_1$ ,  $a_2$ , and  $a_3$  can be obtained by equation expressed in (26):

$$a_1 = \frac{36\mu_f}{(2\rho_p + \rho_f)d_p^2}; a_2 = \frac{3\rho_f}{(2\rho_p + \rho_f)}; a_3 = \frac{18}{(2\rho_p + \rho_f)d_p} \sqrt{\frac{\rho_f\mu_f}{\pi}} \quad (26)$$

For particle response in turbulent flows, the equation of motion can be expressed by the amplitude ratio,  $\eta$ , and the response phase  $\beta$  of the instantaneous particle and fluid motions or as the ratio of the fluctuation energies of the time-averaged particle and fluid motion  $\tilde{u}_p^2 / \tilde{u}_f^2$ . In this section, the first method is approached.

According to [189], the flow and particle velocities can be expressed using Fourier integrals, as presented by Eq. (27) and Eq. (28).

$$U_f = \int_0^\infty (\alpha' \cos \Omega t + \lambda \sin \Omega t) d\Omega \quad (27)$$

$$U_p = \int_0^\infty \eta [\alpha' \cos(\Omega t + \beta) + \lambda \sin(\Omega t + \beta)] d\Omega \quad (28)$$

where  $\Omega$  is the angular frequency of the fluid motion. The second equation shows that the response of the particle to the fluid turbulence is lagged by  $\beta$ , given by Eq. (29), with an amplitude corrected by a factor  $\eta$  (Eq. 30), that is below the unit.

$$\beta = \tan^{-1} \left( \frac{f_2(\Omega)}{1 + f_1(\Omega)} \right) \quad (29)$$

$$\eta = \left[ [1 + f_1(\Omega)]^2 + f_2^2(\Omega) \right]^{1/2} \quad (30)$$

where  $f_1$  and  $f_2$  are obtained by Eq. (31) and Eq. (32), respectively.

$$f_1(\Omega) = \frac{\Omega(\Omega + a_3\sqrt{\pi\Omega/2})(a_2 - 1)}{(a_1 + a_3\sqrt{\pi\Omega/2})^2 + (\Omega + a_3\sqrt{\pi\Omega/2})^2} \quad (31)$$

$$f_2(\Omega) = \frac{\Omega(a_1 + a_3\sqrt{\pi\Omega/2})(a_2 - 1)}{(a_1 + a_3\sqrt{\pi\Omega/2})^2 + (\Omega + a_3\sqrt{\pi\Omega/2})^2} \quad (32)$$

$\beta$  and  $\eta$  are values that vary in function of the fluid oscillation frequencies, the fluid physical properties, and the dimension of the particles. If  $\rho_p/\rho_f = 1$ , the particles track the flow regardless of their size.

In this study, the seeding particles that will be used are olive oil with a density of 908.7 kg/m<sup>3</sup> at ambient temperature [190] and the flow is air which density and dynamic viscosity at ambient temperature is 1.204 kg/m<sup>3</sup> and 1.825×10<sup>-5</sup> kg/m·s, respectively. In order to analyze the behavior of the olive oil droplets in air, in amplitude and phase, with the variation of the oscillation frequency, two graphs are plotted and presented in Figure 36 and Figure 37.

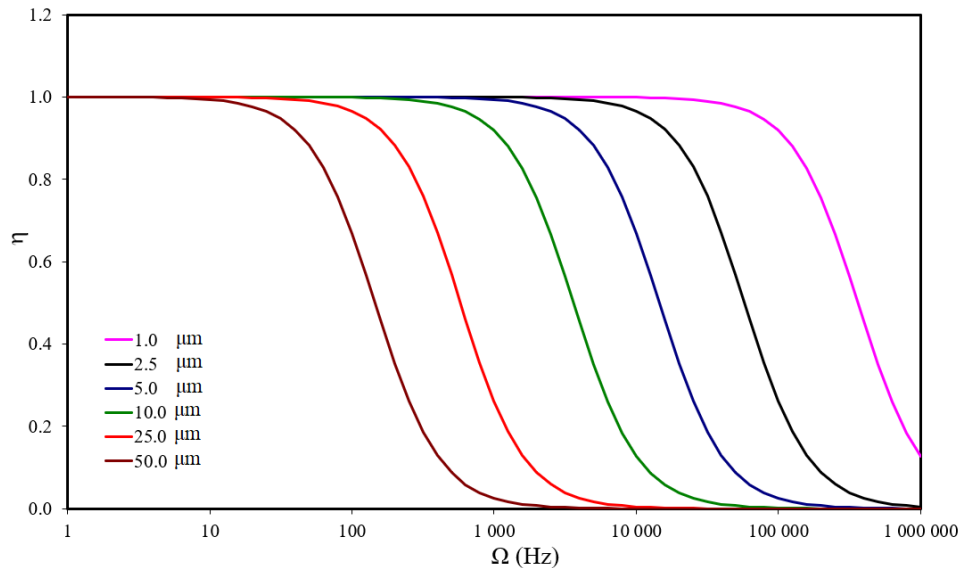


**Figure 36.** Response in amplitude of olive oil droplets in air for different particles diameter.

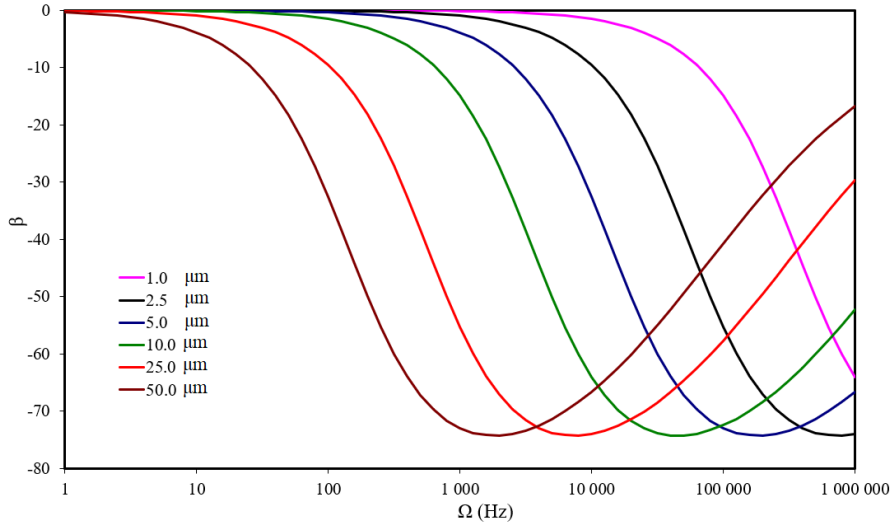


**Figure 37.** Response in phase of olive oils in air at different particles diameter.

From the concepts presented above, the olive oil droplet only can be considered an ideal seeding particle if  $\eta$  is close to the unit. As presented by Figure 36 and Figure 37, highly turbulent flows require tracking particles with small diameters. If the oscillation frequency of the flow is less than 10,000 Hz, olive oil particle with a diameter in the order of 5  $\mu\text{m}$  can be applied, however, the efficiency of the tracking is increased if the diameter lies between 1 and 2.5  $\mu\text{m}$ . However, if  $\Omega > 10,000$  Hz, a diameter of 1  $\mu\text{m}$  must be ensured.

To determine the range of the flow frequency, PIV measurements are conducted and the vorticity magnitude is determined. Vorticity is defined as the curl of the velocity field, given by Eq. (33).

$$\vec{\omega} = \nabla \times \vec{u} \quad (33)$$

From the results, the flow frequency varies between 3,000 Hz and 13,000 Hz. From this analysis and considering the conclusions presented in the above paragraph, to ensure the success of the measurements, a seeding particle with a diameter between 2.5  $\mu\text{m}$  and 1  $\mu\text{m}$  must be ensured. In that sense, a study is conducted in order to determine if the diameter of the tracking particles produced by the seeding generator is within this range.

### b) Seeding generator

The seeding particles generator is from Aerotech Concept and consists of a reservoir filled with liquid olive oil which flows through a probe with a vaporizer at its extremity, as shown in Figure 38. The vaporizer is similar to a tubular heating element used in ovens and comprises a stainless-steel enclosure inside which a fine coil of nichrome (NiCr) alloy wire heater is located, insulated by a ceramic material. The vaporizer heats the olive oil at a temperature above the smoke point and after the contact with the

surrounding air, the smoke condenses into fine droplets, generating the seeding particles that are introduced in the flow. The smoke generator allows the variation of two parameters, the flow rate, and the heater voltage. These two parameters are related to the quantity of oil that flows through the probe and the temperature at which the olive oil is vaporized, generating the seeding. Therefore, their combination influences the diameter and concentration of the seeding particles. In that sense, it is important to understand the relationship between the flow rate and vaporizer temperature on the diameter of the seeding particles. This study is fundamental since, to ensure an accurate PIV measurement, a compromise between a reduced particle size to improve the flow tracking and a large particle size to improve the light scattering must be ensured [187].



**Figure 38.** Concept Smoke Aerotech System.

### c) Experimental setup for the measurement of the seeding particles diameter

To measure the particle's diameter a Laser Diffraction Technique is applied using a Malvern 2600. This method, depicted in Figure 39, uses a low-power He-Ne laser that forms a collimated beam of light. If the beam strikes a particle, light is scattered and it is subsequently collected by a receiver lens which operates as a Fourier transform lens forming the far field diffraction pattern of the scattered light at its focal plane. This scattered light is later gathered over a range of solid angles of scattering, by a detector that consists of 31 concentric annular sectors. The unscattered light passes through a small aperture in the detector and out of the optical system, being monitored in order to determine the volume concentration of the sample. The diffraction angle increases with decreasing particle size and the number of particles can be obtained through the intensity of the diffracted beam at any angle [191]. The measured size range depends on the lens focal length. Using the available lens, the size range can be extended from 0.5  $\mu\text{m}$  up to 2 mm diameters with a dynamic range ( $d_{max}/d_{min}$ ) of approximately 100. To obtain

an accurate measurement, it is recommended that the number of particles in an experiment varies between 100 and 10,000.

The measurement is performed in two steps due to the influence of the external light sources that can also be reflected by the particle. In that sense, the measurement of the background light is performed before the introduction of the particles, and its contribution is subtracted from the sample measurement. To ensure accurate results, both background and sample measurements are performed close in time to each other, to reduce the possibility of stray light conditions changes.

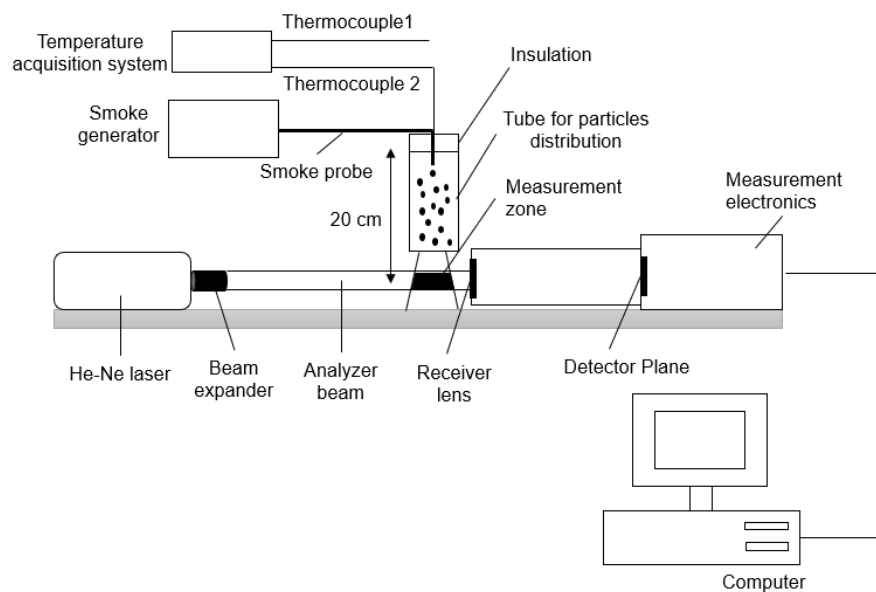


**Figure 39.** Experimental setup scheme for the measurement of the particle's diameter.

Regarding the sample, its concentration is of paramount importance to ensure accurate results. The Malvern 2600 data processing system allows the monitorization of the particle's concentration, showing if it is in the range of acceptability for an accurate measurement. The measurement is performed after the system indicates that the concentration is close to "ideal". To ensure a suitable distribution of the particles, the vaporizer is introduced inside an acrylic tube in order to minimize the interference of external factors such as air currents. To ensure the appropriate measurement conditions, the particles are introduced at a distance of 200 mm from the laser beam. According to Malvern 2600 manual, at this distance, the system should ensure a beam length active of 100 mm for a measurement volume of 8 mm diameter  $\times$  100 mm, represented in Figure 40 as V. Due to the irregularity of the flow that is expelled from the vaporizer, even if the 200 mm condition is maintained, it is difficult to ensure this specific measurement volume throughout all the experiments.

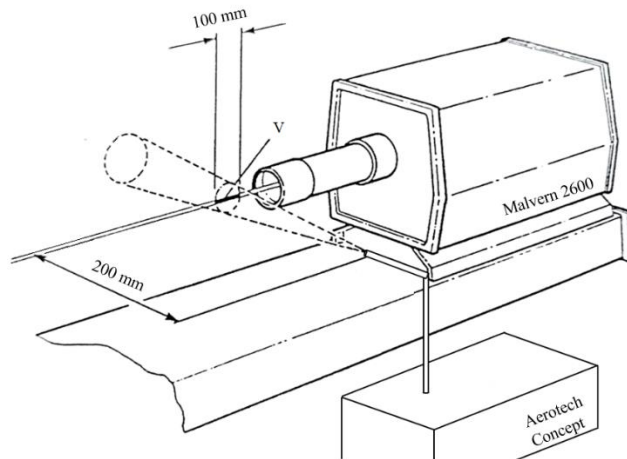


**Figure 40.** Geometry of the experiment.

For the temperature measurement, two type K thermocouples are used, one to record the ambient temperature (Thermocouple 1 in Figure 39) and another connected to the vaporizer (Thermocouple 2 in Figure 39). The data acquisition system NI 9213 allows the continuous measurement of the temperatures from the ambient until the maximum ensuring an error below 0.02 °C. The experimental setup is depicted in Figure 41.

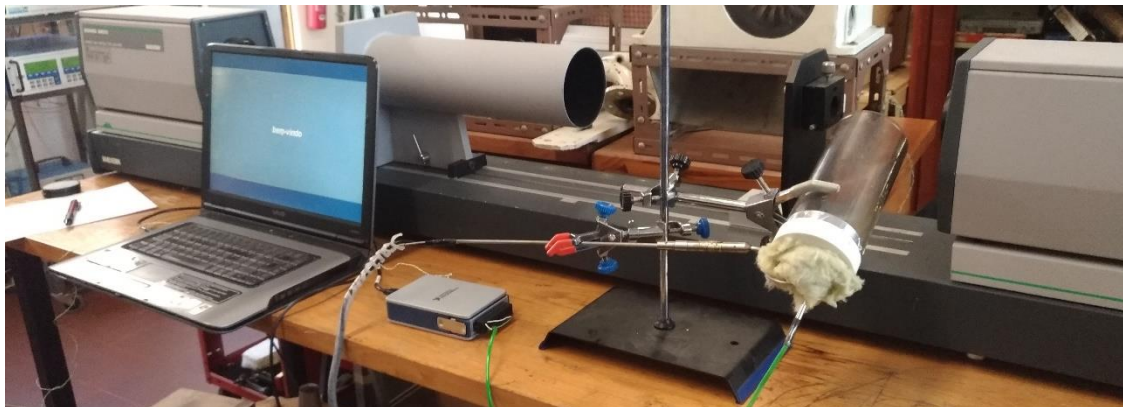


**Figure 41.** Photograph of the experimental setup.

With the measurement of the vaporizer temperature, it is possible to determine the relationship between the vaporizer temperature and the diameter of the particle generated by the seeding generator. To control the vaporizer heating, the seeding generator allows the variation of the heater voltage from 5 V to 30 V. However, from previous experience, the study was restricted between 5 V and 20 V, since higher voltage leads to vaporizer overheating. In that sense, different heater voltage are tested for each flow rate, and a specific vaporizer temperature is recorded. An important information that must be known before the discussion of the results is related to the properties of the olive oil. In this case, the one used for the

experiments is a mixture of refined and virgin olive oil. According to Detwiler & Markley [192], virgin olive oil presents the thermal properties presented in Table 8.

**Table 8.** Virgin olive oil properties.

Property	Definition	Temperature (°C)
Smoke point	Temperature at which the oil starts to produce a continuous and visible smoke	199 - 243
Flash point	Lowest temperature at which vapors of the material will ignite	321
Fire point	Lowest temperature at which vapor will keep burning after the ignition source is removed	361

#### d) Analysis method for the measurement of the seeding particles diameter

In terms of analysis mode used by Malvern 2600, the Model Independent Analysis is selected. This mode estimates a volume distribution based on the measured light energy data, assuming a 15 degree polynomial, and new light energy distribution is calculated using the equation (34) while the residual difference is calculated by equation (35):

$$D_j = U_{ij}V_i \quad (34)$$

$$\text{Log } D = \text{Log}_{10} \left( \sum (D_j - L_j)^2 \right) \quad (35)$$

where  $i$  is the index of size band,  $j$  the index of detector elements,  $U_{ij}$  describes how particles in size band  $i$  scatter light to detector element  $j$ .  $D_j$  is the measured data,  $V_i$  the relative volume of material contained in the particles in size band  $i$  and  $L_j$  the data calculated from the estimated volume distribution. A new set of values of  $L_j$  is calculated from the difference between  $D_j$  and  $L_j$ . This is an iterative process that stops when the residual reaches a minimum.

The result of the measurement corresponds to a volume distribution of the material in the 32 bands. Since the main interest of the measurement is to obtain a particle diameter, the volume distribution must be converted to diameter. The derived diameters are calculated using equation (36):

$$D_{m,n} = \left[ \frac{\sum V_i d_i^{m-3}}{\sum V_i d_i^{n-3}} \right]^{\frac{1}{m-n}} \quad (36)$$

where  $d_i$  represents the mean diameter of size band  $i$ ,  $m$  and  $n$  are subscripts that can take the value 3, if a representation of the diameter in terms of volume is desired, a value of 2 for surface, 1 for length, and 0 for number. The derived diameter usually used in this type of measurement is the Sauter Mean

Diameter (SMD),  $D_{3,2}$ , since the ratio of volume to surface area for the Sauter mean is the same as the ratio for the entire volume of particles [193]. This parameter is calculated through Eq. (37), where  $n_i$  is the number fraction in band  $i$ .

$$D_{3,2} = \frac{\sum n_i d_i^3}{\sum n_i d_i^2} \quad (37)$$

#### e) Seeding particles diameter in function of the seeding generator conditions

Preliminary tests are performed in order to analyze the relationship between the flow rate and the vaporizer temperature varying the flow rate from 2 ml/h to 10 ml/h and the voltage from 5 V to 20 V. From this preliminary analysis, it is observed that for the same voltage, the vaporizer temperature increases with the decrease of the flow rate. Even if a constant voltage is applied to the heater, since a lower quantity of olive oil (at ambient temperature) flows through the vaporizer to be heated, its temperature increases. Due to this fact, an interesting event occurs when 20 V is applied, the measurement of the particle diameter is only possible with a flow rate between 9 ml/h and 10 ml/h. At a lower flow rate, the vaporizer started to burn, meaning that the temperature achieved is too high, leading to an auto-ignition of the olive oil particles, as it is possible to observe in Figure 42.



**Figure 42.** Auto-ignition of the olive oil particles inside the vaporizer.

According to the temperature recorded by the data acquisition system this event happened at approximately 600 °C which is in accordance with [194], who mentioned that the ignition of the olive oil in contact with a hot surface is higher than 495 °C. On the other hand, 5 V seems to be too low to conduct the experiments, since no seeding particles are generated. The vaporizer temperature registered with this voltage is close to 165 °C meaning that the smoke point is not achieved at this temperature, which is in accordance with [192]. In that sense, this study allows to conclude that to perform an accurate

analysis of the particle's diameter, the measurement must be conducted at a voltage between 10 V and 15 V.

- **Variation of the vaporizer temperature with flow rate variation**

The experiments are conducted under controlled conditions. The ambient temperature is registered throughout the experiments, varying between 23 °C and 25 °C when 15 V are tested and 21 °C and 24 °C for 10 V. Figure 43 and Figure 44 show the variation of the vaporizer temperature throughout the experiment for 15 V and 10 V, respectively. FR2 to FR10 represents the different flow rate levels indicated in the Concept Smoke Aerotech System.

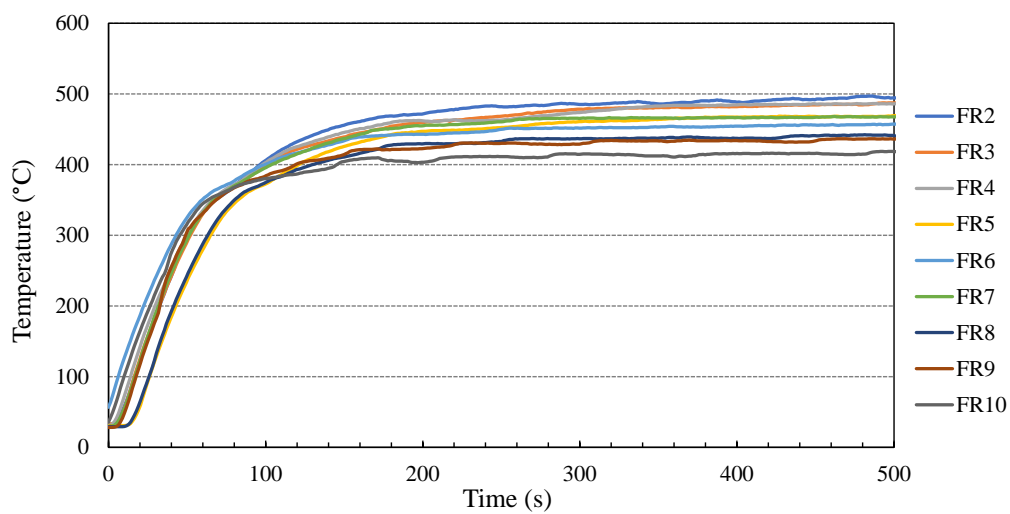


**Figure 43.** Variation of the vaporizer temperature with time at 15 V.

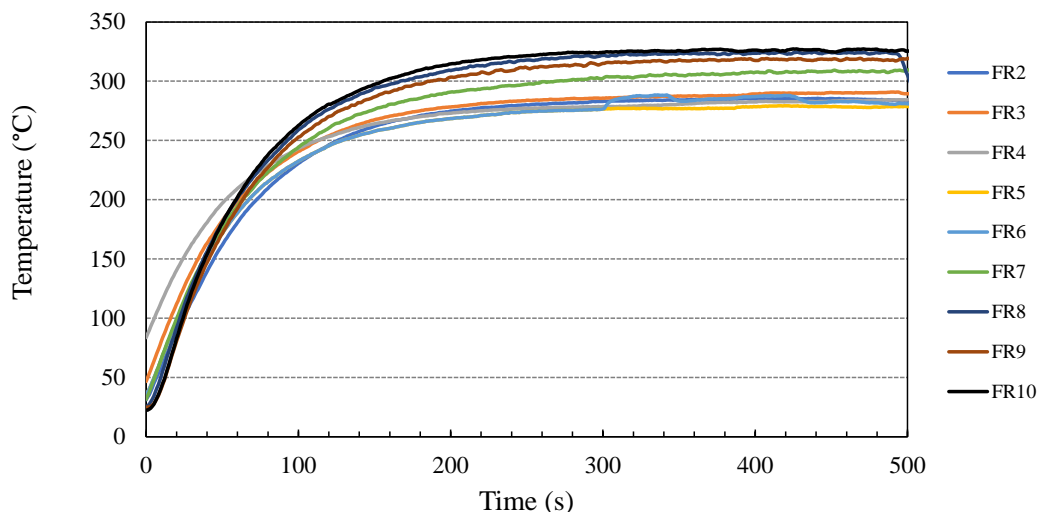


**Figure 44.** Variation of the vaporizer temperature with time at 10 V.

Both plots show a similar heating behavior of the vaporizer, beginning with fast heating followed by a slow temperature rise after approximately 120 s. While in Figure 43, the increase of the vaporizer

temperature with flow rate is observed, in Figure 44 this is not the case, since higher temperatures are achieved for a flow rate of 10 ml/h decreasing with the decrease of the flow rate.

To analyze the influence of the vaporizer temperature on the particle's diameter, the mean maximum temperature achieved by the vaporizer is calculated and presented in Table 9, as well as the uncertainty associated with each measurement.

**Table 9.** Variation of the mean vaporizer temperature in function of the heater voltage and the flow rate in steady-state conditions.

Voltage (V)	Mean Temperature (°C)	Flow rate (ml/h)							
		10	9	8	7	6	5	4	3
15	422.3(0) ± 0.36	439.7(3) ± 0.30	445.1(8) ± 0.39	460.2(8) ± 0.70	468.1(2) ± 0.21	480.9(4) ± 0.16	488.2(4) ± 0.21	491.0(1) ± 0.41	502.6(2) ± 0.68
	10	326.8(9) ± 0.19	318.5(1) ± 0.32	323.8(9) ± 0.43	308.2(1) ± 0.32	287.8(9) ± 0.37	279.1(3) ± 0.15	285.8(8) ± 0.14	290.3(0) ± 0.21

Focusing on the results obtained for the case of a heater voltage of 15 V, it seems that the maximum temperature reached by the vaporizer increases with the decrease of the flow rate, as expected. However, this is not the case in the second experiment with a heater voltage of 10 V. It is clear that a lower heater voltage suggests a lower maximum temperature reached by the vaporizer, nevertheless no correlation between the flow rate and the temperature is identified. It seems that higher temperatures are achieved at a flow rate range between 7 ml/h and 10 ml/h. An important aspect to mention is related to the fact that, with 10 V, some olive oil particles are not vaporized remaining in a liquid state as it is possible to observe in Figure 45. With liquid olive oil flowing outside the vaporizer, a decrease in temperature occurred; however, it is difficult to quantify the volume of olive oil that did not vaporize. This observation shows that to ensure a constant smoke with a good concentration of particles, the vaporizer must work at a temperature above approximately 400 °C, ensuring good vaporization of the olive oil particles.



**Figure 45.** Partial evaporation of the olive oil particles at 10 V.

- **Variation of the particles diameter with flow rate and heater voltage**

The particle's diameter is measured for each flow rate and conducted two times considering a heater voltage of 10 V and 15 V. Since the concentration of particles is not constant throughout the experiments and considering that a minimum air current variation leads to measurement errors, five measurements are performed for each test and the mean is calculated. The results are presented in Figure 46.

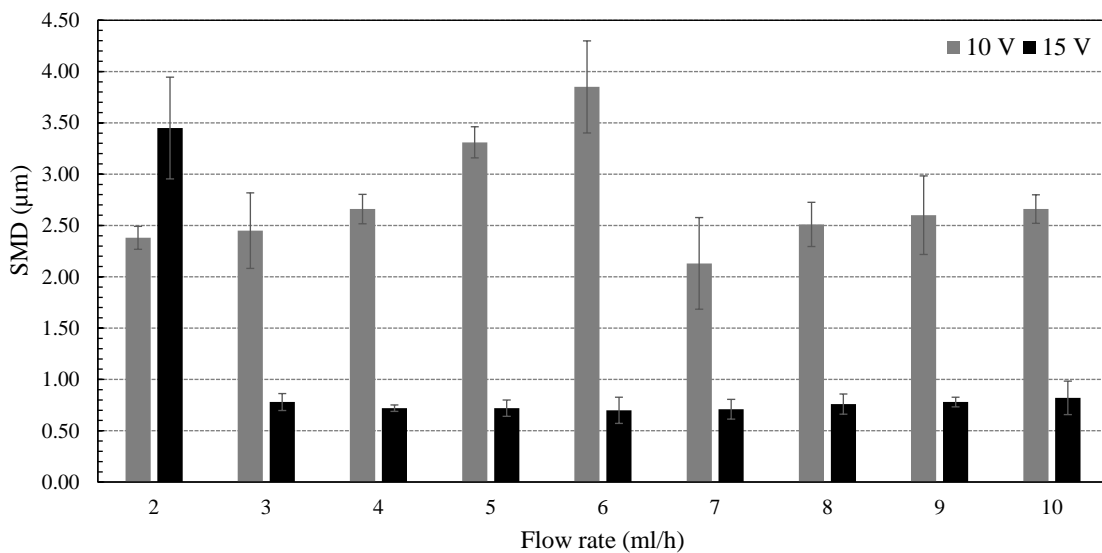


**Figure 46.** Mean particle diameter variation with flow rate and heater voltage for 95 % confidence level.

The results expressed in Figure 46 show a large difference between the data obtained with 10 V and 15 V, with the mean particle's diameter values varying around 2 µm. As mentioned previously, the vaporization of the olive oil particles at a heater voltage of 10 V is performed at lower temperatures compared with 15 V. Considering that the olive oil viscosity and surface tension decrease with the increase

of temperature [190], it seems that these properties are higher for the 10 V case. According to [195] the mean droplet size decreases with increasing liquid density, air density, and air velocity exposed to an air flow and increases with an increase in liquid flow rate, viscosity, and surface tension. This effect explains the difference between the particle's diameter measured using a heater voltage of 10 V and 15 V. Considering these observations and since a lower particle's diameter is achieved for a heater voltage of 15 V, this last parameter is applied to conduct the PIV measurements.

After the selection of the heater voltage, it is important to define the flow rate that ensures the best diameter of particles. As previously mentioned, particles with a diameter of around 1  $\mu\text{m}$ , or smaller, ensure an acceptable tracking of turbulent air flows. Looking at the results shown in Figure 46, the olive oil droplets generated by the seeding generator with the vaporizer working at 15 V, generates droplets with a diameter varying between  $0.70 \pm 0.13 \mu\text{m}$  and  $0.82 \pm 0.16 \mu\text{m}$ , excepts for the case in which the flow rate is equal to 2 ml/h. These results confirm a flow rate varying between 3 and 10 ml/h is suitable for the study of a jet impingement system for a wide range of Reynolds numbers (both in the laminar and turbulent regimes). Focusing on the mean droplet diameter obtained by the lower flow rate, 2 ml/h, the discrepancy of this value compared with the others is too high. Through simple observation of the flow concentration generated using these parameters (flow rate of 2 ml/h and 15 V), it was verified that this concentration is very low to allow accurate measurements using the Laser Diffraction Technique. Thus, the data obtained will not be considered in further analysis.

According to [195], the mean droplet size increases with increasing the liquid flow rate. Looking at the results, this behavior is valid for a specific range of olive oil flow rate values, between a flow rate of 6 and 10 ml/h, with the olive oil droplets diameter increasing from  $0.70 \pm 0.13 \mu\text{m}$  to  $0.82 \pm 0.16 \mu\text{m}$ . Lower than a flow rate of 6 ml/h, the variation of the mean diameter does not follow a specific trend, even if the particles generated presents a satisfactory diameter. According to this study, it seems that the conditions that allow to obtain the most suitable mean particle's diameter are a flow rate of 6 ml/h and the vaporizer working at 15 V. Nevertheless, a flow rate ranging between 3 and 10 ml/h is also suitable.

#### **h) Particle's concentration**

To ensure a reliable analysis of the particle's motion through PIV, a uniform seeding concentration in the flow in the analysis is required. Two major sources of errors can arise from a high seeding concentration, leading to higher uncertainty in the estimative of the particle's motion [196]: (1) the increase of the non-matching particle images and (2) the increase of the over-lapping between particle images with increasing seeding density.

The introduction of the seeding particles inside the system is a critical part of the PIV experiments. According to Tropea [186], seeding particles for air flow tracking must be entrained in the air and then introduced upstream of the measurement region. Since the experimental setup consists of an open system, the seeding particles cannot be recirculated by the fan. Therefore, to ensure accurate mixing between the seeding particles and the air blown by the fan, the vaporizer is placed inside the stabilization chamber.

Once determined the position of the vaporizer to ensure an accurate seeding, the concentration of particles in the system is tested. To acquire accurate velocity field measurements, Grant [187] recommended a concentration of approximately 15 particles per interrogation area. The analysis of the particle's concentration per interrogation area is conducted in each PIV experiment. Through image visualization and the particle density function of the Dynamic Studio™ software, it is possible to estimate the number of particles per interrogation area and to validate the experiment. Figure 47 shows the effect of seeding concentration on the images captured by the PIV system, in which the differences between uniform and non-uniform seeding are observed. Too high concentration can induce opacity and while not enough seeding will generate inadequate vectors, reducing the velocity field accuracy [175]. From the data obtained by PIV measurements, an average of 10 seeding particles per interrogation area is recorded. According to [166] and [187], this value is suitable to obtain an accurate velocity field.

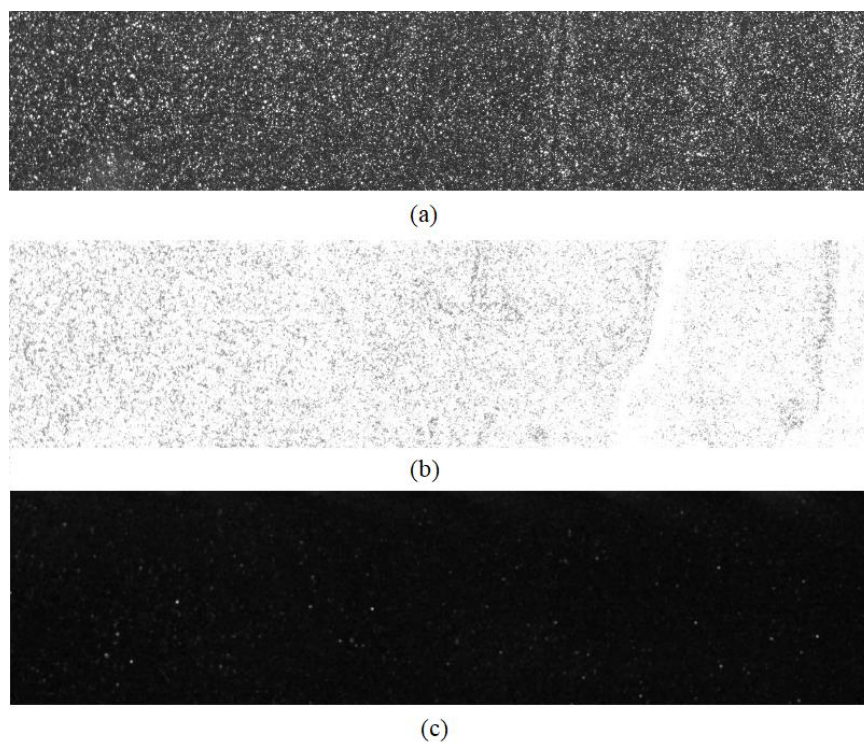


**Figure 47.** Effect of seeding concentration on PIV measurements: (a) uniform; (b) high; (c) low.

A last comment related to the seeding particles concerns the refractive index. As previously mentioned, it is important to ensure that the materials used for flow visualization, i.e. test section walls and seeding particles, have closely matched refractive indices [167]. Considering that olive oil has a refractive index varying between 1.44 and 1.47 and this value for the acrylic walls is equal to 1.49, it can be concluded that the olive oil particles are a good choice to conduct the PIV measurements.

### 3.3.4. Source of Errors

Considering all the aspects previously explored, the two main factors that influence the uncertainty quantification in PIV are the experimental setup and the seeding particles. These factors induce influence quantities that affect the relationship between the indication and the measurement results [163]. Before addressing these factors, attention is given to the calibration process and the time between pulses, since they are directly dependent on the user.

#### a) Calibration

The calibration of the PIV system is performed using a ruler (Figure 48). It has been demonstrated by [197] that the error resulting from calibration, applying as a comparison the scaling factors obtained in each measurement, is insignificant using a ruler or a calibration plate. The ruler is aligned with the laser sheet which passes through the center of the central nozzle. A minimum sheet thickness of 2 mm is ensured to reduce errors induced by the out-of-plane motion of the seeding particles [166].

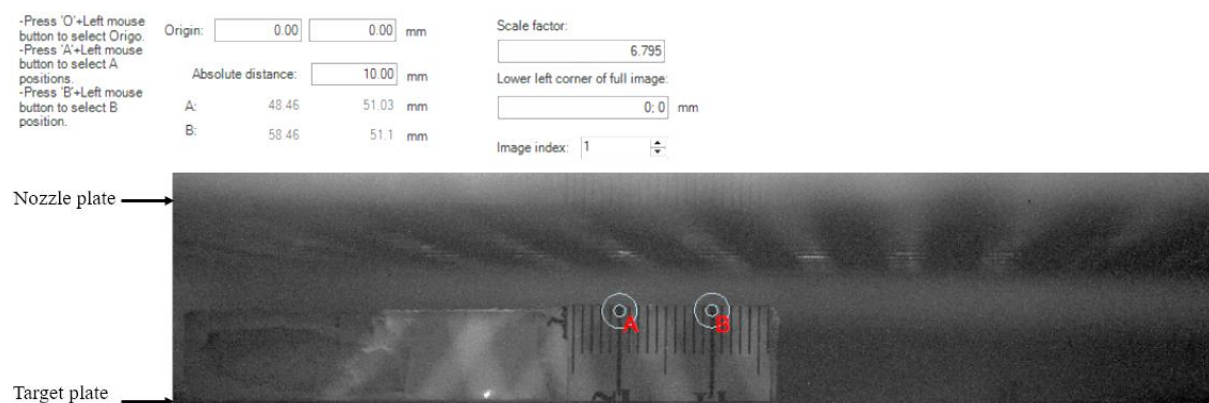


Figure 48. PIV system calibration

#### b) Time between pulses

The definition of a correct time between pulses is fundamental to minimize measurement errors. This parameter must be set according to the flow velocity and must be long enough to determine, with

accuracy, the displacement between particles but short enough to minimize out-of-plane particle's displacement [196]. To analyze the influence of the time between pulses on the velocity magnitude measured by the PIV system, this parameter is varied, and the velocity profile obtained at the exit of the nozzle plate and over the target plate are plotted and presented in Figure 49 and Figure 50, respectively for a Reynolds number equal to 420. While the velocity magnitude normalized by the maximum nozzle exit velocity ( $U/U_{max}$ ) is plotted over all the nozzle orifice diameter, the variation of  $U/U_{max}$  over the target plate is plotted from the jet axis ( $x/D = 0$ ) to one side of the plate since the jet is symmetric. To conduct this analysis the normalized distance from the jet axis to the target plate is considered as  $x/D$ , the ratio between the distance in  $x$  direction and the jet diameter,  $D$ .

Looking at Figure 49, where the maximum velocity is recorded, it appears that too high (600  $\mu$ s) and too low (100  $\mu$ s) time between pulses lead to higher measurement errors, as mentioned previously. Between 200  $\mu$ s and 500  $\mu$ s the difference between the maximum normalized velocity recorded is lower than 1 %.

Focusing on the velocity profile over the target plate, Figure 50, a larger time between pulses (1300  $\mu$ s to 600  $\mu$ s) seems to underestimate the maximum velocity when compared to lower  $\Delta t$ . The maximum normalized velocity of 0.55 is recorded at  $\Delta t = 500 \mu$ s. For  $\Delta t = 300 \mu$ s, a maximum value close to 0.55 is observed but higher velocities are recorded over the target plate compared with  $\Delta t = 500 \mu$ s. In addition, the velocity profile seems to be more uniform at  $\Delta t = 300 \mu$ s.

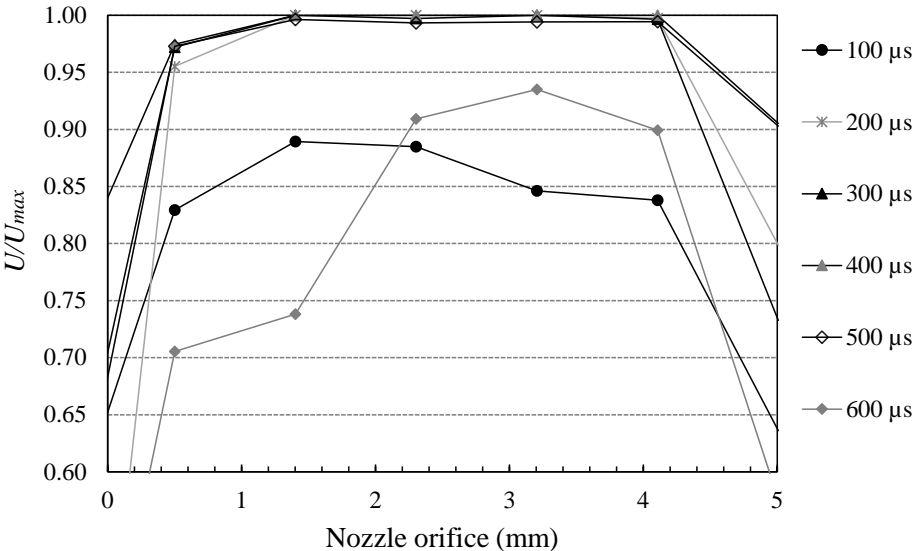


**Figure 49.** Variation of the normalized velocity magnitude at the exit of the nozzle throughout all its diameter for different time between pulses.

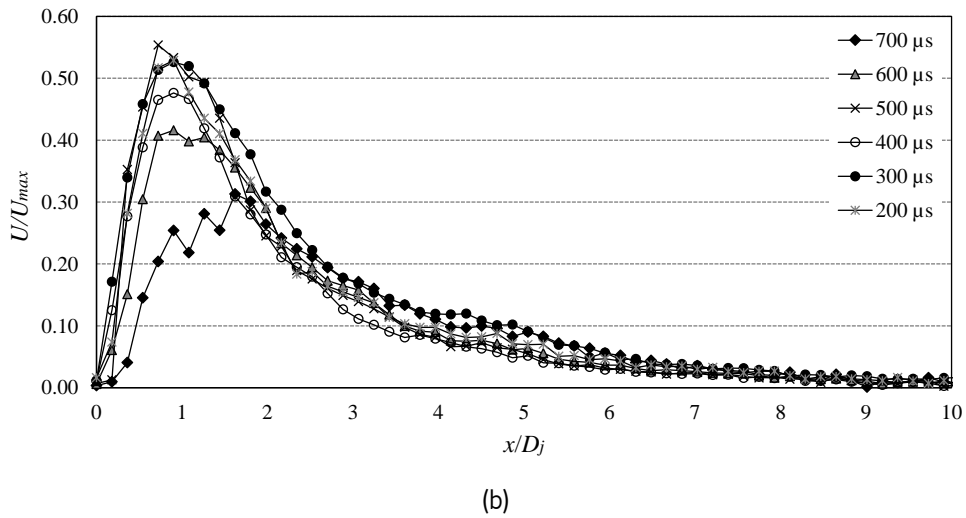
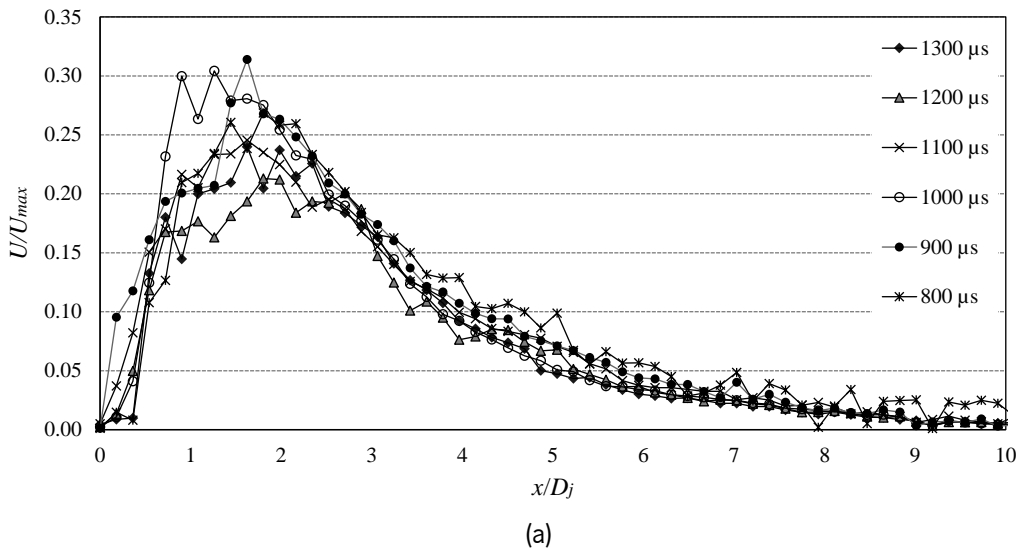


**Figure 50.** Normalized velocity magnitude over the target plate at a different time between pulses (a) 800  $\mu\text{s}$  to 1300  $\mu\text{s}$  (b) 200  $\mu\text{s}$  to 700  $\mu\text{s}$ .

As it can be observed, the maximum value is recorded at the exit of the nozzle orifice and decreases when approaching the target plate, until the stagnation point is reached. From this region, the jet flow is divided, increasing its velocity magnitude near the jet axis. In this specific case of a Reynolds number of 420, the experiments show a velocity decrease of approximately 45 % from the nozzle plate to the maximum velocity recorded over the target plate, if a correct time between pulses is applied. Looking at the data presented in Figure 49 and Figure 50, a  $\Delta t$  between 300  $\mu\text{s}$  and 600  $\mu\text{s}$  seems to be appropriate for the study of an air jet impingement flow for  $\text{Re} = 420$ . More details regarding the selection of the appropriate time between pulses are presented in the next section, based on the uncertainty estimation.

### 3.3.5. Uncertainty Estimation in PIV Measurements

An analysis of different variables, identified in a purpose-built experimental setup, that affects the velocity field of multiple jet impingement, was presented in the previous section. Four main categories were identified in the Ishikawa Diagram (Figure 31): PIV, Seeding, Experimental and Ambient conditions. As mentioned above, the different quantities identified have a great influence on the flow field velocity [169]. However, some of them are difficult to quantify. In that sense, they are not all accounted for in the uncertainty quantification of the velocity measurement. In the case of the PIV and Seeding, they are accounted by the Sciacchitano et al. method [198], which is presented in this section.

As previously stated, the total uncertainty of a measurement is composed of the uncertainty arising from systematic and random effects [169]. The systematic errors are typically constant and mainly related to incorrect calibration and/or incorrect operation of the measurement system. However, these errors are difficult to determine in complex measurement systems such as PIV. Several works have been dedicated to quantify the total uncertainty of PIV systems [198–201]. In this work, the methodology presented by [198] is applied. Regarding the random errors, they are characterized by their non-predictable nature and can change in magnitude and sign for every single measurement [166].

In the PIV technique, the velocity field of the flow is obtained indirectly as a displacement of the tracer particles in a finite time interval as presented in Eq.(38) [202]:

$$D(X; t', t'') = \int_{t'}^{t''} U [X(t), t] dt \quad (38)$$

where,  $D (X; t', t'')$  is the tracer particle displacement and  $U [X(t), t]$  its velocity. For ideal particles,  $U$  must be equal to the velocity of the flow in study. The PIV system analyzes this displacement by image analysis, and so, the instantaneous velocity of the particle ( $U$ ) given by the system is such as Eq. (39):

$$U = S_c \frac{\Delta x_p}{\Delta t} \quad (39)$$

where  $S_c$  is the scale factor,  $\Delta x_p$  is the displacement in pixels, and  $\Delta t$  the time between the two consecutive images recorded by the camera [203]. The scale factor is used to convert pixel coordinates to an object-space position (in mm) [197]. The scale factor value, obtained by image calibration, is used to reconstruct each image obtained by the PIV [204]. The connection between the physical distance, provided by a normalized measurement scale, and the pixel grid is obtained by the image captured by the camera.

The velocity obtained by PIV through Eq. (39), even if determined automatically, is a quantity that depends upon  $\Delta x_p$  and  $\Delta t$ . In that sense, an uncertainty estimation can be obtained by Eq. (40), which results from the development of the Taylor series for the uncertainty of a dependent quantity [169]:

$$u^2 = \sum_{i=1}^N p_i^2 u^2(x_i) \quad (40)$$

where  $u$  is the combined standard uncertainty, while  $u(x_i)$  is a standard uncertainty for a specific quantity  $x_i$  and  $p_i$ , expressed by Eq. (41), is the sensitivity coefficient given in terms of each quantity  $x_i$ .

$$p_i^2 = \left( \frac{\partial f}{\partial x_i} \right)^2 \quad (41)$$

The velocity measured,  $U$ , is composed by two components, in  $x$  direction and  $y$  direction, being the uncertainty related to both components expressed by  $u_{U_x}$  and  $u_{U_y}$ , respectively. In this specific case,  $u_{U_x} = u_{U_y} = u_U$  and  $p_i$  depends on the time between pulses,  $\Delta t$ , the scalar factor variation,  $\Delta S_c$ , and the particle's displacement,  $\Delta x_p$ . Replacing these variables in Eq. (40), one obtains Eq. (42):

$$u_U = \sqrt{\left( \frac{\partial U}{\partial(\Delta S_c)} u_{S_c} \right)^2 + \left( \frac{\partial U}{\partial(\Delta x_p)} u_{x_p} \right)^2 + \left( \frac{\partial U}{\partial t} u_t \right)^2} \quad (42)$$

Since the time between pulses  $\Delta t$ , can be considered infinitely small, for a certain range of flow turbulence, its contribution to the velocity uncertainty can be neglected, simplifying the equation in Eq. (43):

$$u_U = \sqrt{\left( \frac{\partial U}{\partial(\Delta S_c)} u_{S_c} \right)^2 + \left( \frac{\partial U}{\partial(\Delta x_p)} u_{\Delta x_p} \right)^2} \quad (43)$$

Sciacchitano et al. [198] presented a methodology for uncertainty quantification of PIV systems, known as the discrete window offset technique. This method consists of the statistical analysis of the matched particle image disparity, which is the residual distance between two consecutive particle images obtained after the matching. The displacement between two particles in an image is obtained by cross-correlation analysis [174]. The interrogation window obtained in the second image will be shifted toward the first window using the closest integer approximation, from which pairs of particles will overlap. Even if this

measurement procedure is capable, some pairs of particles are expected not to correspond exactly. This mismatch can be related to several factors, namely: the displacement of particle image that can be related to sub-pixel particle image movement, laser power fluctuation, and camera viewing angle; the measurement position coming from the origin correlation and particles distribution; the time between pulses that must be defined in function of the particles velocity gradient; the calibration errors, due to lens image distortion, misalignment between the calibration plate and the laser sheet, image and physical distance of calibration plate dots, but also due to lens aberration and magnification [203]. The uncertainty quantification through discrete windows offset technique follows a sequence presented by Sciacchitano et al. [198]: First, the shift between the first and second interrogation windows is approximated to the closest integer number of pixels, being obtained the best velocity estimator. The particle images identified close to each other are considered as a pair and the distance between each pair is measured from their centroids. In the end, the velocity vector error is estimated by the statistical analysis of the dispersion (i.e. the variability of the observed values about their mean [169]) and the mean value of the disparity vectors of each particle pairs identified in a specific window. The dispersion of the disparity vector returns the estimate of the random error, while the mean value of the disparity indicates the occurrence of systematic errors [198]. In that sense, the accuracy of the error estimation depends on particle image density.

#### a) Random uncertainty in PIV

The random errors in PIV measurements are due to horizontal and vertical displacement,  $\sigma_{\bar{x}_U}$ , and  $\sigma_{\bar{x}_V}$ , respectively. These errors are assumed to be independent and normally distributed with zero mean and standard deviation  $\sigma$ . The resultant random error,  $\sigma_{\bar{x}_R}$ , follows a Rayleigh distribution, being given by the square root of the squared random errors,  $\sigma_{\bar{x}_U}$ , and  $\sigma_{\bar{x}_V}$ , as expressed in Eq. (44) [184]. For this analysis,  $\sigma_{\bar{x}_R}$  is determined considering the level of confidence of 95 % and is obtained by the square root of the squared  $\sigma_{\bar{x}_U}$  and  $\sigma_{\bar{x}_V}$ . A total sample number,  $N$ , equal to 100 is considered, being the 95 % confidence achieved with a factor equal to  $k_p = 1.96$  [165] according to Eq. (45). This equation is used for  $\sigma_{\bar{x}_U}$  and  $\sigma_{\bar{x}_V}$  considering  $\sigma_U$  and  $\sigma_V$ , respectively.

$$\sigma_{\bar{x}_R} = \sqrt{\sigma_{\bar{x}_U}^2 + \sigma_{\bar{x}_V}^2} \quad (44)$$

$$\sigma_{\bar{x}_{U, V}} = k_p \frac{\sigma_{U, V}}{\sqrt{N}} \quad (45)$$

## b) Comparing PIV with Pitot tube

Because of the sensitiveness of the PIV technique, it is fundamental to ensure that all the test conditions are accurately controlled, minimizing the uncertainty associated with random and systematic errors. The Pitot tube is used to confirm if the velocities measured by the PIV lies within the expected range of values, following the methodology presented in section 3.2.3. The test conditions are performed with air at ambient temperature ( $\approx 22$  °C), impinging a flat plate at the same temperature.

As the maximum velocity occurs at the nozzle inlet, this velocity is analyzed to compare both measurement systems. The control of the air velocity is performed using the fan frequency drive Mitsubishi S500. The results presented in Table 10 show the velocity obtained at the nozzle exit recorded by the Pitot tube and PIV. A total of 5 dynamic pressures per fan frequency are considered to estimate the uncertainty associated with the velocity measured by the Pitot tube. These velocities are compared with those measured by the PIV system, being the uncertainty obtained by the statics analysis of 100 images using the methodology presented above. The results demonstrate that the velocities obtained through PIV lie in the range of values measured by the Pitot tube. In addition, the deviation between the velocity values recorded by the two techniques varies between 1 % and 5 %, and between 1 % and 10 % for the Reynolds number, except for the lower velocity, which is expected since the value measured by the Pitot tube is close to the uncertainty value of the measurement system. This study shows a good agreement between both measurement techniques.

**Table 10.** Velocity and Reynolds number at the exit of the orifice nozzle measured indirectly using the Pitot tube and directly by PIV.

Fan Frequency (Hz)	Mean Velocity Pitot (m/s)	Mean Velocity PIV (m/s)	Re Pitot	Re PIV
2.5	1.(8) $\pm$ 0.2	2.7(2) $\pm$ 0.20	601.(2) $\pm$ 5.9	897.2(3) $\pm$ 37.52
5	5.(1) $\pm$ 0.6	5.6(3) $\pm$ 0.40	1,679.(1) $\pm$ 172.5	1,857.1(3) $\pm$ 77.66
10	10.(8) $\pm$ 1.0	10.9(8) $\pm$ 0.80	3,562.(1) $\pm$ 322.2	3,621.9(0) $\pm$ 151.46
15	15.(8) $\pm$ 1.0	15.9(5) $\pm$ 1.05	5,213.(7) $\pm$ 328.0	5,261.3(2) $\pm$ 220.02
20	20.(7) $\pm$ 0.6	20.3(9) $\pm$ 1.20	6,810.(3) $\pm$ 197.8	6,725.9(1) $\pm$ 281.26
30	28.(6) $\pm$ 0.6	27.3(8) $\pm$ 1.45	9,416.(2) $\pm$ 243.8	9,031.6(5) $\pm$ 377.69

Regarding measurement uncertainties for both Pitot tube and PIV, the uncertainty increases with higher velocity values, as expected, however, this value decreases in percentage. Regarding the PIV system, the velocity at the nozzle inlet and Reynolds number uncertainties are close to 7 % and 4 %, respectively. While with Pitot tube, the uncertainty decreases from 10 % to 2 %, for both velocity and Reynolds number measurements. These results are in agreement with several studies [73, 205–207].

### **c) Optimization of the time between pulses based on random uncertainty**

To optimize the time between pulses, the random errors for different  $\Delta t$  are estimated in order to confirm the statements presented in the previous section. Furthermore, the previous analysis shows that the results obtained by the PIV measurements are in agreement with the Pitot tube measurements, and the analysis of the random and systematic errors, obtained for the maximum velocity values, demonstrate that the random errors have a greater influence on uncertainty compared with systematic errors. In that sense, random errors are considered to analyze the accuracy of the velocity measurement using PIV at a different time between pulses. The study is conducted for the case of an isothermal air jet, at a Reynolds number of 420, impinging a flat plate. Figure 51 shows the variation of the random errors over the target plate for a different time between pulses. The results demonstrated that even if a  $\Delta t = 300 \mu\text{s}$  and  $400 \mu\text{s}$  allow to obtain a good profile over the target plate, the random error is higher compared with  $\Delta t = 500 \mu\text{s}$  and  $600 \mu\text{s}$ . The results also demonstrated that the random errors are higher near the jet axis, showing that it is difficult to predict with precision the stagnation region and that this precision is higher for the case of  $\Delta t = 500 \mu\text{s}$  and  $600 \mu\text{s}$ . The higher random errors are estimated at the position where the jet flow is maximum in all cases. They decrease from this maximum with the increase of the distance from the jet axis, where velocity near zero is observed. Looking at the random errors profile in the wall jet region, the results indicate that a low time between pulses ( $\Delta t = 200 \mu\text{s}$  and  $300 \mu\text{s}$ ) presents higher random errors, showing that they are not reliable to predict the jet flow behavior in these conditions. This analysis highlights the fact that the uncertainty related to measurements is highly influenced by the time between pulses, being necessary to select a value that minimizes errors.

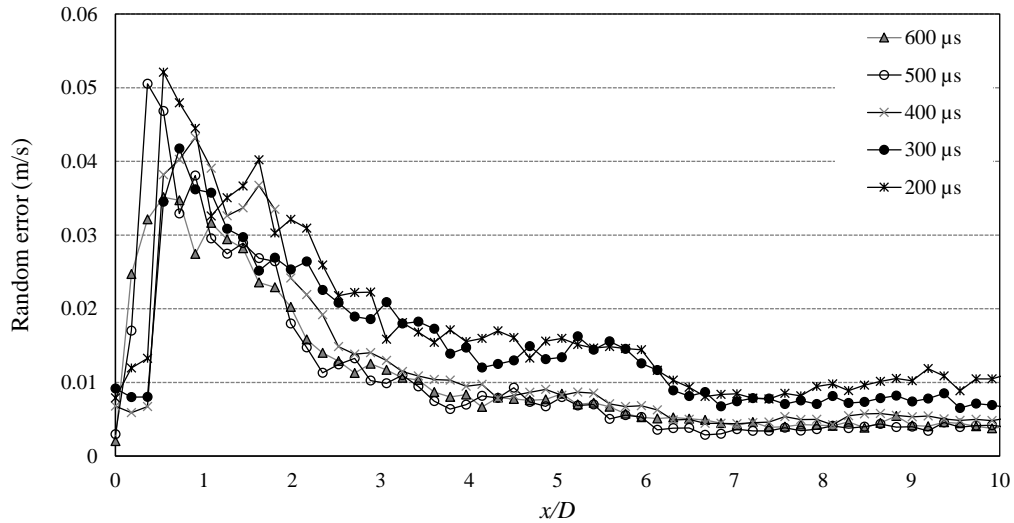


**Figure 51.** Normalized random error estimation for a different time between pulses at  $Re = 420$  and  $H/D = 7$ .

This procedure is conducted for different Reynolds numbers and Table 11 shows the optimized  $\Delta t$  for different Reynolds numbers. In this work, the focus is on  $Re = 420$ ,  $Re = 1,857$ , and  $Re = 5,261$ , which corresponds to laminar, transition, and turbulent flow regimes, respectively.

**Table 11.** Optimized time between pulses for different Reynolds numbers.

<b>Re</b>	<b><math>\Delta t</math> (<math>\mu s</math>)</b>
$897.2(3) \pm 37.52$	250
$1,857.1(3) \pm 77.66$	250
$3,621.9(0) \pm 151.46$	50
$5,261.3(2) \pm 220.02$	40
$6,725.9(1) \pm 281.26$	30
$9,031.6(5) \pm 377.69$	10

#### d) Variation of the random error in function of the Reynolds number

As mentioned throughout this work, the Reynolds number is one of the most important parameters that characterize the flow. To analyze if the behavior of the random errors is the same during the impingement process for different Reynolds numbers, the graph presented in Figure 52 is plotted. A  $H/D = 7$  is preserved and the variation of the Reynolds number is performed by changing the air velocity using the Mitsubishi S500 fan frequency drive.

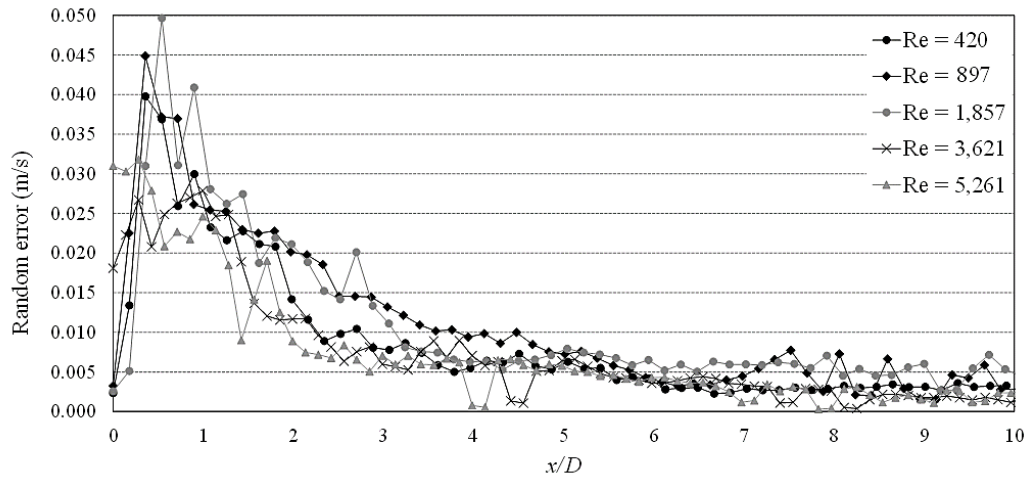


**Figure 52.** Normalized random error estimation for different Reynolds numbers for  $H/D = 7$ .

The results show that by increasing the Reynolds number, the error estimated in the stagnation point increases. This is a critical point that must be correctly defined in jet impingement studies. In that sense, these results confirm that applying jets with high Reynolds number, the PIV setup parameters must be improved, such as the time between pulses and the accuracy of the focus of the images captured by the CCD camera in this specific region, to be able to decrease the measurement errors. As in the previous study, higher measurement errors are detected at the point where the flow velocity is maximum. The higher the velocity the greater the random errors, as expected. In addition, these results demonstrate that the accurate estimative of the velocity field at the stagnation region is difficult to obtain. Proceeding to a global analysis of the random errors profile over the target plate, it seems that the velocity measurements recorded at  $Re = 5,261$  are more accurate than  $Re$  between 897 and 1,857. This specific case breaks the tendency observed in Figure 52, in which the higher the Reynolds number the higher the random errors measured over the wall jet region. These results suggested that by improving the PIV parameters, it is possible to enhance the measurements regardless of the level of turbulence of the flow.

This page is intentionally left in blank.

## 4. NUMERICAL METHODS

### 4.1. Mathematical Modeling

#### 4.1.1. Governing Equations

For a 3D formulation, mass and momentum conservation are described by Eq. (46) to Eq. (49), in which Eq. (46) represents the continuity equation, and Eq. (47) to (49), the Navier-Stokes equations. These governing equations are already simplified for an incompressible flow. If the flow modeling involves temperature variations, the energy equation, expressed by Eq. (50), must be used:

$$\frac{\partial u}{\partial x} + \frac{\partial v}{\partial y} + \frac{\partial w}{\partial z} = 0 \quad (46)$$

$$\frac{\partial u}{\partial t} + u \frac{\partial u}{\partial x} + v \frac{\partial u}{\partial y} + w \frac{\partial u}{\partial z} = -\frac{\partial p}{\partial x} + \nu \frac{\partial^2 u}{\partial x^2} + \nu \frac{\partial^2 u}{\partial y^2} + \nu \frac{\partial^2 u}{\partial z^2} \quad (47)$$

$$\frac{\partial v}{\partial t} + u \frac{\partial v}{\partial x} + v \frac{\partial v}{\partial y} + w \frac{\partial v}{\partial z} = -\frac{\partial p}{\partial y} + \nu \frac{\partial^2 v}{\partial x^2} + \nu \frac{\partial^2 v}{\partial y^2} + \nu \frac{\partial^2 v}{\partial z^2} \quad (48)$$

$$\frac{\partial w}{\partial t} + u \frac{\partial w}{\partial x} + v \frac{\partial w}{\partial y} + w \frac{\partial w}{\partial z} = -\frac{\partial p}{\partial z} + \nu \frac{\partial^2 w}{\partial x^2} + \nu \frac{\partial^2 w}{\partial y^2} + \nu \frac{\partial^2 w}{\partial z^2} \quad (49)$$

$$\frac{\partial T}{\partial t} + u \frac{\partial T}{\partial x} + v \frac{\partial T}{\partial y} + w \frac{\partial T}{\partial z} = \kappa \frac{\partial^2 T}{\partial x^2} + \kappa \frac{\partial^2 T}{\partial y^2} + \kappa \frac{\partial^2 T}{\partial z^2} \quad (50)$$

where  $u$  represents the velocity in  $x$ -direction,  $v$  is the velocity in  $y$ -direction, and  $w$  the velocity in  $z$ -direction.  $p$  is the pressure and  $T$  the temperature, while  $\nu$  and  $\kappa$  are the kinematic viscosity and the thermal diffusivity of the fluid, respectively. These last variables are defined for air at jet inlet temperature, according to [156]. The effect of gravity, angular velocity, and source term are neglected since the major contribution in the process is convection.

### 4.1.2. Turbulence Models

The variables in the previous equations represent the instantaneous quantities. This makes them applicable to laminar flows although their direct application in turbulent flows would require a very fine discretization in space and time to capture the length scale that characterizes fully turbulent flows. Therefore, solving full Navier-Stokes equations is too much accurate and demands high computer resources. Since most engineering problems do not demand high levels of accuracy, averaged values seem to be enough. The method used to average N-S equations is called Reynolds Averaged Navier Stokes (RANS). This method averages the continuity and momentum equations inserting the decomposition of the instantaneous velocity by an average velocity ( $\bar{u}$ ,  $\bar{v}$ ,  $\bar{w}$ ) and a fluctuating component ( $u'$ ,  $v'$ ,  $w'$ ), as exemplified in Figure 53. The same principle is followed for the decomposition of pressure and temperature.

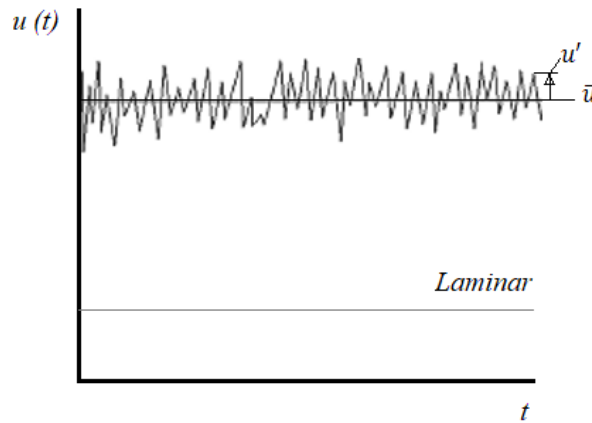


Figure 53. Representation of a turbulent velocity field measurement.

In that sense, the average continuity and momentum equations can be rewritten as Eq. (51) and (52) respectively [16]. For simplification, the averaging of N-S equation will be exemplified for the  $x$  component since the same approach is followed for  $y$  and  $z$  components:

$$\frac{\partial \bar{u}}{\partial x} + \frac{\partial \bar{v}}{\partial y} + \frac{\partial \bar{w}}{\partial z} = 0 \quad (51)$$

$$\frac{\partial \bar{u}}{\partial t} + \bar{u} \frac{\partial \bar{u}}{\partial x} + \bar{v} \frac{\partial \bar{u}}{\partial y} + \bar{w} \frac{\partial \bar{u}}{\partial z} = -\frac{\partial \bar{p}}{\partial x} + \nu \left( \frac{\partial^2 \bar{u}}{\partial x^2} + \frac{\partial^2 \bar{u}}{\partial y^2} + \frac{\partial^2 \bar{u}}{\partial z^2} \right) - \left( \frac{\partial \overline{u'u'}}{\partial x} + \frac{\partial \overline{u'v'}}{\partial y} + \frac{\partial \overline{u'w'}}{\partial z} \right) \quad (52)$$

In tensor form, and considering the three components of velocity  $x$ ,  $y$ , and  $z$ , Eq. (51) and Eq. (52) become equal to Eq. (53) and Eq. (54). This system of equations is known as RANS [208].

$$\frac{\partial \bar{u}_i}{\partial x_i} = 0 \quad (53)$$

$$\frac{\partial \bar{u}_i}{\partial t} + \bar{u}_j \frac{\partial \bar{u}_i}{\partial x_j} = -\frac{\partial \bar{p}}{\partial x_i} + \nu \frac{\partial^2 \bar{u}_i}{\partial x_j \partial x_j} - \overline{u'_i u'_j} \quad (54)$$

where  $\overline{u'_i u'_j} = \tau_{ij}$  is the Reynolds stress term and incorporates the effects of turbulent motion on the mean stresses.

Due to this term, the system for the calculation of the four dependent variables,  $(\bar{u}_i)$  and  $(\bar{p})$ , has more unknown variables than equations since the Reynolds stress tensor contains six additional independent unknowns, thus the system is not closed. Closure requires the specification of  $-\overline{u'_i u'_j}$  in terms of the mean quantities and/or their derivatives through approximations. This is possible using one of two approaches, Eddy Viscosity Models (EVM) or Reynolds Stress Models (RSM). While the models of the first category assume the stress proportional to the gradients of velocity, the second ones derive a transport equation for the Reynolds Stress terms [209]. However, this second method is more complex, with more equations to solve. In that sense, the application of EVM is more usual to solve turbulence problems, since the only new unknown quantity needed is an effective turbulent kinematic viscosity,  $\nu_t$ , as it can be observed through Eq. (55):

$$-\overline{u'_i u'_j} = \nu_t \left( \frac{\partial \bar{u}_i}{\partial x_j} + \frac{\partial \bar{u}_j}{\partial x_i} \right) - \frac{2}{3} k \delta_{ij} \quad (55)$$

Turbulence models are implemented to solve the closure problem. Each model uses different approaches to calculate  $\nu_t$  since this parameter can be determined from a turbulence time scale (or velocity scale) and a length scale [210]. In that sense,  $\nu_t$  must be solved depending on the turbulence model selected: the turbulent kinetic energy ( $k$ ), expressed by Eq. (56), which is the kinetic energy per unit mass of the turbulent fluctuations  $u'_i$  in a turbulent flow; the turbulence dissipation rate ( $\varepsilon$ ), given by Eq. (57), that represents the rate at which turbulence kinetic energy is converted into thermal internal energy; and the specific dissipation rate ( $\omega$ ), obtained by Eq. (58), defined as the rate at which turbulence kinetic energy is converted into thermal internal energy per unit volume and time.

$$k = \frac{\overline{u'_i u'_i}}{2} \quad (56)$$

$$\varepsilon = \nu \frac{\partial \overline{u'_i}}{\partial x_k} \frac{\partial \overline{u'_i}}{\partial x_k} \quad (57)$$

$$\omega = \frac{\varepsilon}{k} \quad (58)$$

The turbulence models can be mainly divided in three groups regarding the methodology used to calculate  $\nu_t$  [210]:

- Spalart-Allmaras model that solves a transport equation for a modified turbulent kinetic viscosity;
- Standard  $k$ - $\varepsilon$ , RNG  $k$ - $\varepsilon$ , and Realizable  $k$ - $\varepsilon$ , solve transport equation for  $k$  and  $\varepsilon$ ;
- Standard  $k$ - $\omega$  and SST  $k$ - $\omega$  solve the transport equation for  $k$  and  $\omega$ .

As presented in chapter 2, section 2.3, from the different RANS models, the majority of the authors agree that the SST  $k$ - $\omega$  model presents more accurate predictions for the modeling of single and multiple jet impingement. In that sense, this turbulence model is implemented in this work.

#### 4.1.3. SST $k$ - $\omega$ model

The SST  $k$ - $\omega$  model, developed by Menter [132], applies the  $k$ - $\omega$  model in the near-wall region and switches to the  $k$ - $\varepsilon$  model in the far field, combining the advantages of both models.  $k$ - $\omega$  model performs much better than  $k$ - $\varepsilon$  model for boundary layer flows, however, it is excessively sensitive to the freestream value of  $\omega$  which is not the case of the  $k$ - $\varepsilon$  model. The combination between the SST and the  $k$ - $\omega$  models improves the near wall treatment since it gradually switches from a classical low-Reynolds formulation on fine meshes to a log-wall function formulation on coarser grids [211]. To describe the flow near a wall, the SST  $k$ - $\omega$  model uses a low-Reynolds number approach allowing the consideration of the details in the viscous sublayer [87]. The equations of the turbulence kinetic energy,  $k$ , and the specific dissipation rate,  $\omega$ , are presented in Eq. (59) and (60).

$$\frac{\partial}{\partial t}(\rho k) + \frac{\partial}{\partial x_i}(\rho k u_i) = \frac{\partial}{\partial x_j} \left( \Gamma_k \frac{\partial k}{\partial x_j} \right) + G_k - Y_k \quad (59)$$

$$\frac{\partial}{\partial t}(\rho \omega) + \frac{\partial}{\partial x_i}(\rho \omega u_i) = \frac{\partial}{\partial x_j} \left( \Gamma_\omega \frac{\partial \omega}{\partial x_j} \right) + G_\omega - Y_\omega + D_\omega \quad (60)$$

where  $\Gamma$  represents the effective diffusivity,  $G$  the generation, and  $Y$  the dissipation of the corresponding variables [137]. Some relevant parameters are presented in this section, however, for a complete analysis of all the equations under each variable, [212] must be explored.

Regarding the effective diffusivity of  $k$  and  $\omega$ , it is given by Eq. (61). In which  $\sigma_k$  is applied to obtain  $\Gamma_k$ , while  $\sigma_\omega$  is used to determine  $\Gamma_\omega$ .

$$\Gamma_{k,\omega} = \mu + \frac{\mu_t}{\sigma_{k,\omega}} \quad (61)$$

where the terms  $\sigma_k$  and  $\sigma_\omega$  are Prandtl number-like parameters for the transport  $k$  and  $\omega$ , obtained by Eq. (62), while the turbulent viscosity,  $\mu_t$ , is computed by combining  $k$  and  $\omega$  as expressed in Eq. (63).  $F_1$  is a blending function that simplifies the combination of the standard  $k - \varepsilon$  model and the Wilcox  $k - \omega$  model [213, 214].

$$\sigma_{k,\omega} = \frac{1}{\frac{F_1}{\sigma_{k,\omega,1}} + (1 - F_1)/\sigma_{k,\omega,2}} \quad (62)$$

$$\mu_t = \alpha^* \frac{\rho k}{\omega} \quad (63)$$

The coefficient  $\alpha^*$  softens the turbulent viscosity causing a low-Reynolds number correction and it is given by Eq. (64). Therefore, for high Reynolds numbers,  $\alpha^*$  must be set equal to 1.

$$\alpha^* = \alpha_\infty^* \left( \frac{0.024 + \text{Re}_t / 6}{1 + \text{Re}_t / 6} \right) \quad (64)$$

where  $\text{Re}_t$  is the turbulent Reynolds number defined by Eq. (65).

$$\text{Re}_t = \frac{\rho k}{\mu \omega} \quad (65)$$

The production term of turbulence kinetic energy  $G_k$  is defined by Eq. (66), where  $S$  is the modulus of the mean rate of the strain tensor, while the production of  $\omega$  is given by Eq. (67).

$$G_k = \mu_t S^2 \quad (66)$$

$$G_\omega = \alpha \frac{\omega}{k} G_k \quad (67)$$

where  $\alpha$  is the slip correction adjustment factor defined in detail by [215].

The standard SST  $k-\omega$  model does not account for several parameters that can be implemented through FLUENT solver to improve the accuracy of the predicted results, such as streamline curvature, and turbulence energy limitation. These parameters are discussed in order to determine if their implementation improves the numerical simulations.

First, according to Eq. (64), the coefficient  $\alpha^*$  softens the turbulent viscosity causing a low-Reynolds number correction. Since the range of Reynolds numbers analyzed in this work is low, the low-Re correction option is activated.

In the jet flow stagnation region, excess of turbulence kinetic energy,  $G_k$ , can occur. To avoid this problem, the generation of turbulence energy can be limited through production limiters. Two methods are available in FLUENT solver. One is based on the application of a coefficient of limitation, which takes the value of 10, and the second one considers the vorticity rate of the flow. As the deformation in the stagnation zone is nearly irrotational, vorticity is close to zero, which leads to a reduction of  $G_k$  [216]. While the first approach is known as Production Limiter, the second one is named Kato-Launder Production Limiter.

To determine the effect of these parameters on the accuracy of the numerical prediction, the SST  $k-\omega$  model with different functions activated is tested and compared with experimental data. The numerical domain consists of a row of ten jets ( $Re = 2,000$ ) spaced  $2D$  impinging a flat plate, spaced  $7D$  from the nozzle plate. These conditions are selected since multiple jets in a confined space and close to each other increase the turbulence and the complexity of the flow. The boundary conditions and solution methods are maintained constant in all simulations. To compare the different approaches, the velocity profiles over the target plate and at the central jet axis are plotted and presented in Figure 54 and Figure 55, respectively.

From the results, it appears that at the central jet axis, there is little influence of the turbulence parameter as the data follows the same profile from the nozzle inlet to the target plate. The higher difference is observed near the stagnation point, in which the SST  $k-\omega$  model with the production limiter activated seems to perform better compared with the others. However, this difference is intensified in the velocity profile over the target plate. From the results, the SST  $k-\omega$  model with the production limiter activated continues to be the one whose predictions are closer to the experimental data, while the SST  $k-\omega$  model with the Kato-Launder production limiter presents the worst results. Considering this analysis, the SST  $k-\omega$  model with low Reynolds number correction and production limiter activated is implemented.

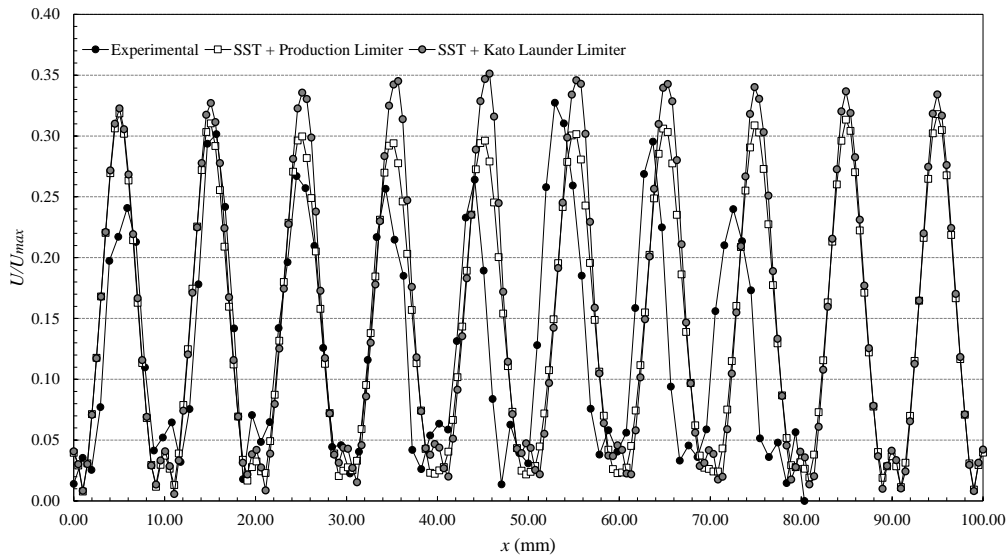


Figure 54. Velocity profile over the target plate, at  $y/D = 0.2$ , for different SST  $k-\omega$  model approaches.

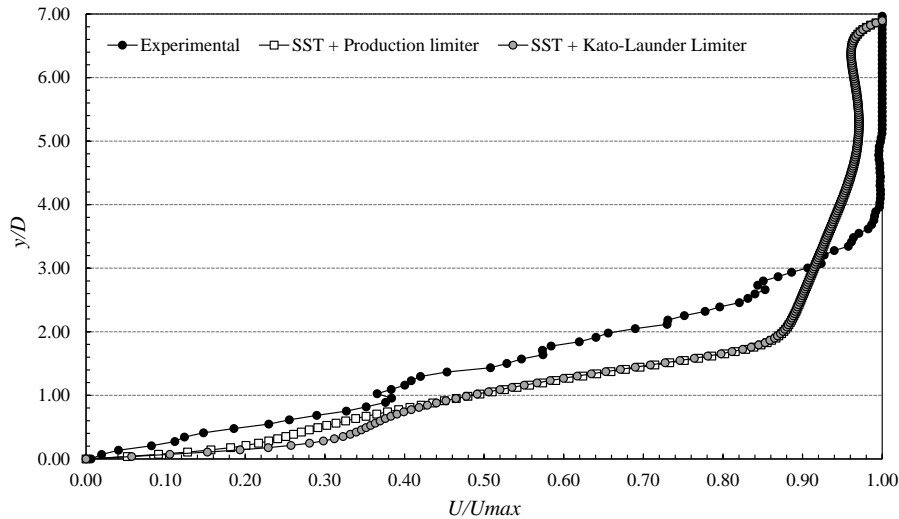


Figure 55. Velocity profile over the central jet axis ( $x/D = 0$ ) for different SST  $k-\omega$  model approaches.

Another parameter that is not accounted for by the SST  $k-\omega$  model is the streamline curvature. This effect, generated in the vicinity of the target surface, can affect the jet flow dynamics, mainly if the target is a curved surface, as stated by [217]. In that sense, it is important to analyze if this parameter has a strong effect on the numerical prediction of multiple jets impinging a flat plate. The model with sensitivity to streamline curvature and system rotation available in FLUENT solver is known as curvature correction, which is presented in detail by [212].

To study the effect of this parameter on the prediction's accuracy, the numerical model was changed in order to intensify the effect of the streamline curvature and system rotation on the jet's flow dynamics. Therefore, a line of five jet with the following conditions is modeled:  $S/D = 4$ , to be able to analyze the effect of the model on the vortices induces between jets,  $H/D = 2$  to increase the overall flow turbulence

intensity due to strong confinement and  $Re = 5,000$  to ensure that the flow is fully turbulent. The SST  $k-\omega$  model with the low Reynolds number correction and production limiter activated is tested with and without curvature correction option, and the predicted results are compared.

The velocity field over the domain, Figure 56, shows that the magnitude of the vortices developed over the surface and between the jets is approximately the same and no significant differences are observed with or without the activation of the curvature correction. In terms of the normalized velocity magnitude in the vicinity of the target plate, presented in Figure 57, the results demonstrate that a slight difference is observed near the stagnation region. However, globally, this difference is insignificant. Since the curvature correction model does not present significant improvements to the model, it will not be considered.

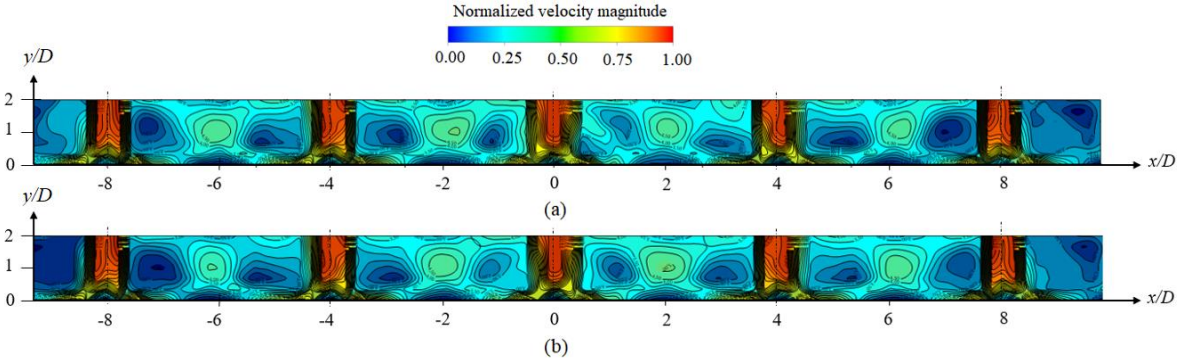


**Figure 56.** Velocity field for  $S/D = 4$ ,  $H/D = 2$ , and  $Re = 5,000$ : (a) without curvature correction; (b) with curvature correction.

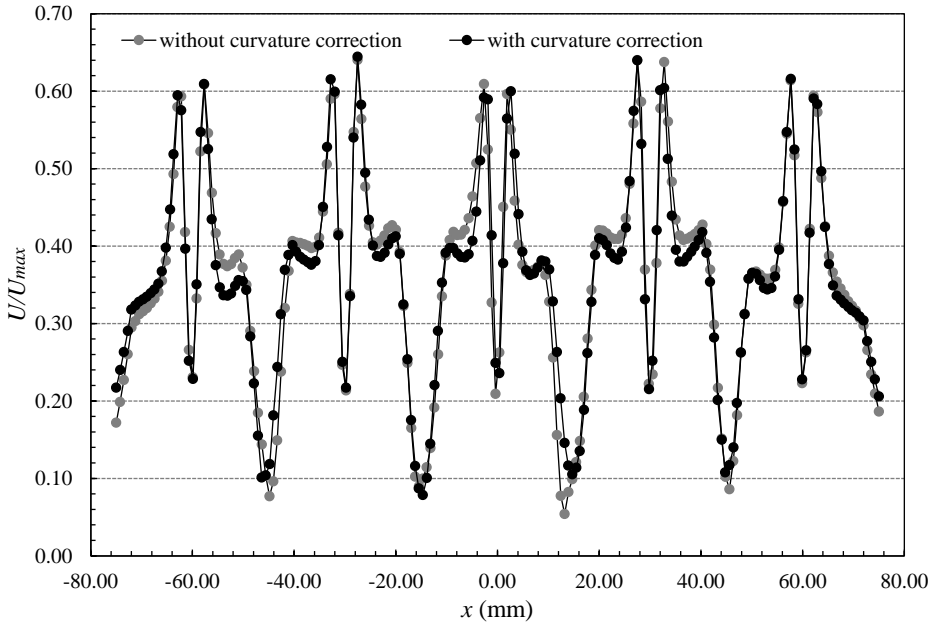


**Figure 57.** Velocity profile over the target plate, at  $y/D = 0.02$ , for  $S/D = 4$ ,  $H/D = 2$ , and  $Re = 5,000$ .

## 4.2. Numerical Softwares

### 4.2.1. ANSYS FLUENT

ANSYS FLUENT solves the governing equations for the conservation of mass, momentum, and energy through a Finite Volume method and the discrete values of any variable  $\phi$  are stored at the cell centers. The discretization on a given cell, solved by ANSYS FLUENT, is expressed by Eq. (68) [209]:

$$\frac{\partial \rho \phi}{\partial t} dV_{ce} + \sum_f^{N_{fa}} \rho_f \vec{v}_f \phi_f \vec{A}_f = \sum_f^{N_{fa}} \Gamma_\phi \nabla_{\phi_f} \vec{A}_f + S_\phi V_{ce} \quad (68)$$

where  $N_{fa}$  is the number of faces enclosing cell,  $\phi_f$  represents the value of  $\phi$  convected through face  $f$ , the term  $\rho_f \vec{v}_f \phi_f \vec{A}_f$  is the mass flux through the face, in which  $\vec{A}_f$  is the area of face  $f$ ,  $\nabla_{\phi_f}$  the gradient of  $\phi$  at face  $f$ ,  $S_\phi$  the source term, and  $V_{ce}$  the cell volume.  $\frac{\partial \rho \phi}{\partial t} dV_{ce}$  is defined in temporal discretization.

However, for the convection terms, face values  $\phi_f$  are required and they are interpolated from the cell center values using a second-order upwind scheme which derived  $\phi_f$  from quantities in the cell upstream relative to the direction of the normal velocity [209]. To compute the face values of pressure from the cell values, a second order interpolation scheme is implemented using a central differencing scheme. The spatial discretization of the convection and diffusion terms is ensured by computing the gradients  $\nabla \phi$  of a scalar  $\phi$  through a Least Squares Cell-Based gradient evaluation. Pressure-velocity coupling is applied to derive an additional condition for pressure and a procedure similar to that outlined by Rhie and Chow [218] is used to prevent checkboarding [210]. The pressure-based solver applies a SIMPLE method, which uses a relationship between velocity and pressure corrections to enforce mass conservation and to obtain the pressure field [210].

To be able to analyze the flow development from the nozzle exit to the target plate, the simulations are transient, so the governing equations are discretized in time through a first-order implicit integration. To perform the transient calculations, an adaptative time step is used. This method adjusts the time step size in function of the truncation error. If the truncation error is smaller than 0.01, the size of the time step is increased, while if the truncation error is greater, the time step size is decreased. The truncation error-based method was selected instead of the CFL method since it presents a suitable accuracy and lower computational time. Moreover, the constant truncation error value was defined based on preliminary

studies which compare different values and the simulation time, being found that an error equal to 0.01 presents good predictions at a lower simulation time.

As previously mentioned, the numerical simulations are conducted for different flow regimes, laminar, transition, and turbulent. While for the jet's flow in the transition and turbulence regime, the SST  $k-\omega$  model is implemented, for the laminar flow, FLUENT has a "Laminar model" option. This is not a DNS method, instead and since is based on Reynolds-averaged Navier-Stokes equations, this model neglected the fluctuating quantity and solves the Navier-Stokes equations considering the time-averaged velocity

The development of numerical simulations using the Laminar model is important in this work since the results obtained will be compared with a DNS formulation, based on a MATLAB framework, to validate the accuracy of FLUENT to model an air jet impingement process.

#### 4.2.2. MATLAB 2.29 Finite Volume framework

2.29 MATLAB Finite Volume framework (2.29 FV) is an in-house code developed by the MSEAS group at MIT. To solve the Navier-Stokes equations, a Boussinesq buoyancy approximation by a Finite Volume discretization on a uniform cartesian mesh using an incremental Pressure Correction in a rotational form projection method is applied. A second-order backward difference-time marching scheme is implemented, and a LU factorization is used to solve the linear systems. The advection uses a Total Variation Diminishing (TVD) advection scheme which is a mixture between the central difference scheme (CDS) and the upwind scheme (UW). TVD limits the slope to ensure that the maximum value of the function is never exceeded, and its minimum value is never undershot.

The projection method implemented by 2.29 FV to solve the Stokes problem is based on a rotational form of the Incremental Pressure correction scheme. In that sense, the time integration is conducted in the following steps, Eq. (69) – (72) [219]:

$$\left[ \frac{I}{\Delta t} - \nu \nabla^2 \right] \tilde{u}^{t+1} = \frac{u^t}{\Delta t} - \nabla P^t + F^{t+1} \quad (69)$$

$$\nabla^2(q^{t+1}) = \frac{I}{\Delta t} \nabla \cdot \tilde{u}^{t+1} \quad (70)$$

$$u^{t+1} = \tilde{u}^{t+1} - \Delta t \nabla q^{t+1} \quad (71)$$

$$P^{t+1} = q^{t+1} + P^t - \nu \nabla \tilde{u}^{t+1} \quad (72)$$

where  $P$  is the “Pseudo-pressure”,  $t$  is the time step,  $t + 1$  is the next time step,  $\nu$  is the kinetic viscosity, and  $q$  the effective order of the method. The nonlinear terms are treated explicitly, i.e., to solve the Navier Stokes equation  $F^{n+1} \approx -u^n \cdot \nabla u^n$ .

The Navier-Stokes solvers implemented in the 2.29 framework require three inputs: the DriverScript, the SetupScript, and the PlotScript. The DriverScript is a structure where all the variables are defined as well as the fields app.Nx, app.Ny and app.dt, which represents the number of interior points in the  $x$ -direction and  $y$ -direction, the time of the simulation, and the time step size respectively. The SetupScript allows to set up the problem from the determination of the mesh to the definition of the boundary conditions and initial conditions. Regarding PlotScript, it allows to plot the solution. To compare FLUENT and 2.29 FV in the same conditions, the plotscript was adapted.

### 4.3. Jet Impingement Models

The numerical models developed in this thesis consist of single and multiple jet impingement. The main focus of the first approach is the development of a numerical model that accurately predicts the flow dynamics of a single jet impinging on a flat plate, considering a Reynolds number in the laminar regime,  $Re = 420$ , and in the transition regime,  $Re = 2,000$ . To conduct this analysis, two different approaches are followed, being presented in detail in section 4.3.1 as “Laminar single jet impingement” and “Single jet impingement in the transition regime”. Regarding the multiple jet impingement, a numerical model is developed to accurately predict the jet’s flow dynamics and heat transfer performance of turbulent multiple air jets ( $Re = 5,000$ ) impinging a moving and static flat plate. Details regarding this model are presented in section 4.3.2.

#### 4.3.1. Single Jet Impingement

The physical problem considered in this study is a 2D single air jet impinging a flat plate in a confined space. The configuration of the jet impingement flow is presented in Figure 58. The jet flows through a circular nozzle of diameter  $D$ , with a velocity,  $\vec{v}$ , and impinges perpendicularly on a flat plate at a distance  $H$  from the nozzle plate. Since the Mach number is below 0.3 in all numerical models, the air jet flow is considered incompressible. The jet impingement flow is characterized by three main regions: free jet, stagnation, and wall jet [19]. The free jet region starts at the nozzle exit, where the dominant velocity component is axial and maximum values are recorded. As the jet flow interacts with the ambient air, a shear layer is generated which induces high lateral velocity gradients. As the flow gets closer to the wall,

it loses axial velocity and turns, generating a stagnation region in which the overall velocity is near zero. The last region is the wall jet, identified once the air jet impacts the target surface. The flow is divided into two streams moving in opposite radial directions along the surface, in which the boundary layer thickens as it moves outward due to the entrainment of the surrounding fluid.

To conduct the numerical simulation,  $L$  is established considering the statement presented by [92], i.e. the outlet must be located at a distance from the jet center, at both sides of the jet, equal to 60 jet diameters, to avoid flow reversal. Considering that  $D = 5$  mm,  $L$  is assumed to be equal to 600 mm.

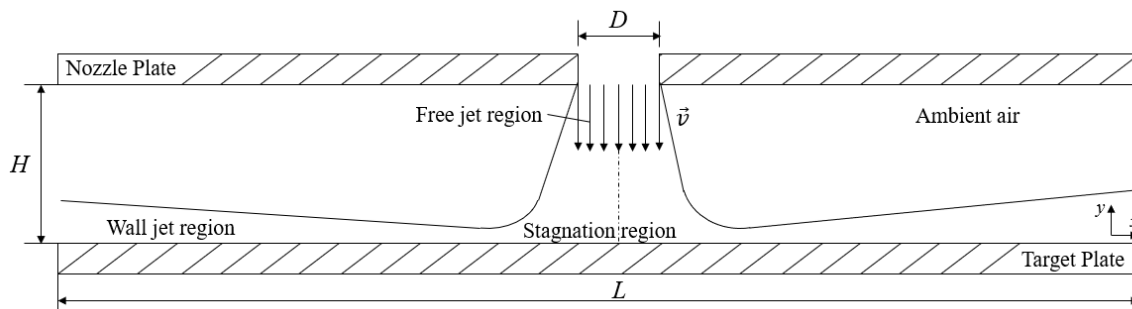


**Figure 58.** Problem statement of a single jet impingement.

Two studies are conducted involving a 2D single jet impingement. While the first study focuses on a Laminar jet, using the Laminar model of FLUENT and the 2.29 FV, the second one consists of a single jet in a transition regime, using the SST  $k-\omega$  model. The great advantage of the first approach is mainly related to the use of a DNS formulation to validate the accuracy of a commercial software to model a laminar single air jet impingement process. In addition, the accurate description and prediction of the jet impingement, at low Reynolds numbers ( $Re < 1,000$ ), helps to understand the jet flow dynamics and physical phenomena for high Reynolds numbers impinging jets. Regarding the second study, it focuses on the validation of the SST  $k-\omega$  model for the numerical modeling of a single air jet in a transition regime. Since several industrial processes, such as drying and reflow soldering, applies jet flows with a Reynolds number between 1,000 and 3,000, it is important to understand if the SST  $k-\omega$  model, whose accuracy has already been validated for the numerical modeling of turbulent flows (as presented in section 2.3), also performs well at low Reynolds numbers ( $Re = 2,000$ ).

#### a) Numerical domain and boundary conditions

##### *Laminar single jet impingement*

The modeling domain consists of a confined single air jet impinging on a flat plate surface, based on the problem statement presented in Figure 58. The air flows through a circular nozzle, spaced  $6D$  from the target plate, at a specific velocity that ensures a  $Re = 420$ . In this study, two case studies are

considered, an isothermal and non-isothermal jet impingement, in order to analyze the effect of the target plate temperature on the jet flow dynamics. For the isothermal case, a constant ambient temperature of 22 °C is applied throughout the domain, at the jet inlet, and over the target plate. While for the non-isothermal case, a constant temperature of 120 °C is considered on the impinging surface.

Regarding the boundary conditions applied at the nozzle plate, which consists of a wall with a circular nozzle located in its center, two different conditions are considered. The circular nozzle, the air flow inlet, consists of the Dirichlet boundary condition. At the exit of the nozzle, a uniform velocity profile (top hat) of the jet flow is considered as well as a constant velocity in the y-direction ( $v \neq 0$  m/s) and a constant ambient temperature ( $T = 22$  °C). The nozzle plate walls are defined by no-slip and adiabatic conditions, meaning that Neuman boundary condition is applied in terms of temperature ( $\partial T/\partial x = 0$ ) and Dirichlet for velocity ( $u = v = 0$  m/s). Regarding the target plate, a constant temperature,  $T = 22$  °C for the isothermal case and  $T = 120$  °C for the non-isothermal case, and no-slip conditions are implemented. The side walls are set as outlets. In 2.29 FV, the pressure is defined automatically through the implementation of an open boundary condition. The Open boundary condition sets:  $\frac{\partial u}{\partial n} = 0$ ,  $\frac{\partial v}{\partial n} = 0$ ,  $\frac{\partial^2 p}{\partial n^2} = 0$ , where  $p$  is pressure and  $n$  is in the normal direction [219]. In FLUENT a pressure outlet boundary condition is implemented. For more details regarding pressure outlet refer to [209].

### ***Single jet impingement in the transition regime***

The numerical conditions set for the single jet impingement in the transition regime, are the same as the ones presented in the previous study for the isothermal case. However, in this case, the nozzle-to-plate distance ( $H/D$ ) is varied between 2 and 6, in order to determine the effect of this important process variable on the jet flow dynamics. In that sense, the uniform velocity distribution is applied at the inlet while no-slip conditions are implemented at both nozzle and target plates. A constant temperature of 22 °C is specified to the inlet and target surface and the adiabatic wall is defined at the nozzle plate. Pressure outlet boundary condition with zero initial gauge pressure is applied to the open sides of the domain.

#### **b) Air flow properties**

The air flow properties are the same for both laminar and transition single jet impingement. To investigate the effect of the density, thermal conductivity, dynamic viscosity, and specific heat capacity on impingement heat transfer, Zhou et al. [133] analyzed the variation of these four variables considering three cases at different temperatures differences (200 K, 400 K, and 600 K) and three Reynolds numbers

(4,000, 8,000 and 12,000) and compared the results with the heat transfer coefficient predicted by changing density and thermal properties, i.e. real gas. Their results show a slight variation between the real heat transfer coefficient and the heat transfer coefficient obtained with constant thermal properties. The maximum difference is obtained for the higher temperature difference, 600 K, and it is not more than 5 %. This study justifies the use of constant thermal properties in the majority of the numerical work performed in jet impingement research [19, 96, 144, 149, 220–222]. The air thermal properties are defined at an ambient temperature according to [156] and presented in Table 12. For the case of density, incompressible ideal gas law [209] is selected instead of a constant value, since previous studies reveal a higher accuracy of the predicted values compared with constant density.

**Table 12.** Air Properties at 22 °C.

Properties	Values
Density [kg/m <sup>3</sup> ]	Incompressible ideal gas
Specific Heat [J/kg·K]	1006
Thermal Conductivity [W/m·K]	0.0242
Dynamic Viscosity [kg/m·s]	$1.789 \times 10^{-5}$

### c) Grid Discretization

#### *Laminar single jet impingement*

A structured grid with square elements is applied in both numerical models using FLUENT Laminar model and 2.29 FV framework. Considering that 2.29 FV requires the implementation of a uniform grid, no wall refinement must be applied. The two meshes implemented in this study are presented in Table 13, and the information regarding the mesh size and the simulation parameters are mentioned.

**Table 13.** Simulation data information.

Simulation Tool	Mesh	Reynolds number	Simulation time	Time step	Computational time
Laminar model- FLUENT	5050 × 300	420	1 s	Adaptive mode starting on 1E-5 s	≈ 20h
2.29 FV	2000 × 250			Fixed mode 1E-5 s	≈ 1 day and 5 h

As it can be observed, while 2.29 FV performs the numerical calculations with a fixed time step, FLUENT allows both fixed and adaptive time step methods. Using the adaptive time step, the calculation starts with a pre-defined time step, which can be changed automatically throughout the simulation, based on the estimation of the truncation error associated with the time integration scheme [209]. If the truncation error is smaller than 0.01, the size of the time step is increased, while if the truncation error is greater, the time step size is decreased. Preliminary analysis shows that the adaptive time step is accurate to model a single jet impingement, therefore, it is used in this study since it decreases the simulation time. However, since the time step size is not a fixed low value kept during all the simulations, to ensure accurate results, a higher number of cells is needed. In that sense, the velocity profiles obtained numerically using different mesh sizes (250,000 to 2,000,000) were analyzed and compared with experimental data. From the preliminary study, a mesh size with a total of 1.5 million elements is used, allowing a good compromise between the solution accuracy and the computational time.

Regarding 2.29 FV mesh size, preliminary studies were conducted, varying the mesh size (from 250,000 to 750,000 elements) and the time step size (from 1E-4 s to 1E-6 s). The velocity profiles obtained numerically were compared with experimental data and the analysis shows that the flow profile predicted by a mesh with 500,000 cells is accurate enough to predict the jet flow profile while decreasing the computational time by 25 %. The time step is also defined by preliminary analysis, based on the Courant-Friedrichs-Lewy (CFL) condition, expressed in Eq (73). 2.29 FV follows the CFL stability criterion on the numerical solution of the advection equations, which means that the maximum allowable information propagation speed in a numerical scheme must exceed the physical advection speed [219]. If this condition is violated, the numerical simulation may become unstable and crash.

$$\frac{\Delta t}{\Delta x} C \leq 1 \quad (73)$$

where  $C$  is the physical advection speed,  $\Delta t$  represents the time step and  $\Delta x$  is the length between mesh cells. From this study, it is verified that 1E-5 s is the higher suitable value that allows to run of the numerical simulations without violating the CFL condition.

Considering that the interest of this study is to analyze the flow development from the jet inlet to the target plate, a simulation time of 1 s is considered to highlight the transient dynamics of the impingement process.

### ***Single jet impingement in the transition regime***

The spatial discretization of the domain is performed using a block-structured grid with square elements, using the ANSYS 19.1 version. While in the previous study a structured and uniform grid with

a high number of elements was implemented, in this study, since the SST  $k-\omega$  model is used, a near wall refinement is required, meaning that the grid is non-uniform. Moreover, since the results will not be compared with DNS data, a lower number of elements is implemented to reduce the simulation time.

In order to obtain a reasonable mesh without excessively increasing the overall mesh size and to reach a higher accuracy level, a mesh sensitivity analysis is conducted. This method is important to determine the accuracy of the predictions as a function of the mesh quality. To perform this analysis two parameters are considered, the number of elements and the bias factor. The bias factor is the ratio of the largest to the smallest element, i.e., a higher bias factor implies a greater refinement close to the walls. In that sense, a bias factor of 4 and 8 is implemented in order to refine the mesh near the target surface. However, a compromise between the mesh refinement close to the walls and the quality of the elements must be ensured. Skewness, aspect ratio, and element quality factors are used as criteria for element's evaluation: Skewness determines how close to the ideal a face or cell is (i.e. equilateral or equiangular), a value close to zero defines the equilaterality of the element; aspect ratio is the ratio of the longest edge length to the shortest edge length, being one for an equilateral cell; element quality represents the ratio of the volume to the sum of the square of the edge lengths for 2D, in which a value of 1 defines a perfect square [209]. Nevertheless, ensuring the recommended values is difficult since a refinement implies smaller elements close to the walls and higher elements in the remaining domain.

To ensure the accuracy of the numerical simulation using the SST  $k-\omega$  model, the near wall grid quality must be ensured. In that sense, it is required that the value of the dimensionless distance of the first node to the wall [137], known as  $y^+$  factor, be lower than 2. This variable is determined by Eq. (74), where  $U_\tau$  is the shear velocity,  $\mu$  the kinematic viscosity of the fluid, and  $\Delta x$  the absolute distance of the first grid cell to the wall [87].

$$y^+ = \frac{U_\tau \cdot \Delta x}{\mu} \quad (74)$$

To analyze the meshes, the quality parameters of each one, the computation time, as well as the  $y^+$  value, are presented in Table 14. Looking at the computation time, it is observed that the higher the number of elements, the greater the simulation time, as expected. In addition, it appears that increasing the bias factor does not increase the complexity of the mesh. In contrast, it seems to improve the convergence of the results, thus the simulation time is 6 h higher for a mesh with a lower bias factor. Regarding the mean wall  $y^+$ , it appears that its value is given by a combination of the number of elements and the refinement close to the wall. Mesh 3 and Mesh 5 are the only ones that comply with the SST  $k-\omega$  model requirement, i.e.  $y^+ < 2$  [44].

**Table 14.** Mesh Properties.

Mesh	1 (coarse)	2 (medium)	3 (fine)	4 (fine)	5 (fine)
N° of Elements	10,080	36,800	124,500	124,500	336,000
Bias factor	8	8	8	4	4
Skewness			$1.30 \times 10^{10}$		
Aspect Ratio	1.93	1.93	1.93	1.56	1.88
Element Quality	0.82	0.82	0.82	0.90	0.83
Mean wall $y^+$	5.16	2.66	1.31	2.2	1.03
Simulation Time ( $t = 1s$ )	30 min	5h	11h	17h	3 days

To determine the optimum grid size, the normalized velocity variation ( $U/U_{max}$ ) over the target surface is analyzed and compared. As it can be observed in Figure 59, the velocity profile over the target surface presents some differences in the five cases. These results prove that the SST  $k-\omega$  turbulence model is sensitive to the quality of the mesh. Increasing the number of elements, the maximum velocity predicted near the stagnation point reaches a value close to 0.7, in contrast to the coarse and medium grids that predict a peak of 0.3 and 0.55, respectively. Moreover, it is observed that the mesh with 124,500 (bias equal to 8) presents similar values compared with a mesh with 336,000 elements and a bias factor of 4. The results demonstrate that to ensure a good accuracy of the simulation with fewer elements, a bias factor must be applied. These observations are important, since the higher the number of elements, the greater the computation time and the memory required. In addition, the data demonstrate that the improvement of the results using a mesh with more elements does not justify the simulation time required. Considering the analysis, it is suggested that Mesh 3 presents the best conditions to conduct the numerical simulations of a single air jet impinging a flat plate at  $Re = 2,000$ .

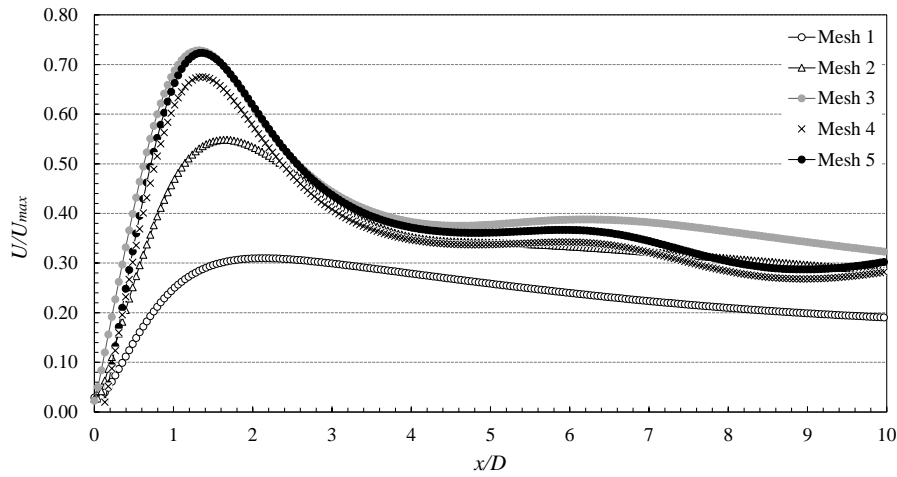


Figure 59. Normalizes velocity profile, at  $y/D = 0.02$ , over the surface for different grids.

### 4.3.2. Multiple Jet Impingement

The physical problem considered in this study is a 3D multiple air jet impingement. The analysis of turbulent jets impinging on a hot moving and static flat plate is the focus of this research. After the analysis of jet flow in the laminar and transition regime, in which the jet flow dynamics are analyzed in detail as well as the influence of some relevant variables, such as the target plate temperature and the nozzle-to-plate distance, the complexity of the jet flow is highly increased in this study. Besides the interactions between jets due to  $S/D$  and  $H/D$  process variables, this analysis considers the effect of the target plate motion, following the configuration depicted in Figure 60. Through this study, the dynamic plate is compared with a static one and a detailed characterization of the jet's flow field and heat transfer over the target plate are conducted.

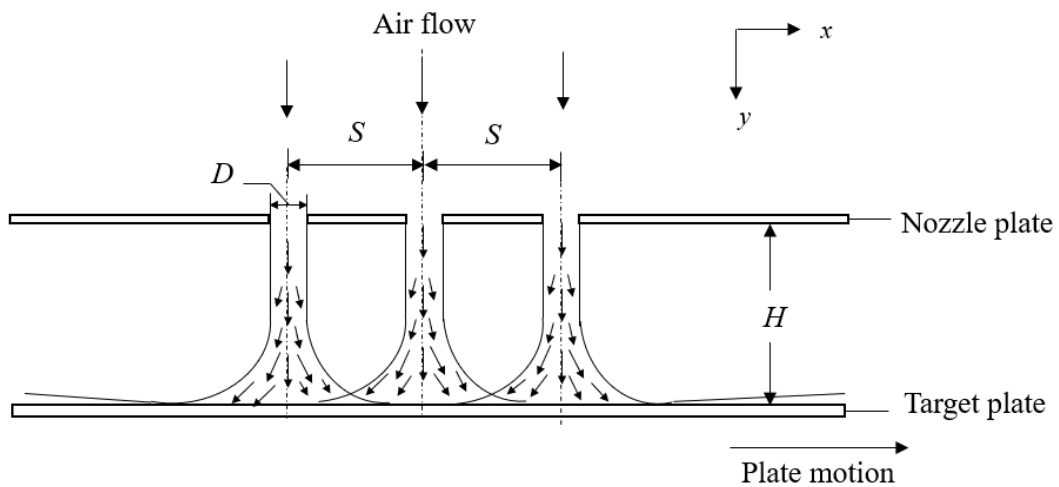
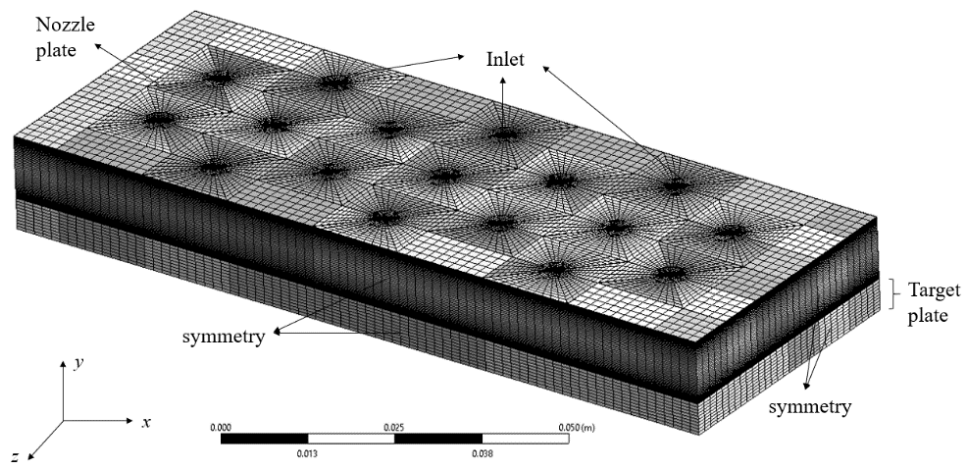


Figure 60. Problem statement of a multiple jet impingement.

### a) Numerical domain and boundary conditions

The numerical domain consists of confined multiple air jets impinging on a flat plate surface. The air flows through circular nozzles at a velocity of 15 m/s, which induces a Reynolds number near to 5,000. The impingement consists of a cooling process, therefore an ambient temperature of 25 °C is applied to the jet's inlet, while the target plate is defined with a constant temperature of 120 °C. Since only a portion of the total jets array is modeled, a symmetry condition is applied in each side of the domain, as depicted in Figure 61.



**Figure 61.** Numerical domain.

Although the domain consists of a total of 17 jets, the analysis in this work focuses on the central row, i.e., the central jet and two adjacent jets. However, since the multiple jet configuration is staggered, the influence of the jets located in the front and back rows is strong and must be considered throughout the analysis. The jets are spaced  $3D$  in both spanwise and streamwise directions and the distance between the target and the nozzle plate is equal to  $2D$ .

The boundary conditions applied to the nozzle plate are defined by no-slip and adiabatic conditions. The air flow inlets, which consist of circular orifice nozzles, are defined with a uniform velocity profile at constant velocity and temperature. The target plate, which is an aluminium alloy plate with 5 mm thickness, is characterized by constant temperature and no-slip conditions. The side walls are defined with a symmetry boundary condition, meaning that zero normal velocity and zero normal gradients of all variables are implemented at the symmetry plane.

### b) Air flow properties

Following the same approach presented in section 4.3.1 b), the air thermal properties are defined at an ambient temperature according to [156] and presented in Table 15. A value of 25 °C was selected since the experiments were conducted at this temperature.

**Table 15.** Air Properties at 25 °C.

Properties	Values
Density [kg/m <sup>3</sup> ]	Incompressible ideal gas
Specific Heat [J/kg·K]	1007
Thermal Conductivity [W/m·K]	0.02551
Dynamic Viscosity [kg/m·s]	1.849×10 <sup>-5</sup>

### c) Grid Discretization

A block-structured grid with square elements is applied for the spatial discretization of the domain. The mesh is refined near the nozzle plate and the target surface, to ensure that the shear layer generated at the exit of the jets and the development of the boundary layer over the surface are accurately predicted. As previously mentioned, to guarantee the accuracy of the numerical simulation using the SST  $k-\omega$  model, the near wall grid quality must be ensured. In that sense, it is required that  $y^+ < 2$ .

To estimate the accuracy of the numerical results, a mesh sensitivity analysis is conducted. Three grid sizes, presented in Table 16, are considered to check the grid independence of the numerical simulation.

**Table 16.** Properties of the three grids analyzed.

Grid	N° cells	Max $y^+$
Coarse	387,072	3.27
Medium	756,000	1.69
Fine	1,134,000	1.64

The grid independence test has been conducted for the static plate case and the variable considered is the average heat transfer over the plate, expressed as the average Nusselt number, considering half the area impinged by the central jet, in which  $x/D = 0$  represents the central jet axis. Moreover, the influence of the numerical grid on the results was estimated by the Grid Convergence Index (GCI). This

method, based on Richardson extrapolation, is recommended by the Fluid Engineering Division of ASME [223] since it is considered the most reliable method available for the prediction of numerical uncertainties. The GCI is considered a procedure for the uniform reporting of grid refinement studies and represents an effective measure of mesh dependency, through which it is possible to quantify the error due to an insufficient spatial resolution [87]. All the steps followed in the application of the GCI method are clearly presented in [223]. The results for each grid density, presented in Figure 62, show a typical jet heat transfer behavior at a low nozzle-to-plate distance [224]. Moreover, as the grid is refined, the variation in  $\overline{Nu}$  becomes less evident. As expected, the higher deviation between the medium and the fine mesh is identified near the stagnation point ( $x/D = 0$ ), with a maximum difference equal to 7 %. The local discretization error distribution, with regards to the average Nusselt number, on the fine and medium grids was calculated using the GCI method, as expressed in Figure 62. Aside from moderate peaks identified in the vicinity of the stagnation point, the overall GCI value is quite low. The mean discretization uncertainty was estimated to be close to 2.4 % for the medium mesh and 2.2 % for the fine mesh. Considering the slight difference between the medium and fine grids as well as the small discretization error, the medium mesh is considered to conduct the numerical simulations.

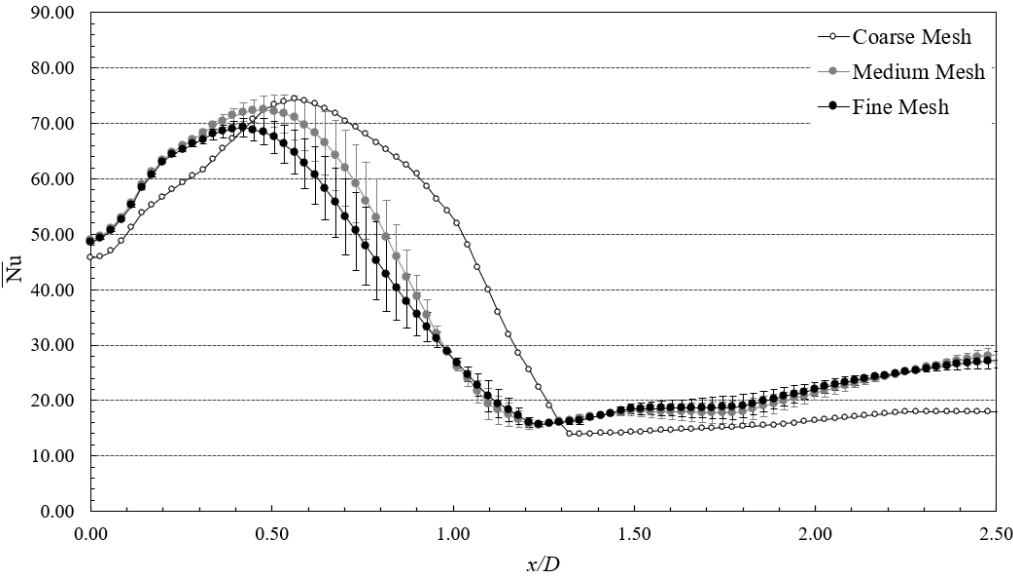
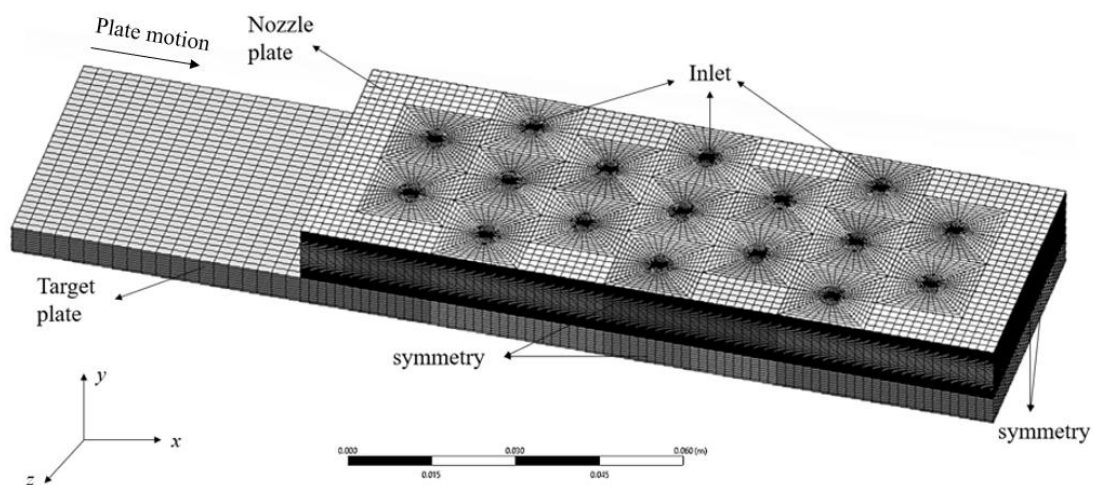


Figure 62. Variation of the average Nusselt number over the target plate ( $y/D = 0$ ) for different meshes.

#### d) Mesh Motion

The difference between the grid implemented in the static and the moving cases is only related to the target plate since the length implemented is slightly higher (Figure 63) in order to analyze the flow without the interference of the boundary layer generated in front of the plate during its motion. As mentioned by [104], this strong boundary layer induces an increase of the flow velocity in the vicinity of the plate and the downstream jets are highly deflected. To ensure accurate predictions, an interface between the flow and the surface is implemented to be able to visualize the motion of the surface with time. In this study, the plate motion is considered from the left to the right.

Several methods can be implemented to perform the numerical simulations of the moving plate. ANSYS FLUENT allows the implementation of three different methodologies, dynamic mesh, sliding mesh, and frame motion [209]. The first method is applied to simulate problems that involve boundary motion and grid deformation, while the sliding mesh allows the motion of domain without grid deformation. In this second method, a non-conformal interface is applied to the junction of cell zones that have relative motion.



**Figure 63.** Numerical domain to conduct the dynamic simulations.

Finally, frame motion does not involve the motion of the cell zones since the motion is given to the reference frame, so the cell zones have zero relative motion concerning their reference frame. This leads to the same conservation equations as those without motion with force terms added. Since the interest of this study is the prediction of the heat transfer across the interface flow/surface without grid deformation, the sliding mesh is implemented in this work. This method was also implemented by [138].



interfere with the air jets temperature. The data reduction and uncertainty estimation of the heat transfer was presented in section 3.2.5. The uncertainty related to the PIV measurements is obtained through a statistical analysis of the data for 300 images. Following the concepts presented in section 3.3.5, the uncertainty obtained for the maximum velocity recorded by the system is close to 10 %.

## 5.2. Laminar Single Jet Impingement

The jet impingement involves several variables that increase the flow interactions, from the jet flow parameters (velocity and temperature) to the target surface and process geometry (nozzle-to-plate distance, ribs, etc.). In that sense, several studies have been conducted in order to fully characterize the flow field of a jet impingement process [19, 21, 54, 225, 226]. However, few works characterize the flow of laminar jets. Even if the applicability of laminar flow is reduced in industrial processes, they are very important to fully characterize the jet impingement flow. Experimental studies, enable the identification of complex structures under impinging jets and to understand their propagation throughout the target plate, which leads to increased flow turbulence and consequently to heat transfer enhancement. The accurate description and prediction of the process, at low Reynolds numbers, helps to understand the phenomena for high Reynolds numbers impinging jets.

This first analysis focuses on the effect of the plate temperature on the jet flow development over the target plate, therefore, two cases are considered, an isothermal and non-isothermal single jet impingement. Experiments are conducted, followed by a numerical validation using both 2.29 FV and FLUENT. The results obtained by the numerical simulations are compared with the data collected from the experiments and they allow to determine the accuracy of the numerical predictions.

### 5.2.1. Experimental Results

The measurements collected by the PIV system are presented in this section. The flow structure and velocity profiles obtained experimentally over the target plate and along the jet axis are discussed.

#### a) Flow dynamics of a laminar single jet

Regarding the PIV measurements, non-dimensional distances are used to discuss the data, in which  $H/D$  represents the normalized nozzle-to-plate distance,  $x/D$  the normalized radial distance from the jet axis ( $x/D = 0$ ), and  $y/D$  the normalized axial distance, in which  $y/D = 0$  represents the location of the target plate and  $y/D = 6$  is the location of the nozzle plate. One image of the instantaneous flow profile

captured by the CCD camera, and presented in Figure 65, reveals that, even for low Reynolds numbers, the jet is unstable and no steadiness is reached after several minutes of the experiment. At the nozzle exit, in which a uniform profile at a maximum velocity occurs [21], the flow seems to be stable. However, at approximately  $y/D = 1$  downstream of the nozzle orifice, flow perturbations are identified. This phenomenon occurs due to the shear layer induced when the jet flow interacts with the low momentum ambient flow. This velocity discontinuity induces Kelvin-Helmholtz instabilities, resulting finally in a vortex structure [227] that dominates the flow. As the jet flow approaches the target plate, the axial velocity component decreases, and, at the moment the plate is reached, the jet spreads radially over the target plate, this is the stagnation region. In this region, the kinetic energy of the flow decreases rapidly and is transformed into a rise in pressure energy which induces an acceleration in the radial component of velocity [26]. After the stagnation zone, the jet flow passes through the acceleration zone, where strongly favorable pressure gradients are induced over the impinging surface, essentially due to the impact of the vortices on the wall which causes a thin boundary layer [126, 228]. From Figure 65, it is possible to identify a decrease of the boundary layer thickness at  $1 < x/D < 2$ , growing again at  $x/D > 2$ . At  $x/D = 2.75$ , it is possible to observe the presence of vortical structures that propagate over the wall and seems to increase in magnitude as the flow develops along the surface. As mentioned by [26], these vortices entrained surrounding fluid, compress the fluid layer, and cause the penetration of the wall jet flow into the boundary layer, leading to fluctuations in wall pressure. The strength of these large-scale structures leads to increased stress into the boundary layer and consequently, an enhancement of the heat transfer is expected [126]. The axisymmetry of the vortices pattern throughout the impingement wall is clear, being also identified by [8]. The motion of the wall jet over the surface continues until the jet flow has enough kinetic energy. Looking at Figure 65, the exact location where the jet flow detaches from the wall occurs at  $x/D$  close to 8.5. At this specific point, it is observed that the boundary layer detaches the wall, the flow deflects upwards until the nozzle plate is reached and rolls up, originating two large and symmetric vortices. The development of these two large vortices is limited by the confinement and induces flow interactions at the edges of the jet. This interaction can interfere with the velocity profile observed at the jet axis. The axisymmetry of the flow is clearly identified, with identical vortical structures detected at both sides of the jet axis. Since Figure 65 represents an instantaneous velocity field, the correct definition of the different regions of the jet is possible through the statistical analysis of the 300 images which is presented in the next section.

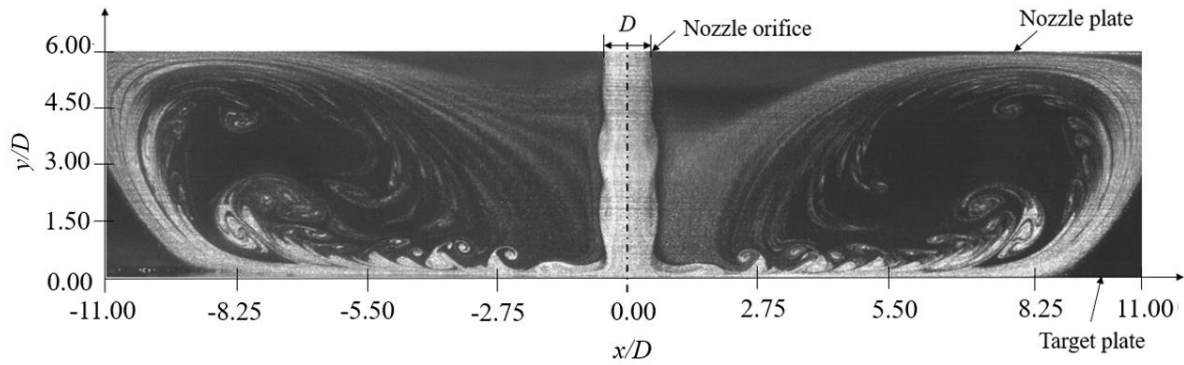


**Figure 65.** Instantaneous flow profile of an isothermal air jet impinging a flat plate at  $Re = 420$  and  $H/D = 6$ .

### b) Jet velocity profiles

The jet velocity profiles obtained for both isothermal and non-isothermal jets are discussed in this section.

#### *Isothermal Jet*

The jet velocity profiles, for the isothermal case, are plotted in Figure 66. As presented in the previous section, the experimental data are obtained by statistical analysis of time-averaged velocity fields of 300 images captured and post-processed by the PIV system. A contour plot, Figure 66 (a), allows to analyze the variation of the velocity magnitude normalized by the maximum nozzle exit velocity ( $U/U_{max}$ ) throughout the domain. Higher velocities are recorded at the jet inlet, immediately followed by a decrease in velocity just downstream of the nozzle orifice. As mentioned previously, this decrease is due to the shear layer induced by the interaction between the flow and the surrounding air. However, this decrease throughout the jet axis ( $x/D = 0$ ) is not uniform. This seems to be in agreement with the observations stated in the previous section. Even if the flow is laminar, the vortices generated interfere with the jet flow, decreasing its velocity, as observed with more detail in Figure 66 (b). A similar profile is also detected by [8]. The maximum velocity is recorded at the exit of the orifice nozzle, followed by a decrease due to the generation of the shear layer, inducing high lateral velocity gradients. As presented in Figure 66 (b), the higher the distance from the jet axis, the stronger the influence of the shear layer on the velocity profile. After this region with strong perturbations,  $5.9 < y/D < 4.2$ , the maximum velocity is recovered at the jet axis. The potential core, defined by Livingood & Hrycak [23] as the distance from the nozzle exit to the position where the jet velocity reaches 95 % of its original value, starts from the jet inlet and ends at  $y/D = 2.4$ , which is in accordance with [8]. From the end of the potential core, a deceleration region is identified, followed by an acceleration region, essentially due to the growth of the vortices generated in

the free-jet shear layer. Finally, below  $y/D = 1$ , a stagnation region is reached, and the stagnation point is identified over the target plate at the jet axis, as expected.

After impinging the target plate, the wall jet develops radially, increasing in velocity, as expressed in detail in Figure 66 (c). Even if the velocity profile is not totally axisymmetric, the velocity over the target plate increases from the stagnation point, reaching its maximum at  $x/D = 1.4$ . This acceleration zone  $0 < x/D < 1.4$  is mainly related to the growing boundary layer, which induces a fast acceleration of the flow due to larger pressure gradients [24]. The location of this zone varies as a function of the Reynolds number and the nozzle-to-plate distance. Increasing the distance from  $x/D = 1.4$ , a uniform decrease in velocity is observed until the flow detaches the wall. As presented in Figure 66 (c), this moment seems to occur near  $x/D = 8.5$ . The velocity field develops radially over the wall and, at this specific point, the results presented in Figure 66 (a) demonstrated that the velocity vectors move upward, showing the complete detachment from the wall.

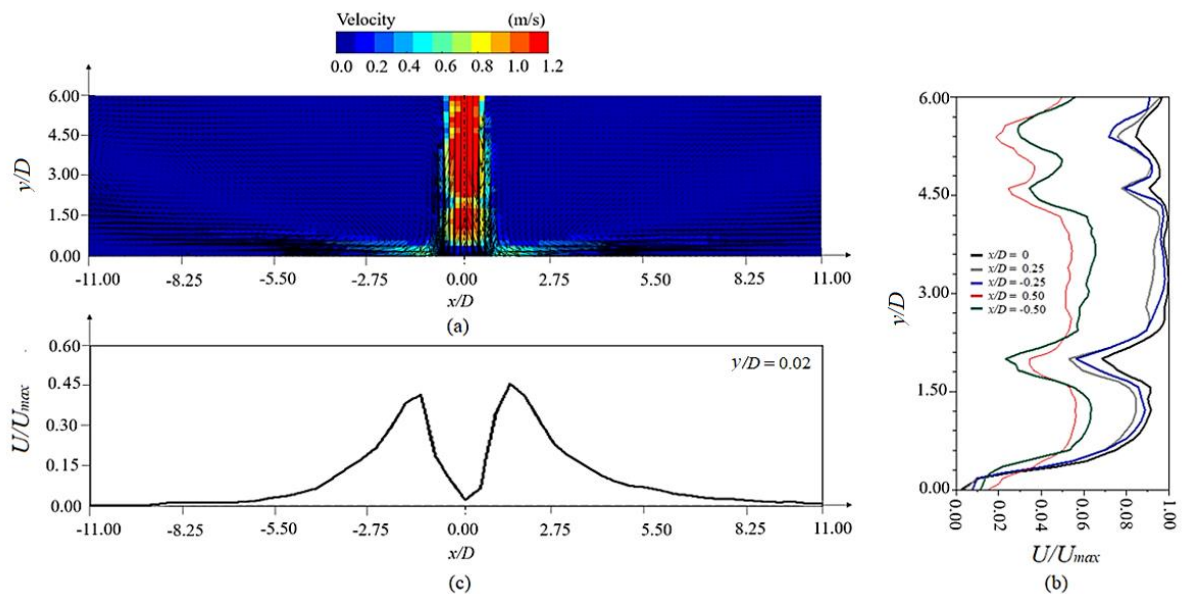


**Figure 66.** Normalized time-averaged velocity magnitude at  $Re = 420$  (a) all the domain; (b) throughout and near the jet axis; (c) over the target plate.

### *Non-isothermal Jet*

The velocity profiles for a non-isothermal jet are expressed in Figure 67. The contour plot presented in Figure 67 (a) indicates that the effect of the natural convective heat transfer plays an important role in the jet flow structure.

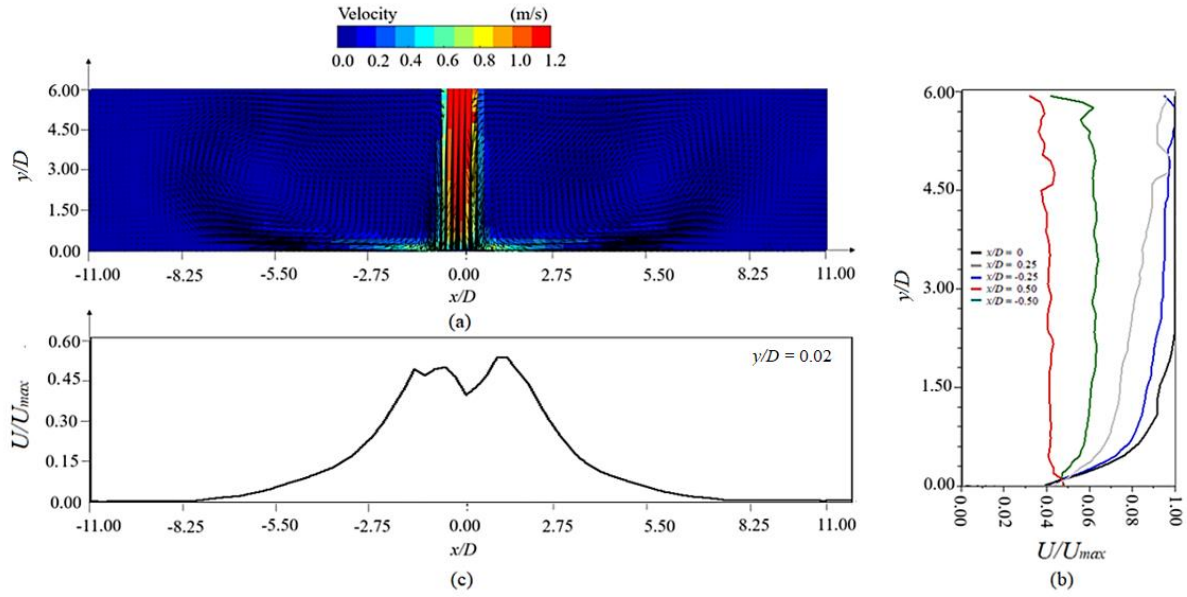


**Figure 67.** Normalized time-averaged velocity magnitude at  $Re = 420$  (a) all the domain; (b) throughout and near the jet axis; (c) over the target plate.

Compared with the isothermal jet case, a stronger complexity of the jet flow due to the increased temperature of the target plate is clearly demonstrated by the higher magnitude of the velocity vectors expressed in Figure 67 (a) compared with Figure 66 (a). The mixing between the ambient air and the hot air that comes from the target plate is increased by the temperature difference, increasing the jet flow velocity over the surface as well as between the nozzle and the target plates. This effect promotes the heat transfer over the impinging surface and can be explained by the increase of flow driving forces in the vertical direction due to stronger buoyancy forces. While in turbulent flows the buoyancy effect can be neglected, in laminar flows the impinging regime may fall in natural, forced, or mixed convection, depending on the relative strengths of the inertia/viscous forces and the buoyancy forces involved [229]. To support these conclusions, it is important to determine the convection regime of the laminar jet flow analyzed in this work. Therefore, the Richardson number must be determined, Eq. (75). If  $Ri \ll 1$  the forced convection regime is dominant, while  $Ri \gg 1$ , natural convection prevails, and if  $Ri \approx 1$ , the flow is in a mixed convection regime.

$$Ri = \frac{Gr}{Re^2} \quad (75)$$

According to [229], the Grashof number ( $Gr$ ) can be determined by Eq. (76):

$$Gr = \frac{g \beta^* (T_w - T_\infty) H^3}{\nu^2} \quad (76)$$

where  $H$  is the nozzle-to-plate distance ( $H = 0.03$  m),  $g$  is the acceleration of gravity ( $9.81$  m/s<sup>2</sup>),  $\beta^*$  is the coefficient of volumetric expansion ( $1/T$ ), and  $\nu$  the air kinematic viscosity. In this case, the air properties are considered at film temperature,  $T$ , given by Eq. (77):

$$T = \frac{T_w + T_\infty}{2} \quad (77)$$

Considering that the average temperature of the target plate ( $T_w$ ) is  $120$  °C and the air jet temperature at the exit of the nozzle ( $T_\infty$ ) is  $22$  °C,  $T$  is equal to  $71$  °C, therefore  $\beta^* = 0.014$  and  $\nu = 1.995 \times 10^{-5}$  m<sup>2</sup>/s. These values lead to a  $Gr = 912,132$ , and considering that  $Re = 420$ ,  $Ri$  takes a value of  $5.17$ .

This analysis demonstrates that natural convection is dominant, and it supports the statements presented above since the strength of the buoyancy forces affects the inertia/viscous forces. The buoyancy force tends to move the air upwards, promoting the mixing between the surrounding air and the jet flow, increasing the heat transfer over the target plate. In that sense, it seems that both natural and forced convection affects the total heat transfer rate, meaning that the heat transfer falls in a mixed convection mode. In addition, looking at the two vortices generated on each side of the jet axis, it seems that their development is different from those induced in the isothermal case. This shows once again the effect of natural convection on jet flow development. As the heated air from the target plate moves upwards, cold air coming from the outlets is entrained and constrains the development of the recirculating vortices, increasing the global turbulence intensity of the flow.

Furthermore, looking in detail at the velocity magnitude over the jet axis, Figure 67 (b), the velocity profile presents no significant variations over the jet axis, with maximum velocities recorded over the potential core length, followed by a decrease until the stagnation region is reached. Compared with the isothermal jet, this profile is substantially different. As expressed in Figure 66 (b), without temperature variation, the flow is mainly affected by inertia/viscous forces, therefore, small variations in the shear layer affect the jet velocity profile, inducing acceleration and deceleration zones. Whereas, with temperature gradients induced by the heated plate, the effect of buoyancy forces increases the flow driving forces in the vertical direction, increasing the flow intensity and therefore, affects the inertia/viscous flow. In that sense, it seems that the effect of the shear layer variation on the jet axis velocity profile is negligible when the flow turbulence is increased. The increased complexity of the flow in the vicinity of the wall leads to a reduction of the accuracy of the velocity at the stagnation point, as observed in Figure 67 (a), showing the limitation of PIV in resolving near-wall measurements [230]. As previously mentioned, to enhance the accuracy of the measurements a macro lens must be used to zoom this region combined with a higher time between pulses.

### c) Heat transfer measurements

To conduct the heat flux measurements, the OMEGA® HFS-4 thin film heat flux sensor is mounted at the center of the target surface, just below the nozzle, and data is collected over a time span of 30 min, as previously presented in chapter 3, section 3.2.1. The average heat flux is measured, and the heat transfer coefficient is determined considering the temperature difference between the target plate and the air jet, as presented by Eq. (18). From the heat transfer coefficient, the flow properties ( $\rho$  and  $\mu$ ), and the jet diameter, the Nusselt number is calculated and a value equal to  $5.52 \pm 0.80$  is obtained. The uncertainty analysis applied in this study for 95 % of confidence follows the methodology presented by [165]. These results are in agreement with those obtained by [83, 231] and the correlation presented by [112]. Even if the heat flux sensor provides an average value, it is expected that the maximum heat transfer is recorded at the stagnation region and decreases with the increased distance from the jet axis. This behavior is in agreement with the jet flow development over the surface. As previously mentioned, higher flow velocities are recorded at the vicinity of the stagnation region, in which a growing boundary layer is generated, leading to a fast acceleration of the flow. This region promotes the mixing between the jet flow and the surrounding air increasing the average heat transfer.

To determine if the average Nusselt number determined experimentally is within the range of other studies presented in the literature, it is compared with correlations, experimental and numerical results. From the results presented in Table 17, it seems that a maximum difference of approximately 30 % is observed. This discrepancy can be explained by the fact that the laminar jet is highly influenced by small variations of the flow and the geometrical variables. Even if the correlation and experimental data selected present parameters close to those implemented in this experiment, there are some variations that interfere with the average Nusselt number. While in turbulent jets momentum governs the jet's flow, in laminar jets the temperature difference between the plate and the jet plays an important role in the jet flow dynamics, influencing the heat transfer performance. However, no published correlation has this aspect into consideration since it is very difficult to quantify. Regarding the two studies presented in Table 17, the implemented temperature difference is not mentioned.

**Table 17.** Comparison between the experimental heat transfer values and data presented in the literature.

$\overline{Nu}$			
Measured	Huang Correlation [112] ( $750 < Re < 27,000$ and $3 < H/D < 16$ )	Chattopadhyay ( $Re = 500$ ) [123]	Sparrow & Wong ( $Re = 450$ and $H/D = 5$ ) [232]
$5.5(2) \pm 0.80$	3.85	6.88	8.21

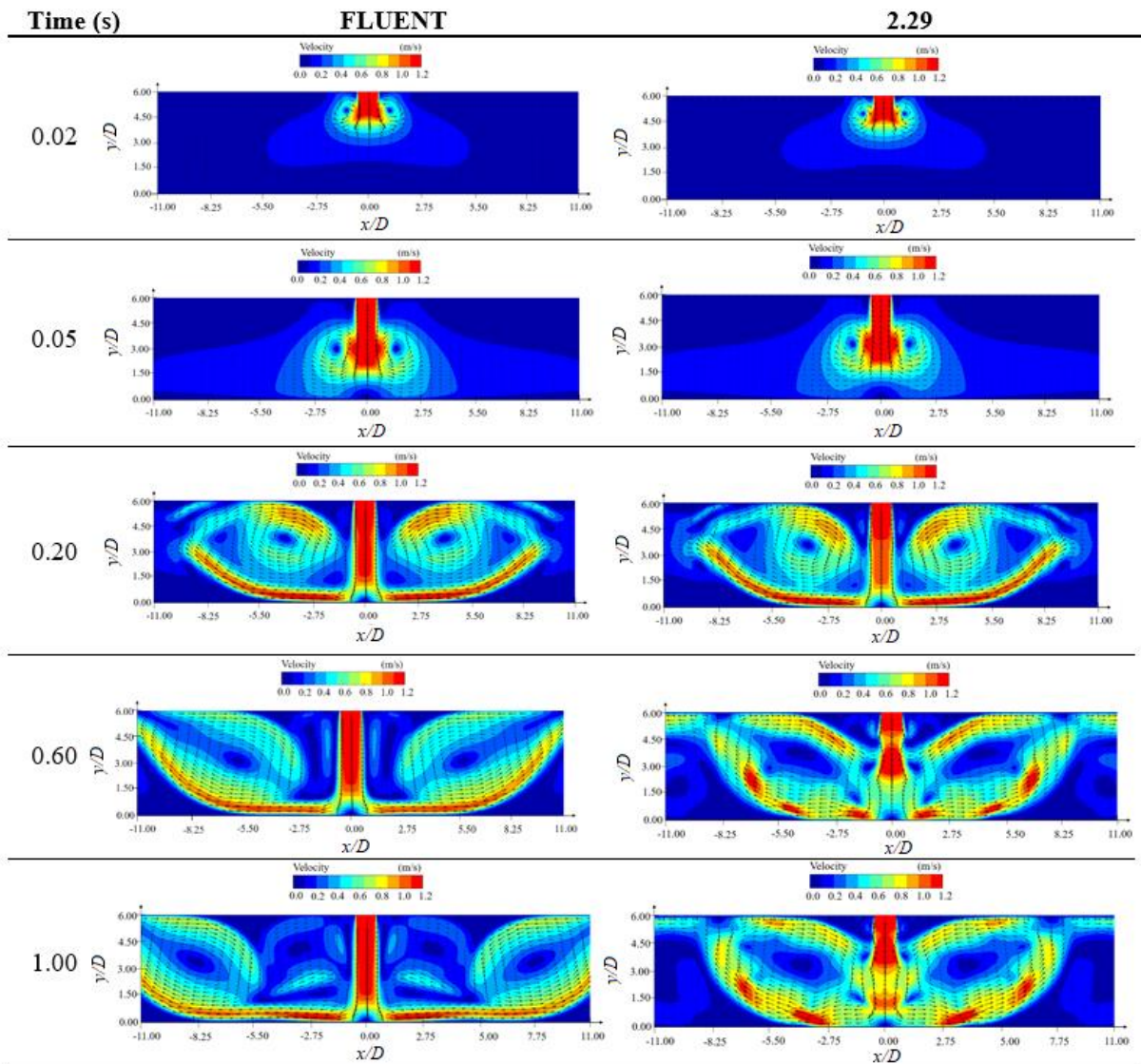
### 5.2.2. Numerical Validation

The jet flow structure and velocity profiles obtained numerically by FLUENT Laminar Model and 2.29 FV MATLAB Framework are presented and discussed in this section. The jet flow velocity profiles at different simulation times are analyzed and compared. From the numerical results, it is intended to determine the accuracy of both numerical tools to capture the jet flow dynamics from the nozzle to the impinging plate. In that sense, the analysis was conducted from 0 to 1 s, which gives enough time for the jet flow to develop from the jet exit to the target plate. Furthermore, the heat transfer over the plate is analyzed for the non-isothermal case and compared with the experimental results.

#### a) Jet flow

The development of the jet flow profile over time was predicted using both 2.29 FV MATLAB Framework and FLUENT software and the results are presented in Table 18. The interaction between the ambient fluid and the jet flow is clearly observed at 0.02 s, resulting in the formation of an initial jet shear layer and the generation of a primary vortex due to Kelvin-Helmholtz instabilities. As the jet moves downstream, the vortex grows, entraining more fluid and decreasing the jet axial velocity. Due to the low Reynolds number, the structure of the vortex is preserved further downstream of the nozzle orifice exit. A longer potential core is predicted by FLUENT, being defined by Livingood & Hrycak [23] as the distance from the nozzle exit to the position where the jet velocity reaches 95 % of its original value. The end of the potential core region is identified near  $y/D = 2$  in FLUENT results at 0.2 s, 0.6 s, and 1 s, while 2.29 FV predictions show that this region does not exceed  $y/D = 3$ . The end of the core region is followed by the decaying region, characterized by the linear variation of the axial velocity [21]. As the flow approaches the target, it loses axial velocity and turns. This is the stagnation region, where velocities near 0 m/s are detected, being predicted by both 2.29 FV and FLUENT at an extent between  $0 < y/D < 1$ . The stagnation point was clearly identified over the target plate at the jet axis ( $x/D = 0$ ) as expected.

**Table 18.** Instantaneous velocity profile at  $Re = 420$  obtained by FLUENT and 2.29 FV.



As the jet impinges the target plate, the flow is divided into two streams moving in opposite radial directions, the primary vortices progress downstream along the wall and a wall jet is developed. This region is characterized by a growing boundary layer, as can be observed in Table 18 ( $t = 0.2$  s to 1 s), which was identified both numerically and experimentally by several authors [8, 121, 124, 125, 230]. Near the stagnation region, an increase in velocity is recorded due to a rapid acceleration of the flow caused by larger pressure gradients [21, 205], as clearly identified at 0.2 s, 0.6 s, and 1 s, for a location between  $2 < x/D < 3$ . These observations are supported by [24, 121, 230]. As presented in Figure 65, this is the location where the primary vortex rolls up, which affects the flow in the near-wall region, generating unsteady pressure gradients. According to [233] these primary vortices induce flow deceleration close to the surface and flow acceleration in the inner shear layer. Results obtained by 2.29

FV allow to identify this unsteadiness of the wall jet, while FLUENT only identifies a decrease in velocity at  $x/D > 3$ . Even if no vortical structures are identified by 2.29 FV in the wall jet region, this flow instability identified numerically is a result of their effect on the jet flow velocity. This aspect can be analyzed with higher detail by looking at the velocity profile over the target plate, which is presented later.

As the distance from the jet axis increases, the thickening of the boundary layer is observed, being mainly due to the entrainment of more ambient fluid during the impingement, reducing the flow velocity. The exact location where the boundary layer detaches the target surface is identified by 2.29 FV at  $x/D$  close to 5.5 for  $t = 1$  s, meaning that this point is predicted to occur earlier, compared with the experimental results. On the other hand, the FLUENT simulations show that this point occurs at  $x/D$  near to 8.5, which is in accordance with the experiments. Once detaching the surface, the flow deflects upwards, rolls up into a vortex ring, until the nozzle plate is reached. Due to the dimensions of the confinement space, the vortex ring development is constrained by this upper wall and interacts with the jet flow, as clearly demonstrated from 0.2 s to 1 s both in FLUENT and 2.29 FV results. The predictions of the numerical simulations are in accordance with the experimental data, in which two large vortices are identified on both sides of the jet axis. The effect of these vortical structures on the jet flow is identified with higher detail numerically. Furthermore, the predictions obtained by the 2.29 FV and FLUENT Laminar model are very similar from the jet inlet to the target plate. However, as the flow develops throughout the wall, differences are observed. The effects of the vortical structures on the flow development are predicted with higher detail in 2.29 FV. The main reason for this difference must be mainly related to the different numerical methods implemented in 2.29 FV and ANSYS FLUENT but also to the outlet boundary condition which is also different. Since the flow is laminar, the Laminar model neglected the fluctuating quantity and solves the Navier-Stokes equations considering the time-averaged velocity. This fact could explain the difference in the numerical results expressed in time equal to 0.6 s and 1 s. In addition, the experimental results show that the vortices size, during the impingement, is independent of the nozzle plate and target surface dimensions. The flow structure is mainly related to the nozzle-to-plate distance ( $H/D$ ) and Reynolds number. Overall, these results demonstrate that 2.29 FV is accurate to conduct the analysis of the flow dynamics of a single jet impinging a target plate and present similar results compared with FLUENT Laminar model.

#### **b) Jet velocity profiles**

In this section, the jet velocity profile obtained by 2.29 FV framework and ANSYS FLUENT software are analyzed for both isothermal and non-isothermal cases.

### Isothermal jet

The normalized velocity magnitude obtained by FLUENT and 2.29 FV is plotted over the target plate, Figure 68, for different simulation times. The results show the unsteadiness of the flow, with different velocity profiles recorded over time.

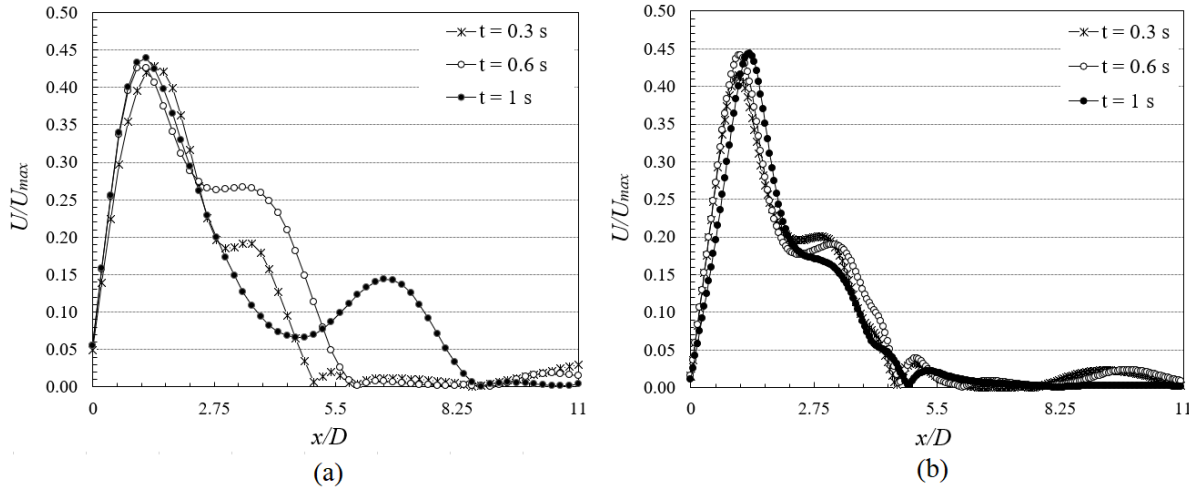


**Figure 68.** Instantaneous normalized velocity variation over the target plate ( $y/D = 0.02$ ) at  $Re = 420$ : (a) FLUENT (b) 2.29 FV.

The velocity profile over the target plate obtained by FLUENT, Figure 68 (a), shows that the stagnation point is not predicted with accuracy, as a zero velocity is expected. However, this point is accurately predicted by 2.29 FV, as can be observed in Figure 68 (b). Near the jet axis, the acceleration zone is identified with maximum velocity reached at approximately  $x/D = 1.2$ , predicted by FLUENT and  $x/D$  close to 1.4 by 2.29 FV. This region is correlated to the first peak of heat transfer over the target plate. These results are in accordance with [8, 124], being this maximum value attributed to a thin boundary layer. The prediction of the maximum velocity is approximately 1 % higher in 2.29 FV compared with FLUENT.

As the flow moves through the wall, a decrease in velocity is identified due to the expansion of the wall jet, reaching a minimum value at  $x/D = 2.3$  predicted by 2.29 FV and  $2.4 < x/D < 4.6$  predicted by FLUENT. The higher differences between the predictions performed by the two numerical tools are recorded from this region. Although 2.29 FV predicts a similar velocity profile over time, with a secondary peak value identified at  $x/D$  near 3 and a complete detachment of the flow from the wall at  $x/D > 5$ , the scenario is different in FLUENT. Figure 68 (a) shows that at  $t = 0.6$  s, the results are similar to those presented by 2.29 FV, with a secondary stagnation point estimated at  $x/D$  near 3 and a detachment of the flow from the wall at  $x/D$  near 5. However, increasing the simulation time, the secondary maximum

moves away from the jet axis. At  $t = 1$  s, the secondary peak is identified at  $x/D$  near 7, and the detachment of the flow from the wall at  $x/D = 8.5$ . Comparing these results with the literature [8, 24, 121, 124, 205, 230], it seems that the secondary maximum at low Reynolds number and low nozzle-to-plate spacing ( $0.5 < H/D < 6$ ) are recorded at  $1.4 < x/D < 5$ , as predicted by 2.29 FV. This secondary maximum velocity is located at the same point where interaction between the primary vortex and the wall boundary layer was identified experimentally in Figure 65, at  $x/D$  near 2.75, leading to the increased complexity of the flow. Looking at the velocity vectors presented in the velocity contours represented in Table 18, it seems that this second peak is due to the acceleration of the primary vortices, as also identified by [127]. From this peak, the velocity continues to decrease until a separation point, characterized by zero velocity gradient and zero shear stress [26], occurs at  $x/D$  near 5. After the separation point, a slight increase in velocity is detected. This effect is also identified by [24, 26, 121, 122, 230, 233] and it appears to be a reattachment of the flow downstream the separation point. The detachment of the flow followed by reattachment is likely to be related to the generation of a secondary vortex. According to [233], a local shear layer generated by an unsteady wall pressure gradient caused by the primary vortex causes the secondary vortex, identified by [234] as a local flow reversal. This secondary vortex induces flow separation and reattachment throughout the target surface. The separation zone leads to a decrease in heat transfer, while an attachment increases this property [26]. The local increase of velocity is clearly observed at  $x/D$  close to 5.3, meaning that a tertiary peak is expected in heat transfer distribution [26]. At  $x/D > 5.5$  the low kinetic energy of the jet flow induces a complete detachment of the boundary layer from the wall, as it can be observed at the velocity contour at  $t = 1$  s presented in Table 18.

The variation of the velocity along the jet axis is also plotted and presented in Figure 69, the profiles presented by 2.29 FV and FLUENT are different. However, at  $t = 0.3$  s, a similar profile is observed. A decrease in velocity is recorded due to the strong interactions between the flow and the surrounding air, achieving a minimum value near  $y/D = 4.5$  with the velocity predicted by FLUENT being 3 % higher when compared with 2.29 FV. The maximum velocity is reestablished at the jet axis.

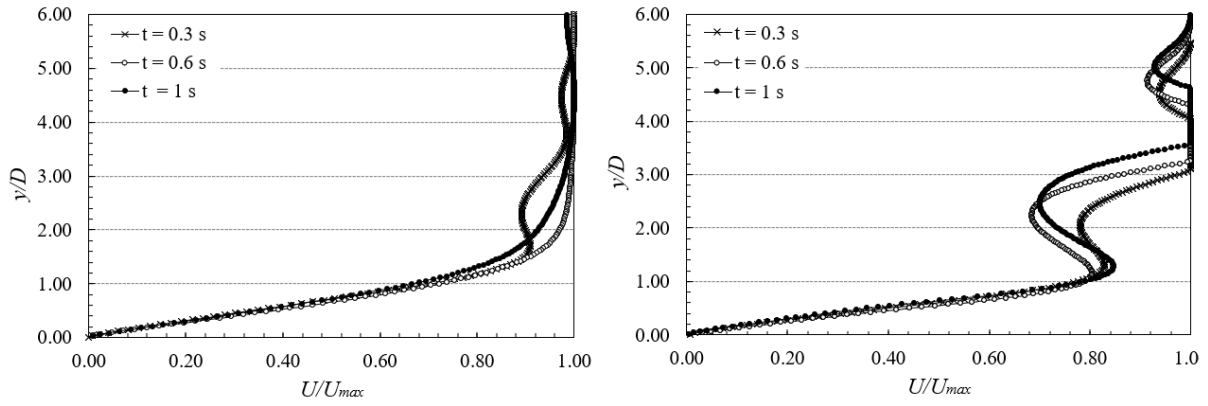


**Figure 69.** Instantaneous normalized velocity variation along the jet axis at  $Re = 420$ : (a) FLUENT; (b) 2.29 FV

Decreasing the distance from the target plate, it seems that the jet flow passes through a deceleration region at  $y/D$  near 3, followed by an acceleration zone induced by the primary vortex. At  $y/D = 1$ , the stagnation region is reached, achieving finally the stagnation point at  $y/D = 0$ . While in 2.29 FV this profile is preserved, with a higher intensification of both acceleration and deceleration zones with the increase of the simulation time, in FLUENT, the opposite is observed. It seems that, with time, the effects of the perturbations close to the jet inlet and the primary vortices downstream, are minimized. This can be an effect of the outlet boundary condition implemented in FLUENT. The model is able to capture the unsteadiness of the flow at the beginning of the simulation, but with time the flow tends to stabilize. The maximum velocities are recorded at the jet axis, until the end of the potential core region is reached, i.e. 95 % of the maximum velocity, at approximately  $y/D = 2$ .

### *Non-isothermal jet*

The normalized velocity magnitude over the target plate and at the jet axis is predicted numerically by both FLUENT and 2.29 FV. However, its analysis will be performed in the next section, while here, the focus is on heat transfer.

To analyze the variation of the heat transfer over the surface, the Nusselt number was calculated. For both FLUENT and 2.29 FV, the Nusselt numbers and heat transfer coefficients are obtained following the same approach presented in section 3.2.4. However, the difference is in the measurement of the heat flux,  $\bar{q}$ . According to [209], the surface heat flux in laminar flows can be determined using Eq. (78):

$$\bar{q} = -k \frac{(T_{w-adj} - T_w)}{\Delta x} \quad (78)$$

where  $k$  is the thermal conductivity of the air jet,  $\Delta x$  is the distance between the centroid of the fluid cell near the wall and the wall,  $T_{w-adj}$  represents the temperature of the fluid adjacent to the wall and  $T_w$  is the temperature of the target surface. The same method is applied by the 2.29 FV framework.

The variation of Nusselt number over the target plate, predicted by FLUENT and 2.29 FV, is presented in Figure 70. Since the numerical simulations are 2D, the heat transfer analysis is limited to the length of the sensor ( $-4 < x/D < 4$ ).

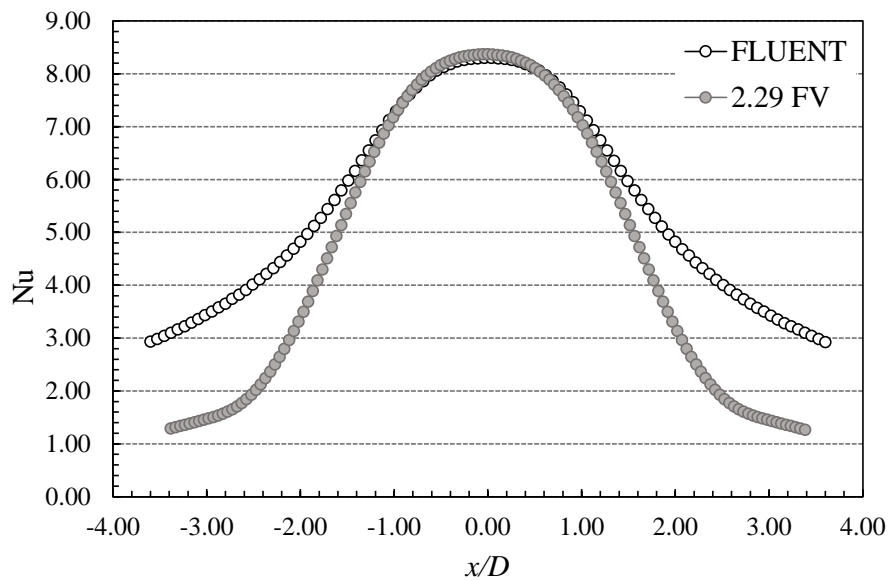


**Figure 70.** Averaged Nusselt number over the target plate at  $t = 1$  s ( $y/D = 0$ ).

As shown in Figure 70, a higher heat transfer rate occurs at the stagnation region, with a maximum Nusselt number equal to approximately 8.3 at the stagnation point. The same value was predicted by 2.29 FV and FLUENT. The stagnation region, characterized by high static pressure over the surface, induces the turning of the flow which creates high normal and shear stresses that promote the heat transfer [21]. As the wall jet develops over the surface, increasing the distance from the jet axis, Nu decreases gradually with the boundary layer thickening. These conclusions are in agreement with numerical works conducted by [10, 83, 125, 231]. However, the main difference between the two numerical tools is identified at  $x/D > \pm 1.2$ . However, the wall jet development over the surface is different, being observed an increased deviation from 0 % at the end of the stagnation region to 44 % at the end of the sensor. These lower heat transfer rates predicted by 2.29 FV can be explained by a thicker boundary layer compared with FLUENT, as identified in Table 18. Lower velocities in the vicinity of the target plate induce lower flow mixing and consequently a decrease in heat transfer.

### c) Numerical vs experimental data

The numerical data validation is conducted in two sections. While the first section compares in detail the numerical and experimental velocity profiles obtained in the isothermal case, the non-isothermal section mainly focuses on the average heat transfer.

#### *Isothermal jet*

To determine if both 2.29 FV MATLAB Framework and FLUENT Laminar model are accurate to predict the laminar single air jet impingement over a flat plate, the numerical results are compared with the experimental data. Figure 71 compares the normalized velocity profile over the target plate obtained using the three methods.

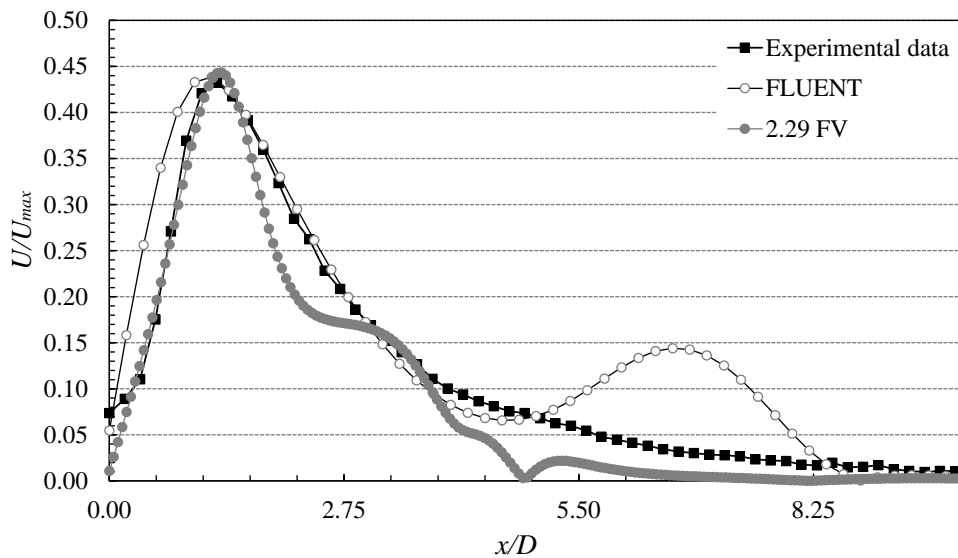


**Figure 71.** Normalized velocity profile over the target plate ( $y/D = 0.02$ ) at  $t = 1$  s and  $Re = 420$ .

The results demonstrate that at  $y/D = 0.02$ , 2.29 FV predicts a value equal to zero at the stagnation point, while it is not the case with FLUENT and PIV measurements, showing once again the need to increase the measurement accuracy at this point. FLUENT Laminar model presents a steeper increase in velocity near the stagnation point when compared with 2.29 FV and the experimental results. However, the maximum velocity is observed at approximately  $x/D = 1.2$  for each case and starts to decrease as the distance from the jet axis increases. However, while in FLUENT this decrease follows the experimental data, 2.29 FV predicts slightly lower velocity values. While the decrease in velocity predicted by 2.29 FV seems to be symmetric to the increasing velocity profile, experimentally, this decrease is less pronounced. The higher difference is observed at  $x/D = 3$ , where a secondary maximum velocity was predicted by 2.29 FV. This secondary peak was also detected by FLUENT near  $x/D = 7$ . This increase in velocity was

found both numerically and experimentally by several authors [8, 20, 121, 235, 236]. Looking at the jet flow structure presented in Figure 65, it seems that this increase results from the interaction of the wall with the primary vortices, generating a secondary peak that is not detected experimentally. As mentioned by [230], PIV is limited in resolving near wall measurements, and this statement is confirmed by these results. Therefore, enhancements of the measurement process are needed. These results demonstrated once again the efficiency of 2.29 FV to predict with accuracy the flow near the wall jet. Furthermore, these conclusions show that even if the vortices are not clearly identified by the velocity field (Table 18), the effects of their interaction with the wall jet are predicted and in accordance with other studies presented in the literature [24, 121, 122, 230, 233]. To support this statement, the instantaneous vorticity field obtained numerically by 2.29 FV is plotted and presented in Figure 72 (a). For comparison, the vorticity plot is also generated for FLUENT results and depicted in Figure 72 (b).

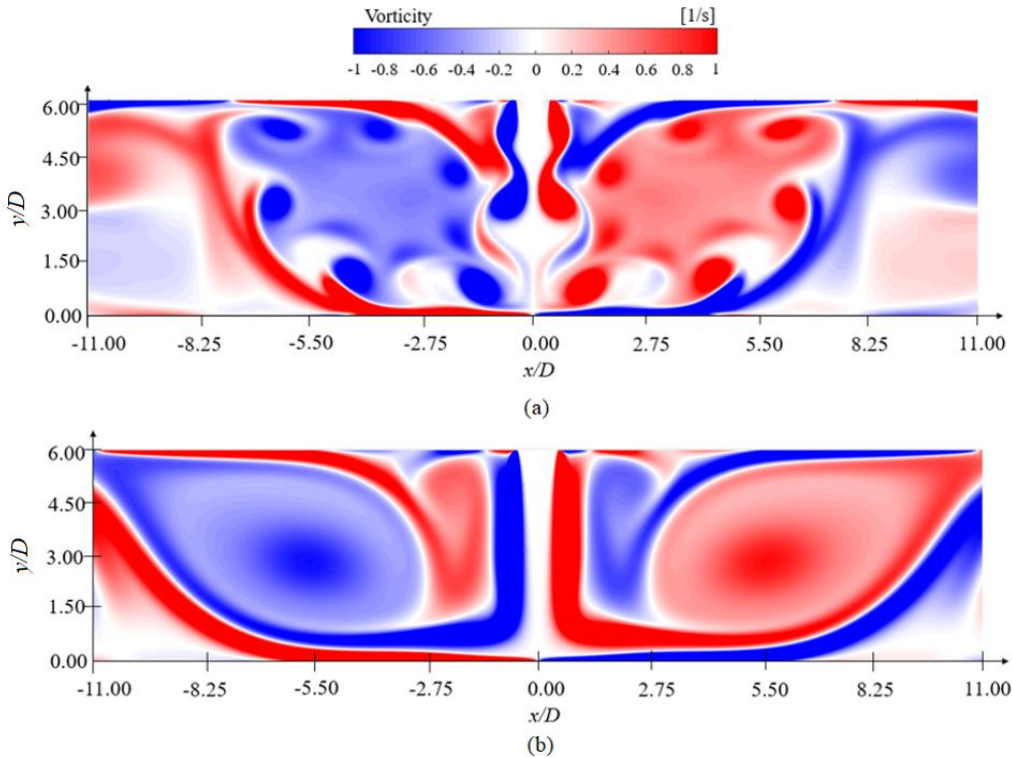


**Figure 72.** Instantaneous vorticity field at  $Re = 420$  and  $t = 0.6$  s: (a) 2.29 FV; (b) FLUENT.

The main difference observed by the two numerical tools is related to the prediction of the large and small scale motions throughout the domain. While 2.29 FV both captures the large and small vortices from the jet inlet to the wall jet, FLUENT captures the two large vortices and their interactions with the jet axis. These results show the accuracy of the 2.29 FV to predict the jet flow dynamics and the vorticity profile seems to be very close to the profile obtained experimentally in Figure 65. As expected, the vorticity is zero on the jet axis and maximum where the shear is largest. The primary vortices are clearly identified,

starting from the Kelvin Helmholtz instabilities generated downstream of the nozzle in the shear layer. These vortical structures grow in magnitude with the increased mixing between the jet flow and the ambient air and the symmetry of the flow is clearly observed. At the wall jet, the growing boundary layer is identified, being expected the maximum velocity values near the stagnation region, where the boundary layer is thinner, due to the strong interactions between the vortical structures induced at the free jet shear layer. Figure 72 shows an increase in magnitude at  $x/D$  near to 5.4 in 2.29 FV. The vortical structures induced at this location are the secondary vortices, clearly observed in Figure 72 (a) at both sides of the jet axis, while in Figure 72 (b), the prediction of the secondary vortex is not clear. These results demonstrate that even if FLUENT is able to predict the overall structure of the flow, the 2.29 FV Matlab framework allows to identify the small scales that characterize this flow, as proved by Figure 65.

Looking at the variation of the velocity along the jet axis, presented in Figure 73, it seems that 2.29 FV is more accurate to predict the acceleration and deceleration zones compared with FLUENT. The data obtained by FLUENT show a uniform variation of velocity, with a maximum recorded through the potential core. The end of the core was estimated to be at  $y/D = 2.5$ , which is close to the results obtained experimentally. From this point, the velocity started to decrease, passing through the decaying region at  $1 < y/D < 2.5$  and finally reaching the stagnation region at  $y/D < 1$ , until the stagnation point, recorded at  $y/D = 0$  and  $x/D = 0$ . However, these results are different from those obtained experimentally, as can be verified in Figure 73.

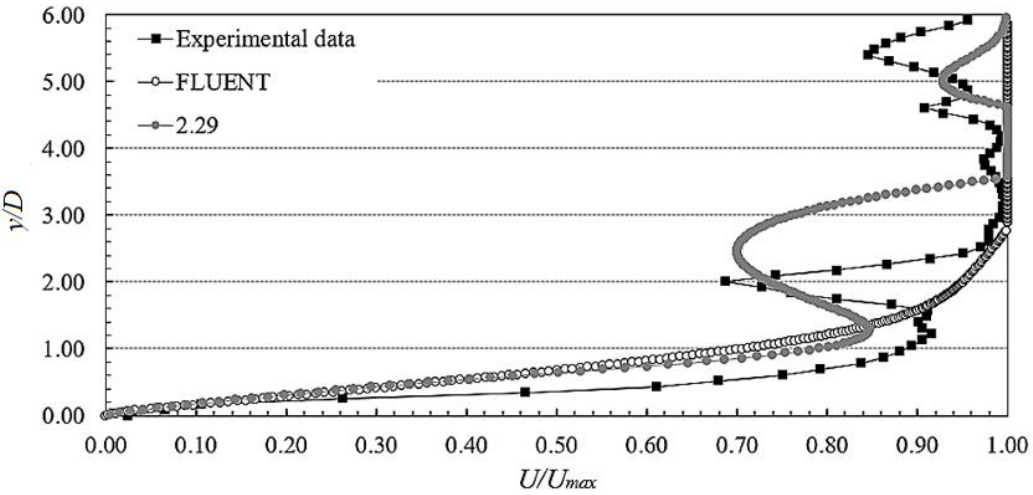


**Figure 73.** Normalized velocity variation along the jet axis, at  $t = 1$  s,  $x/D = 0$  and  $Re = 420$  (isothermal jet).

The experimental data show a decrease in velocity close to the nozzle exit. As mentioned previously, this occurs due to the shear layer generated by the mixture between the jet flow and the ambient air, which was also identified by 2.29 FV. The minimum velocity estimated by 2.29 FV is 10 % higher than

that obtained experimentally, and the location is slightly different,  $y/D = 5.4$  experimentally against  $y/D = 4.9$  predicted numerically. The maximum velocity is reestablished at the jet axis, until the end of the potential core is reached, at  $y/D$  close to 3.5 predicted by 2.29 FV, and  $y/D = 2.5$ , experimentally. These results reveal that the end of the potential core region is accurately predicted by FLUENT, since 2.29 FV predicts a smaller potential core length compared with experimental data and FLUENT. From this point, the jet flow passes through a deceleration region, in which the velocity loses almost 30 % of the maximum velocity, identified at  $y/D = 2$ , experimentally, and at  $y/D = 2.4$  by 2.29 FV. An acceleration zone is identified at  $1 < y/D < 2$ . The increase in velocity predicted by 2.29 FV and experimentally is approximately equal to 20 % and the maximum value is detected at  $y/D$  near to 1.3. At  $y/D = 1$  the stagnation region is identified both numerically and experimentally, as well as the stagnation point, where velocity at  $y/D = 0$  is equal to zero. Comparing numerical and experimental data, it is possible to conclude that the prediction performed by 2.29 FV is closer to the experimental data compared with FLUENT Laminar model. These differences are explained by the numerical schemes implemented by each numerical model. Since FLUENT is based on RANS equations, it is clear that it is not appropriate to predict all the small scales generated throughout the jet flow. For that, the 2.29 FV framework is more appropriate. However, generally, the results are not far away from the truth. The velocity profiles obtained by experimental data, 2.29 FV, and FLUENT laminar model are similar. The large-scale structures and the wall jet are analogous in both numerical tools. In that sense, this study proves the reliability of the Laminar model of FLUENT for the numerical model of a single air jet impingement. However, if the analysis of the small scales development throughout the domain is relevant for the study, the 2.29 FV must be implemented instead of FLUENT Laminar model.

### Non-isothermal jet

The velocity profiles predicted numerically and measured experimentally, over the target plate and along the jet axis, are compared in Figure 74 and Figure 75, respectively.

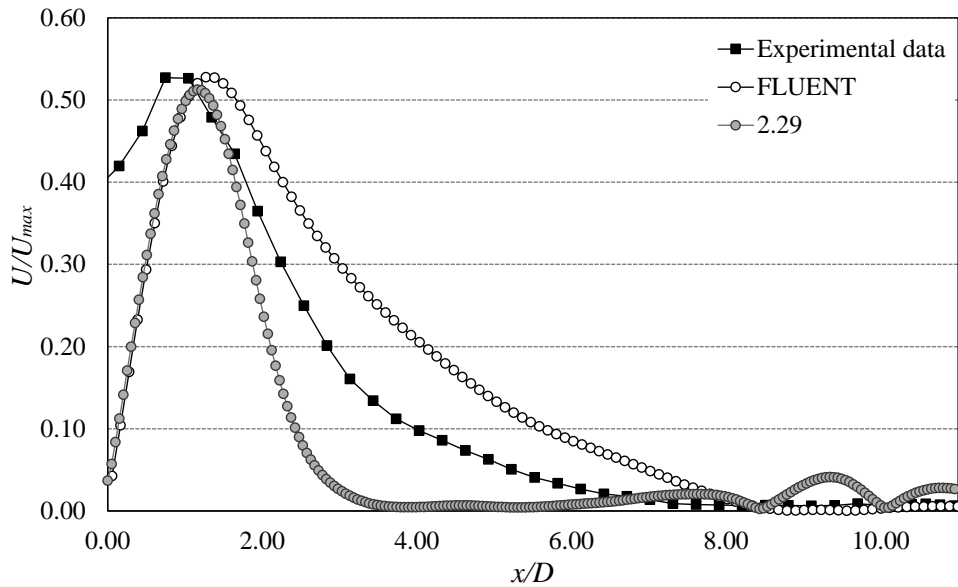


Figure 74. Normalized velocity profile over the target plate ( $y/D = 0.02$ ) at  $t = 1$  s and  $Re = 420$  (non-isothermal jet).

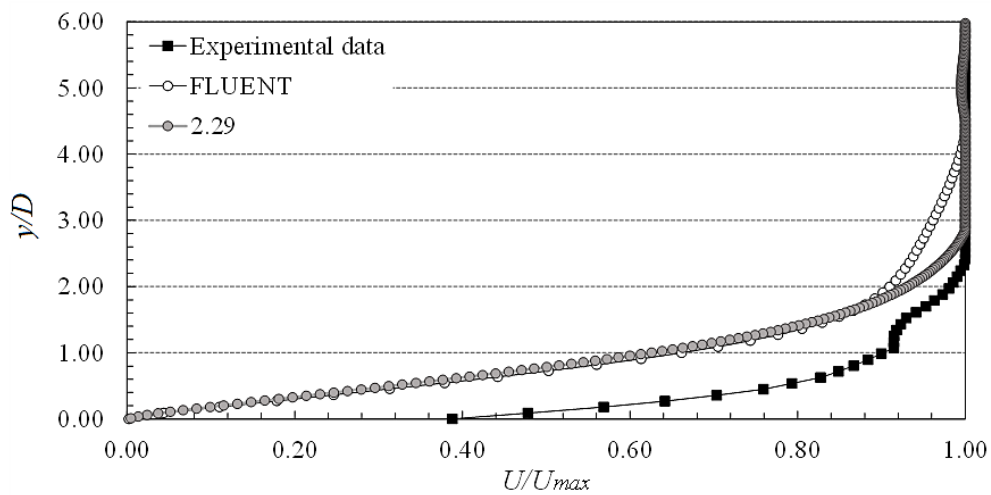


Figure 75. Normalized velocity variation along the jet axis, at  $t = 1$  s,  $x/D = 0$ , and  $Re = 420$  (non-isothermal jet).

Compared with the isothermal case, it seems that higher velocities are recorded over the impinging surface, which is in agreement with the analysis performed on the experimental data. The heated plate increases the temperature of the air in the vicinity of the surface, inducing buoyancy forces that increase

the velocity of the flow. A mixed heat transfer effect is observed due to forced convection induced by the jet flow and buoyancy driven natural convection flow near the surface. Moreover, experimental data shows a limitation in the measurement of the stagnation point. Even if the same issue was identified in the isothermal case, it is intensified by the heated plate. Considering the flow characterization presented in the previous sections, it is clear that the increased turbulence induced in the vicinity of the target plate due to buoyant driven flow makes it difficult to capture particular details such as the stagnation point. Therefore, the improvement of the PIV measurements is required near the wall. Even if the decrease in velocity follows the same profile for both numerical and experimental results, from the stagnation point to the velocity peak, identified near  $x/D = 1.2$ , FLUENT over-predict velocities as the distance from the velocity maxima increases, while these values are under-predicted by 2.29 FV. Regarding the point where the flow detaches the plate, it is identified at  $x/D = 8$  by FLUENT and experimental data, while 2.29 FV predicts this point near  $x/D = 4$ . This difference can be explained by an over prediction of the interactions of the air flow coming from the outlets. The strong effect of the natural convection interferes with jet flow development over the wall and forces the flow to detach from the surface. This flow detachment occurs at a distance closer to the jet axis compared to the isothermal case.

Looking at the velocity profile along the jet axis (Figure 75), the results show that the potential core length is under-predicted by FLUENT. While experimentally the end of the potential core is detected near  $y/D = 2$ , numerically this value is recorded near  $y/D = 3$ . Moreover, a smooth transition between the decaying region and the stagnation region is observed numerically, while experimentally, the effect of the shear layer expansion inward to the jet center is identified. This induces a slight acceleration of the flow just before the transition to the stagnation region at  $y/D = 1$ . However, 2.29 FV predicts a velocity profile at the jet axis similar to that obtained experimentally, with the end of the potential core identified at the same distance. Regarding the velocities at the stagnation region, the same values as FLUENT are predicted, showing a discrepancy of approximately 5 % compared with the experimental data. An important aspect identified in Figure 75 is the fact that, in contrast to Figure 73 (velocity profile at the axis of the isothermal jet), the velocity is constant over the potential core in all cases. This means that the small vortices detected experimentally and by 2.29 FV near the shear layer and over the surface for the isothermal jet, are not observed in the non-isothermal jet and this conclusion is supported by the instantaneous vorticity profile generated by 2.29 FV (Figure 76). These results are in agreement with the analysis previously presented regarding the effect of natural convection on the flow development over the surface. Since the Reynolds number is low, the buoyancy forces highly affect the inertia of the flow, preventing the generation of the vortical structures at the shear layer and over the surface. Moreover,

Figure 76 proves that the detachment of the flow from the wall occurs closer to the jet axis ( $x/D = 2.75$ ) compared with the isothermal jet ( $x/D = 5.4$ ), as expected.

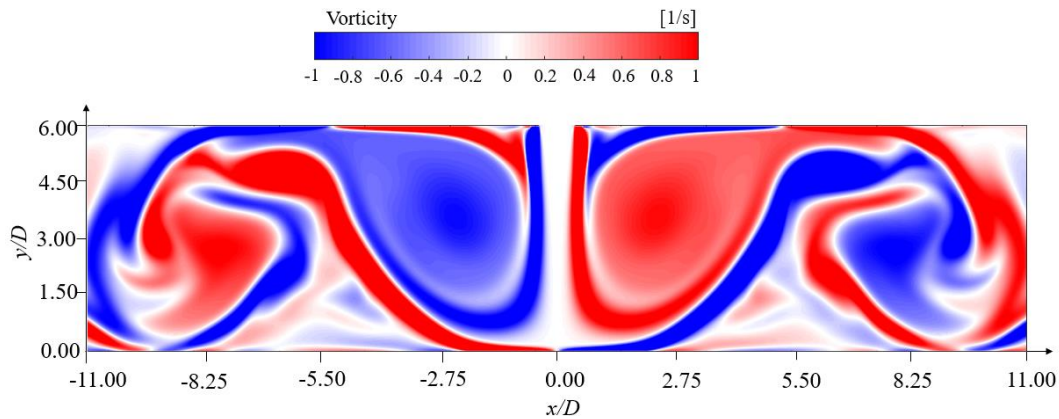


**Figure 76.** Instantaneous vorticity field at  $t = 1$  s and  $Re = 420$  predicted by 2.29 FV.

Finally, the average heat transfer over the target plate measured experimentally is compared with the numerical results, as the average Nusselt number (Table 19). The results show that FLUENT predicts with accuracy the average heat transfer over the surface. However, a 2.29 FV under predicts this value by 17 %. As mentioned previously, this difference is mainly due to the prediction of a smaller wall jet region compared with FLUENT and experimental data.

**Table 19.** Average Nusselt number obtained experimentally and numerically.

Data	Experimental	FLUENT	2.29 FV
$\bar{Nu}$	$5.5(2) \pm 0.80^*$	5.51	4.72

\*Heat flux uncertainty for 95 % of confidence level.

### 5.2.3. Conclusions

A single air jet impinging a flat plate was analyzed numerically and experimentally. Two numerical tools were implemented, and the results obtained were compared with the experimental data. The experiments show that jet impingement is an unsteady process, with perturbations induced from the moment the jet starts to mix with the ambient air. These perturbations grow, generating vortices that propagate over the flow. During the impingement, these vortices develop throughout the wall jet, entraining ambient air which increases the boundary layer thickness. The maximum velocities are higher near the stagnation region, where the boundary layer is thinner. In addition, acceleration zones are identified, due to the interaction between the vortices and the wall jet, which induces local maximum

velocity, beneficial for the heat transfer. The 2.29 FV framework demonstrated a high potential in predicting the flow profile near the wall compared with the FLUENT Laminar model. The effects of primary and secondary vortices were detected by data processing in both 2.29 FV and FLUENT. To analyze in detail the vortical structures generated throughout the jet flow and over the target plate, a vorticity field provides useful insight. Regarding the heat transfer over the target plate, FLUENT and 2.29FV predicted a similar variation of the Nusselt number over the target plate. Comparing experimental and numerical results, the average Nu was accurately predicted by FLUENT, while 2.29 FV underpredicts this value by 17 %. This difference is explained by stronger interactions between the air flow coming from the outlets and the jet flow, which reduces the wall jet region, forcing the flow to detach from the surface. From this study, the reliability of FLUENT Laminar model was proved. However, if the prediction of small-scale structures is important for the research, the 2.29 FV presents a better approach and must be implemented. Future works will consist of the comparison between these two models for a jet impingement flow with higher levels of turbulence. In addition, completing a probabilistic study of the flow and heat transfer dynamics using optimal dynamic stochastic reduced-order models [237–240] would be most useful.

### 5.3. Single Jet Impingement in a Transition Regime

Amongst the different process variables, nozzle-to-plate distance ( $H$ ) is considered one of the most important geometrical parameters in jet impingement due to its strong influence on heat transfer performance. In addition, data collected from the industry shows that in reflow soldering, the flow lies in the transition region. However, the research conducted in jet impingement with this flow regime is very scarce, since the majority of the research focuses on fully turbulent jets. In that sense, an isothermal jet in the transition regime ( $Re = 2,000$ ) is characterized in this section and the influence of  $H/D$  in the jet flow dynamics is analyzed.

#### 5.3.1. Experimental Results

The velocity field of an isothermal jet impinging a flat plate at different  $H/D$  is measured using the PIV technique, following the methodology presented in chapter 3, section 3.3.2. The experimental results are presented in Figure.

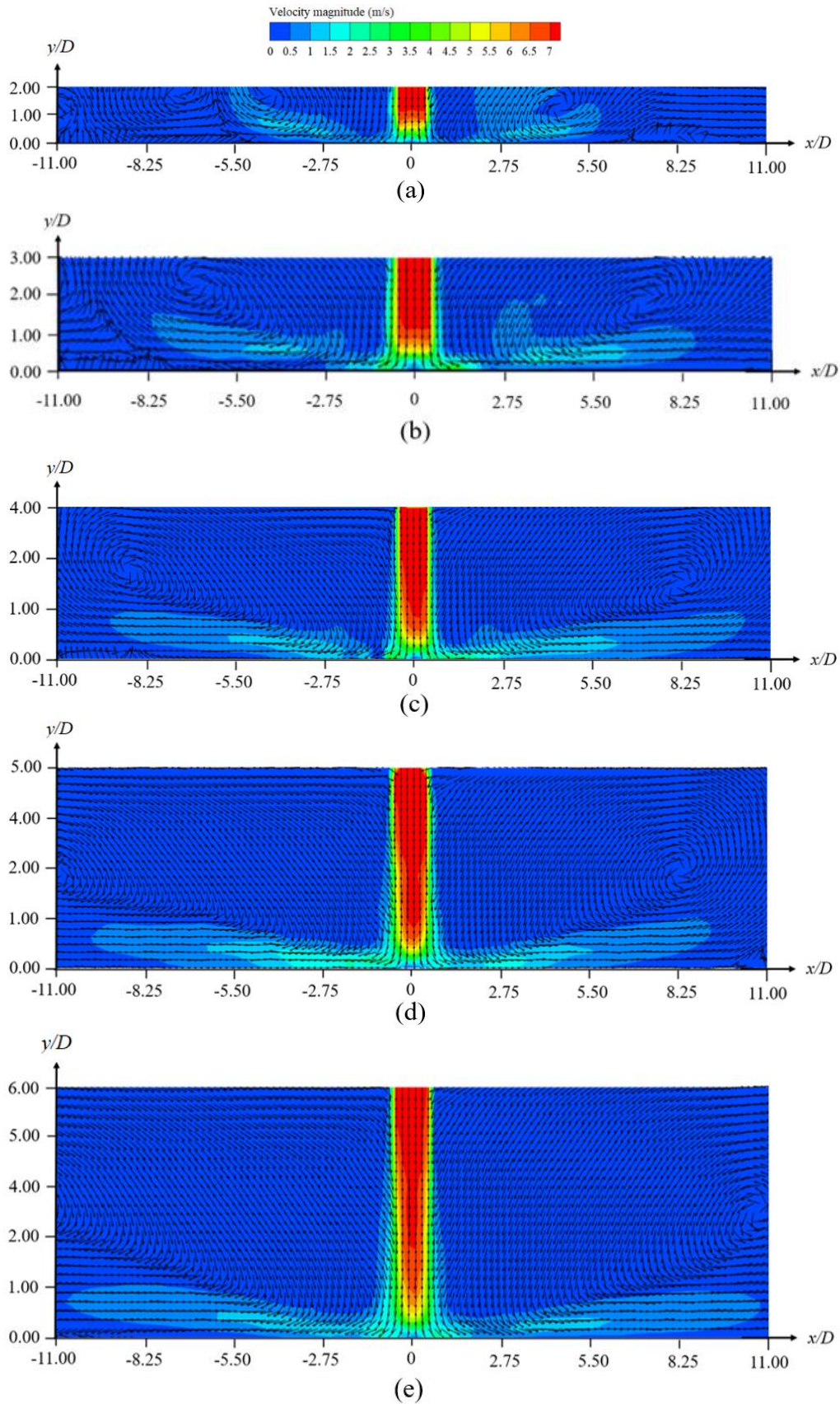


Figure 77. Jet velocity profile: (a)  $H/D = 2$ ; (b)  $H/D = 3$ ; (c)  $H/D = 4$ ; (d)  $H/D = 5$ ; (e)  $H/D = 6$ .

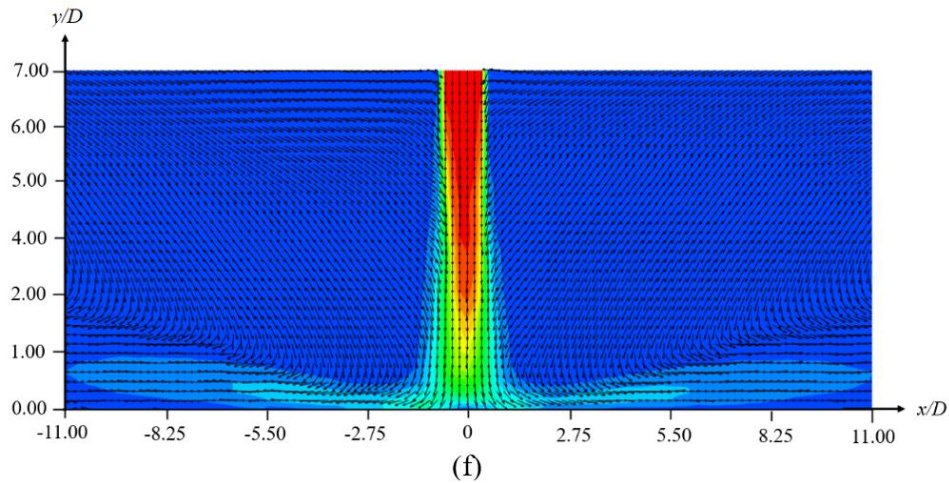
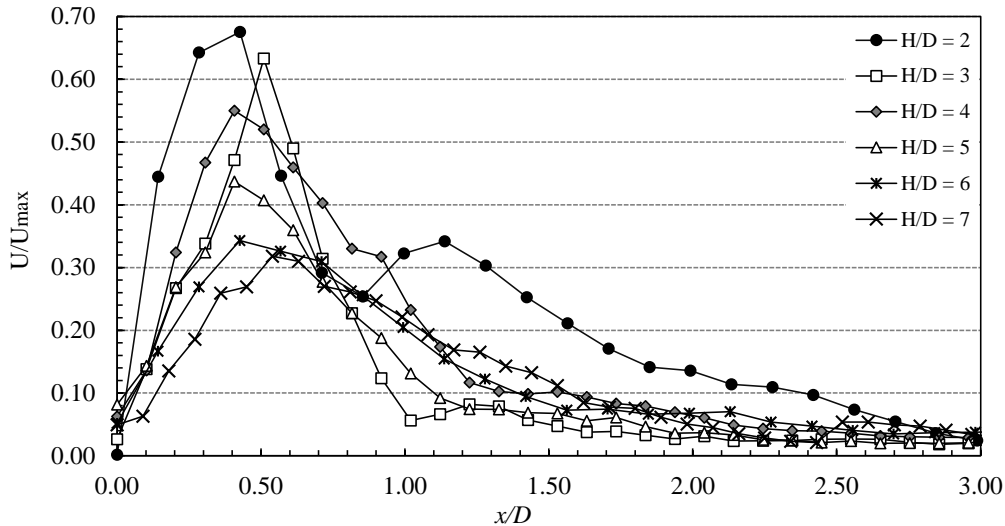


Figure 77 (cont.). Jet velocity profile: (f)  $H/D = 7$

From Figure, it is observed that increasing  $H/D$  leads to a decrease of the potential core length due to the higher dissipation of the jet velocity, showing that a low  $H/D$  yields a uniform velocity profile in this region. The end of the core region is followed by the beginning of the decaying region which is characterized by the linear variation of the axial velocity and the jet width with the axial position [21]. As the flow gets closer to the wall, it loses axial velocity and turns, generating a stagnation region in which the overall velocity is near zero [24]. The last region, the wall jet, is identified once the air jet impacts the target surface. Increasing the distance from the jet axis, the wall jet entrains flow and increases in thickness, while the flow velocity decreases. In the vicinity of the stagnation point, an increase of the velocity is detected in all cases which can be explained by a rapid acceleration of the flow due to larger pressure gradients. High heat transfer coefficients can be obtained in this specific region, in the transition from the laminar to turbulent boundary layer [241]. The separation of the flow occurs where the boundary layer detaches the surface of the plate and occurs closer to the jet axis as the nozzle-to-plate distance decreases. The results also demonstrate that the wall jet thickness increases with decreasing the nozzle-to-plate distance due to higher local pressure induced by strong interactions between the jet and the surrounding air. Furthermore, an increase of the wall jet region in the radial direction with the increase of  $H/D$  is observed, which is in accordance with other confined jet impingement studies at higher Reynolds numbers [8, 241]. Looking at the vortices generated on both sides of the jet axis, it seems that the higher the nozzle-to-plate distance, the lower the magnitude of the vortices generated, which is essentially due to the larger space for the flow to develop.

Through the previous analysis, it seems that experimental results predict with accuracy the flow structure of a single jet in the transition region. Focusing on quantitative data, the time-averaged velocity over the target surface for different  $H/D$  is presented in Figure 78. Considering an air jet at ambient

temperature impinging a flat plate at the same temperature, the experimental results show the evolution of the non-dimensional velocity,  $U/U_{max}$ , where  $U$  is the time-averaged velocity magnitude obtained by PIV measurements and  $U_{max}$  is the maximum velocity recorded at the nozzle exit, over the target surface.



**Figure 78.** Time-averaged velocity over the target surface ( $y/D = 0.15$ ) at different  $H/D$  and  $Re = 2,000$ .

The maximum velocity is achieved for  $H/D = 2$ . This is in accordance with the jet flow structure presented in Figure, in which highly confined spaces induce a stronger interaction between the surrounding air and the vortices generated by the jet impingement, leading to higher velocities over the wall. Results also show that the higher the nozzle-to-plate distance, the lower the velocity in the vicinity of the stagnation point. The maximum value is recorded in all cases at a distance from the jet axis ( $x/D$ ) near 0.5, which is in agreement with [8, 123, 133], slightly increasing with the increase of  $H/D$ . Moreover, as expected, the jet wall increases with increasing  $H/D$ , leading to a smoother decrease of the velocity throughout the target plate. For  $H/D = 2$  but also  $H/D = 3$ , even if less pronounced, an interesting phenomenon is observed. After reaching the maximum velocity, its value starts to decrease, achieving a minimum velocity at approximately  $x/D = 0.9$ . From this point, as opposed to the other cases, the velocity rose again achieving a second maximum point at about  $x/D = 1.1$ . This secondary point is identified in several studies, such as Zuckerman & Lior [21] and Viskanta [20], being attributed to the transition of the boundary layer from laminar to turbulent flow along the wall. However, with the increase of the nozzle-to-plate distance, the interactions between the jet and the surrounding air in the confined space decrease, and since the Reynolds number is low, no secondary peak is identified at higher  $H/D$ . Viskanta [20] summarized the influence of the nozzle-to-plate distances smaller than the jet potential core length on the radial distribution of the convective heat transfer coefficient and pointed out three main

factors: (a) the laminar boundary layer behavior under strongly accelerated surrounding flow in the vicinity of the stagnation point; (b) the interaction of large-scale turbulence induced in the mixing zone; but also (c) the transition of the boundary layer from laminar to turbulent over the wall jet.

Regarding the stagnation point, it is detected with higher accuracy at  $H/D = 2$ , with a velocity value very close to zero at the jet axis, as expected. However, this is not observed in the other cases. This can be explained by the fact that to detect this point with accuracy, an interrogation area with a higher resolution than the one used in this experiment must be used. To reduce the difference between the expected value ( $U = 0$ ) and those obtained experimentally, the observation zone should be zoomed onto the stagnation region. However, since this experiment is expected to characterize all the flow, from the nozzle exit to the target plate, the observation area should be large. Another reason to explain this difference is related to factors that can generate systematic errors such as the concentration of particles as well as the time between pulses. These are two fundamental factors that can decrease the accuracy of the PIV measurements. It is verified that even if the same Reynolds number is maintained throughout the experiments since higher velocities are recorded over the wall region for lower nozzle-to-plate distance, it is necessary to decrease the time between pulses to increase the accuracy of the results. Meaning that for  $2 \leq H/D \leq 5$  a lower time between pulses is implemented compared with  $H/D$  of 6 and 7. This adjustment of the time between pulse in function of the flow velocity is crucial to ensure accurate results.

### 5.3.2. Numerical Validation

The experimental data is used for the validation of the numerical model of a single jet impingement in the transition regime. In that sense, the experimental and numerical time-averaged velocity over the target surface at different nozzle-to-plate spacings for a Reynolds number of 2,000 are compared. The velocity field predicted numerically for different  $H/D$  is presented in Figure 79.

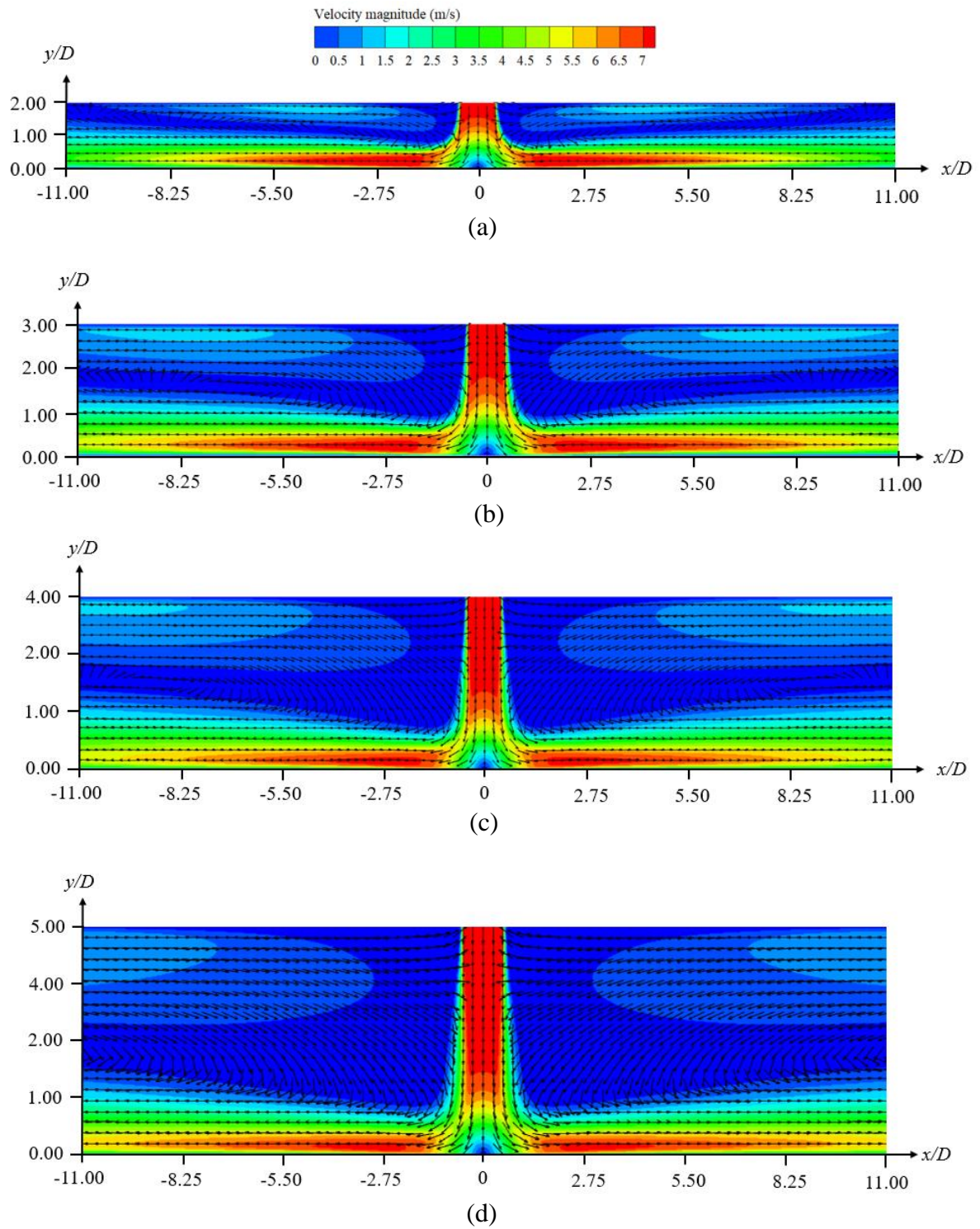
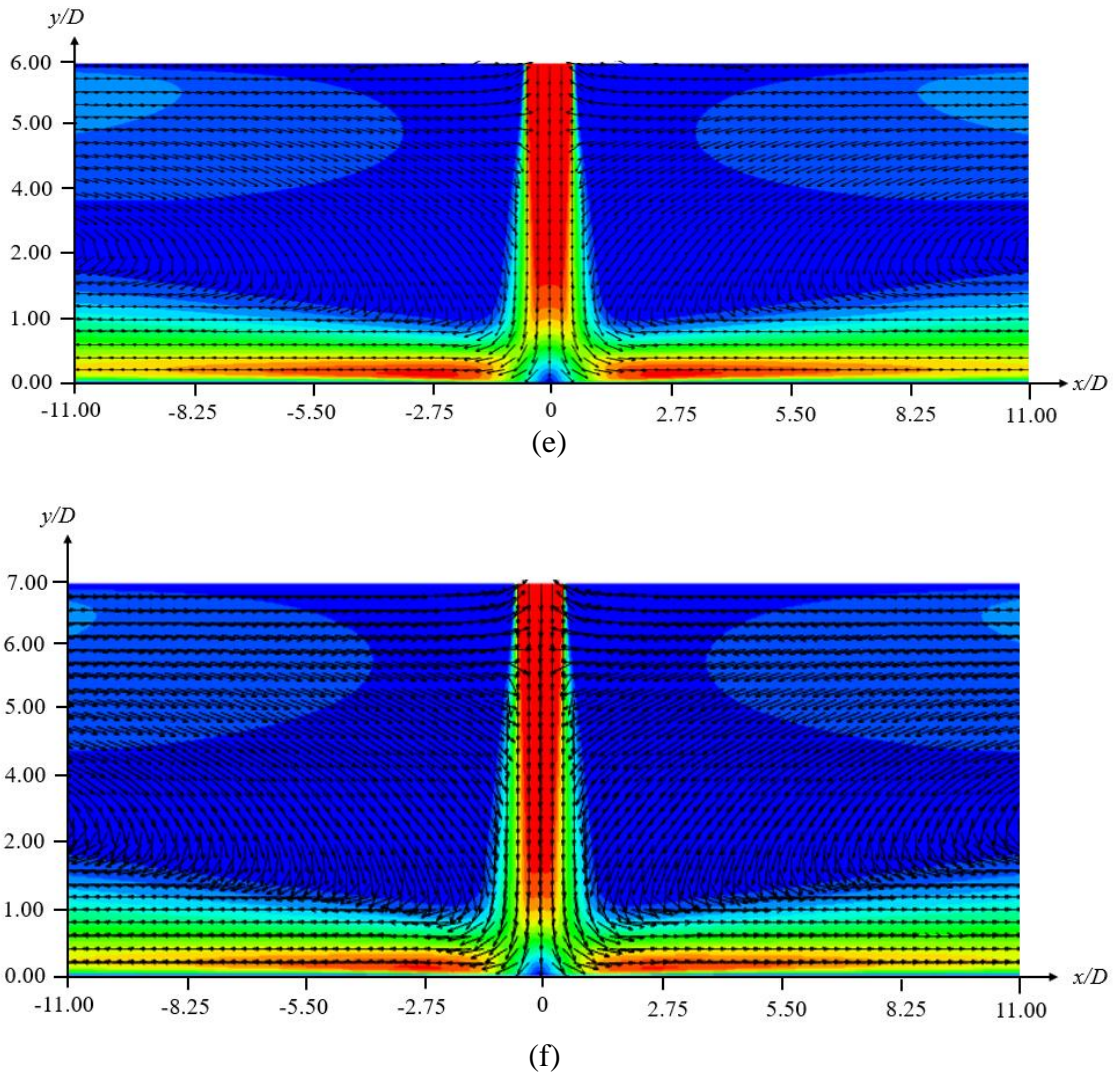


Figure 79. Velocity field: (a)  $H/D = 2$ ; (b)  $H/D = 3$ ; (c)  $H/D = 4$ ; (d)  $H/D = 5$ .



**Figure 79 (cont).** Velocity field: (e)  $H/D = 6$ ; (f)  $H/D = 7$ .

Observing in detail Figure 79 and compared with Figure, it is clear that the SST  $k-\omega$  model does not predict with accuracy the wall jet region for low  $H/D$ . While the experimental data demonstrated that at low  $H/D$  the detachment of the jet flow from the wall occurs closer to the jet axis, this is not verified numerically. This seems to be related to the outlet boundary conditions. Even if [92] mentioned that the outlet boundary conditions must be implemented at a large distance to avoid flow reversal, the pressure outlet seems to affect the flow development over the wall. Regarding the boundary layer, the numerical results show a higher thickness in all cases compared with the experimental results. To determine if this difference is related to the boundary conditions or a low resolution of the PIV near the wall, more measurements must be conducted.

To analyze in detail the flow development over the wall, the normalized velocity magnitude at the vicinity of the surface was plotted and presented in Figure 80. The results show that the stagnation point,

it is not captured at a distance of  $y/D = 0.15$  from the target plate, since a value of  $U/U_{max} = 0.3$ . However, it is clearly observed in Figure 79.

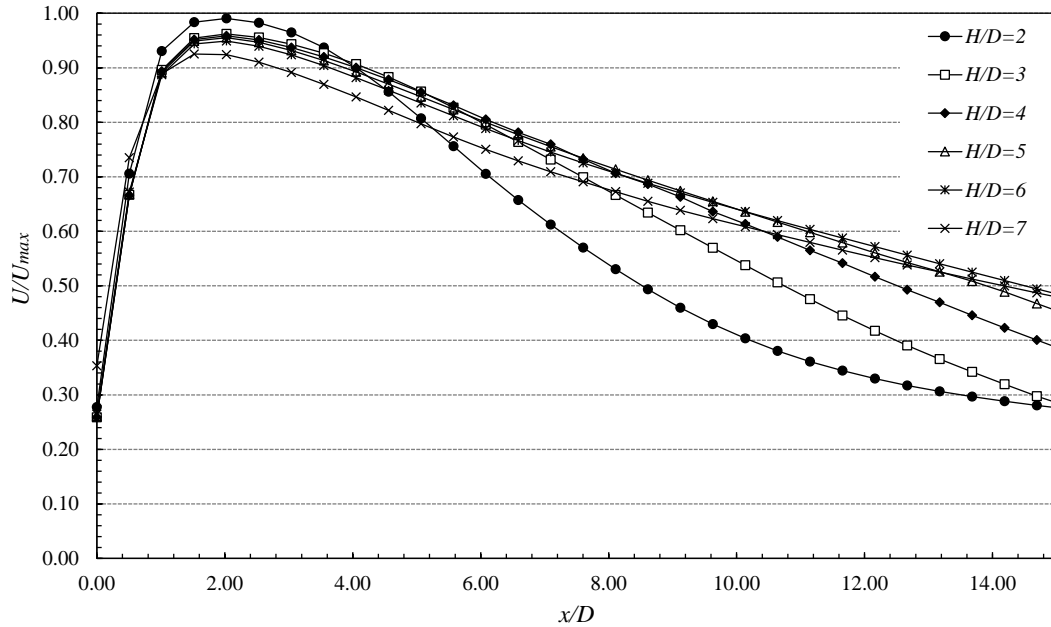


**Figure 80.** Velocity near the target surface ( $y/D = 0.15$ ) at different  $H/D$  and  $Re = 2,000$  (SST  $k-\omega$  turbulence model).

The first important differences, compared with the experimental data (Figure 78), are higher velocities predicted in the vicinity of the target plate and the wall jet is extended to a higher distance from the jet axis. These results are in agreement with the velocity field presented in Figure 79. The maximum velocity value is recorded in the vicinity of the stagnation point, as expected. However, in contrast to the experimental data, this peak is detected at  $x/D \approx 2$  for all nozzle-to-plate distances and seems to decrease with increasing  $H/D$ . However, this decrease is more pronounced in the experimental results. For  $H/D = 2$ , the non-dimensional velocity  $U/U_{max}$  obtained both experimentally and numerically is close to 1, while in the other cases ( $3 \leq H/D \leq 6$ ), it is predicted to be around 0.95, and the lower value is obtained at  $H/D = 7$ ,  $U/U_{max} = 0.92$ . In contrast, the experimental results present a decrease from 0.7 at  $H/D = 2$  to approximately 0.3 at  $H/D = 7$ . This discrepancy between numerical and experimental results shows that the boundary conditions implemented in the model must be improved. The overall velocity profile in the vicinity of the target plate demonstrates once again the limitation of the SST  $k-\omega$  model to predict with accuracy the flow development over the wall jet, since at a distance between 0 and 3 from the jet axis ( $0 < x/D < 3$ ), a secondary peak is identified experimentally for the case of  $H/D = 2$  and 3 at  $x/D = 1.1$ , but it is not predicted numerically.

The variation of  $U/U_{max}$  throughout the jet axis in the case of  $H/D$  equal to 2 and 7 is presented in Figure 81, where  $y/D$  represents the normalized distance between the nozzle and the target plate. The profile predicted numerically is very close to that obtained experimentally, with a maximum deviation near 10 %. A maximum velocity is recorded close to the nozzle (maximum  $y$  value). After leaving the nozzle, the air jet started to entrain surrounding air, decreasing the velocity which became steeper near the target plate. This velocity decrease is more pronounced at  $H/D = 7$ , due to the lower potential core length compared with  $H/D = 2$ . The minimum velocity value is achieved at the stagnation point, as expected. However, it is clear that the velocity profile obtained numerically is more uniform compared with the experimental ones. This deviation is essentially due to external factors, discussed in section 3.2.4, which are not considered by the numerical simulation since it is challenging to define, with accuracy, the realistic boundary conditions. Moreover, it is verified that higher velocities are recorded over the jet axis at lower nozzle-to-plate spacing, which is in agreement with the previous results. A lower  $H/D$  leads to an increase in turbulence between the main jet and the wall jet.

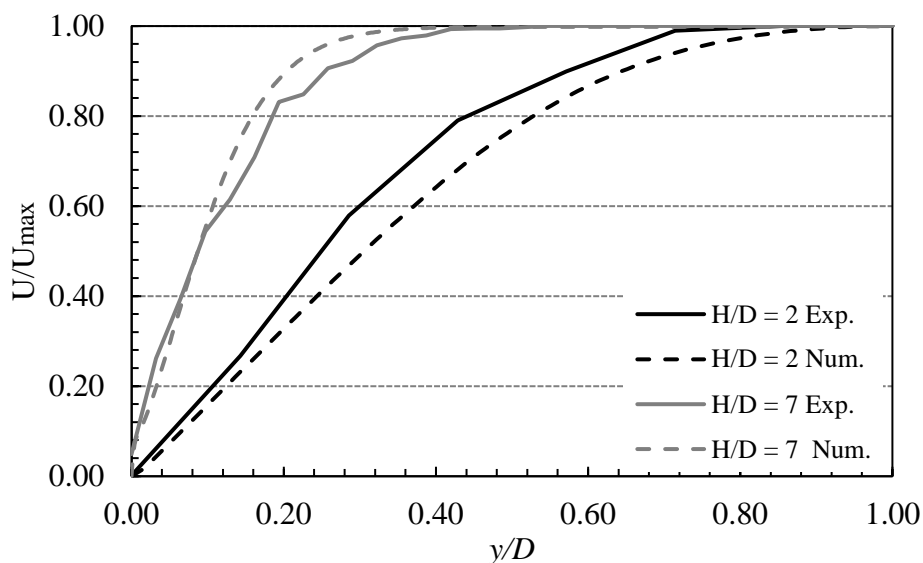


**Figure 81.** Variation of the normalized velocity through the jet axis ( $x/D = 0$ ).

### 5.3.3. Conclusions

This study demonstrated that the lower the  $H/D$ , the higher the velocities induced all over the domain. This increased velocity increases the magnitude of the turbulence intensity, therefore higher heat transfer coefficients are expected to be obtained over the target plate. As the  $H/D$  increases, the jet loses momentum as it approaches the target plate, therefore, the heat transfer in the vicinity of the plate is expected to reduce. The jet flow captured by the PIV system demonstrates the accuracy of this technique

to analyze the velocity field from the nozzle to the target plate. However, limitations are identified in the vicinity of the stagnation point. The use of a macro lens can be an interesting solution to analyze the flow in the surface transition, with higher detail.

The comparison between numerical and experimental results shows a fair agreement between the two approaches, essentially regarding qualitative data. The SST  $k-\omega$  model was able to predict the typical jet flow structure. However, compared with the experimental data a difference is observed regarding the wall jet development over the target plate. According to the PIV measurements, the lower the  $H/D$ , the shorter the wall jet region, but this is not observed numerically, at least at the same distance from the jet axis. Focusing on the quantitative data, the maximum velocity is predicted in the vicinity of the stagnation region and decreases with increasing  $H/D$ , as also observed experimentally. However, higher velocities are predicted numerically. To determine if this difference is related to the accuracy of the PIV measurements at the vicinity of the target plate or due to the boundary conditions implemented in the numerical model, more experiments are needed. Regarding the velocity profile over the jet axis, a deviation of approximately 10 % is observed between experimental and numerical data, showing a good agreement between these two methods. In general, it can be concluded that the SST  $k-\omega$  model presents good qualitative predictions of the single jet impingement flow at Reynolds number in the transition region.

## 6. RESULTS AND DISCUSSION OF A MULTIPLE JET IMPINGEMENT

### 6.1. Test Conditions: DoE Method

The study of multiple jet impingement systems must be designed properly since it is a process that involves complex relationships between several parameters that affect the heat transfer rate over the target plate. The analysis of all possible combinations between parameters involves huge costs and time, which is prohibitive in both industrial and academic research. In that sense, the statistical design of experiments (DoE) is an efficient procedure to obtain relevant conclusions regarding the object of this study. DoE was first introduced by Fisher [242] to determine the relationship between various factors and responses to them [243]. Through this methodology, it is possible to quantify effects, understand interactions between variables, model relationships, and measure experimental errors to obtain unambiguous answers to specific research questions, at a minimum cost [244]. A traditional DoE determines how different design factors affect the average result level. However, if the variation is more relevant than the average, Taguchi's DoE must be applied. Taguchi's methodology, widely applied in quality engineering, follows five main considerations [245]: (1) Definition of quality - minimum loss measured as the consistency of performance; (2) Standardized DoE – application of orthogonal arrays which represent the smallest fractional factorials; (3) Robust Design Strategy - which takes into consideration the influence of noise factors; (4) Loss function – quantification of the deviation from the target value; (5) Signal-to-noise ratio ( $S/N$ ) –for analysis of multiple-sample tests. Taguchi's approach is a three-step process, starting with System Design, going through Parameter Design, and finalizing with Tolerance Design. While the first step focuses on determining the suitable working levels of design factors, Parameter Design identifies the factor levels that produce the best performance of the process, and the last step uses tolerances to reduce manufacturing and lifetime costs [246]. Considering that multiple jet impingement involves several operational variables (factors), it is extremely important to define the values (levels) that increase the heat transfer performance over the target plate.

The main focus of this study is to provide a scientifically-based answer to the questions: *Which are the parameters that mainly influence the heat transfer over a complex moving surface impinged by multiple*

*air jets?*; and *The effect of these parameters in heat transfer is the same for the case of a static and an in-motion plate?*

The multiple jet impingement process has a great number of variables that influence the process. The analysis of the influence of each variable, as well as the interaction between them, is a great challenge. Based on a careful analysis, the following 14 variables were identified in the literature review: jet pattern; jet-to-jet spacing; nozzle shape; nozzle-to-plate distance; jet inclination; target surface geometry; target surface inclination; target surface motion; nozzle plate motion; crossflow; jet temperature; Reynolds number; Prandtl number; Mach number. If for each variable, 2 values (or levels) are tested, the number of possible different combinations rises up to  $2^{14} = 16,384$  experiments, if a full factorial method is applied. Considering that conclusions should not be drawn based on a single evidence, each experiment should be repeated, increasing the total number of experiments. This is impracticable in the laboratory, or in industry, which could be considered an unjustified waste of time and resources. In that sense, the use of Taguchi's method requires the application of a fractional factorial instead of a full factorial which is based on the selection of a limited number of experiments that produce the most information [247]. These fractional factorials are displayed in standard tables known as orthogonal arrays (OA).

To perform a correct design of experiment based on Taguchi's approach to parameter design, the following steps need to be conducted [248]: (1) Determination of the quality characteristic to be optimized; (2) Identification of the noise factors and test conditions; (3) Identification of the control factors and their levels; (4) Design of the matrix experiment and definition of the data analysis procedure; (5) Conduct the matrix experiment; (6) Data analysis and determination of the optimum levels for control factors; (7) Prediction of the performance at these levels.

### 6.1.1. Quality Characteristic

This work consists of the analysis of the influence of several process parameters on the average heat transfer rate through the Nusselt number over a target plate. This parameter represents the ratio between convection and conduction across a fluid, meaning that a larger Nusselt number represents more effective convection [156]. In that sense, and for Taguchi's method, the Nusselt number is the quality characteristic to be optimized.

The average Nusselt number is calculated using the Eq. (18), presented in section 3.2.5 b), and depends on the average convective heat transfer coefficient,  $\bar{h}$ , the nozzle diameter,  $D$ , and the thermal conductivity of the jet's flow,  $k$ . While the nozzle's diameter is a constant geometrical parameter equal to

5 mm and  $k$  is temperature-dependent obtained directly from the literature [156] in function of the air temperature,  $\bar{h}$  is determined by Eq. (19), as stated in section 3.2.5 b).  $\bar{h}$  is obtained by the heat flux measured by the heat flux sensor ( $\bar{q}$ ), the average plate temperature ( $\bar{T}_w$ ) and the average jet's temperature ( $\bar{T}_j$ ).

$$\overline{\text{Nu}} = \frac{\bar{h} D}{k} \quad (18)$$

$$\bar{h} = \frac{\bar{q}}{(\bar{T}_w - \bar{T}_j)} \quad (19)$$

As previously mentioned, the wall temperature is considered constant and equal to 120 °C. The jet is at ambient temperature, measured by a thermocouple placed inside the acrylic box.

To determine the deviation between the experimental and the desired values, Taguchi's method applies a loss function which is transformed into a signal-to-noise ratio ( $S/N$ ) [80]. Three  $S/N$  can be considered: larger the better, smaller the better, and on-target, minimum variation [249]. Considering the quality characteristic, the "larger the better"  $S/N$  is selected to obtain the optimum quality characteristic, since it is desired to obtain the maximum heat transfer over the target surface. The conversion of the experimental data in a single  $S/N$  ratio is possible through the calculation of the mean square deviation [245], expressed by the term in brackets in Eq. (79), which statistically quantifies the deviation from the target value. According to [243], the "larger the better"  $S/N$  can be determined using Eq. (79), in which, the inverse of each large value becomes a small value and the unstated target is zero.

$$S/N = -10 \log \left( \frac{1}{n} \sum_{i=1}^n \frac{1}{Y_i^2} \right) \quad (79)$$

where  $S/N$  is the signal to noise ratio for each test or combination given by a matrix row;  $n$ , is the number of repetitions of each combination; and  $Y_i$  is the quality characteristic measured in each experiment [245]. In this case, as previously mentioned,  $Y_i$  represents the Nusselt number.

### 6.1.2. Noise factor and test conditions

Temperature and humidity are two factors that vary over the course of the experiments, being difficult to control in the laboratory. The temperature is adjusted by using an air conditioning system. However, it is difficult to ensure a variation within 1 °C throughout the day. This makes it difficult to warrant that these parameters are constant throughout each experiment, a problem that also occurs in industrial

facilities. In that sense, temperature and humidity are considered noise factors, i.e., they are uncontrollable parameters that can interfere with the performance of the system.

To obtain robust conclusions, three repetitions of each experiment are conducted, with different levels and noise factors. In addition, the ambient humidity and temperature values are recorded using a weather station (W.155 Weather station from Ventus, Denmark) with a resolution of 0.1 °C for temperature and 1 % for humidity.

Even if the air humidity is important to fully characterize the impinging flow, for the conditions of this study, its effect can be neglected since the jets impinge on a hot surface. However, this parameter could be relevant if the reverse condition was analyzed, a hot jet impinging a plate at ambient temperature since moisture condensation could occur at the vicinity of the plate giving erroneous heat transfer coefficients.

### 6.1.3. Control factors and levels

The fourteen variables that influence the heat transfer of a multiple jet impingement have been identified in the previous section. However, the analysis of each parameter is too costly, due to the high number of possible combinations, considering that each factor has two or more levels. In that sense, the control factors selected consist of the ones that are known to have a major effect on heat transfer performance, and which are in accordance with the objective of this work - the study of convection from multiple jets over a complex moving surface. From the careful analysis, the control factors and respective levels tested in this work are summarized in Table 20, as well as the degrees of freedom (DoF).

Table 20. Selected factors and their levels.

Control Factor	Level				DoF
	1	2	3	4	
Jet-to-jet spacing (A)	2 <i>D</i>	3 <i>D</i>	4 <i>D</i>	6 <i>D</i>	3
Nozzle-to-plate distance (B)	2 <i>D</i>	3 <i>D</i>	5 <i>D</i>	7 <i>D</i>	3
Jets pattern (C)	Inline	Staggered			1
Plate geometry (D)	Flat	Non-Flat	-	-	1
Reynolds number (E)	2,000	5,000	-	-	1

Two jets configurations are analyzed, inline and staggered. The streamwise pitch ( $S_x$ ) and the spanwise pitch ( $S_y$ ) are the same,  $S_x = S_y = S$ , and four levels are considered 2 *D*, 3 *D*, 4 *D*, and 6 *D*. The distance

between the target and the nozzle plate varies between  $2D$ ,  $3D$ ,  $5D$ , and  $7D$ . Regarding the plate geometry, two configurations are investigated, the flat plate and the non-flat plate which consists of a surface with a step. The Reynolds number varies between 2,000 and 5,000.

According to Table 20, it is possible to conclude that this study focuses on the analysis of two control factors with four levels and three control factors with two levels. If Taguchi's method was not applied in this study, the number of experiments would reach a total of 768, i.e.,  $4^2 \times 2^3$  combinations  $\times$  3 repetitions  $\times$  2 scenarios. With the selection of an appropriate orthogonal array (OA), this number is highly reduced, as described in the following section.

The DoF, defined by Taguchi [243] as the number of levels minus one, is used to select the OA and expressed in Table 20. Each parameter is assigned with a letter from A to E, which represents each column of the OA.

#### 6.1.4. Selection of the Orthogonal Array

The selection of the OA is an important step of Taguchi's method. To conduct the study with accuracy, the number of DoF must be computed, i.e., the number of trials minus one, and an OA with the same or more DoF must be selected. Looking at the orthogonal arrays proposed by Taguchi's model, the  $L_{16}$  seems to be the most appropriate since it is the smallest OA, allowing to study the previously defined factors and levels, but also because it allows a mix between 2 and 4 levels.

The OA is created using the Minitab™ software which is designed to perform the necessary statistical functions [59]. Table 21 presents the  $L_{16}$  OA generated by Minitab™. According to [247, 248], trials should be repeated to confirm the data obtained, to reveal the influence of the noise factors, and to analyze the variance around a target value [250]. As mentioned previously, temperature and humidity are noise factors that can affect the measurements. In that sense, each experimental condition is repeated three times. With this repetition number, an uncertainty analysis of the measurements for a confidence level equal to 95 % can be conducted [169]. The OA presents the experiments that must be conducted to analyze the influence of the design parameters on the heat transfer performance. From the analysis of the results, three main conclusions can be obtained [245]: (1) response of the quality characteristic to the variation of the control factors; (2) ANOVA Test which gives a percentage contribution of each factor; (3) Estimation of the optimum result.

The DoE expressed in Table 21 is conducted twice, with the plate in motion and static. Considering that 16 experiments are conducted and repeated three times for each scenario, the total number of experiments amounts to 96. This shows the great advantage of Taguchi's method compared to the full

factorial technique (768) since it is possible to reduce the total number of trials eight times. The results are analyzed and compared to understand if the contribution of each factor is the same for both cases.

**Table 21.** Design Orthogonal Array generated using Minitab™.

Experiment	A	B	C	D	E
1	2 <i>D</i>	2 <i>D</i>	Inline	Flat	2,000
2	2 <i>D</i>	3 <i>D</i>	Inline	Flat	2,000
3	2 <i>D</i>	5 <i>D</i>	Staggered	Non-Flat	5,000
4	2 <i>D</i>	7 <i>D</i>	Staggered	Non-Flat	5,000
5	3 <i>D</i>	2 <i>D</i>	Inline	Non-Flat	5,000
6	3 <i>D</i>	3 <i>D</i>	Inline	Non-Flat	5,000
7	3 <i>D</i>	5 <i>D</i>	Staggered	Flat	2,000
8	3 <i>D</i>	7 <i>D</i>	Staggered	Flat	2,000
9	4 <i>D</i>	2 <i>D</i>	Staggered	Flat	5,000
10	4 <i>D</i>	3 <i>D</i>	Staggered	Flat	5,000
11	4 <i>D</i>	5 <i>D</i>	Inline	Non-Flat	2,000
12	4 <i>D</i>	7 <i>D</i>	Inline	Non-Flat	2,000
13	6 <i>D</i>	2 <i>D</i>	Staggered	Non-Flat	2,000
14	6 <i>D</i>	3 <i>D</i>	Staggered	Non-Flat	2,000
15	6 <i>D</i>	5 <i>D</i>	Inline	Flat	5,000
16	6 <i>D</i>	7 <i>D</i>	Inline	Flat	5,000

## 6.2. Results and Discussion

In this section, the experimental results obtained from the heat transfer measurements are presented. The average Nusselt number is converted into a  $S/N$  in order to perform a main-effect and ANOVA analysis. The effect of the process variables on heat transfer and jets flow dynamics are discussed based on the PIV measurements. The control factors that optimize the heat transfer efficiency over the impinging plate are then determined.

### 6.2.1. Average Nusselt Number

The results collected in each experiment are analyzed and an uncertainty estimation is conducted based on the concepts presented in section 3.2.5. The average Nusselt numbers obtained and their respective total uncertainty are presented in Table 22 for both static and moving plate experiments.

**Table 22.** Nusselt number obtained from the static and moving plate experiments.

Experiment number	Average $\overline{Nu} \pm u_{Nu}$	
	Static Plate	Moving Plate
1	18.8(0) $\pm$ 0.27	19.7(1) $\pm$ 0.34
2	19.3(6) $\pm$ 0.28	20.3(3) $\pm$ 0.45
3	29.1(3) $\pm$ 0.42	30.8(0) $\pm$ 0.73
4	22.6(8) $\pm$ 0.33	23.9(3) $\pm$ 0.60
5	33.9(3) $\pm$ 0.49	35.5(6) $\pm$ 1.66
6	33.5(4) $\pm$ 0.49	35.2(7) $\pm$ 1.25
7	16.4(5) $\pm$ 0.24	17.1(6) $\pm$ 0.52
8	15.7(9) $\pm$ 0.23	16.8(8) $\pm$ 0.58
9	33.4(6) $\pm$ 0.48	35.0(3) $\pm$ 0.60
10	26.1(3) $\pm$ 0.38	27.1(3) $\pm$ 0.74
11	13.8(0) $\pm$ 0.20	14.7(4) $\pm$ 0.48
12	13.0(8) $\pm$ 0.19	13.6(5) $\pm$ 0.31
13	16.3(1) $\pm$ 0.24	16.8(9) $\pm$ 0.52
14	15.8(7) $\pm$ 0.26	16.6(5) $\pm$ 0.30
15	18.5(4) $\pm$ 0.27	19.6(6) $\pm$ 0.53
16	18.2(5) $\pm$ 0.26	19.0(7) $\pm$ 0.53

As it can be observed in Table 22, the uncertainty related to the average Nusselt number, expressed in percentage, is around 1.5 % for the static plate case, which is in accordance with [43, 60, 90, 251, 252]. An increase of the uncertainty is observed for the case of the moving plate, which can be explained by the increasing flow complexity, with values ranging up to around 3.5 %. The results demonstrate that for a Reynolds number near to 2,000, the Nusselt number varies between 20 and 13, depending on the level applied for each variable, while for  $Re = 5,000$ , it lies between 18 and 34. To validate the accuracy of these results, they are compared with average Nusselt number values obtained from correlations

presented by Florschuetz et al. [48], Huber & Viskanta [67] and Kercher & Tabakoff [118] for the static plate case and Chitsazan & Glamacher [111] for the moving plate.

The measured ( $\overline{Nu}_e$ ) versus predicted ( $\overline{Nu}_{pre}$ ) Nusselt number values are plotted in Figure 82 and Figure 83. As it can be observed, for the static plate case, Florschuetz et al. [48] correlation fits the experimental data, while the others present a greater deviation. Regarding the moving plate case, the measurements are clustered along the diagonal line and the major deviations are detected for higher Nusselt number values. Overall, it can be concluded that the present measurements are in good agreement with the available correlations. However, as the Nusselt number increases, the difference between measured and predicted values increases for both static and moving plate cases.

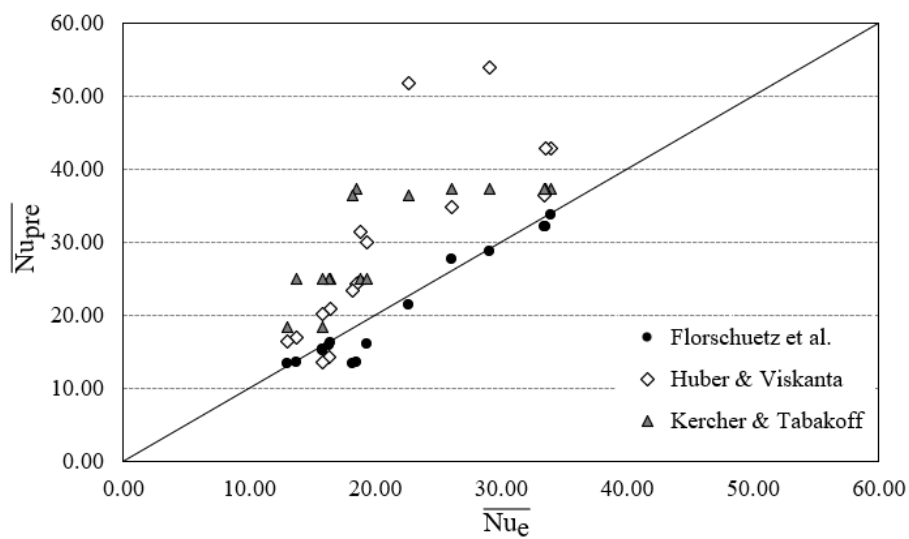


**Figure 82.** Predicted vs measured Nusselt numbers for a static plate case.

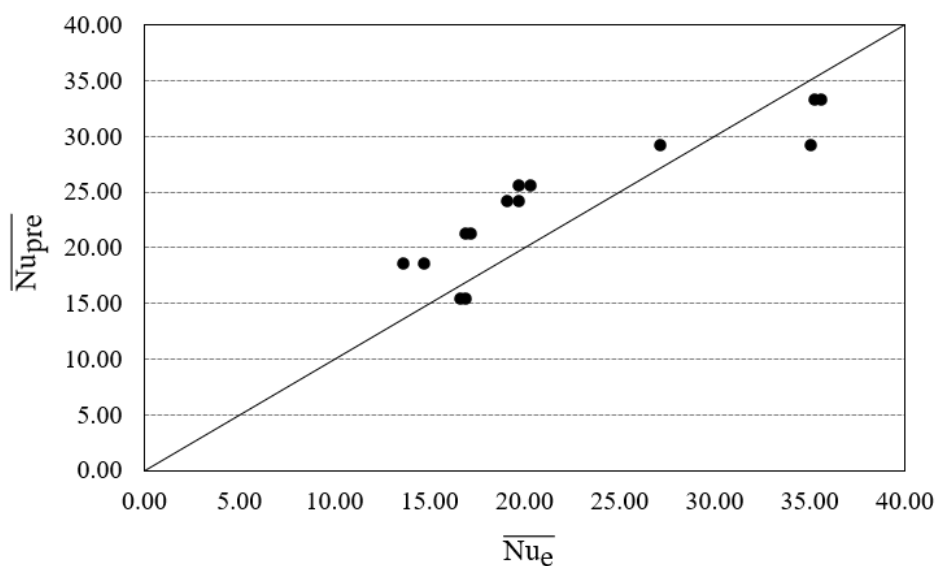


**Figure 83.** Predicted vs measured Nusselt numbers for a moving plate case.

Looking at the average heat transfer measured by the heat flux sensor and expressed by the corresponding Nusselt number in Table 22, measurements show that higher values are recorded for higher Reynolds numbers and lower nozzle-to-plate distances. These results are in agreement with [45], [7] and [90] and demonstrate that, regardless of the geometry of the target plate, a ratio  $H = 2 D$  increases the heat transfer over the surface. In addition, the motion of the target plate shows an increase of the heat transfer of around 5 %, which is explained by strong shear layer regions generated in direction of the plate motion. Compared with the static plate, a modification of the boundary layer is expected, increasing the heat transfer rates, as also explained by [107]. Conversely, lower Nusselt numbers are obtained for higher jet-to-jet spacing and nozzle-to-plate distances, and lower Reynolds numbers for both static and moving cases.

Focusing on the results, it seems that the experiment that allows the higher average heat transfer rate is test 5, with  $S = 3 D$ ,  $H = 2 D$ , and  $Re = 5,000$  for an inline configuration and a non-flat plate. While the worst case is test 12, with  $S = 4 D$ ,  $H = 7 D$ , and  $Re = 2,000$  for an inline configuration and a non-flat plate geometry. From these results, it may be concluded that the jet-to-jet spacing, nozzle-to-plate distance, and Reynolds number play an important role in heat transfer performance, while the effect of the jet pattern and plate geometry seems to be weaker when compared with these three variables. The analysis of the effect of the control factor on heat transfer efficiency is conducted with detail in the next two sections.

## 6.2.2. Design Analysis of Experimental Results

As previously mentioned, Taguchi's method uses a loss function which is transformed into a signal-to-noise ratio ( $S/N$ ) [80]. The great advantage of the  $S/N$  analysis instead of averaged values is mainly because it provides both proximity of the average value to the target and variability around that target. In that sense, Nusselt numbers were converted into  $S/N$  ratios. Since higher Nusselt numbers indicate a better performance of the multiple jet impingement system, the "larger the better" case is implemented, meaning that optimum parameter levels correspond to the highest  $S/N$  ratios. Using Eq. (79), previously presented,  $S/N$  are determined for each experiment and plotted in Figure 84 and Figure 85, for static and moving plate cases, respectively. The data analysis is conducted using Minitab™ software.

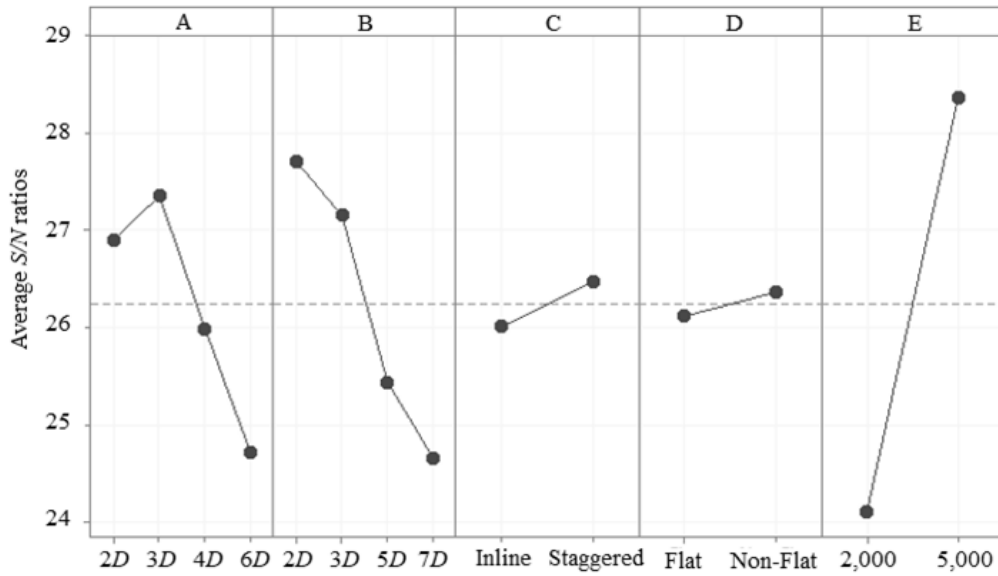


**Figure 84.** Effects of design parameters on Nusselt number for the static plate case.

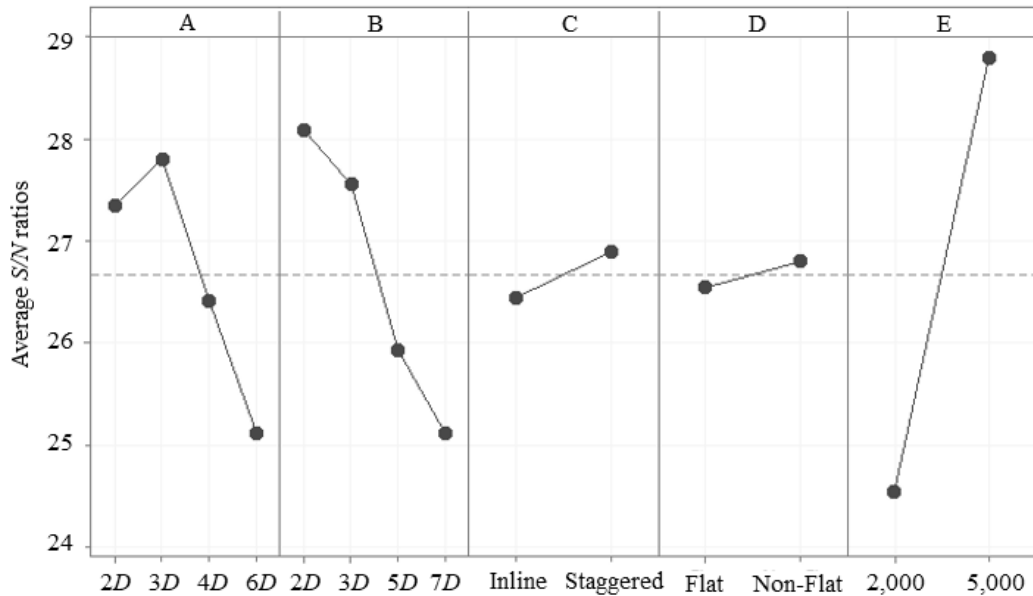


**Figure 85.** Effects of design parameters on Nusselt number for the moving plate case.

Through the analysis of the average  $S/N$  ratios presented in Figure 84 and Figure 85, the optimum factor levels are determined. The first conclusion highlighted by the results is that the moving plate case presents slightly higher  $S/N$  ratios when compared with the static plate, showing that the average heat transfer rate is enhanced by the motion. Regarding the influence of each factor on heat transfer, the results present a similar variation in both cases.

### a) Effect of the jet-to-jet spacing

Starting with the jet-to-jet spacing factor, it is clear that the Nusselt number varies inversely with  $S$ . However, a peak is identified at  $S = 3 D$ , this effect was also observed experimentally by [7]. At  $S = 2 D$ , strong interactions occur, the jet's flow deflects prior to the impingement and weakens the normal penetration of the jets, reducing the heat transfer, and this is observed in Figure 86 (a). When  $S = 3 D$ , the increase of the Nusselt number shows that the interaction between jets prior to the impingement is lower compared with  $S = 2 D$ , allowing the wall jet to develop, leading to an increase of the average heat transfer. Even if the cases presented in Figure 86 are not exactly in the same conditions, the velocity field measurements presented in Figure 86 (b) show that at  $S = 3 D$ , strong vortices are induced between each jet, mainly due to the collision between the wall jets. These vortices increase the turbulence in the vicinity of the target plate and promote heat transfer. However, looking at the flow development for  $S = 2 D$ , Figure 86 (a), the interference between two adjacent jets, upstream the impingement, is very strong, weakening the jet's strength and restricting the flow development over the wall, as also observed by [29, 62]. In addition, the intensification of the jet-induced crossflow for low  $S/D$  is also identified, especially for  $S = 2 D$ . As the remaining part of the spent fluid leaves the control volume, an asymmetric jet flow field is observed, being stronger for the jets located near the outlet. This effect, if too strong, can reduce the heat transfer over the target plate.

As the jet-to-jet spacing increases,  $S = 4 D$  and  $6 D$ , less effective surface coverage is observed, leading to a decrease in local and average heat transfer, as clearly presented in Figure 86 (c) and Figure 86 (d). As expected, a large distance between jets reduces the interaction between the wall jets and weakens the jets induced crossflow, reducing the average Nusselt number. This effect was also identified by [38, 63].

In that sense, level 2 ( $S = 3 D$ ) is the optimal value for both static and moving plate cases. The improvement of the heat transfer over the target plate observed for low  $S$  values is in agreement with other studies [7, 27, 45, 48, 55, 56]

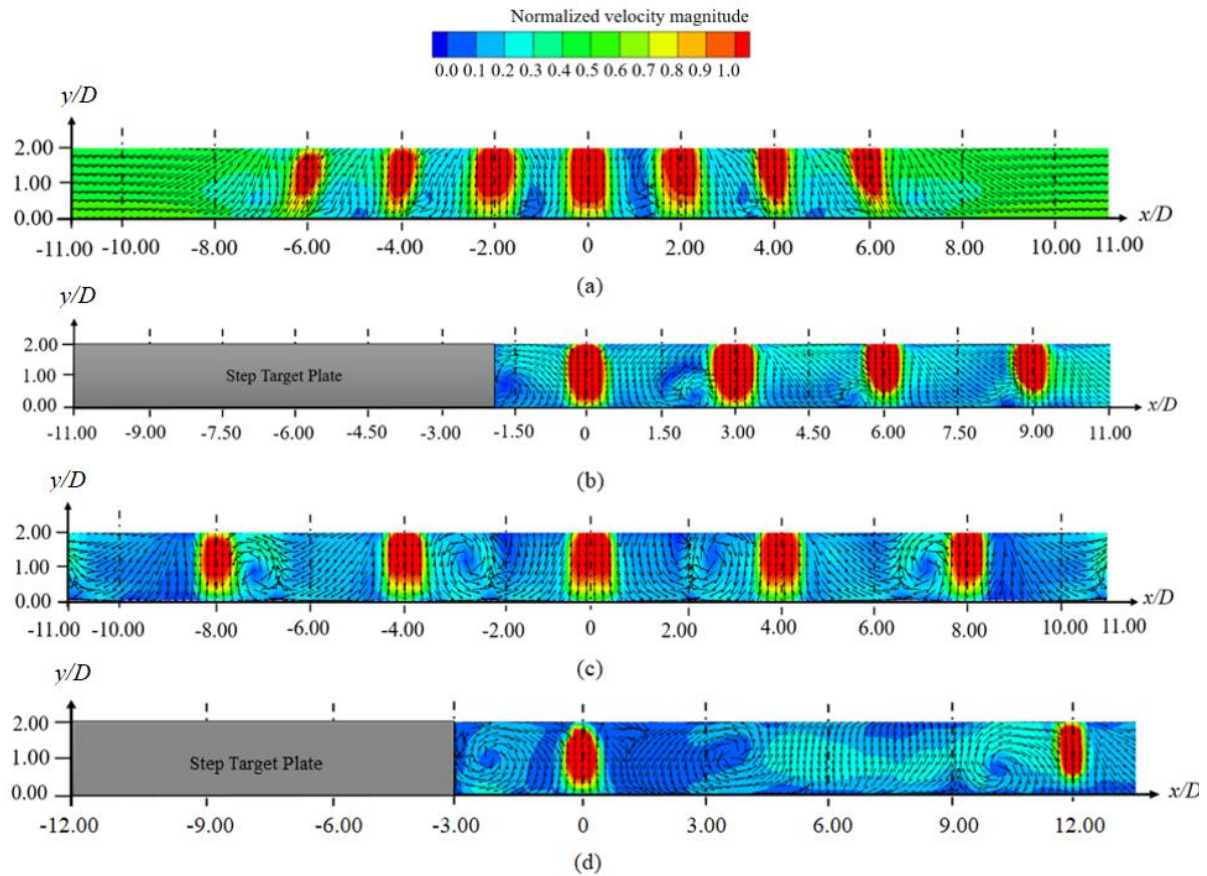


**Figure 86.** Jet's velocity field for different jet-to-jet spacing: (a)  $S/D = 2$ ; (b)  $S/D = 3$ ; (c)  $S/D = 4$ ; (d)  $S/D = 6$ .

### b) Effect of the nozzle-to-plate spacing

Looking at the influence of the nozzle-to-plate distances,  $H = 2 D$  (level 1), presents the best results compared with the other cases, followed by  $H = 3 D$ . However, larger distances ( $H = 5 D$  and  $7 D$ ) show a sharp decrease in heat transfer performance. These results confirm that the higher the distance of the nozzles from the target plate, the lower the Nusselt number, as supported by [29, 33, 75, 253–256]. An optimized value of  $H/D = 2$  was also obtained numerically and experimentally by [28, 29, 45, 78–80]. This enhanced efficiency is enlightened by the generation of strong vortices in a confined space, while larger distances increase the mixing between jets flow and the surrounding air prior to the impingement, decreasing the heat transfer over the target surface.

This study is in agreement with the analysis presented in chapter 5, section 5.3 – Influence of the nozzle-to-plate distance on an isothermal single jet in a transition regime, in which it was concluded that highly confined spaces ( $H/D = 2$ ) induce a stronger interaction between the surrounding air and the vortices generated by the jet impingement, leading to higher velocities at the vicinity of the wall. Moreover,

as  $H/D$  increases, the potential core length decreases, the jets lose momentum as they approach the target plate, reducing the turbulence intensity and consequently the heat transfer over the target plate. To support these conclusions, the velocity fields for different  $H/D$  for the optimized value  $S/D = 3$  are plotted and presented in Figure 87.

First, it is clear that, compared with a single jet (section 5.3), the effect of  $H/D$  on multiple jets is intensified. The interference between jets, due to shear layer growth from the nozzle inlet to the target plate and wall jets collision in the vicinity of the plate, promotes the flow mixing and this effect is intensified in confined spaces, i.e., low  $H/D$ . In addition, reduced  $H/D$  leads to thicker wall jets induced by stronger interactions between jets and the surrounding air in the confined space. Moreover, the jet's momentum is preserved from the nozzle inlet to the target plate, due to the uniform velocity profile in the jet's potential core, which increases the flow turbulence, as observed in Figure 87 (a) and Figure 87 (b) and supported by [29]. As  $H/D$  increases, larger but weaker primary vortices are generated, as identified in Figure 87 (c) and Figure 87 (d). These vortices interfere with the flow development of the adjacent jets, weakening the jet's momentum and reducing the heat transfer in the vicinity of the target surface. This effect is more pronounced for  $H = 7 D$  than  $H = 5 D$ . Moreover, the velocity field shows that the central jet is less affected by the adjacent jets, and a longer potential core is identified compared with the adjacent jets. The increased turbulence intensity due to the staggered configuration is also observed between the central and adjacent jets.

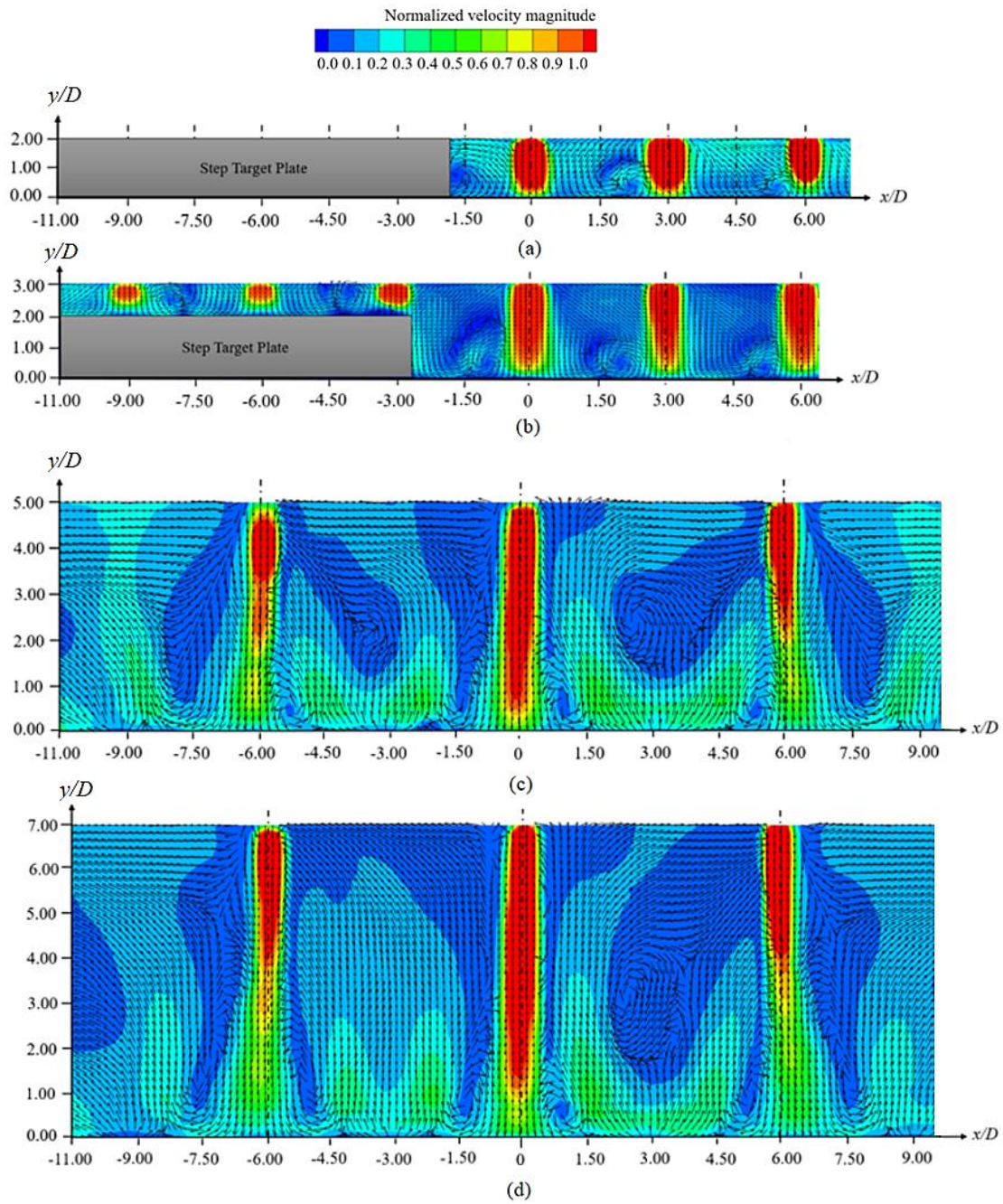


**Figure 87.** Jet's velocity field for different nozzle-to-plate distances: (a)  $H/D = 2$ ; (b)  $H/D = 3$ ; (c)  $H/D = 5$ ; (d)  $H/D = 7$ .

From this analysis, it can be concluded that, independently of the other process variable,  $H/D = 2$  always increases the heat transfer over the impinging surface. The velocity fields obtained by PIV measurements corroborate this conclusion and show that even for a flat plate or a step plate, low nozzle-to-plate distances always enhance the heat transfer. These observations are in agreement with [43] and [76].

### c) Effect of the jet pattern

Regarding the jet pattern, results indicate that the heat transfer over the target surface is slightly enhanced by the staggered configuration compared with the inline array. This observation is in agreement with [7] and [50]. It seems that combining the staggered configuration with the confinement induces stronger interference of upstream jet-induced crossflow on downstream jets, slightly increasing the heat transfer over the impinging surface. However, as presented by [31], higher Reynolds numbers increase the difference between the effects of inline and staggered arrangements in heat transfer.

To support these conclusions and considering that  $S/D = 3$  and  $H/D = 2$ , the PIV measurements for test 5 with and without motion are compared. In addition, another test is conducted in the same conditions but for a staggered configuration instead of an inline one. The results are presented in Figure 88. As it can be observed in Figure 88 (b), the influence of the jets located on the back and front rows highly influence the flow of the central row, the one which is measured. The upwash flow, due to wall jets collisions is clearly identified near the step and between jets, inducing a flow acceleration, which is expected to increase the heat transfer in the vicinity of the target plate. Therefore, considering the measurement zone of the heat flux sensor (near the step), an increase in the average heat transfer is expected when compared with an inline configuration. In inline arrays, Figure 88 (a), the downstream jets seem to be protected by upstream jets, and the effect of the crossflow is reduced, yielding a reduction of the heat transfer rate. From this analysis, it seems that combining the staggered configuration with the confinement induces stronger interference of upstream jet-induced crossflow on downstream jets, enhances the flow mixing, and increases the flow velocity near the target plate mainly due to the recirculation region. Therefore, the heat transfer over the impinging surface is expected to increase slightly. This effect was also demonstrated numerically by [52] and is in agreement with [7, 50, 51].

Comparing the static and the dynamic cases, it seems that the effect of the jet pattern is slightly more evident for the static plate than for the moving plate, proving that the shear-driven flow generated over the surface, due to the plate motion, takes control of the flow and thermal fields, which in accordance with Achari & Das [107]. In conclusion, considering the conditions of the experiments conducted in this study, level 2 of the jet pattern factor optimizes the heat transfer over the target plate.

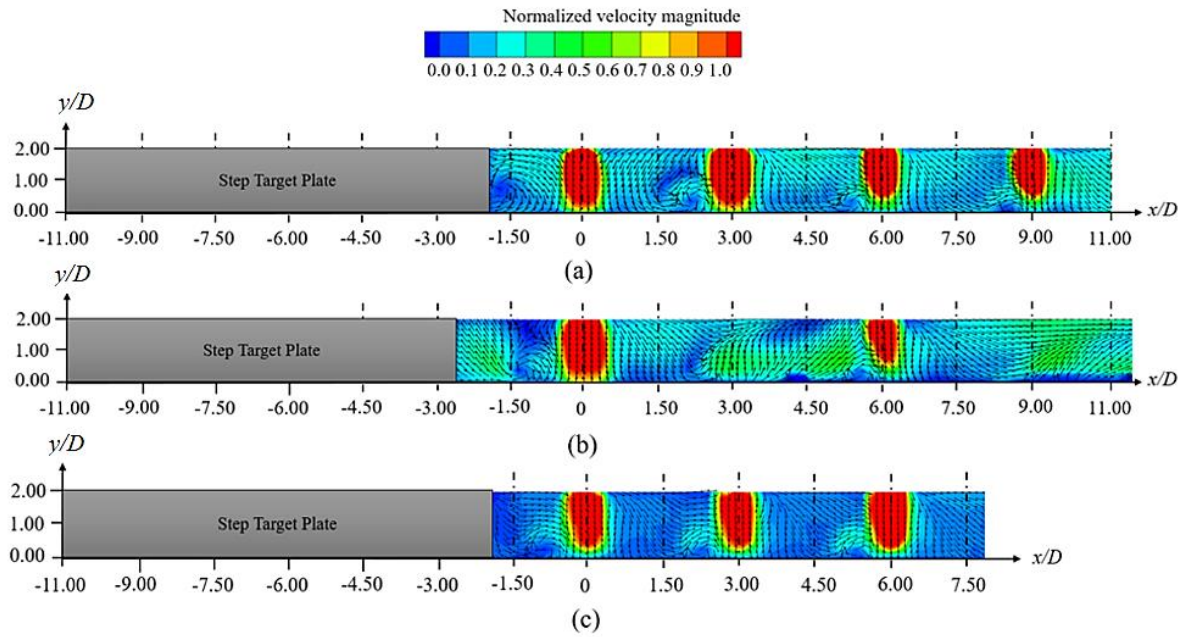


**Figure 88.** Jet's velocity field at  $S/D = 3$ ,  $H/D = 2$  for different jet patterns: (a) Inline; (b) Staggered; (c) Inline with motion.

#### d) Effect of plate geometry

Average  $S/N$  ratios presented in Figure 84 and Figure 85 demonstrated that a non-flat plate (plate geometry level 2) slightly increases the average heat transfer in both static and moving plates. Including a step over the target leads to a deflection of the jet's flow near the step, as it can be observed in Figure 89. In addition, the flow reversal induced by the step increases the Nusselt number, which is in agreement with [257]. This factor plays an important role in heat transfer. The wall jet induced by the central jet is blocked by the step, leading to a flow reversal. In addition, the step deflects the flow from the adjacent jets located just above the step. The combination of these two effects increases the flow turbulence and affects the central jet flow. The vortex induced on the left-hand side of the central jet deflects the central jet flow and the stagnation point is moved to the right in the plate motion direction. Even if the primary structure of the central jet is affected, the vortex promotes the mixing which may enhance the heat transfer at the stagnation point [54]. Over the step, the fountain flow generated at  $x/D = -6$  occurs exactly in the midpoint between the two adjacent jets. Looking at the wall jet developed by the jet located at  $x/D = -4$ , it is observed a strong deflection of the flow due to the step corner, which induces an acceleration of the flow and intensifies the magnitude of the vortices. Comparing Figure 89 (a) with Figure 89 (b), it seems that lower  $H/D$  increases the flow turbulence over and at the bottom of the step, as expected. Another interesting phenomenon identified when the step and flat plates are compared is the crossflow

development. While Figure 89 (c) shows that the flow follows an axial direction at the central jet and then starts to disperse radially towards the outlets, in a non-flat plate, this flow development is limited by the step. Moreover, Figure 89 (c) confirms that the maximum crossflow, induced by the total opening of the measurement region, is strong. While two uniform vortices are generated on both sides of the central jet, the vortices at the adjacent jets are pushed towards the outlets. This effect increases the heat transfer near the jet's stagnation points.

However, more studies regarding the dynamics of the flow are needed to understand the effect of the step on the jet's structure. Furthermore, steps with different heights must be analyzed since this parameter plays an important role in the jet's flow development over the target plate [258]. This analysis is presented in section 6.3 for the optimized multiple jet impingement configuration.

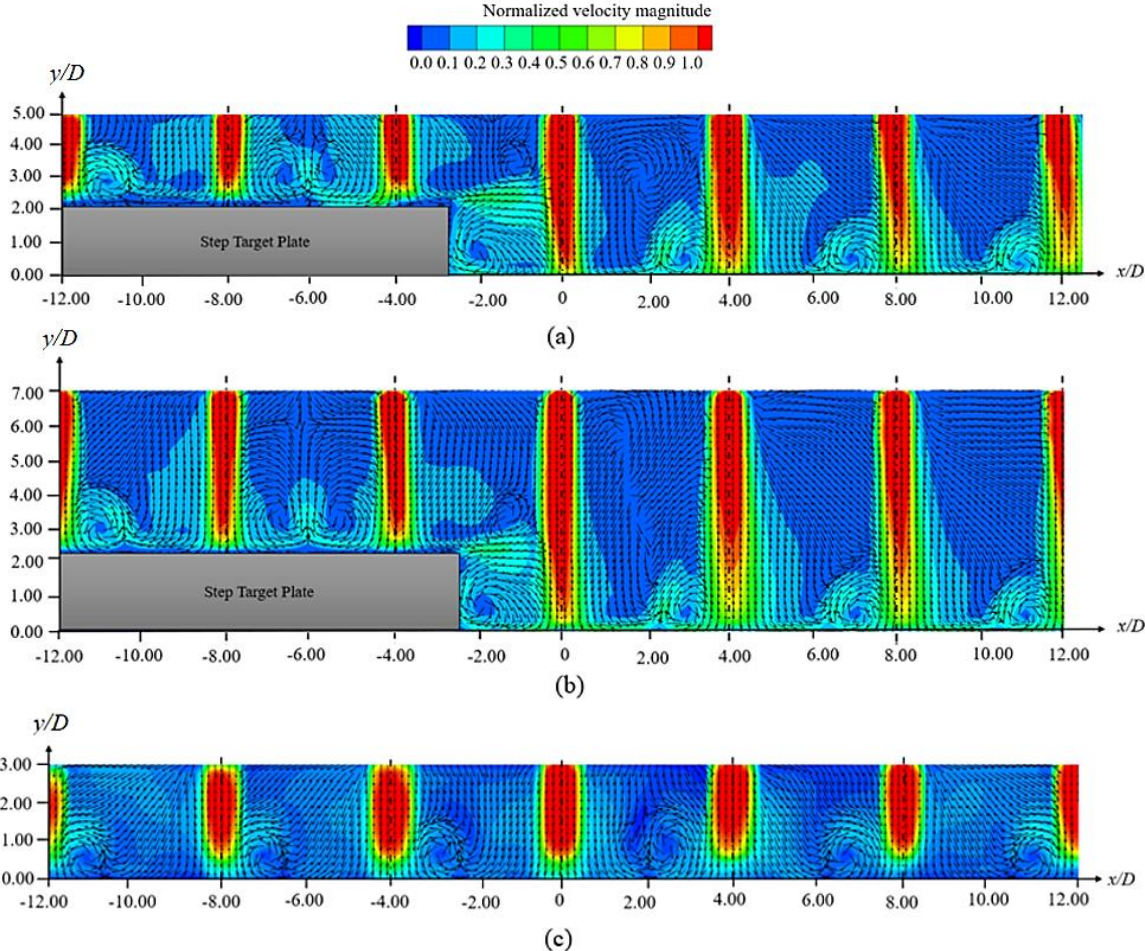


**Figure 89.** Jet's velocity profile for  $S/D = 4$  for different plate geometry: (a) Step plate  $H/D = 5$ ; (b) Step plate  $H/D = 7$ ; (c) Flat plate  $H/D = 3$ .

### e) Effect of the Reynolds number

Finally, the Reynolds number is the factor that mostly affects the heat transfer performance of a multiple jet impingement system. As expected, the higher the Reynolds number the greater the Nusselt number [59, 79, 80], meaning that level 2 is the optimized parameter. High  $Re$  increases the flow turbulence which promotes the mixing between the jet's flow and the surrounding air, increasing the heat transfer. However, the heat transfer measurements show that  $S/D$  and  $H/D$  control factors also play an important role, since tests 1 and 2 present a higher average Nusselt number than tests 15 and 16. These results demonstrate that to increase the heat transfer over the target plate, it is necessary to find the best combination between  $Re$ ,  $S/D$ , and  $H/D$  and do not only implement an increase in Reynolds number.

It is clear that, for the same conditions, the higher the Reynolds number, the higher the local and average heat transfer over the target plate. However, depending on the process conditions, it can be more convenient to find the best compromise between the  $Re$ ,  $S/D$ , and  $H/D$ . As presented in Figure 90, although test 15, Figure 90 (b), presents a higher  $Re$  than test 1, Figure 90 (a), the high confinement allied with a reduced space between jets induces a strong turbulence intensity of the flow which increases the heat transfer.

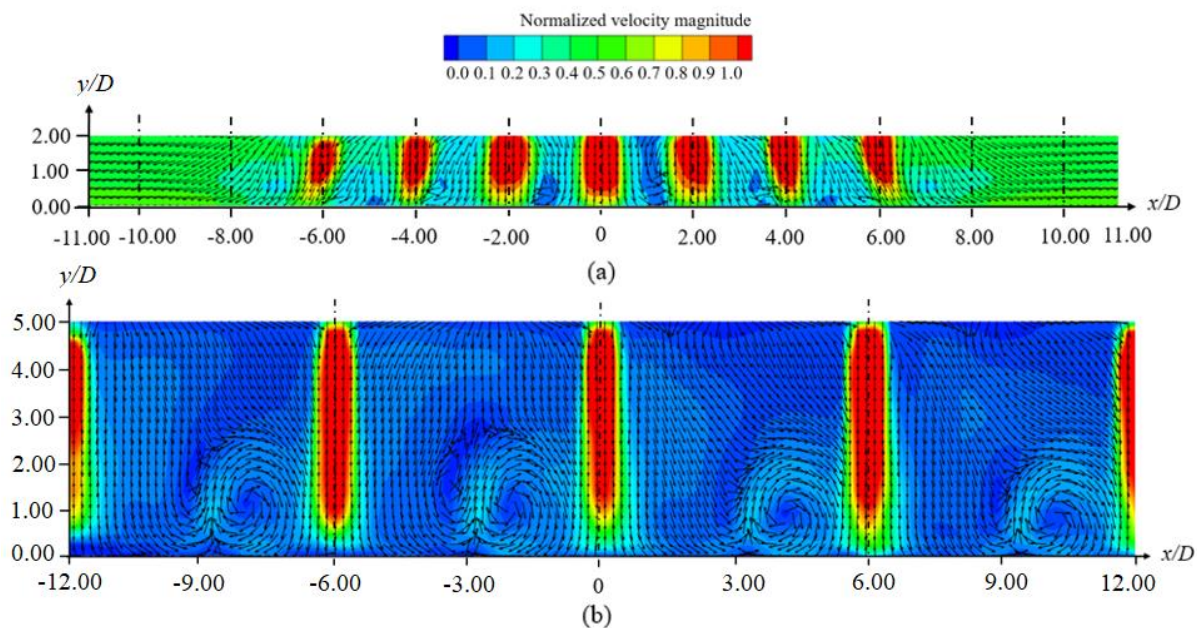


**Figure 90.** Jet's velocity profile for different Reynolds numbers: (a) Test 1 -  $Re = 2,000$ ,  $S/D = 2$ ,  $H/D = 2$ ; (b) Test 15 -  $Re = 5,000$ ,  $S/D = 6$ ,  $H/D = 5$ .

### g) Effect of plate motion

From the results presented in this section, the main-effect plots show that the effect of the control factors analyzed is the same for both static and moving plates. However, heat transfer measurements presented an increase of this value compared with the static plate, which can vary between 3 and 6 %.

To analyze with higher detail the effect of the plate motion, the results of a dynamic and a static plate are compared. For this analysis, two tests are selected, Test 11 and Test 9. Test 11 presents an inline configuration with jets spaced  $S/D = 4$  that allows the flow to develop through the domain with lower jet interaction, giving space to the primary vortices to develop throughout the wall. In addition, medium confinement ( $H/D = 5$ ) and a jet flow in the transition regime are selected ( $Re = 2,000$ ). These factor levels decrease the effect of the crossflow, emphasizing the effect of the plate motion, and since the jet's impingement is still in the length of the potential core, the jet's momentum weakening is minimal. Moreover, a non-flat plate is selected to analyze the effect of the step, combined with movement, on the vortices. In contrast, test 9, occurs at a completely confined space ( $H/D = 2$ ), the jets are fully turbulent ( $Re = 5,000$ ) and the plate is flat. The jet's pattern is inline and the jet-to-jet spacing is equal to 4 as test 11, to allow the analysis of the flow development between jets. To conduct this analysis, streamlines are plotted instead of vectors, to observe more clearly the vortices development over the target plate.

The results presented in Figure 91 show the streamlines development over the domain for test 11 with a static plate, Figure 91 (a), and a dynamic plate, Figure 91 (b). To improve the analysis of the plate in motion, different times are considered from  $t = 0$  s to  $t = 7.5$  s. As identified in Figure 91 (a), a strong vortex is induced in the vicinity of the step, while a smaller vortex is detected just above it due to the interaction between the jets that impinges the step, located at  $x/D = -8$  and  $x/D = -4$ , and the step corner. As previously mentioned, the step limits the uniform dissipation of the flow through the outlets since the step blocks the flow induced by the wall jet developed at the left-hand side of the central jet. With the motion this effect is intensified, therefore an increase of the heat transfer is expected in this region. The streamlines indicate that the magnitude of the vortices increases as the plate moves from the left to the right compared with the static plate. As depicted in Figure 91 (b), the step pushes the flow in direction of the motion, increasing the interaction of the upstream jet's flow with the downstream jets. This leads to a slight deflection of the jets in direction of the motion and, consequently, to a deviation of the stagnation points. Moreover, the potential core of the central jet is reduced compared with the adjacent jets due to the reversal flow induced by the step. Looking at the boundary layer development at the vicinity of the target plate, the results show that higher velocities are observed in Figure 91 (b) compared with Figure 91 (a). The same is observed for the shear layer development in the vicinity of the

jet axis, from the nozzle to the target plate. The plate motion increases the turbulence of the overall flow, promoting the mixing between the surrounding air and the jets.

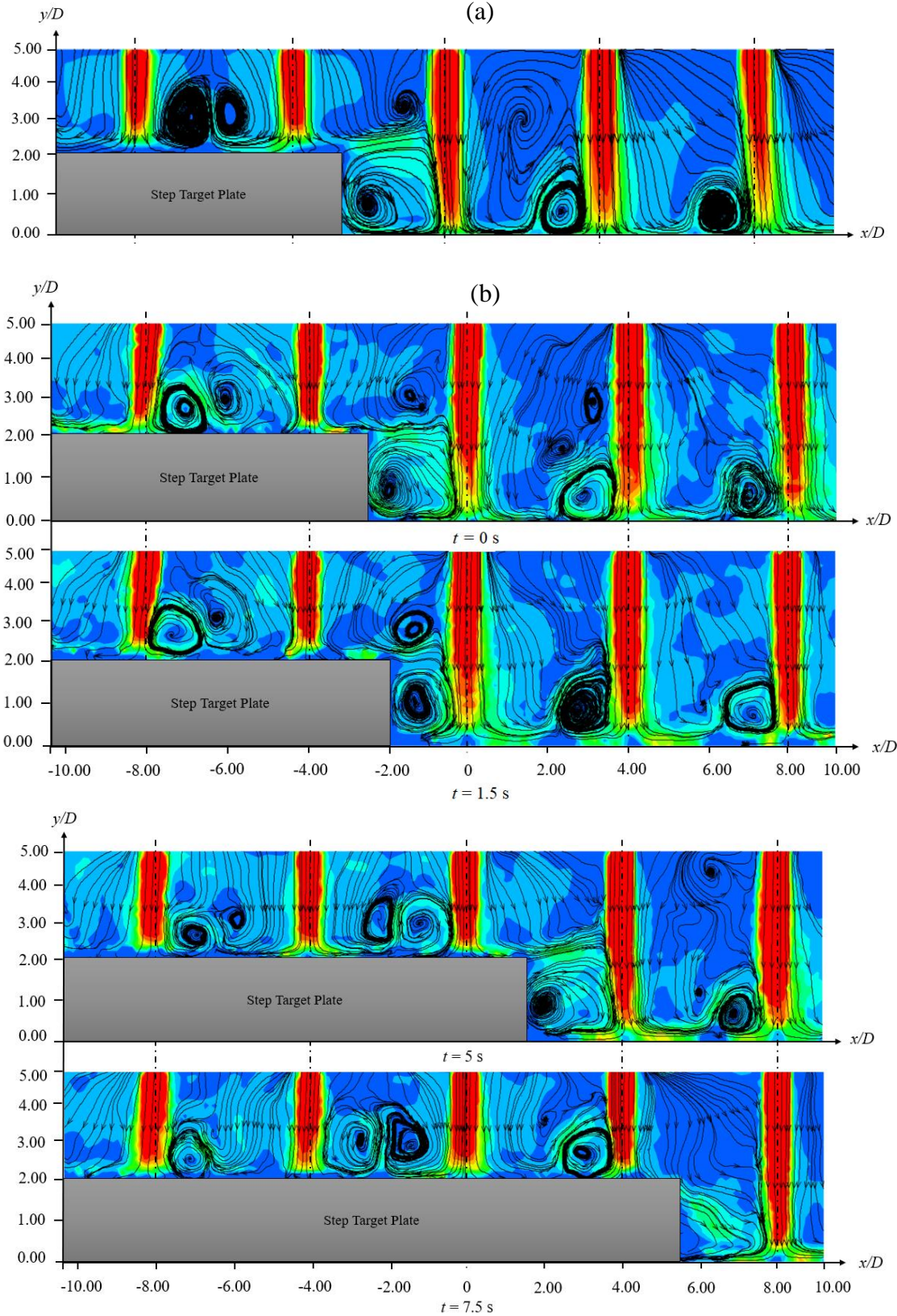


Figure 91. Test 11: (a) Static plate; (b) Dynamic plate:  $t = 0$  s;  $t = 1.5$  s;  $t = 5$  s;  $t = 7.5$  s;

The streamlines obtained in test 9 (Figure 92) demonstrate that the difference between the velocity field obtained in the dynamic and static plates is lower compared with test 11. The vortices induced on the right end side of the central jet seem to be slightly stronger in the dynamic case. These results show that, since the plate velocity implemented in this study is low, the effect of the plate motion on the jet's flow dynamics is more evident in a domain where the crossflow is weaker. In addition, it is clear that the step surface plays an important role since it pushes the flow in direction of the plate motion, which is not the case in test 9.

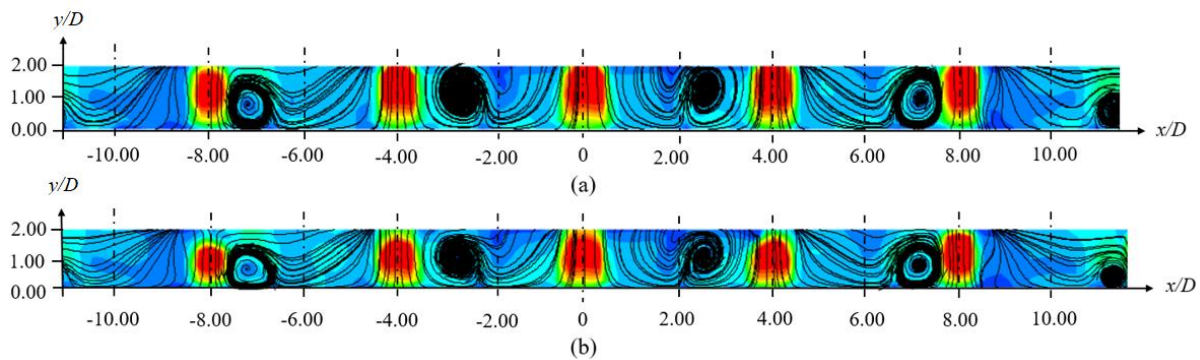


Figure 92. Test 9: (a) dynamic plate; (b) static plate.

### 6.2.3. Analysis of Variance (ANOVA)

The analysis of variance (ANOVA) is a statistical tool that enables a deeper understanding of the design parameters on the Nusselt number. This method allows to determine the relative influence of a design parameter (on a percent basis) and to separate the significant from those negligible [245]. The methodology and equations used by ANOVA are clearly expressed [80, 245]

Table 23 and Table 24 present the results obtained from ANOVA for both static and moving plate cases, respectively. The tables present the degrees of freedom (DoF) of the experiments, the sequential sum of squares ( $SS$ ) which indicates the variation of the data for different factors, the variance ( $V$ ), the variance ratio ( $F$ ), and the percentual contribution. The DoF of error is given by the difference between the total number of observations minus one and the number of factor levels minus one [245]. In this specific case, 16 experiments are conducted, so the subtraction between the total number of DoF ( $DoF_{Total} = 15$ ) and the DoF of each factor's levels (sum of DoF A to E = 9) gives a DoF of error equal to 6. From the ratio between  $SS$  and DoF for each factor and error term,  $V$  can be obtained. In its turn,  $F$  results from the ratio between the variance of the factor and the error variance. A large  $F$  is an indication of a statistically significant factor [245]. Finally, the contribution of each factor on the Nusselt number is presented in the last column of Table 23 and Table 24. This parameter is obtained from the ratio between

the pure sum of squares  $SS'$  of each factor and the total  $SS$  and expresses the impact of a factorial effect in percent [243].  $SS'$  is the sum square of a factor minus the degrees of freedom times the error variance [245].

**Table 23.** ANOVA results for Signal-to-Noise ratios for the static plate case.

Factor	DoF	Sum of Square (SS)	Pure sum of square ( $SS'$ )	Variance (V)	$F$	Contribution (%)
A	3	16.31	14.78	5.44	10.62	12.58
B	3	24.49	22.95	8.16	15.94	19.54
C	1	0.87	0.36	0.87	1.70	0.31
D	1	0.24	-0.27	0.24	0.48	-0.23
E	1	72.46	71.94	72.46	141.52	61.26
Error	6	3.07	7.68	0.51	-	6.54
Total	15	117.44	-	-	-	100.00

**Table 24.** ANOVA results for Signal-to-Noise ratios for the moving plate case.

Factor	DoF	Sum of Square (SS)	Pure sum of square ( $SS'$ )	Variance (V)	$F$	Contribution (%)
A	3	16.94	15.30	5.65	10.36	13.11
B	3	23.13	21.49	7.71	14.15	18.42
C	1	0.79	0.25	0.79	1.45	0.21
D	1	0.26	-0.29	0.26	0.47	-0.25
E	1	72.32	71.77	72.32	132.69	61.50
Error	6	3.27	8.16	0.55	-	7.01
Total	15	116.70	-	-	-	100.00

Looking at the ANOVA results expressed in Table 23, it is clear that the parameter that has a greater influence on the Nusselt number is the Reynolds number (61.26 %), followed by the nozzle-to-plate distance (19.54 %) and jet-to-jet spacing (12.58 %). These results are in agreement with [18, 19]. The jets pattern and the plate geometry are the factors with a weaker effect on the Nusselt number compared with the others, presenting a contribution of 0.31 % and -0.23 %, respectively. In terms of factor's significance, the  $F$ -ratios, expressed in the fifth column of Table 23, are compared with standard table values at a confidence level of the experiments equal to 95 % [245]. From the  $F$ -table, the  $F$ -value for factors A and B is equal to 4.757, while for factors C, D, and E is 5.987. Comparing the  $F$ -ratios obtained

with the tabled  $F$ -values, it seems that factors A, B, and E are statistically significant for 95 % confidence, while C and D are negligible.

To determine if the contribution of the parameters is similar when the target plate is moving, the results expressed in the ANOVA table (Table 24) are analyzed following the same steps presented for the static plate case. The data prove that, as for the static plate case, the Reynolds number is the major contributor to the Nusselt number, with a contribution near 62 %. The effect of the plate geometry on heat transfer is the most reduced, presenting a contribution equal to  $-0.25$  %, followed by the jet pattern, 0.21 %. The influence of the nozzle-to-plate distance (18.42 %) continues to be slightly higher than the contribution of the jet-to-jet spacing (13.11 %). These values show that the effect of the jet-to-jet spacing is slightly higher in the case of the plate in motion than in rest, which is a consequence of the increasing flow complexity due to the thicker boundary layer generated by the plate motion allied with the jet's interactions. The reduced space between jets increases the jet's flow interactions, increasing the turbulence and consequently the heat transfer. These results express the relevance of the target plate configuration in a flow whose complexity is increased in the vicinity of the surface since stronger vorticity and flow mixing are expected. These conclusions are supported by [107], as mentioned in the previous section. In terms of significant factors for 95% of confidence, the comparison between  $F$ -ratios and tabled  $F$  values, data show that the factors that are statistically insignificant in the moving plate case are the jet pattern and plate geometry. Regarding the experimental errors, the results indicate that they have a slightly higher contribution on moving plate measurements compared with the static plate, 6.5 % against 7 %. These observations are expected due to the increased complexity of the flow in the moving plate, leading to a highly unsteady flow in the vicinity of the surface and consequently higher heat flux measurement errors.

The results allow to conclude that in a multiple jet impingement process, where fluid flow properties and velocities are previously determined and fixed, as well as the target plate geometry, it is more effective to vary the jet-to-jet spacing and the nozzle-to-plate distance to enhance the heat transfer performance over the impinging surface than changing the jet's pattern. In addition, the effect of the process parameters is increased by the motion of the target plate. Regarding the plate geometry, which in this specific case consists of a step, the results show that, when compared with the other factors, its influence on heat transfer is low. However, it is extremely important to understand the flow behavior in the vicinity of the step, which increases the average heat transfer, as experimentally observed.

#### 6.2.4. Confirmation Experiment

The confirmation experiment is the final step of the Taguchi method, being important to validate assumptions mentioned in the previous analysis [245]. It is particularly important when the experimental plan did not test the combination of levels identified as optimal. Therefore, it is expected that the average results from the confirmation test agree with the estimated optimum performance. The performance of the optimum condition is predicted from the significant factors. Considering that the contribution of factors C and D are statistically insignificant, they can be pooled, i.e. its contribution is disregarded and new non-zero  $SS_{(error)}$  and  $F_{(error)}$  are estimated, meaning that the contribution of the other factors needs to be adjusted. All the steps followed in this process can be analyzed with higher detail in [245] and the new ANOVA table is presented in Table 25 and Table 26, from the static and moving cases, respectively. From the analysis, no relevant differences are verified, only a slight reduction of the factor's contribution and an increase of the errors.

**Table 25.** ANOVA results for Signal-to-Noise ratios for the static plate case.

Factor	DoF	Sum of Square (SS)	Pure sum of square (SS')	Variance (V)	F	Contribution (%)
A	3	16.31	14.74	5.44	10.40	12.55
B	3	24.49	22.92	8.16	15.61	19.52
C				pooled		
D				pooled		
E	1	72.46	71.93	72.46	138.54	61.25
Error	8	4.18	7.84	0.52	-	6.68
Total	15	117.44	-	-	-	100.00

**Table 26.** ANOVA results for Signal-to-Noise ratios for the moving plate case.

Factor	DoF	Sum of Square (SS)	Pure sum of square (SS')	Variance (V)	F	Contribution (%)
A	3	16.94	15.32	5.65	10.36	13.13
B	3	23.13	21.51	7.71	14.15	18.42
C				pooled		
D				pooled		
E	1	72.32	71.78	72.32	132.69	61.51
Error	8	4.32	8.10	0.54	-	6.94
Total	15	116.70	-	-	-	100.00

Following the projection of optimum performance presented by Taguchi [243], its value can be estimated by Eq. (80) [245]:

$$Y_{opt} = \frac{T^*}{N} + \left( \bar{A} - \frac{T^*}{N} \right) + \left( \bar{B} - \frac{T^*}{N} \right) + \left( \bar{C} - \frac{T^*}{N} \right) + \left( \bar{D} - \frac{T^*}{N} \right) + \left( \bar{E} - \frac{T^*}{N} \right) \quad (80)$$

where  $Y_{opt}$  represents the estimated performance at optimum condition,  $T^*$  is the grand total of all results,  $N$  is the total number of results, 16 in this specific case, and  $\bar{A}$ ,  $\bar{B}$ ,  $\bar{C}$ ,  $\bar{D}$  and  $\bar{E}$  are the average performance of the optimum combination. For both static and moving cases this combination is A<sub>2</sub>B<sub>1</sub>E<sub>2</sub>. However, for simplification of the experimental layout, level 2 of factors C and D was introduced in both experiments. These combinations do not correspond to any one of the experiments conducted in this study. Therefore, two confirmation tests are conducted, one for the static and another for the moving plate cases, following the same procedure mentioned in section 3.1, with three repetitions for each scenario. The results predicted by Eq. (80) are compared with the experimental data and presented in Table 27.

**Table 27.** Confirmation test results.

Test	Static		Moving	
	Predicted	Experimental	Predicted	Experimental
<b>Nusselt number</b>	34.37	37.3(9) ± 0.56	36.02	39.2(6) ± 1.37

From the analysis of data presented in Table 27, it seems that the Nusselt number obtained by Taguchi's predictive equation, for the static plate case, is found to be 34.37, while the experimental result is approximately 8 % higher. Regarding the moving plate scenario, a difference near 9 % was observed between predicted and experimental data. These results demonstrate the success of the confirmation test since the experimental value is very close to the estimated optimum performance calculated through Taguchi's method.

By comparing the Nusselt number measured in the confirmation test with the results presented in Table 22, it is proved that the optimized configuration, obtained by Taguchi's method, ensures the higher average heat transfer.

### 6.2.5. Conclusions

In summary, the heat transfer of a multiple jet impingement configuration is enhanced by  $S = 3 D$ ,  $H = 2 D$  for a staggered configuration, and a higher Reynolds number for both static and moving plates.

The ANOVA analysis shows that jet's pattern and plate geometry can be neglected when compared with these control factors. However, the heat transfer and velocity field measurements demonstrate that a staggered configuration and non-flat plate promotes flow mixing and enhance the heat transfer. In that sense, it is important to clarify this topic and to analyze with more detail the effect of the non-flat plate on both jet's flow dynamics and heat transfer efficiency over the target plate. Therefore, this study is conducted in section 6.3.

In addition, this analysis reveals that, even if the velocity of the plate is low, the effects of the motion are clearly identified. According to [107], while in a static plate the effect of the jet impingement governs the fluid flow and heat transfer behavior, in a moving plate, the shear-driven flow generated over the surface takes control of the flow and thermal fields. This phenomenon is identified in this work but it is expected to be intensified with higher plate velocities. Considering the relevance of this topic, section 6.4 presents the numerical validation of the numerical model of multiple air jets impinging on a static and moving flat plate. Besides the model validation, an analysis including a higher plate velocity is implemented numerically.

## 6.3. Non-flat Plate

In the previous section, it was stated that the analysis of different step heights is important to clearly determine the influence of the non-flat plate on both heat transfer and flow velocity field. Therefore, an experimental analysis, based on PIV measurements is conducted to characterize the jet's flow dynamics over surfaces with a step, and the results are compared with a flat plate. From the experiments, velocity fields and heat transfer rates are obtained in order to characterize the flow and to determine the influence of the step configuration on heat transfer performance and surface coverage.

### 6.3.1. Test Conditions

To conduct this study, the optimized configuration obtained in section 6.2.4 is implemented. The experiments consist of air that flows through circular nozzles spaced  $H = 2D$  from the target plate, inducing turbulent multiple jets ( $Re = 5,000$ ) which impinge different plate configurations, a flat plate, and two non-flat plates with  $1 D$  and  $2 D$  steps. The jets follow a staggered configuration and are spaced  $3 D$  in both spanwise ( $S_y$ ) and streamwise ( $S_x$ ) directions, as presented in Figure 93. The row illuminated by the laser sheet contains the central jet and two adjacent jets, one on each side. However, the effect of the jets located at the front and back rows must also be quantified due to the staggered configuration. In

summary, the multiple jet flow analysis consists of seven jets. Even if the measuring zone is totally open, the effect of the outlets on the impingement only can be considered in the right and left end side of the impingement plate, since a total of nine rows (four on each side of the central row) are considered. The jets and plate temperature are equal to 22 °C and 120 °C, respectively.

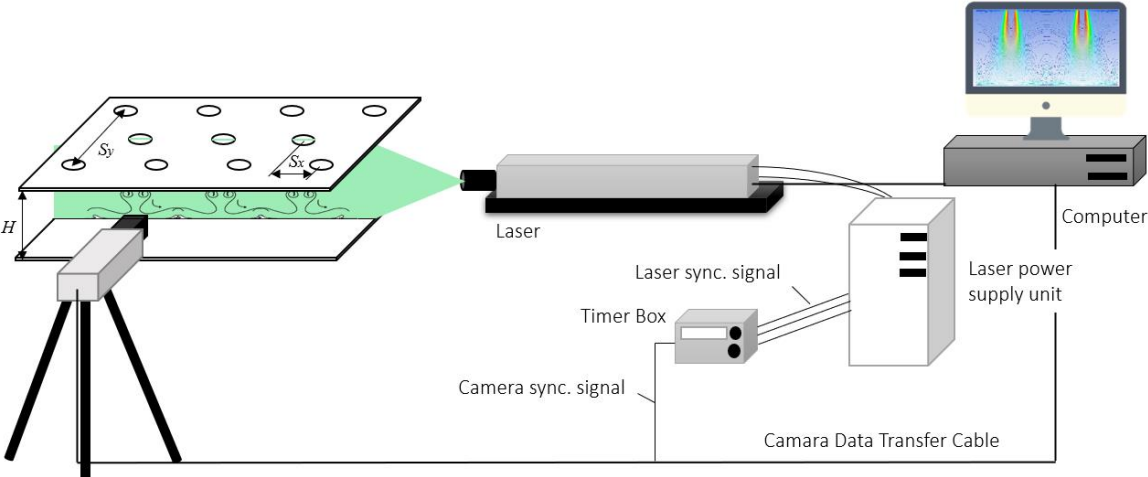


Figure 93. Experimental setup for the study of multiple jet impingement.

6.3.2. Flow Dynamics Characterization

The averaged velocity field of multiple jets impinging on target plates with different configurations is obtained from PIV measurements and the results are presented in Figure 94.

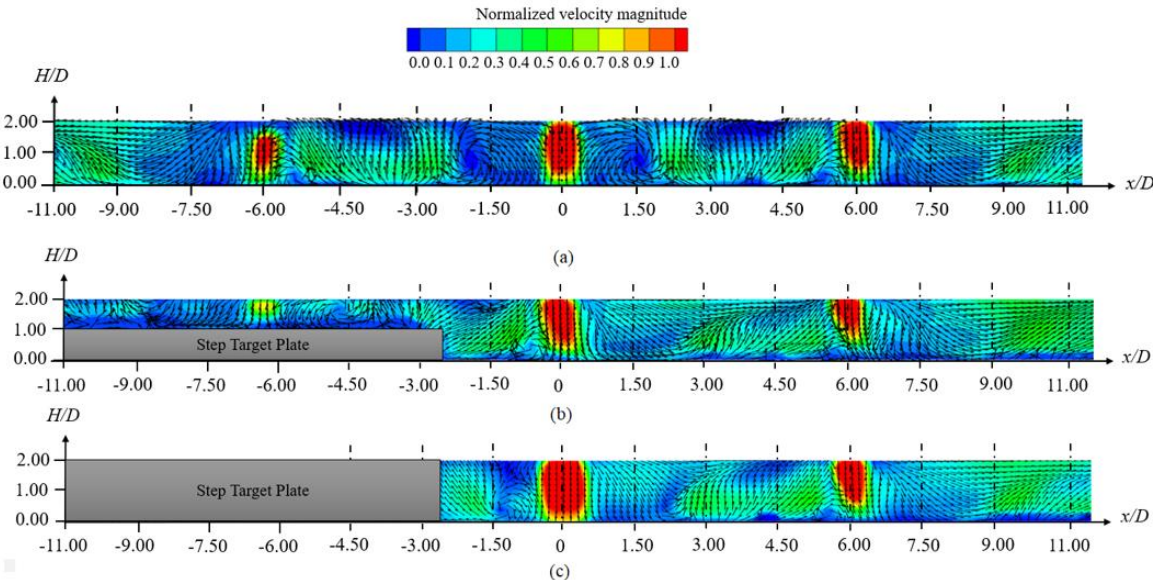


Figure 94. Staggered multi-jets configuration impinging a flat and non-flat plate at  $Re = 5,000$ ,  $H/D = 2$ , and  $S/D = 3$  (a) Flat plate (b) Non-flat with 1 D step (c) Non-flat with 2 D step.

Looking at the overall flow field, it is observed that the air flows through the circular nozzles at a maximum velocity and starts to mix with the surrounding air, entraining mass, momentum, and energy [20]. This is known as the free jet region. From the mixing between the jet flow and the ambient air, a shear layer is generated leading to high lateral velocity gradients. As mentioned by [256], jet impingements characterized by  $0.5 < H/D < 5$  are within the length of the potential core. This means that no decaying or fully developed regions are expected to be identified. As the jets approach the wall, the axial velocity decreases and is converted into an accelerated horizontal component [54]. This is identified as the stagnation region which is characterized by a higher static pressure and a thin boundary layer [21]. The development of the flow over the target plate induces a wall jet region, in which the flow velocity is accelerated from zero to a maximum value, which occurs at a specific distance from the stagnation point. The jet's flow is divided into two streams moving in opposite directions, being characterized by a growing boundary layer [24]. Considering this jet flow structure, higher heat transfer coefficients are expected to be recorded in the vicinity of the stagnation region, but a portion of the wall jet region significantly contributes to the heat exchange [8]. However, as presented in Figure 94, the jet's flow complexity is increased by the jet's interactions prior to and after the impingement but also by the non-flat plate. Since the ratio  $H/D$  is small, a high velocity magnitude is identified from the nozzle exit to the target surface. Close to the central jet, the results show that the wall jet develops through the surface until it collides with the wall jet of adjacent jets located in the back and front rows. These interactions induce a fountain flow at  $x/D$  close to  $\pm 3$  and recirculation regions, identified by Caliskan et al. [28] as primary vortices. The magnitude and structure of these vortices, located on both sides of the central jet axis, seem to be symmetric in the flat plate case [Figure 94 (a)].

As the flow goes through the outlets, an increase in velocity magnitude is observed at the adjacent jets located at  $x/D$  equal to  $\pm 6$ . The interactions between the wall-jets induced by the central jet and the adjacent jets located at the front and back rows lead to a deflection of the adjacent jets flow, located at  $x/D = \pm 6$ . This deflection is mainly due to the development of primary vortices generated on the right end side of the left jet and on the left end side of the right jet, which is intensified by the wall-jets development and jet-induced crossflow generated by the upstream jets. As mentioned by [21], the jet-induced crossflow causes asymmetric jet flow field, disturbs other wall jets, moves the stagnation points, and develops thicker boundary layers, resulting in a reduction of the average heat transfer rates. This behavior is clearly observed in the three cases presented in Figure 94. Thus, a reduction of the stagnation region of adjacent jets located at  $x/D = \pm 6$  is verified and a decrease in heat transfer is expected in this region. A second increase in velocity magnitude is observed at  $x/D$  close to  $\pm 9$ , which represents the

position of adjacent jets located at the front and back rows. The increased flow velocity is clear near the outer boundaries, which evidences the strength of the crossflow generated by the flow of the upstream jet.

Regarding the non-flat plate case, the flow dynamics are slightly different. As identified in Figure 94 (b), the wall jet development induced by the central jet is blocked by the step, inducing a flow reversal. In addition, the step deflects the flow from the adjacent jets located just above the step. The combination of these two effects increases the flow turbulence and affects the central jet flow. The vortex induced in the left-hand side of the central jet deflects the central jet flow and the stagnation point is moved to the right. Even if the primary structure of the central jet is affected, the vortex promotes the mixing which may enhance the heat transfer at the stagnation region [54]. Comparing the two step configurations, with a height of  $1 D$  [Figure 94 (b)] and  $2 D$  [Figure 94 (c)], the velocity field shows that the  $2 D$  step blocks the flow resulting from the jets located immediately above step while in  $1 D$  case, there is space to develop the flow over the step surface, promoting its cooling. In that sense, higher velocities are induced in the vicinity of the  $2 D$  step, increasing the overall turbulence of the flow. The deflection of the central jet is weaker compared with the  $1 D$  step and therefore, the stagnation point remains in the same location. It is expected that this increased flow turbulence enhances the average heat transfer rates compared with the flat plate and the  $1 D$  step.

As in the flat plate case, an increased velocity between the central jet and the adjacent jets, promoted by the jets located at the front and back rows, is identified. As the wall jet induced by the central jet goes towards the outlet boundary, colliding with the wall jets from the adjacent jets, a deflection of the adjacent jets located at  $x/D = -6$  is observed. This leads to a decrease in the impingement area and thus, a reduced average heat transfer is expected in this region.

Beyond the influence of the target plate configuration, PIV measurements confirm that the confined space plays an important role in the velocity magnitude. Since the jet's flow have a reduced space to develop, an increase of the flow vorticity is observed. The increase in velocity leads to an overall increase in the flow turbulence. Including a step over the target plate, this space becomes even smaller, which induces a stronger mixing between the multiple jet's flow and the surrounding air. In that sense, higher average heat transfer rates are expected over a non-flat plate with the configurations presented in this study.

### 6.3.3. Velocity profiles

The velocity profile over the target plate is plotted in Figure 95, for the three plate configurations. To conduct the analysis, the velocity magnitude is normalized by the maximum velocity ( $U/U_{max}$ ), while the distance from the central jet axis is normalized by the jet diameter ( $x/D$ ).

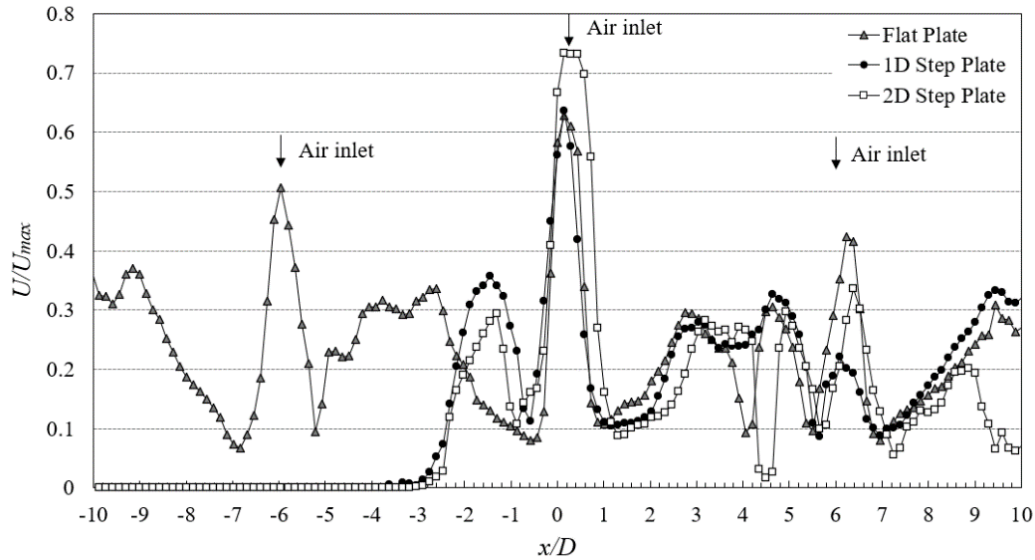


**Figure 95.** Velocity profile over the target plate ( $y/D = 0.15$ ) for different plates geometry at  $Re = 5,000$ ,  $H/D = 2$ , and  $S/D = 3$ .

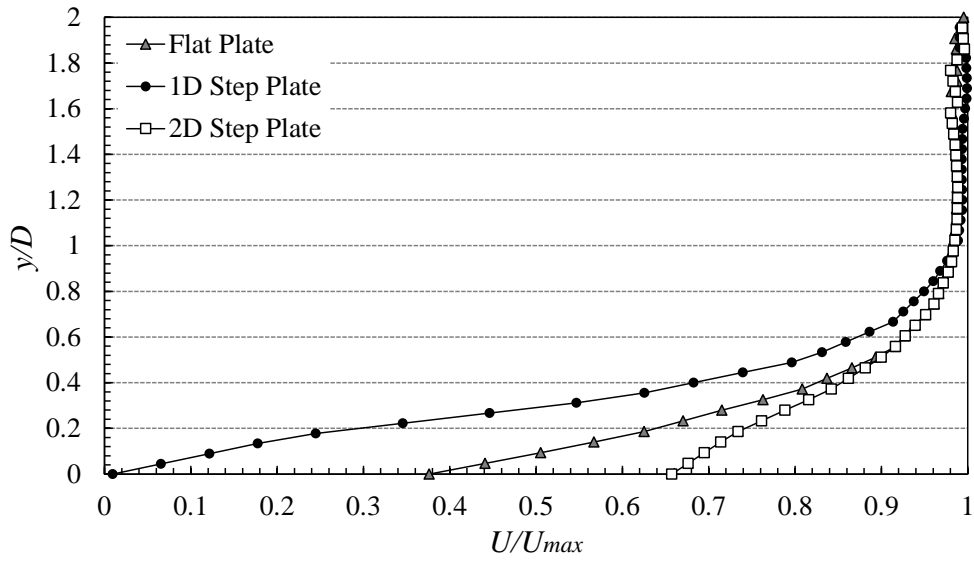
An overall view of the velocity field over the target plate, depicted in Figure 95, shows that higher velocities are recorded at the stagnation region of the central jet in all cases, characterized by a thin boundary layer. As previously discussed, the central jet's flow keeps its regular structure while the adjacent jets are affected by the interaction of the upstream jet's flow. This deflection leads to a decrease of the velocity recorded at the adjacent jet's stagnation zone located at  $x/D = 6$ . As expected from the previous analysis, higher velocities are achieved near the stagnation region of the central jet impinging the  $2D$  step plate, therefore, higher heat transfer rates are expected to be recorded. The velocity magnitude over the plate starts to decrease as the radial distance ( $x/D$ ) from the central jet axis increases. This reduction is approximately the same for the three cases, achieving a minimum value at  $x/D = 1$ . This point represents the end of the stagnation region [9]. As the central wall jet develops over the target plate, flow interactions occur with the wall-jet of the adjacent jets. These interactions increase the flow turbulence and an increase in velocity are observed, achieving a secondary peak at  $x/D$  near 3. This location corresponds to the stagnation region of adjacent jets located at the front and back rows. As the results demonstrated, the magnitude of the secondary peak is approximately the same for all the cases. Near  $x/D = 4$ , a decrease in velocity is observed and must correspond to a stagnation point induced by

the collision between the wall jet's flow. The third velocity peak is identified near the adjacent jet, located at  $x/D = 6$ , as expected. Comparing the different cases, it appears that the highest velocity is identified for the flat plate case. This proves that the deflection of the adjacent jet flow is stronger for the non-flat plates, leading to a degradation of the local velocity. As the flow goes through the outlets an increase in flow velocity is identified also due to the interaction of the upstream jets-induced crossflow with the adjacent jets located at  $x/D = 9$ .

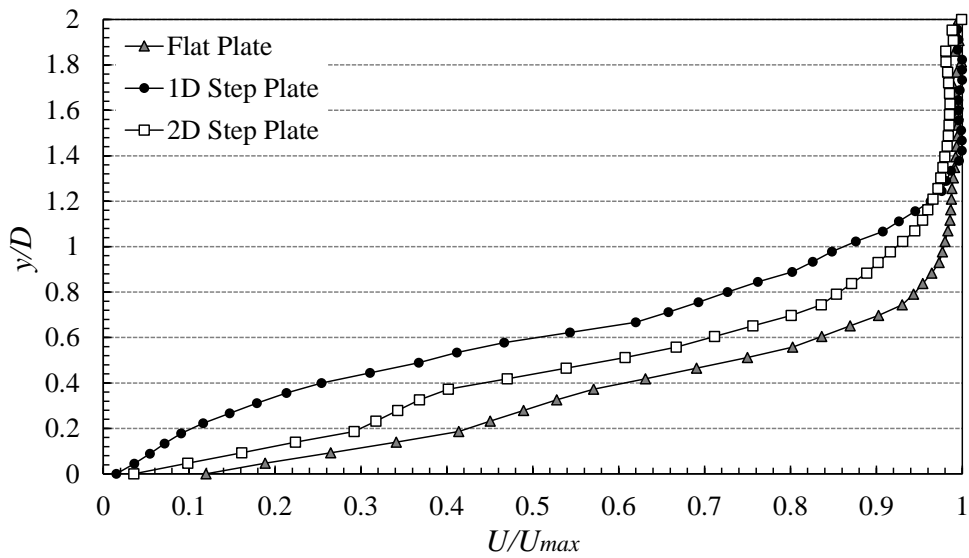
Looking at the left-end side, the velocity profile shows a peak near  $x/D = -1.5$  for the non-flat plate cases. This peak is induced by the increased flow vorticity generated by the collision of the central wall jet with the step surface. This peak is slightly higher for the  $1 D$  step due to the combined effect of the deflection of the adjacent jet flow located at  $x/D = -3$  with the step corner and the central wall jet. At the bottom of the step, a stagnation point is identified, being recorded with a velocity close to zero. In the flat plate case, a peak is recorded near  $x/D = -3$  due to the strong interactions between the wall jets of the jets positioned in the front and back row with the one located in the central row. Finally, another maximum velocity is observed at  $x/D = -6$ , being higher than that identified at  $x/D = 6$ , indicating that the magnitude of the vortex which induces the deflection of the adjacent jet ( $x/D = -6$ ) and identified in Figure 94, is lower than the vortex which interferes with the jet located at  $x/D = 6$ . These results demonstrate the complexity of the flow field and the difficulty to obtain uniform development of the flow over the target surface. These effects are stronger when non-flat target plates are applied.

To complement the analysis, the velocity profile obtained at the central jet axis and the right adjacent jet axis are presented in Figure 96 (a) and Figure 96 (b), respectively. The velocity profile recorded at the jet's axis indicates the effect of the target plate geometry on the jet's flow development.

The results from the central jet demonstrate that near zero velocities at the stagnation point are only identified in the  $1 D$  step plate case, while higher velocities are recorded in the case of the flat plate and  $2 D$  step plate. These results show the limitation of the PIV system to measure, with accuracy, the velocities near the target plate. To increase these measurements and to be able to capture the stagnation points, the CCD camera should target the flow at the surface transition instead of the overall field, from the nozzle to the target plate.



(a)



(b)

**Figure 96.** Velocity profile over the jet axis ( $x/D = 0$ ): (a) Central jet; (b) Right adjacent jet.

While the velocity field recorded by the PIV system and presented in Figure 94 does not allow to clearly identify the different jet's regions, the velocity profile at the jet axis (Figure 96) shows that 95 % of the maximum velocity, the end of the potential core, is achieved at  $y/D$  near 0.7 for the flat and  $2D$  step plates and 0.8 for the  $1D$  step plate. These data demonstrate that the  $1D$  step induces higher fluctuations of the flow, due to the jet's flow separation near the step. The vortex previously identified in Figure 94, highly contributes to this reduction of the potential core length when compared with the other cases. These interactions are not observed in the  $2D$  step, since the step height is similar to the nozzle-to-plate separation. Comparing these values with those obtained at the axis of the adjacent jets,

measurements show a reduction of the physical length of the potential core. A decrease of 20 % is identified in the flat plate case, and 40 % and 65 % for the 2 *D* step and 1 *D* step cases, respectively. These results evidence that the adjacent jets are strongly affected by the upstream jet's, but also that the non-flat plate increases the flow turbulence. The highest decrease is identified in the 1 *D* step configuration, as expected. The end of the potential core indicates the beginning of the stagnation region that extends from  $y/D$  near 0.8 to  $y/D = 0$ .

Considering that the distance between the nozzle and the target plates is small,  $H/D = 2$ , other jet's regions identified by [8], such as the decaying and acceleration regions, are not identified in the central jet. However, this is not the case for the adjacent jets. As mentioned above, the reduction of the potential core length is mainly due to the increased magnitude of the primary vortices. The intensity of the flow turbulence increases with more complex surfaces and a gradual acceleration between the end of the potential core and the stagnation region is observed. In addition, while velocities near zero at the stagnation point were not detected in all central jets, this is not the case for the adjacent jets.

### 6.3.4. Average heat transfer over a flat and non-flat plate

The average heat transfer of multiple air jets impinging a flat and non-flat plate is analyzed in this section. As mentioned in section 3.1, the heat flux sensor is mounted at the center of the target plate. The scheme presented in Figure 97, shows the configuration of the jets over the target plate.

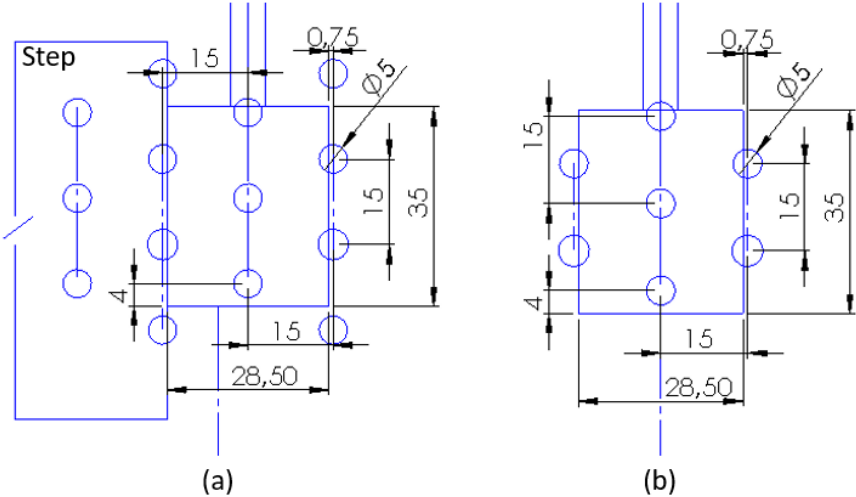


Figure 97. Jets position in relation to the heat flux sensor. (a) Non-flat plate; (b) Flat plate.

As presented in Figure 97, the average heat transfer is obtained from the impingement of seven jets but the flow interaction induced by the adjacent jets located near the heat flux sensor is also considered.

The average Nusselt numbers obtained from the heat flux measurements for the flat and non-flat plate cases are summarized in Table 28, as well as the uncertainty of the measurement.

**Table 28.** Average Nusselt number measurements.

Plate Geometry	$\overline{Nu}$
Flat	29.9(0) $\pm$ 0.45
Non-flat – Step 1 $D$	32.7(2) $\pm$ 0.49
Non-flat – Step 2 $D$	37.3(9) $\pm$ 0.56

The results demonstrated that the heat transfer is increased for the non-flat plate. These observations are in agreement with the velocity profiles discussed in the previous sections. Compared with the flat plate, the average heat transfer increases by about 10 % for the case of the 1  $D$  step plate and by 25 % for the 2  $D$  step plate. As mentioned previously, the step surface increases the turbulence inside the confined space between the nozzle and the target plates. As a consequence, higher velocities are measured by the PIV system compared with the flat plate. This increased turbulence promotes the mixing between the jet's flow and the surrounding air, increasing the average heat transfer. Besides the global increase of the flow turbulence, the step induces a deflection of the jets that directly impinge over it and prevents the wall jet development coming from the central jet, inducing a flow recirculation. This phenomenon leads to an increase in heat transfer as also observed by [91]. However, the average heat transfer over the target plate is expected to increase more in the case of the 2  $D$  step than in the 1  $D$  step. This observation can be explained by the larger stagnation zone of the central jet compared with the other cases, which induces higher heat transfer rates. According to [259], the heat transfer mechanism in the stagnation region is caused by the dynamics of recirculation zones characterized by stagnant heated fluid and the sweeping of heated fluid. Thus, these recirculation zones are expected to be identified with a stronger intensity in the 2  $D$  step plate. To support these conclusions, more analysis with steps of smaller dimensions is needed.

### 6.3.5. Conclusions

The analysis of the overall flow field shows that combining the staggered configuration with the confinement induces stronger interference of upstream jet-induced crossflow on downstream jets, slightly increasing the heat transfer over the impinging surface. This effect is intensified in the non-flat plates due to the reduction of the overall area by the step. The velocity profiles over the jet's axes were extracted

from the post-processed PIV data and allowed to analyze, in detail, the variation of the velocity magnitude. The results demonstrate the complexity of the flow due to adjacent jets interactions which are intensified by the non-flat plate. The step induces a flow reversal of the central wall jet. This effect combined with the jet's interactions leads to an increase of the velocity magnitude in the vicinity of the step. Compared with the flat plate, the average heat transfer increases by approximately 10 % for the case of the 1  $D$  step plate and by 25 % for the 2  $D$  step plate. The higher average heat transfer value must be explained by the fact that the central jet of the 2  $D$  step plate presented a larger stagnation region. However, to support these conclusions, more analysis with smaller step dimensions is needed.

## 6.4. Numerical Validation

This final section has two main goals. The first one is to validate the numerical model of a multiple jet impingement system impinging on a static and moving plate. The second goal consists of the analysis of the jet flow dynamics for a static plate and a moving plate considering two plate velocities,  $V_s = 0.003$  m/s and  $V_s = 0.03$  m/s. The numerical simulations are conducted considering the optimized configuration presented in section 6.2.4:  $S/D = 3$ ,  $H/D = 2$ ,  $Re = 5,000$ , and a staggered jet pattern configuration.

### 6.4.1. Accuracy of the Numerical Model

To determine the accuracy of the numerical model, the numerical predictions for the static and moving plate case are compared with the experimental results, presented in the previous sections, and correlations for the average Nusselt number.

For the static plate, the correlations developed by [48] and [42], expressed by Eq. (81) and Eq. (82) respectively, are considered, while for the moving plate case, the correlation presented by [111], Eq. (83) is applied.

$$\overline{Nu} = A Re^m \{1 - B[(H/D)(U_c/U_j)]^n\} Pr^{1/3} \quad (81)$$

$$\overline{Nu} = 0.328 Re^{0.8} (H/D)^a A_f^{0.595} \quad (82)$$

$$\overline{Nu} = 0.85 Re^{0.49} (S/D)^{-0.46} \sin \theta \quad (83)$$

where  $Pr$  is the Prandtl number and  $A_f$  the non-dimensional area. The coefficients  $A$ ,  $B$ ,  $m$ , and  $n$  are defined in [48], while  $a$  is described in [42].

The average Nusselt number is determined in the region that corresponds to the location of the heat flux sensor over the target plate, as depicted in Figure 98, to ensure that the heat transfer is measured at the same location in both experimental and numerical methods.

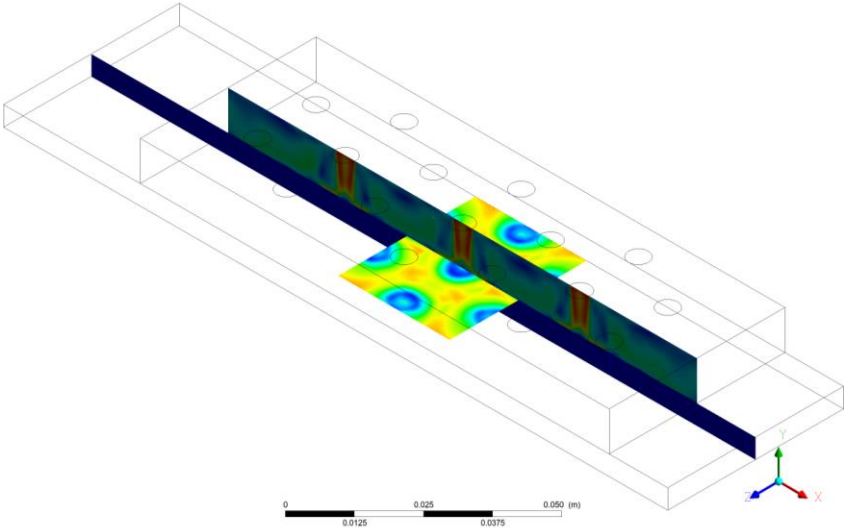


**Figure 98.** Position of the heat flux sensor on the numerical domain.

The  $\overline{Nu}$  values, presented in Table 29, are within the range predicted by the correlations with a maximum error of 12 %, which seems to be reasonable according to other studies [52, 54, 55, 112]. Compared with the experimental data, this difference is only 4 % which is very good. Thus, the numerical model for the static plate case is validated. Regarding the dynamic case, summarized in Table 30, the numerical results are in very good agreement with the predicted values, while a discrepancy of approximately 8 % is observed compared with the experimental data. However, since the correlation presented by [111] is based on numerical analysis, it would be interesting to determine a correlation based on this experimental work. This study is presented in section 6.5.

**Table 29.** Average Nusselt number over the static plate.

$\overline{Nu}$			
Numerical result	Experimental results	Florshuetz et al. [48]	Obot and Trebold [42]
28.65	29.9(0) ± 0.51	32.63	25.55

**Table 30.** Average Nusselt number over the moving plate.

$\overline{Nu}$		
Numerical result	Experimental results	Chitsazan & Glasmacher [111]
33.80	$31.1(0) \pm 1.70$	33.30

### 6.4.2. Characterization of the Flow Dynamics

The previous section demonstrated that the average heat transfer measured experimentally and predicted numerically are in good agreement. While in the static case, a difference of 5 % is observed, in the moving case this difference jumps to 8 %. To complement the numerical validation analysis, the jet's flow structure for the case of static and moving plates is discussed in this section. The numerical and experimental velocity fields for both static and moving cases are depicted in Figure 99 and Figure 100, respectively.

From a global analysis of the velocity field, it is clear that in both cases the maximum jet flow velocity is recorded at the nozzle exit and decreases as the jet's flow approaches the target plate. However, the experimental data show a higher uniformization of the velocity over the potential core length, while numerically slightly lower velocities are predicted at the jet center. This difference can be caused by the prediction of stronger effects of the shear layer, produced by the mixing between the jet flow and the surrounding air. This strong mixing is the primary source of turbulence characterized by entrainment of mass, momentum, and energy [20], therefore the intensity of the flow turbulence, and consequently of the primary vortices generated, is slightly higher when compared with the experimental data.

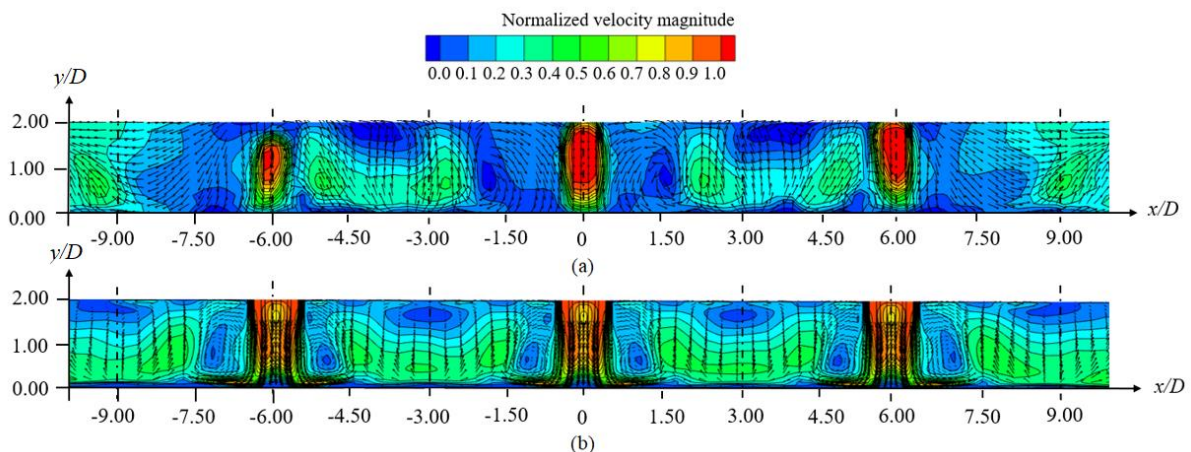


**Figure 99.** Static case: (a) Experimental data; (b) Numerical data.

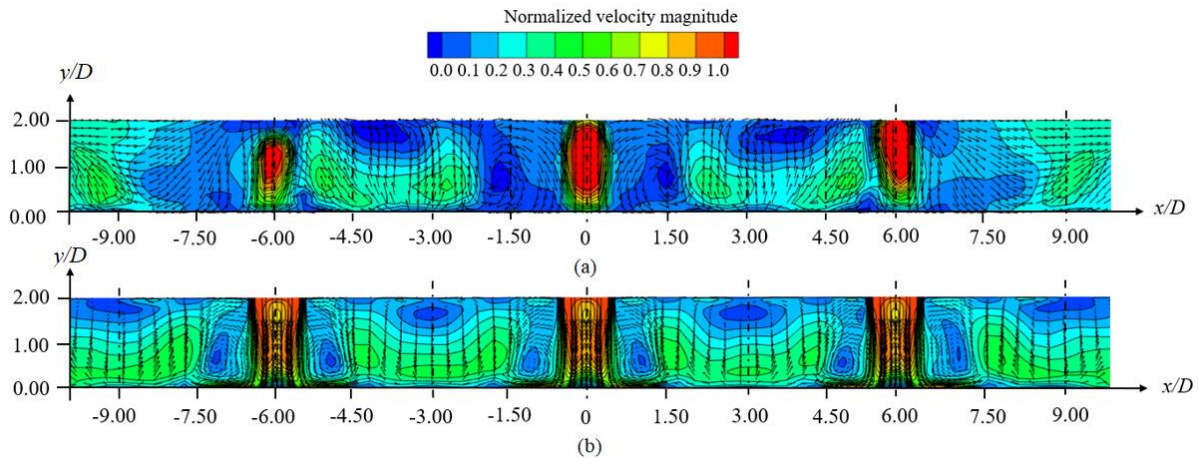


**Figure 100.** Moving case: (a) Experimental data; (b) Numerical data.

The stagnation region, characterized by the loss of axial momentum of the jet as it approaches the target wall [24], is clearly identified in Figure 99 and Figure 100. However, this stagnation region is identified in higher detail by the numerical models. As already mentioned in this work, to increase the accuracy of the PIV measurement, a macro lens must be used to zoom the measurement region close to the surface. In this region, the flow is characterized by higher static pressure on and above the wall, the eddies are stretched and distorted, and the flow is gradually reoriented to be roughly parallel to the wall [25]. This induces the wall upstream effect, which is clearly identified both numerically and experimentally. After the impingement, an increase in velocity in the radial direction is identified in the vicinity of the stagnation region due to the fast decrease of the kinetic energy which is transformed into a corresponding rise in pressure energy [26]. A laminar boundary layer is formed, showing a constant thickness [19], and therefore, high heat transfer coefficients are expected in this region. The boundary layer grows until maximum levels of turbulence are reached, away from the jet axis [9, 22]. This growth is identified with higher resolution by the numerical models, proving once again the need to increase the PIV resolution in the vicinity of the surface. The development of the boundary layer over the surface is highly influenced by the jet's configuration. As presented in Figure 99 and Figure 100, the staggered configuration induces strong interactions between the central jet and the adjacent jets which limits the growth of the boundary layer over the target plate. The velocity field shows that the wall jet coming from the adjacent jets located in the front and back rows yield an increase in velocity. The interference between the wall jets induces a fountain flow at  $x/D = \pm 3$  and  $x/D = \pm 9$  which pushes the flow in direction to the jets, as observed by the velocity vectors. Secondary stagnation points are expected to occur at these positions, however, due to the strong turbulence of the flow in this region, they are not captured in the experimental and numerical velocity fields. These fountains cause recirculating flows which interact with

the flow of the adjacent jet, re-entering the jet's core and increasing the shear layer. While the effect of these strong interactions is clearly identified experimentally, inducing a deflection of the adjacent jets, this jet's deflection is not identified numerically. Moreover, these recirculation flows interfere with the wall jet region, in the vicinity of the surface, forcing the flow to detach the surface at a distance from the jet's axis approximately equal to  $x/D = \pm 1.5$ . At  $x/D$  near  $\pm 2.5$ ,  $\pm 4$ ,  $\pm 8$ , secondary vortices are identified, but only numerically. According to [233], a secondary vortex, characterized by a local flow reversal [234], is associated with a local shear layer generated by an unsteady wall pressure gradient caused by the primary vortex. This secondary vortex induces flow separation and reattachment throughout the target surface, leading to secondary maxima of the heat transfer. These secondary vortices are expected to occur experimentally, even if they are not clearly identified by the PIV measurements. In addition, two strong vortices are observed on the left-hand side of the left adjacent jet and on the right-hand side of the right adjacent jet showing the strong interaction of the crossflow induced by the upstream jets on the flow structure. The crossflow arises from the spent air of the accumulated jets and flows in direction to the outlets, meaning that the flow and heat transfer of adjacent jets are influenced by this phenomenon [32]. This effect is increased for low  $H/D$ , which is the case in this study since  $H/D = 2$ . The confinement of the jets leads to an increase of the local shear stress and local turbulent transport downstream the impingement [33]. Therefore, the increased velocity, identified near the adjacent jets located in the right and left-hand sides, is mainly due to the accumulated jet-induced crossflow, which is clearly identified both experimentally and numerically.

Comparing the static plate with the moving plates, it seems that the overall velocity is slightly higher when the target plate is in motion. The vortices generated in the vicinity of each jet increase in magnitude as the plate moves, being more pronounced on the left-hand side of the jets which is expected since the plate moves from the left to the right. Looking at the left-hand side and right-hand side of the domain, the numerical results show stronger flow interactions as the plate moves. This effect induces an increase in turbulence intensity, an intensification of the vortices, and a thicker shear layer is generated at the edges of the jets. Moreover, the experimental results and numerical predictions demonstrate that this shear layer thickens with the motion of the target plate, being thicker on the right-hand side of the last jet. This effect can be explained by the accumulated crossflow induced by the jet's flow interactions which are intensified by the plate motion since the crossflow induced by the upstream jet's flow interfere with the downstream jets and increases the turbulence intensity of the flow. While the numerical data predicts similar flow dynamics compared with the experimental results, the overall turbulence intensity of the flow is slightly higher numerically. This difference can be explained by the symmetry boundary conditions

implemented in the numerical domain. Overall, the predictions of the jet's flow dynamics are in good agreement with the experimental results, validating the accuracy of the numerical model for both static and moving target plates.

### 6.4.3. Heat transfer over the target plate

Since the numerical model was validated in the previous sections and considering that the experimental data does not provide information regarding the variation of the heat transfer in different locations of the target plate (only the average Nusselt number for a specific location), these data are determined numerically. To conduct this analysis, a line over the surface which crosses the central row of the multiple jet array is selected and the Nusselt number is predicted from one side of the plate to the other, for both static and moving plates. The results are represented in Figure 101.

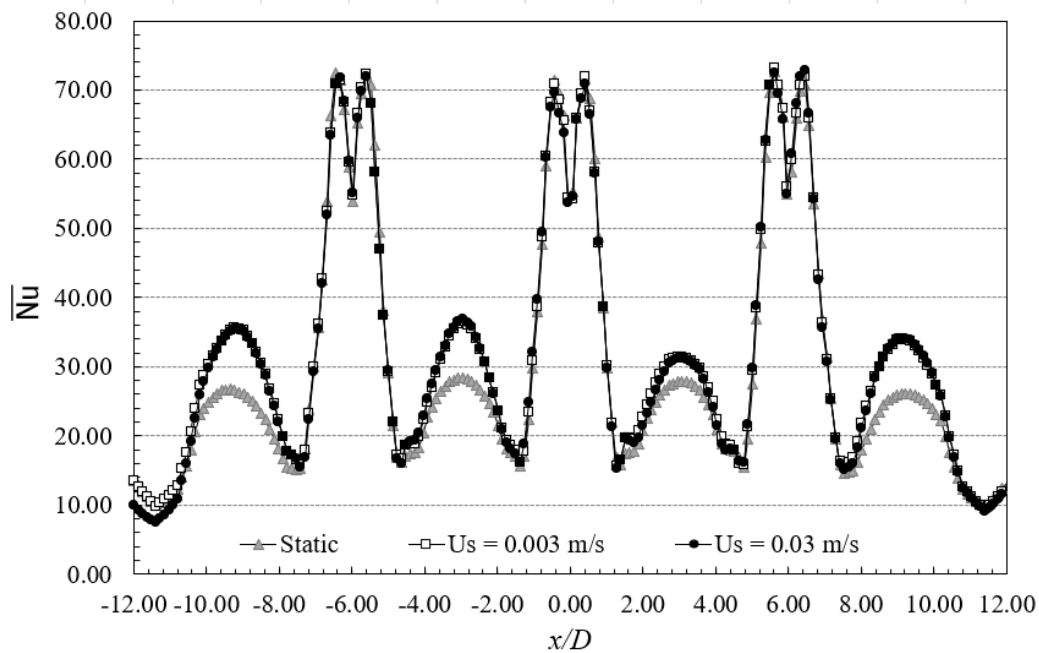


**Figure 101.** Nusselt number over the target plate ( $y/D = 0$ ) at the central row.

The data show that the maximum Nusselt numbers are obtained in the vicinity of the jet axis of each jet, assuming a value close to 70. Looking at the predicted values for the static and moving plates, results indicate that the variation is very smooth from the jet axis to a distance close to  $1.2 D$ . These results are in agreement with [69, 111, 260] which demonstrates that low  $V_s$  values induces slight variations of the heat transfer compared with the static plate. The maximum heat transfer rate is achieved at a distance of  $0.4 D$  from the jet's axis. At this location, a minimum boundary layer thickness is expected to occur due to the flow acceleration. As the wall develops over the surface, the boundary layer grows and the heat transfer decreases achieving a minimum value at a distance near  $1.2 D$  from the jet's axis. From this

point, interactions with the wall jet of the adjacent jets induce an increase in heat transfer. A secondary peak occurs at  $x/D = \pm 3$  and  $x/D = \pm 9$ , which corresponds to the positions where the adjacent jets at the front and back rows are located. Looking at the numerical predictions, it is clear that the higher difference between the moving and the static plates occurs in this region. As the plate moves from the left to the right, the crossflow induced by the motion combined with the jet-induced crossflow increases. The turbulence intensity of the flow rises and therefore, an increase in heat transfer rate is observed compared with the static plate. Comparing the secondary peak values, results indicate an increase of 58 % at  $x/D = -9$ , 28 % at  $x/D = -3$ , 11 % at  $x/D = 3$ , and 30 % at  $x/D = 9$ . These results reveal that the central jet seems to be slightly shielded from the crossflow compared with adjacent jets and therefore a lower difference between the static and moving plate is observed. In addition, the results show that the variation of the secondary peak over the surface varies 8 % for the static case and approximately 16 % for the moving case. In that sense, it is possible to conclude that the crossflow induced by the plate motion is stronger than the jet-induced crossflow. Moreover, looking at the variation of the heat transfer rates for  $U_s = 0.003$  m/s and  $U_s = 0.03$  m/s the results show a smooth difference between both cases. Therefore, data for higher  $V_s$  values are needed to determine with higher detail the influence of the plate velocity on heat transfer.

#### 6.4.4. Effect of the plate velocity

From the analysis discussed in section 6.2, it was stated that even if the target plate motion is low, it increases the flow turbulence and consequently, the heat transfer over the target plate. However, it was mentioned that it would be interesting to implement a higher plate velocity to confirm if the data follows the same trend. Considering that the accuracy of the numerical model of multiple jets impinging a moving plate was validated in the previous section, a higher plate velocity is implemented in order to clearly understand its effect on the jet's flow dynamics. To conduct this analysis, three cases are analyzed in this section, one static and two moving plates ( $U_s = 0.003$  m/s and 0.03 m/s). The turbulence intensity of the flow is the variable selected to conduct this study. This parameter,  $I$ , represents the ratio of the root mean square of the turbulent velocity fluctuation,  $U'$ , to the mean flow velocity,  $\bar{U}$ , and it is given by Eq. (84) [209]:

$$I = \frac{U'}{\bar{U}} \quad (84)$$

The development of the turbulence intensity is analyzed from the left to the right side of the domain, and it is represented in Figure. Focusing on Figure (a), the numerical predictions show that the turbulence intensity induced by the adjacent jets increases with the target plate velocity. While for the static plate a global turbulence intensity of 9 % is observed, increasing 1 % when the plate moves. Regarding the development of vortices in the vicinity of the left adjacent jet, the turbulence intensity is recorded to be near to 9 % while when the plate moves, this intensity increases 3 %. This increased vorticity induces stronger turbulence at the jet edges with a maximum turbulence intensity of 16 % compared with 14 % for the static case. The increased mixing with the plate motion is also observed.

Looking at the central jet, Figure (b) shows that higher turbulence intensity occurs in the jet edges, due to the shear layer induced by the flow mixing. Compared with the adjacent left-hand side jet, higher turbulence intensity is recorded at the central jet, mainly due to the crossflow induced by the upstream jet. Comparing the static case with the two moving cases, it is observed that at the shear layer of the central jet, the turbulence intensity varies between 14 % and 16 %. However, the overall turbulence intensity is still higher for the moving case mainly due to a stronger mixing between the jet's flow and the surrounding air.

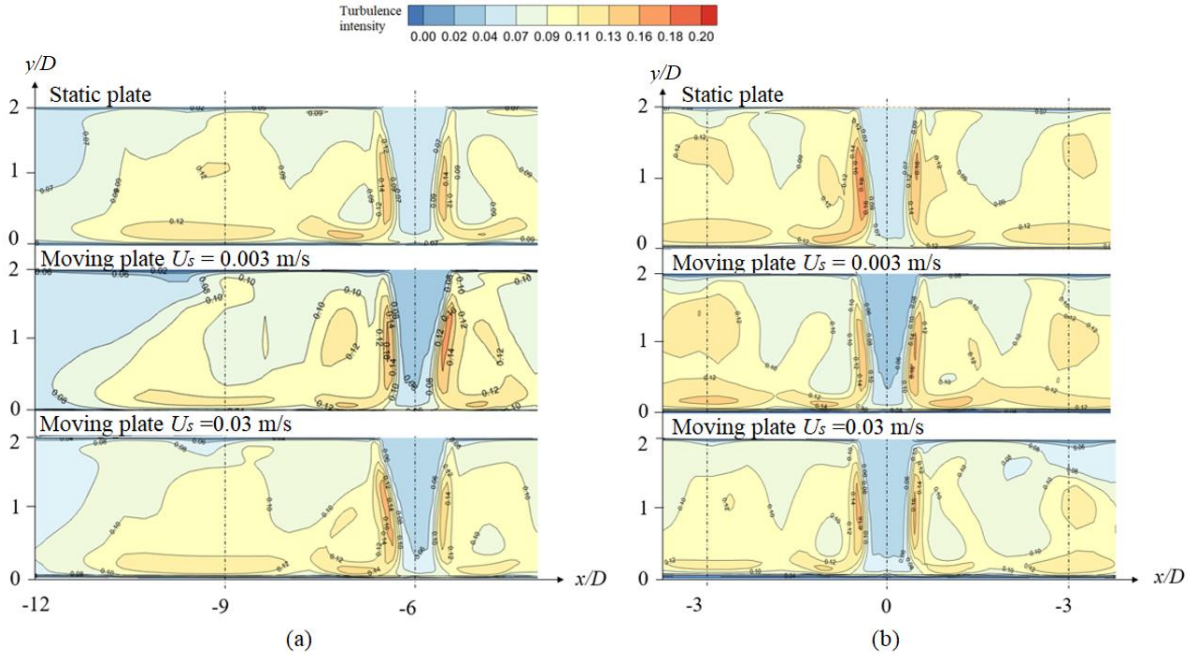
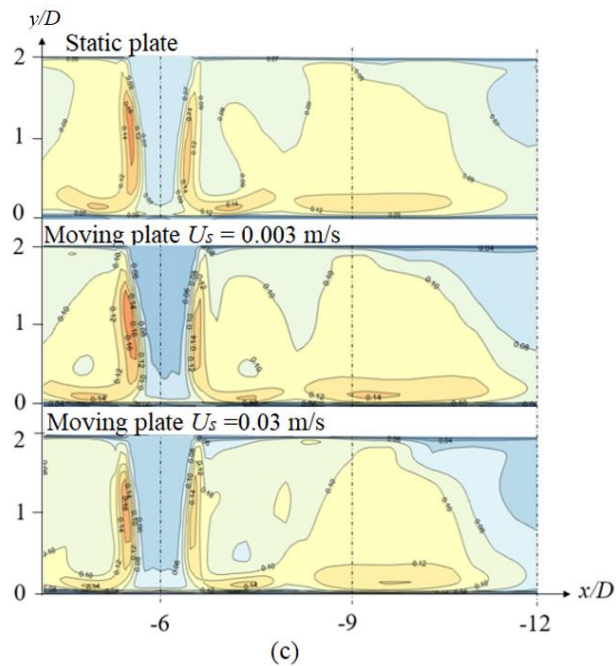


Figure 102. Turbulence intensity: (a) at the left-hand side jet (b) at the central jet.



**Figure 102 (cont).** Turbulence intensity: (c) at the right-hand side jet

As the flow moves downstream with the plate motion, the turbulence intensity near the right-hand side adjacent jet is increased, as observed in Figure (c). Compared with the static case, higher values are recorded with increasing plate velocity, achieving 18 % for  $U_s = 0.03$  m/s. As expected, this last jet is that most influenced by the crossflow induced by the upstream jet but also by the crossflow induced by the plate motion. This effect was reported by several authors [109, 111, 260] for higher  $U_s$ . However, the results presented in this study show that even for low plate velocities, the effect of the jets-induced crossflow combined with the crossflow generated by the plate motion leads to an intensification of the turbulence intensity.

#### 6.4.5. Conclusions

This section presented the numerical validation of multiple cold air jets impinging a hot flat plate with and without motion. From the average heat transfer and jet's flow dynamics measured experimentally and predicted numerically, the comparison between the results shows a good agreement between the two approaches. Regarding the heat transfer, a difference of 5 % is obtained between the experimental and numerical data for the static plate case, with the moving plate this difference increases almost 8 %. More studies are needed to clarify if this discrepancy is due to the effect of the boundary conditions or due to different conditions between the experiments and the simulations. Concerning the jet's flow dynamics for both static and moving plates, the measurements and predictions present similar results,

however, the accuracy of the PIV measurements must be improved in the vicinity of the target plate. Future developments must be conducted in that sense.

From the analysis conducted, the numerical models for both static and moving plates were validated. This allows to conduct two important analyses to conclude this work, that cannot be performed experimentally due to the limitations of the experimental setup, i.e., the analysis of the variation of the heat transfer coefficient over the target plate, and the analysis of the effect of a higher velocity in the jet flow dynamics. From the results, it was concluded that while near each jet the heat transfer is mainly caused by the jet flow momentum, between jets, the increase in heat transfer is mainly due to crossflow momentum, which is intensified by the plate motion. Regarding the turbulence intensity of the flow with the increase of the plate motion, results show the effect of the jets-induced crossflow combined with the crossflow generated by the plate motion leads to an intensification of the turbulence intensity. These results confirm previous statements that mentioned that increasing the plate motion, the shear-driven flow generated over the surface takes control of the flow and thermal fields, increasing the turbulence intensity and consequently, the heat transfer will arise. These conclusions are valid for the conditions of these experiments.

## 6.5. Proposed Correlation

The final step of this work consists of the development of a correlation to predict the average Nusselt number for both static and dynamic plates. As presented in section 2.2.8, several correlations are proposed by different authors for single and multiple jets impinging on a static plate. However, correlations for dynamic plates are scarce. From the results presented by the ANOVA tables (section 6.2.3), the Reynolds number, jet-to-jet spacing, and nozzle-to-plate distance are the variables that mainly contribute to the heat transfer over the surface. Moreover, even if the experiments with the dynamic plate were conducted for only one surface-to-jet velocity ratio,  $V_s$ , the results clearly show that this factor strongly influences the heat transfer. Therefore, these variables are considered in the correlations. The least-squares methodology is applied to find the coefficients for the logarithmic multivariable problem. The correlation used to define the predicted Nusselt number is expressed by Eq. (85) and Eq. (86) for the static and dynamic plate cases, respectively. While the logarithmic multivariable function implemented is presented in Eq. (87).

$$\overline{Nu}_{pre} = c_1 \text{Re}^{c_2} \left(\frac{H}{D}\right)^{c_3} \left(\frac{S}{D}\right)^{c_4} \quad (85)$$

$$\overline{Nu}_{pre} = c_1 Re^{c_2} \left(\frac{H}{D}\right)^{c_3} \left(\frac{S}{D}\right)^{c_4} (1 + V_s)^{c_5} \quad (86)$$

$$\min \sum_{\overline{Nu}_{pre}}^{\overline{Nu}_e} (\overline{Nu}_e - \overline{Nu}_{pre})^2 \quad (87)$$

Subject to:  $c_1 > 0$

where  $\overline{Nu}_e$  is the average Nusselt number measured experimentally,  $\overline{Nu}_{pre}$  is the predicted average Nusselt number, while the correlation coefficients are expressed from  $c_1$  to  $c_5$ .

#### a) Static plate

The proposed correlation for the average Nusselt number of a static plate impinged by multiple air jets is presented in Eq. (88) for the following conditions and range of values:  $2 \leq H/D \leq 7$ ,  $2 \leq S/D \leq 6$ ,  $2,000 \leq Re \leq 5,000$ , for both inline and staggered configuration and minimum crossflow.

$$\overline{Nu} = 0.39 \cdot Re^{0.58} \cdot \left(\frac{H}{D}\right)^{-0.25} \cdot \left(\frac{S}{D}\right)^{-0.34} \quad (88)$$

The measured versus the predicted average Nusselt numbers are plotted in Figure 103. To analyze the accuracy of the proposed correlation, other correlations, presented in the literature, are implemented. The results show that the measurements are clustered along the diagonal line, showing a good agreement between experimental and predicted  $\overline{Nu}$ . The average deviation obtained between predicted and measured values is around 8 %. Compared with data from the literature, the proposed correlation seems to provide accurate predictions, close to those obtained by Florschuetz et al. [48] correlation, which also presents a deviation from the experimental data of approximately 8 %. Moreover, this correlation fits the experimental data better than Huber & Viskanta [67] and Kercher & Tabakoff [118] correlations which is a very satisfying result.

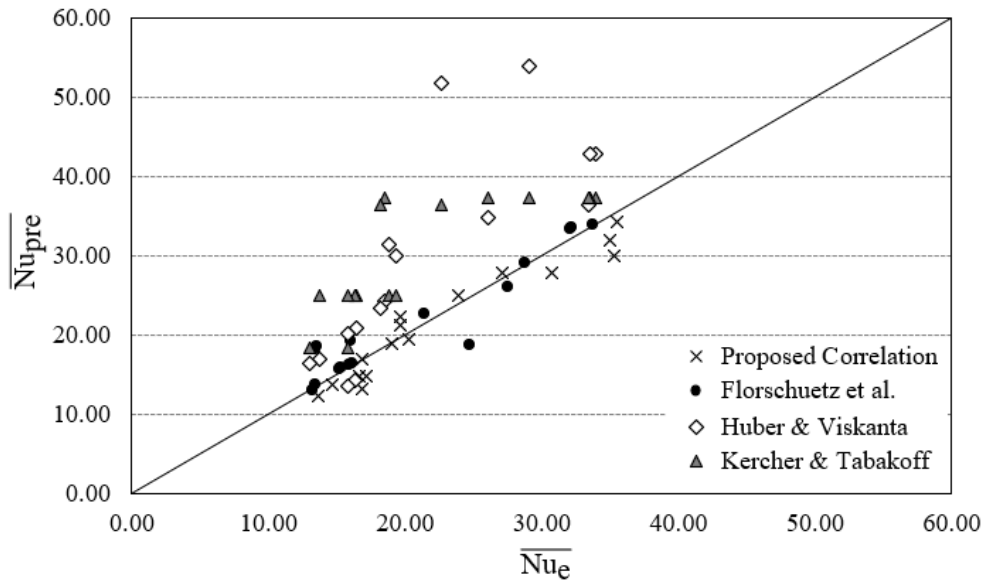


Figure 103. Measured values vs predictions with the present correlation.

To determine the sensitivity of the proposed correlation to other Reynolds numbers, Figure 104 and Figure 105 show the variation of  $\overline{Nu}$  in function of  $Re$  for  $2,000 \leq Re \leq 5,000$  and  $6,000 \leq Re \leq 15,000$ , respectively. The variables considered for this analysis are  $H/D = 2$ ,  $S/D = 3$ , and  $Pr = 0.73$ .

The results show that the proposed correlation is in good agreement with the Florschuetz et al. [48] correlation for low Reynolds numbers ( $Re < 8,000$ ). However, for high  $Re$  values,  $Re > 8,000$ , the data of the proposed correlation fit well with Kercher & Tabakoff correlation [118] mainly for the range  $9,000 \leq Re \leq 13,000$ , while for  $Re > 13,000$ , the present data follows the trend presented by Obot & Trabold [42] correlation.

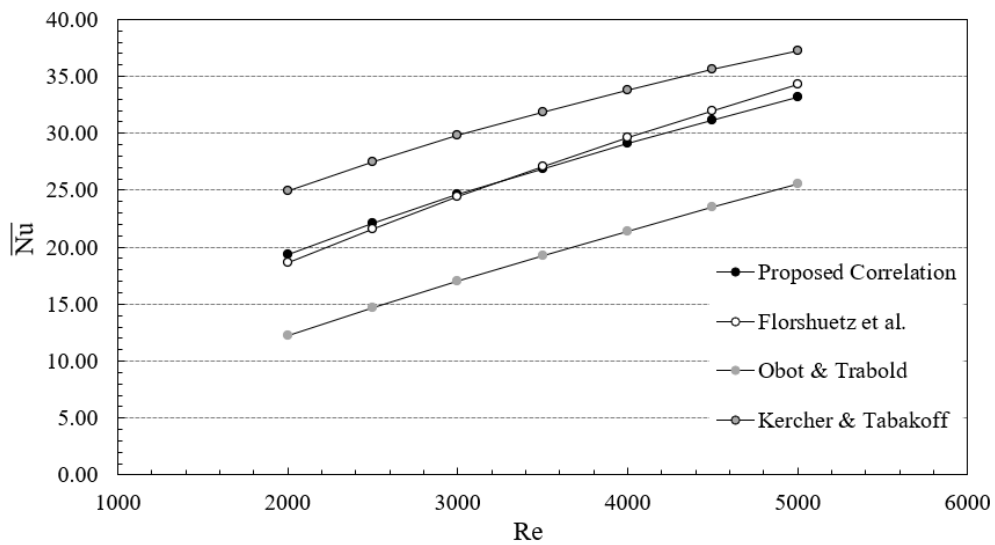


Figure 104. Variation of the Nusselt number in function of the Reynolds number ( $2,000 \leq Re \leq 5,000$ ).

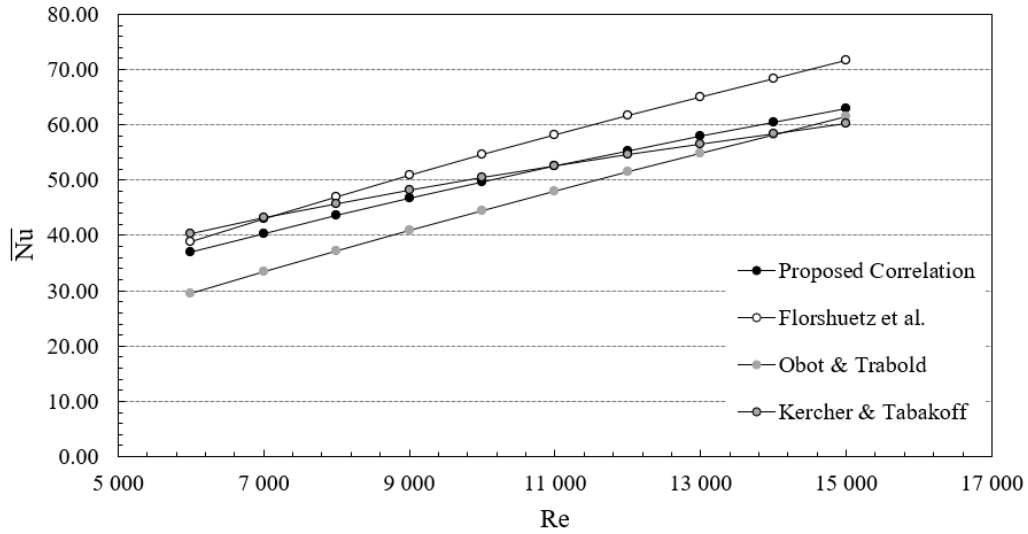


Figure 105. Variation of the Nusselt number in function of the Reynolds number  $6,000 \leq Re \leq 15,000$ .

#### b) Dynamic plate

The proposed correlation for the average Nusselt number of a dynamic plate impinged by multiple air jets is presented in Eq. (89) for process variables varying between the following range:  $2 \leq H/D \leq 7$ ,  $2 \leq S/D \leq 6$ ,  $2,000 \leq Re \leq 5,000$ , for both inline and staggered configuration and minimum crossflow.

$$\overline{Nu} = 0.80 \cdot Re^{0.48} \cdot \left(\frac{H}{D}\right)^{-0.31} \cdot \left(\frac{S}{D}\right)^{-0.36} (1+V_s)^{-0.04} \quad (89)$$

Figure 106 shows the measured versus the average Nusselt numbers predicted by the proposed correlation and Chitsazan & Glasmacher [111] correlation, which is the only correlation found for multiple jets impinging on a dynamic plate. The results show that the measurements are clustered along the diagonal line, showing a good agreement between experimental and predicted  $\overline{Nu}$ , with the proposed correlation, performing better than Chitsazan & Glasmacher [111] correlation. While the proposed correlation presents an average deviation between experiments and predictions of approximately 13%, this difference increases up to 23% when Chitsazan & Glasmacher [111] correlation is applied.

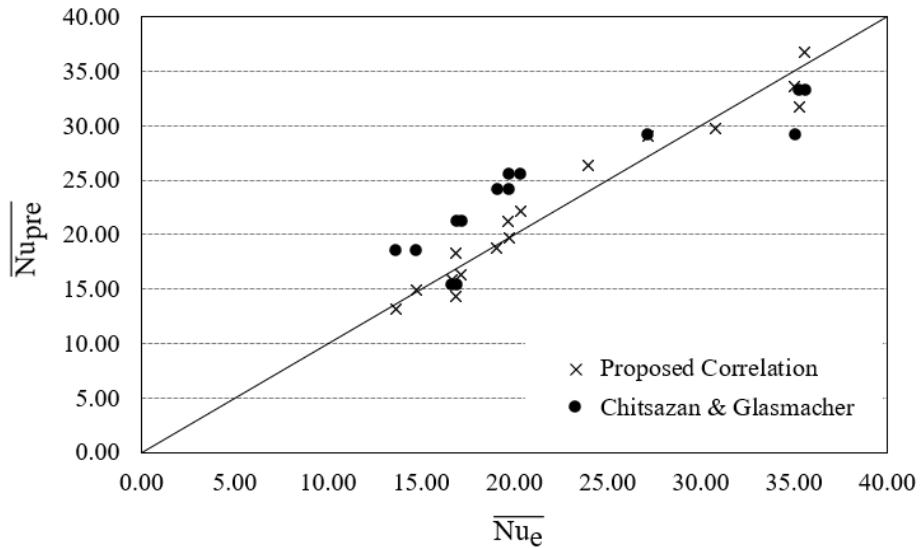


Figure 106. Measured values vs predictions with the present correlation.

To determine the sensitivity of the proposed correlation, and considering that there are few data regarding the multiple jet impingement over moving surfaces, the predicted  $\overline{Nu}$  is compared with Chitsazan & Glasmacher [111] correlation and the numerical data presented by Kadiyala & Chattopadhyay [261] and Shah [69]. The results are presented in Figure 107 and Figure 108.

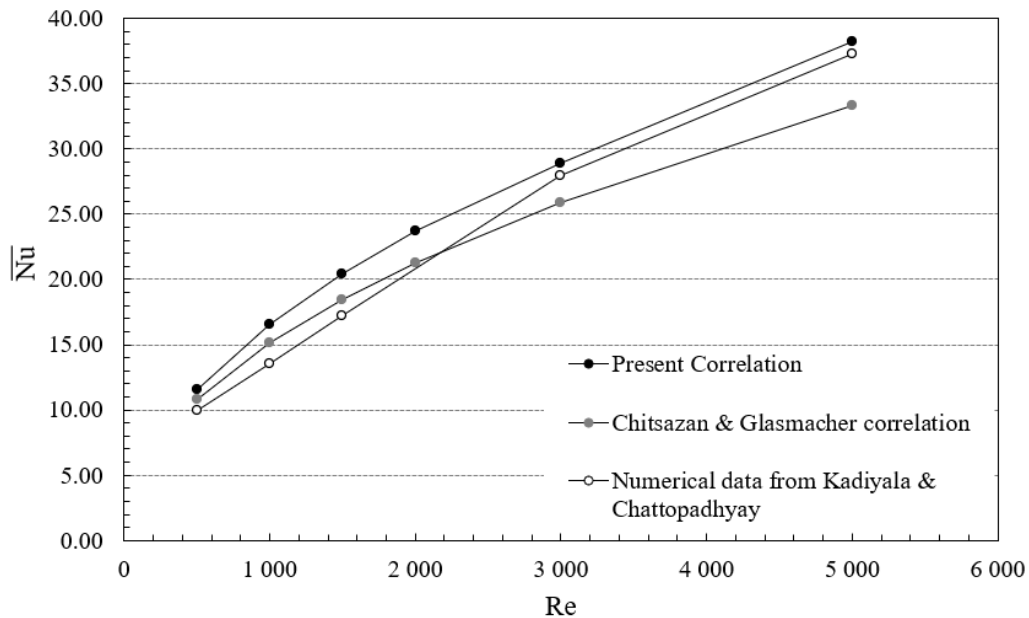
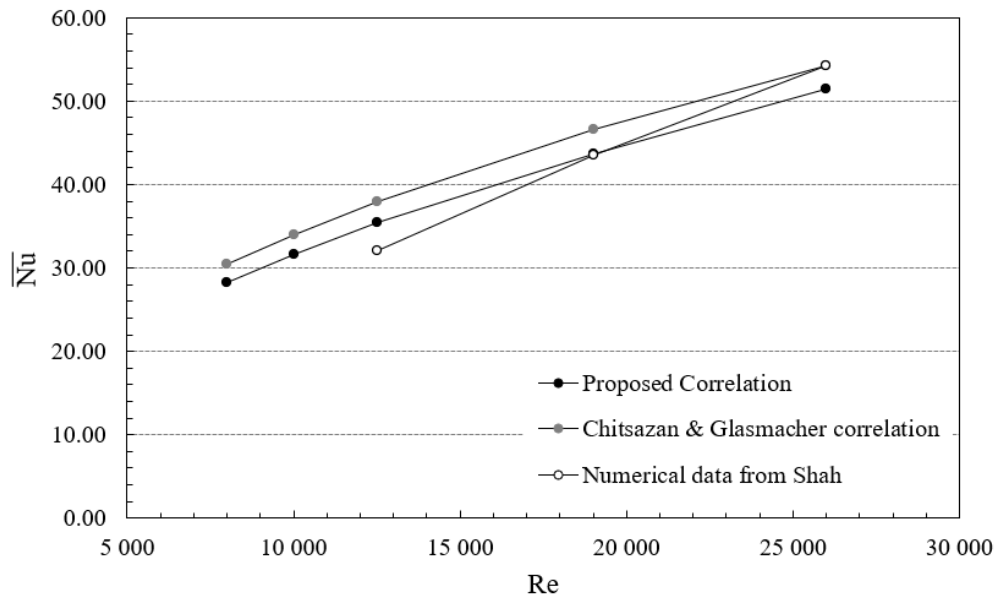


Figure 107. Variation of the Nusselt number in function of the Reynolds number for  $H/D = 2$  and  $S/D = 3$ .



**Figure 108.** Variation of the Nusselt number in function of the Reynolds number for  $H/D = 6$  and  $S/D = 6$ .

The results show that the proposed correlation follows the trend of the literature data. Even if Chitsazan & Glasmacher [111] correlation seems to perform better for low Reynolds numbers, the proposed correlation predicts with higher accuracy the average Nusselt number for the Reynolds numbers ranging between 3,000 and 20,000.

Overall, the proposed correlation for both static and dynamic target surfaces seems to be in good agreement with the data available in the literature. However, more experiments must be conducted mainly for a wide range of  $V_s$  to clearly determine the accuracy of these two correlations.

This page was intentionally left in blank.

## 7. CONCLUSIONS AND FUTURE DEVELOPMENTS

### 7.1. Conclusions

A comprehensive study on the experimental and numerical modeling of a convection process from multiple jets impinging a complex moving surface has been presented in this thesis. Throughout the manuscript, conclusions were summarized and closed each chapter. In this section, the main conclusions are highlighted.

- To conduct the experimental work, a setup was designed and constructed. The accuracy of the velocity field and the heat transfer measurements, including the source of errors, was identified and discussed. From this analysis, it was concluded that the seeding particles play an important role, and that olive oil particles with a diameter near 1  $\mu\text{m}$  were found to be a good option for the range of air flow velocities involved in this work. Other aspects such as the particle's concentration and the time between pulses are determined to optimize the process in function of the jet's flow velocity. For low Reynolds numbers ( $\text{Re} \leq 2,000$ ) a  $\Delta t \approx 250 \mu\text{m}$  was found to be suitable to obtain accurate velocity fields, while for turbulent flows,  $\text{Re} > 2,000$ , a  $\Delta t$  ranging between 50  $\mu\text{m}$  and 10  $\mu\text{m}$  was the most appropriate;
- The uncertainty associated with the temperature, heat transfer, and Reynolds number measurements was estimated using the ASME 98 [165] methodology for a confidence level of 95 %. From this analysis, it was verified that the temperature uncertainty varies between 0.8 % and 2 %, and for the case of the heat transfer measurements, a value between 1.5 % and 5 % is estimated, depending on the experimental conditions. The Reynolds number is assessed with an uncertainty of around 4 %. Regarding the PIV system, the Sciacchitano et al. [262] methodology was implemented and uncertainty of approximately 10 % was estimated;
- Numerical models were developed, based on a finite volume method using the ANSYS FLUENT software, for the analysis of single and multiple jets lying in all flow regimes, while a DNS formulation based on MATLAB framework (2.29 FV) is applied to conduct the numerical simulations of a laminar jet. The velocity field and heat transfer of a laminar jet impinging a flat plate predicted by FLUENT and 2.29 FV were compared with experimental data. The experimental results validated both models

and the reliability of FLUENT Laminar model was proved. However, 2.29 FV is able to capture the flow complexities near the wall compared with the FLUENT Laminar model, predicting with accuracy the large and small structures generated over the domain;

- The interactions between the jet flow and the wall are observed in both FLUENT and 2.29 FV, and the velocity profiles identified, with accuracy, the different regions of the jet. The differences between the jet flow dynamics under isothermal and non-isothermal conditions are clearly identified, showing the effect of plate temperature on the flow development over the surface. Moreover, a mixed heat transfer effect is observed due to forced convection induced by the jet flow and buoyancy driven natural convection. The heat transfer was predicted and the highest deviation from experimental data is obtained for the 2.29 FV, below 17 %;
- Regarding the study of a single jet in the transition regime, the effect of the nozzle-to-plate distance on the jet flow dynamics was analyzed for isothermal conditions. The results show the reduction of the jet momentum as  $H/D$  increases, as expected, and the best configuration was determined for  $H/D = 2$ . The experimental data were used to validate the numerical model and show that the SST  $k-\omega$  model presents good qualitative predictions of the single jet impingement flow at Reynolds number in the transition region;
- A DoE based on Taguchi's method was implemented for the study of multiple jets impinging a complex moving and static surface, reducing the total number of experiments from 768 to 96. The cause-effect diagrams and ANOVA analysis determined the variables that mainly affect the average heat transfer performance of the multiple jet impingement. The Reynolds number presented the higher contribution ( $\approx 62\%$ ), followed by the nozzle-to-plate distance ( $\approx 19\%$ ) and the jet-to-jet spacing ( $\approx 13\%$ ), for both static and moving plates;
- The optimized configuration was determined and corresponds to an  $S/D = 3$ ,  $H/D = 2$  for a high Reynolds number for both static and moving plates. The effect of the jets configuration and target plate geometry was considered negligible compared with the other variables. However, a staggered configuration and a non-flat plate seem to slightly enhance the heat transfer;
- The heat transfer measurements show that the Nusselt number increases with the plate motion. The heat transfer enhancement varies between 3 % and 6 % depending on the experimental conditions and it is mainly due to the increased flow turbulence induced by the plate motion. The effect of the plate motion is intensified when combined with a non-flat plate since the step drives the flow in direction of the plate motion, increasing the crossflow in this direction;

- Even if the ANOVA analysis shows that the effects of the plate geometry are of lesser relevance when compared with the other variables, it is clear that its influence on the average heat transfer, and mainly on the jet flow dynamics, is important. An experimental study compared the flat plate with a  $1 D$  and  $2 D$  step surface and show that the average heat transfer is enhanced by the step surface. Furthermore, the flow complexity is increased by a non-flat plate, mainly in the vicinity of geometric transitions;
- Comparing the numerical models of a multiple jet impinging a static and moving surface with the experiments, the results show a good agreement between the experimental data and the numerical predictions of both heat transfer and jets flow dynamics;
- The numerical results demonstrated that even if the plate velocity is low, the effect of the surface motion is observed, leading to a slight increase in the average heat transfer. Moreover, compared with a static plate, the overall turbulence intensity of the flow is increased by the plate motion, showing that the shear-driven flow generated over the surface takes control of the flow and thermal fields;
- Correlations for the average Nusselt number over a static and dynamic plate impinged by multiple air jets are proposed based on the experimental results and show a good agreement with data from the literature.

## 7.2. Future Developments

Although this work has accomplished the objectives defined, the complex nature of the physics involved has opened new doors that should be exploited in the future and improve the knowledge on multiple jet impingement. Also, such developments could take advantage of the test facility and instrumentation available. Some lines of work that may be explored can be organized into:

1. The analysis of multiple jets impinging over a dynamic target plate can be extended to higher velocities to determine the effect of different velocity ratios between the jets and the plate on the jet's flow dynamics and heat transfer. These results will allow to determine the accuracy of the correlation presented in this work. This is of utmost relevance since correlations involving the target plate motion are very scarce but of need since several industrial processes involve this variable;
2. The study of the effect of higher Reynolds numbers on a complex moving surface is another subject of interest since many practical applications of jet impingement systems involve fully turbulent flows

( $Re > 5,000$ ). In that sense, it is important to verify if the conclusions presented in this work hold if very high  $Re$  jets are implemented;

3. The implementation of a more complex surface is another important topic since there has been a growing demand for target surfaces that increases the heat transfer, such as cellular structures, to be implemented in solar systems. Therefore, multiple jet impingement coupled with complex surfaces can be of great impact in a research field that has been at the frontline, renewable energies;
4. The target surface inclination is another topic of interest, since, besides having a complex geometry, the impinging surface is at an angle with the jet's axis. This increases the complexity of the flow, and few studies are reported in the literature regarding such configurations. This can be a relevant topic for the aerospace field, mainly related to the cooling of the gas turbine blades. Moreover, it is expected that the inclination of the plate increases the mixing between forced and natural convection. Therefore, a detailed analysis of the physics under this phenomenon is relevant and must be conducted.

Besides the experimental work, important developments must be conducted in the numerical simulation. First, this thesis presented a DNS formulation based on the MATLAB framework. Nowadays, the use of DNS for the prediction of complex flows is completely prohibitive for the industry. However, this tool can be used for parametric analysis and uncertainty quantification, instead of conducting deterministic numerical simulations. This is an interesting approach to be followed, for example for the parametric analysis of the variables implemented in the turbulence model. In that sense, the numerical model can be improved at reduced computational costs and time. Considering the relevance of this topic in numerical modeling, it must be explored in future works. A second aspect is related to the improvement of the numerical model mainly for predicting multiple jets impinging a moving surface. Increasing the velocity of the plate motion as well as its complexity will require high computational costs and time that must be reduced.

In conclusion, multiple air jet impingement is a field with high potential for the enhancement of the heat transfer process in several engineering applications. Therefore, this field can provide great research opportunities which are both challenging from a scientific point of view and simultaneously with potential impact in the industry.

## REFERENCES

- [1] Global Market Insights, "Printed Circuit Board (PCB) Market Size | Industry growth report 2027," 2021. [Online]. Available: <https://www.gminsights.com/industry-analysis/printed-circuit-board-pcb-market>.
- [2] D. C. Whalley, "A simplified model of the reflow soldering process," *J. Mater. Process. Technol.*, vol. 150, pp. 134–144, 2004.
- [3] C. S. Lau, M. Z. Abdullah, and F. Che Ani, "Three dimensional thermal investigations at board level in a reflow oven using thermal-coupling method," *Solder. Surf. Mt. Technol.*, vol. 24, no. 3, pp. 167–182, 2012.
- [4] I. Balázs and G. Harsányi, "Heating characteristics of convection reflow ovens," *Appl. Therm. Eng.*, vol. 29, no. 11–12, pp. 2166–2171, 2009.
- [5] J. M. G. Costa, "Numerical Simulation of the Reflow Soldering Process," M.S. dissertation, Department of Mechanical Engineering, University of Minho, Guimarães, Portugal, 2015.
- [6] T. N. Tsai, "Thermal parameters optimization of a reflow soldering profile in printed circuit board assembly: A comparative study," *Appl. Soft Comput. J.*, vol. 12, no. 8, pp. 2601–2613, 2012.
- [7] S. Yong, J. Z. Zhang, and G. N. Xie, "Convective heat transfer for multiple rows of impinging air jets with small jet-to-jet spacing in a semi-confined channel," *Int. J. Heat Mass Transf.*, vol. 86, pp. 832–842, 2015.
- [8] M. Angioletti, R. M. Di Tommaso, E. Nino, and G. Ruocco, "Simultaneous visualization of flow field and evaluation of local heat transfer by transitional impinging jets," *Int. J. Heat Mass Transf.*, vol. 46, pp. 1703–1713, 2003.
- [9] V. Katti and S. V. Prabhu, "Influence of spanwise pitch on local heat transfer distribution for in-line arrays of circular jets with spent air flow in two opposite directions," *Exp. Therm. Fluid Sci.*, vol. 33, no. 1, pp. 84–95, 2008.
- [10] V. A. Chiriac and A. Ortega, "A numerical study of the unsteady flow and heat transfer in a

- transitional confined slot jet impinging on an isothermal surface," *Int. J. Heat Mass Transf.*, vol. 45, pp. 1237–1248, 2002.
- [11] S. M. Zahraee, G. Rezaei, and J. Afshar, "Teaching the Design of Experiment and Response Surface Methodology Using Paper Helicopter Experiment," in *The 4th International Graduate Conference on Engineering Science & Humanity*, 2013.
- [12] L. A. Silva and A. Ortega, "Convective Heat Transfer in an Impinging Synthetic Jet : A Numerical Investigation of a Canonical Geometry," *J. Heat Transfer*, vol. 135, pp. 7–9, 2013.
- [13] I. Balázs, "Comparing 2D and 3D numerical simulation results of gas flow velocity in convection reflow oven," *Solder. Surf. Mt. Technol.*, vol. 26, pp. 223–230, 2014.
- [14] M. A. R. Sharif and A. Banerjee, "Numerical analysis of heat transfer due to confined slot-jet impingement on a moving plate," *Appl. Therm. Eng.*, vol. 29, pp. 532–540, 2009.
- [15] Z. U. Ahmed, Y. M. Al-Abdeli, and F. G. Guzzomi, "Flow field and thermal behaviour in swirling and non-swirling turbulent impinging jets," *Int. J. Therm. Sci.*, vol. 114, pp. 241–256, 2017.
- [16] M. Can, A. B. Etemoglu, and A. Avci, "Experimental study of convective heat transfer under arrays of impinging air jets from slots and circular holes," *Heat Mass Transf. und Stoffuebertragung*, vol. 38, no. 3, pp. 251–259, 2002.
- [17] V. Katti and S. V Prabhu, "Experimental study and theoretical analysis of local heat transfer distribution between smooth flat surface and impinging air jet from a circular straight pipe nozzle," *Int. J. Heat Mass Transf.*, vol. 51, pp. 4480–4495, 2008.
- [18] R. Gharraei, A. Vejdani, S. Baheri, and A. A. Davani D., "Numerical investigation on the fluid flow and heat transfer of non-Newtonian multiple impinging jets," *Int. J. Therm. Sci.*, vol. 104, pp. 257–265, 2016.
- [19] H. Martin, "Heat and Mass Transfer between Impinging Gas Jets and Solid Surfaces," *Adv. Heat Transf.*, vol. 13, pp. 1–60, 1977.
- [20] R. Viskanta, "Nusselt-Reynolds Prize Paper - Heat Transfer to Impinging Isothermal Gas and Flame Jets," *Exp. Therm. Fluid Sci.*, vol. 6, pp. 111–134, 1993.
- [21] N. Zuckerman and N. Lior, "Jet Impingement Heat Transfer : Physics, Correlations, and Numerical Modeling," *Adv. Heat Transf.*, vol. 39, no. 06, pp. 565–631, 2006.
- [22] D. Cooper, D. C. Jackson, B. E. Launder, and G. X. Liao, "Impinging jet studies for turbulence

- model assessment-I. Flow-field experiments," *Int. J. Heat Mass Transf.*, vol. 36, no. 10, pp. 2675–2684, 1993.
- [23] J. N. B. Livingood and P. Hrycak, "Impingement heat transfer from turbulent air jets to flat plates: A literature survey," Cleveland, Ohio, USA, NASA Technical Memorandum (NASA TM X-2778), May 1973.
- [24] R. Ben Kalifa, S. Habli, N. M. Saïd, H. Bournot, and G. Le Palec, "Parametric analysis of a round jet impingement on a heated plate," *Int. J. Heat Fluid Flow*, vol. 57, pp. 11–23, 2016.
- [25] S. Pieris, X. Zhang, S. Yarusevych, and S. D. Peterson, "Vortex dynamics in a normally impinging planar jet," *Exp. Fluids*, pp. 60–84, 2019.
- [26] A. You, M. A. Y. Be, and I. In, "Effect of vortical structures on velocity and turbulent fields in the near region of an impinging turbulent jet," *Phys. Fluids*, vol. 30, no. 035107, 2018.
- [27] M. Draksler, B. Končar, L. Cizelj, and B. Ničeno, "Large Eddy Simulation of multiple impinging jets in hexagonal configuration – Flow dynamics and heat transfer characteristics," *Int. J. Heat Mass Transf.*, vol. 109, pp. 16–27, 2017.
- [28] S. Caliskan, S. Baskaya, and T. Calisir, "Experimental and numerical investigation of geometry effects on multiple impinging air jets," *Int. J. Heat Mass Transf.*, vol. 75, pp. 685–703, 2014.
- [29] Y. Ichikawa, Y. Kameya, and S. Honami, "Three-dimensional flow characterization of a square array of multiple circular impinging jets using stereoscopic PIV and heat transfer relation," *J. Vis.*, vol. 19, no. 1, pp. 89–101, 2016.
- [30] X. Bu, L. Peng, G. Lin, L. Bai, and D. Wen, "Experimental study of jet impingement heat transfer on a variable-curvature concave surface in a wing leading edge," *Int. J. Heat Mass Transf.*, vol. 90, pp. 92–101, 2015.
- [31] M. Wae-Hayee, P. Tekasakul, and C. Nuntadusit, "Influence of nozzle arrangement on flow and heat transfer characteristics of arrays of circular impinging jets," *Songklanakarin J. Sci. Technol.*, vol. 35, no. 2, pp. 203–212, 2013.
- [32] M. Wae-Hayee, P. Tekasakul, S. Eiamsa-ard, and C. Nuntadusit, "Effect of cross-flow velocity on flow and heat transfer characteristics of impinging jet with low jet-to-plate distance," *J. Mech. Sci. Technol.*, vol. 28, no. 7, pp. 2909–2917, 2014.
- [33] J. Lee, Z. Ren, P. Ligrani, D. H. Lee, M. D. Fox, and H. K. Moon, "Cross-flow effects on

- impingement array heat transfer with varying jet-to-target plate distance and hole spacing," *Int. J. Heat Mass Transf.*, vol. 75, pp. 534–544, 2014.
- [34] J. J. Otero-Pérez, R. Sandberg, S. Mizukami, and K. Tanimoto, "High-fidelity simulations of multi-jet impingement cooling flow," *J. Turbomach.*, vol. 143, no. 8, p. 081011, 2021.
- [35] P. S. Penumadu and A. G. Rao, "Numerical investigations of heat transfer and pressure drop characteristics in multiple jet impingement system," *Appl. Therm. Eng.*, vol. 110, pp. 1511–1524, 2017.
- [36] S. Lu, Q. Deng, P. M. Ligrani, H. Jiang, and Q. Zhang, "Effects of coolant and wall temperature variations on impingement jet array thermal performance," *Numer. Heat Transf. Part A Appl.*, vol. 79, no. 1, pp. 68–82, 2021.
- [37] F. V Barbosa, S. F. C. F. Teixeira, and J. C. F. Teixeira, "Experimental Study of Multiple Jets Impinging a Flat Surface," in *Proceedings of the 33rd International Conference on Efficiency, Cost, Optimization, Simulation and Environmental Impact of Energy Systems, June 29 - July 3, 2020*, pp. 92–103.
- [38] W. Li, X. Li, J. Ren, H. Jiang, and L. Yang, "Effect of Reynolds Number, Hole Patterns, Target Plate Thickness on Cooling Performance of an Impinging Jet Array: Part II – Conjugate Heat Transfer Results and Optimization," *J. Turbomach.*, vol. 139, no. April, p. 041002, 2016.
- [39] L. W. Florschuetz, D. E. Metzger, and C. R. Truman, "Streamwise Flow and Heat Transfer Distributions for Jet Array Impingement with Crossflow.," *ASME, Gas Turbine Div.*, no. January, pp. 1–10, 1981.
- [40] J. M. M. Barata, "Fountain Flows Produced by Multiple Impinging Jets in a Crossflow," *AIAA J.*, vol. 34, no. 12, pp. 2523–2530, 1996.
- [41] Y. H. Lo and Y. H. Liu, "Heat transfer of impinging jet arrays onto half-smooth, half-rough target surfaces," *Applied Thermal Engineering*, vol. 128, pp. 79–91, 2018.
- [42] N. T. Obot and T. A. Trabold, "Impingement Heat Transfer Within Arrays of Circular Jets: Part 1—Effects of Minimum, Intermediate, and Complete Crossflow for Small and Large Spacings," *J. Heat Transfer*, vol. 109, no. 4, pp. 872–879, 1987.
- [43] R. Brakmann, L. Chen, B. Weigand, and M. Crawford, "Experimental and Numerical Heat Transfer Investigation of an Impinging Jet Array on a Target Plate Roughened by Cubic Micro Pin Fins," *J.*

- Turbomach.*, vol. 138, no. 11, p. 111010, 2016.
- [44] Y. Xing, S. Spring, and B. Weigand, "Experimental and Numerical Investigation of Heat Transfer Characteristics of Inline and Staggered Arrays of Impinging Jets," *J. Heat Transfer*, vol. 132, no. 9, p. 092201, 2010.
- [45] W. Li, M. Xu, J. Ren, and H. Jiang, "Experimental Investigation of Local and Average Heat Transfer Coefficients Under an Inline Impinging Jet Array, Including Jets With Low Impingement Distance and Inclined Angle," *J. Heat Transf. Asme*, vol. 139, no. 1, p. 12201, 2017.
- [46] A. Terzis, "On the correspondence between flow structures and convective heat transfer augmentation for multiple jet impingement," *Exp. Fluids*, vol. 57, no. 9, pp. 1–14, 2016.
- [47] J. Harrington, A. Nayebzadeh, W. Wang, J. Kapat, M. Maurer, and S. Thorpe, "Effect of Target Wall Curvature on Heat Transfer and Pressure," *J. Turbomach.*, vol. 139, pp. 1–13, 2017.
- [48] L. W. Florschuetz, D. E. Metzger, D. I. Takeuchi, and R. A. Berry, "Multiple Jet Impingement Heat Transfer Characteristic - Experimental Investigation of in-Line and Staggered Arrays With Crossflow.," *NASA Contract. Reports*, vol. 3217, no. 84, 1980.
- [49] A. Terzis, P. Ott, J. von Wolfersdorf, B. Weigand, and M. Cochet, "Detailed Heat Transfer Distributions of Narrow Impingement Channels for Cast-In Turbine Airfoils," *J. Turbomach.*, vol. 136, no. 9, p. 091011, 2014.
- [50] K. W. Van Treuren, Z. Wang, P. Ireland, and T. V Jones, "Comparison and Prediction of Local and Average Heat Transfer Coefficients Under an Array of Inline and Staggered Impinging Jets," in *International Gas Turbine and Aemengine Congress & Exhibition, June 10-13, 1996*, pp. 1–9.
- [51] F. V. Barbosa, S. D. T. Sousa, S. F. C. F. Teixeira, and J. C. F. Teixeira, "Application of Taguchi Method for the Analysis of a Multiple Air Jet Impingement System with and without Target Plate Motion," *Int. J. Heat Mass Transf.*, vol. 176, no. 121504, 2021.
- [52] S. Debnath, M. Khan, and Z. Ahmed, "Turbulent swirling impinging jet arrays: A numerical study on fluid flow and heat transfer," *Therm. Sci. Eng. Prog.*, vol. 19, 2020.
- [53] S. Pachpute and B. Premachandran, "Turbulent multi-jet impingement cooling of a heated circular cylinder," *Int. J. Therm. Sci.*, vol. 148, no. June 2019, p. 106167, 2020.
- [54] B. Weigand and S. Spring, "Multiple Jet Impingement - A Review," *Heat Transf. Res.*, vol. 42, no. 2, pp. 101–142, 2011.

- [55] J. Badra, A. R. Masri, and M. Behnia, "Enhanced Transient Heat Transfer From Arrays of Jets Impinging on a Moving Plate From Arrays of Jets Impinging on a Moving Plate," *Heat Transf. Eng.*, vol. 34, no. 4, pp. 361–371, 2013.
- [56] F. V Barbosa, S. F. C. F. Teixeira, and J. C. F. Teixeira, "Numerical analysis of the influence of the jet-to-jet spacing between two adjacent air jets impinging a flat plate," in *4th Thermal and Fluids Engineering Conference (TFEC) April 14–17, 2019 Las Vegas, NV, USA*, 2019.
- [57] Y. Li, B. Li, F. Qi, and S. C. P. Cheung, "Flow and heat transfer os parallel multiple jets obliquely impinging on a flat surface," *Appl. Therm. Eng.*, vol. 133, pp. 588–603, 2018.
- [58] S. Caliskan and S. Baskaya, "Experimental investigation of impinging jet array heat transfer from a surface with V-shaped and convergent-divergent ribs," *Int. J. Therm. Sci.*, vol. 59, pp. 234–246, 2012.
- [59] S. Caliskan, M. Nasiri Khalaji, S. Baskaya, and I. Kotcioglu, "Design analysis of impinging jet array heat transfer from a surface with V-shaped and convergent-divergent ribs by the taguchi method," *Heat Transf. Eng.*, vol. 37, no. 15, pp. 1252–1266, 2016.
- [60] N. Celik, "Effects of dimples' arrangement style of rough surface and jet geometry on impinging jet heat transfer," *Heat Mass Transf. und Stoffuebertragung*, vol. 56, no. 1, pp. 339–354, 2020.
- [61] J. M. Buchlin, "Convective heat transfer in impinging- gas-jet arrangements," *J. Appl. Fluid Mech.*, vol. 4, no. 2, pp. 137–149, 2011.
- [62] J. Y. San and M. De Lai, "Optimum jet-to-jet spacing of heat transfer for staggered arrays of impinging air jets," *Int. J. Heat Mass Transf.*, vol. 44, no. 21, pp. 3997–4007, 2001.
- [63] L. Chen, R. G. A. Brakmann, B. Weigand, M. Crawford, and R. Poser, "Detailed heat transfer investigation of an impingement jet array with large jet-to-jet distance," *Int. J. Therm. Sci.*, vol. 146, no. January, p. 106058, 2019.
- [64] D. E. Metzger, L. W. Florschuetz, D. I. Takeuchi, R. D. Behee, and R. A. Berry, "Heat Transfer Characteristics for Inline and Staggered Arrays of Circular Jets with Crossflow of Spent Air," *J. Heat Transfer*, vol. 101, no. August 1979, pp. 526–531, 1979.
- [65] Y. Ichikawa, M. Motosuke, Y. Kameya, M. Yamamoto, and S. Honami, "Three-dimensional flow characterization of a square array of multiple circular impinging jets using stereoscopic PIV and heat transfer relation," *J. Vis.*, vol. 19, no. 1, pp. 89–101, 2016.

- [66] M. Goodro, J. Park, P. Ligrani, M. Fox, and H. K. Moon, "Effects of hole spacing on spatially-resolved jet array impingement heat transfer," *Int. J. Heat Mass Transf.*, vol. 51, no. 25–26, pp. 6243–6253, 2008.
- [67] A. M. Huber and R. Viskanta, "Effect of jet-jet spacing on convective heat transfer to confined, impinging arrays of axisymmetric air jets," *Int. J. Heat Mass Transf.*, vol. 37, no. 18, pp. 2859–2869, 1994.
- [68] L. B. Y. Aldabbagh and A. A. Mohamad, "A three-dimensional numerical simulation of impinging jet arrays on a moving plate," *Int. J. Heat Mass Transf.*, vol. 52, no. 21–22, pp. 4894–4900, 2009.
- [69] S. Shah, "Numerical analysis of heat transfer between multiple jets and flat moving surface," *Int. J. Heat Mass Transf.*, vol. 171, no. 121088, 2021.
- [70] L. Gao and S. V Ekkad, "Impingement Heat Transfer , Part I : Linearly Stretched," *J. Thermophys. Heat Transf.*, vol. 19, no. 1, p. 8722, 2005.
- [71] E. I. Esposito, S. V. Ekkad, Y. Kim, and P. Dutta, "Comparing Extended Port and Corrugated Wall Jet Impingement Geometry for Combustor Liner Backside Cooling," in *Proceedings of GT 2007 ASME Turbo Expo 2007: Power for Land, Sea and Air, May 14-17, Montreal, Canada, 2007*, pp. 1–8.
- [72] S. V. Garimella and V. P. Schroeder, "Local Heat Transfer Distributions in Confined Multiple Air Jet Impingement," *J. Electron. Packag.*, vol. 123, no. 3, p. 165, 2001.
- [73] S. A. Reodikar, H. C. Meena, R. Vinze, and S. V. Prabhu, "Influence of the orifice shape on the local heat transfer distribution and axis switching by compressible jets impinging on flat surface," *Int. J. Therm. Sci.*, vol. 104, pp. 208–224, 2016.
- [74] Y. Ozmen and G. Ipek, "Investigation of flow structure and heat transfer characteristics in an array of impinging slot jets," *Heat Mass Transf. und Stoffuebertragung*, vol. 52, no. 4, pp. 773–787, 2016.
- [75] H. Shariatmadar, S. Mousavian, M. Sadoughi, and M. Ashjaee, "Experimental and numerical study on heat transfer characteristics of various geometrical arrangement of impinging jet arrays," *Int. J. Therm. Sci.*, vol. 102, pp. 26–38, 2016.
- [76] A. Tepe, U. Uysal, Y. Yetisken, and K. Arslan, "Jet impingement cooling on a rib-roughened surface

- using extended jet holes," *Appl. Therm. Eng.*, vol. 178, no. 115601, pp. 1–12, 2020.
- [77] Y. Xing and B. Weigand, "Experimental investigation of impingement heat transfer on a flat and dimpled plate with different crossflow schemes," *Int. J. Heat Mass Transf.*, vol. 53, no. 19–20, pp. 3874–3886, 2010.
- [78] J. Lee and S. J. Lee, "The effect of nozzle configuration on stagnation region heat transfer enhancement of axisymmetric jet impingement," *Int. J. Heat Mass Transf.*, vol. 43, no. 18, pp. 3497–3509, 2000.
- [79] P. Chandramohan, S. N. Murugesan, and S. Arivazhagan, "Heat Transfer Analysis of Flat Plate Subjected to Multi- Jet Air Impingement using Principal Component Analysis and Computational Technique," *J. Appl. Fluid Mech.*, vol. 10, no. 1, pp. 293–306, 2017.
- [80] N. Celik and E. Turgut, "Design analysis of an experimental jet impingement study by using Taguchi method," *Heat Mass Transf.*, vol. 48, no. 8, pp. 1407–1413, 2012.
- [81] J. Park, M. Goodro, P. Ligrani, M. Fox, and H. K. Moon, "Effects of Mach number and Reynolds number on jet array impingement heat transfer," *Int. J. Heat Mass Transf.*, vol. 50, no. 1–2, pp. 367–380, 2007.
- [82] M. V. Jensen and J. H. Walther, "Numerical analysis of jet impingement heat transfer at high jet reynolds number and large temperature difference," *Heat Transf. Eng.*, vol. 34, no. 10, pp. 801–809, 2013.
- [83] H. Shariatmadar, A. Momeni, A. Karimi, and M. Ashjaee, "Heat transfer characteristics of laminar slot jet arrays impinging on a constant target surface temperature," *Appl. Therm. Eng.*, vol. 76, pp. 252–260, 2015.
- [84] W. C. Buzzard, Z. Ren, P. M. Ligrani, C. Nakamata, and S. Ueguchi, "Influences of target surface small-scale rectangle roughness on impingement jet array heat transfer," *Int. J. Heat Mass Transf.*, vol. 110, pp. 805–816, 2017.
- [85] A. Tepe, Y. Yetisken, U. Uysal, and K. Arslan, "Experimental and numerical investigation of jet impingement cooling using extended jet holes," *Int. J. Heat Mass Transf.*, vol. 158, no. 119945, pp. 1–12, 2020.
- [86] R. Chauhan, T. Singh, N. Kumar, A. Patnaik, and N. S. Thakur, "Experimental investigation and optimization of impinging jet solarthermal collector by Taguchi method," *Appl. Therm. Eng.*, vol.

- 116, pp. 100–109, 2017.
- [87] S. Spring, Y. Xing, and B. Weigand, “An Experimental and Numerical Study of Heat Transfer From Arrays of Impinging Jets With Surface Ribs,” *J. Heat Transfer*, vol. 134, no. 8, p. 082201, 2012.
- [88] G. E. Andrews, R. A. A. Abdul Hussain, and M. C. Mkpadi, “Enhanced impingement heat transfer : Comparison of co-flow and cross-flow with rib turbulators,” in *Proceedings of the International Gas Turbine Congress, Tokyo, Japan, IGTC2003Tokyo TS-075*, 2003.
- [89] M. O. Annerfeldt, J. L. Persson, and T. Torisson, “Experimental investigation of impingement cooling with tubulators or surface enlarging elements,” *Proc. ASME Turbo Expo 2001, New Orleans, Louisiana, USA, 2001-GT-0149*, pp. 1–9, 2001.
- [90] S. Caliskan and S. Baskaya, “Experimental investigation of impinging jet array heat transfer from a surface with V-shaped and convergent-divergent ribs,” *Int. J. Therm. Sci.*, vol. 59, pp. 234–246, 2012.
- [91] A. H. Alenezi, A. Almutairi, H. M. Alhajeri, A. Addali, and A. A. A. Gamiil, “Flow Structure and Heat Transfer of Jet Impingement on a Rib-Roughened Flat Plate,” *Energies*, vol. 11, no. 1550, 2018.
- [92] A. K. Shukla and A. Dewan, “Convective Heat Transfer Enhancement using Slot Jet Impingement on a Convective Heat Transfer Enhancement using Slot Jet Impingement on a Detached Rib Surface,” *J. Appl. Fluid Mech.*, vol. 10, no. 6, pp. 1615–1627, 2017.
- [93] P. M. Ligrani, Z. Ren, and W. C. Buzzard, “Impingement jet array heat transfer with small-scale cylinder target surface roughness arrays,” *Int. J. Heat Mass Transf.*, vol. 107, pp. 895–905, 2017.
- [94] Z. Ren, W. C. Buzzard, P. M. Ligrani, C. Nakamata, and S. Ueguchi, “Impingement Jet Array Heat Transfer: Target Surface Roughness Shape, Reynolds Number Effects,” *J. Thermophys. Heat Transf.*, vol. 31, no. 2, pp. 346–357, 2017.
- [95] K. Kanokjaruvijit and R. F. Martinez-Botas, “Heat transfer correlations of perpendicularly impinging jets on a hemispherical-dimpled surface,” *Int. J. Heat Mass Transf.*, vol. 53, no. 15–16, pp. 3045–3056, 2010.
- [96] J. Ortega-Casanova and F. J. Granados-Ortiz, “Numerical simulation of the heat transfer from a heated plate with surface variations to an impinging jet,” *Int. J. Heat Mass Transf.*, vol. 76, pp. 128–143, 2014.
- [97] Q. Jing, D. Zhang, and Y. Xie, “Numerical investigations of impingement cooling performance on

- flat and non-flat targets with dimple/protrusion and triangular rib," *Int. J. Heat Mass Transf.*, vol. 126, pp. 169–190, 2018.
- [98] K. Nagesha, K. Srinivasan, and T. Sundararajan, "Enhancement of jet impingement heat transfer using surface roughness elements at different heat inputs," *Exp. Therm. Fluid Sci.*, vol. 112, no. July 2019, p. 109995, 2020.
- [99] A. Dewan, R. Dutta, and B. Srinivasan, "Recent trends in computation of turbulent jet impingement heat transfer," *Heat Transf. Eng.*, vol. 33, no. 4–5, pp. 447–460, 2012.
- [100] K. S. Raju and E. U. Schlunder, "Heat Transfer Between an Impinging Jet and a Continuously Moving Flat Surface," *Warme-und Stoffubertragung Thermo - Fluid Dyn.*, vol. 10, pp. 131–136, 1977.
- [101] J. Senter and C. Sollicec, "Flow field analysis of a turbulent slot air jet impinging on a moving flat surface," *Int. J. Heat Fluid Flow*, vol. 28, pp. 708–719, 2007.
- [102] C. M. Or, K. M. Lam, and P. Liu, "Potential Core Lengths of Round Jets in Stagnant and Moving Environments Potential Core Lengths of Round Jets in Stagnant and Moving Environments," *J. Hydro-Environment Res.*, vol. 5, no. 2, pp. 81–91, 2010.
- [103] M. Mobtil, D. Bougeard, and C. Sollicec, "Inverse determination of convective heat transfer between an impinging jet and a continuously moving flat surface," *Int. J. Heat Fluid Flow*, vol. 50, pp. 83–94, 2014.
- [104] F. V. Barbosa, S. F. C. F. Teixeira, C. A. P. Costa, F. D. P. Marques, and J. C. F. Teixeira, "Experimental study of multiple air jets impinging on a moving flat plate," in *Proceedings of the ASME 2020 International Mechanical Engineering Congress and Exposition. Volume 11: Heat Transfer and Thermal Engineering. Virtual, Online. November 16–19, 2020. V011T11A051.*, 2020, pp. 1–9.
- [105] H. Chattopadhyay, G. Biswas, and N. K. Mitra, "Heat Transfer From a Moving Surface Due to Impinging Slot Jets," *ASME, Heat Transf. Div.*, vol. 124, pp. 433–440, 2002.
- [106] M. Aghahani, G. Eslami, and A. Hadidi, "Heat transfer in a turbulent jet impinging on a moving plate considering," *J. Mech. Sci. Technol.*, vol. 28, no. 11, pp. 4509–4516, 2014.
- [107] A. M. Achari and M. K. Das, "Conjugate heat transfer study of a turbulent slot jet impinging on a moving plate," *Heat Mass Transf. und Stoffuebertragung*, vol. 53, no. 3, 2017.

- [108] M. Rahimi and R. Azimi, "Slot jet impingement heat transfer for the cases of moving plate and moving nozzle," *J. Brazilian Soc. Mech. Sci. Eng.*, vol. 38, pp. 2651–2659, 2016.
- [109] P. K. Kadiyala and H. Chattopadhyay, "Numerical Analysis of Heat Transfer from a Moving Surface due to Impingement of Slot Jets," *Heat Transf. Eng.*, vol. 39, no. 2, pp. 98–106, 2018.
- [110] R. Liu, Y. Sun, and J. Ni, "Research on flow and heat transfer characteristics of multiple impinging jets on a moving conveyor belt," in *Proceedings of the ASME 2020 International Mechanical Engineering Congress and Exposition IMECE2020 November 16-19, 2020, Virtual, Online, 2020*, pp. 2–7.
- [111] A. Chitsazan and B. Glasmacher, "Numerical Investigation of Heat Transfer and Pressure Force from Multiple Jets Impinging on a Moving Flat Surface," *Int. J. Heat Technol.*, vol. 38, no. 3, pp. 601–610, 2020.
- [112] G. C. Huang, "Investigations of Heat-Transfer Coefficients for Air Flow Through Round Jets Impinging Normal to a Heat-Transfer Surface," *J. Heat Transfer*, vol. 85, no. 3, pp. 237–243, 1963.
- [113] R. Gardon and C. Akfirat, "Heat Transfer Characteristics of Impinging Two-Dimensional Air Jets," *J. Heat Transf. Asme*, vol. 88, no. 1, pp. 101–107, 1966.
- [114] A. A. Tawfek, "Heat transfer and pressure distributions of an impinging jet on a flat surface," *Heat Mass Transf.*, vol. 32, pp. 49–54, 1996.
- [115] D. Lytle and B. W. Webb, "Air jet impingement heat transfer at low nozzle-plate spacings," *Int. J. Heat Mass Transf.*, vol. 37, no. 12, pp. 1687–1697, 1994.
- [116] M.-Y. Wen and K.-J. Jang, "An impingement cooling on a flat surface by using circularjet with longitudinal swirling strips," *Int. J. Heat Mass Transf.*, vol. 46, pp. 4657–4667, 2003.
- [117] R. Gardon, "Heat Transfer Between a Flat Plate and Jets of Air Impinging on It," *Int. Dev. Heat Transf.*, pp. 454–460, 1962.
- [118] D. M. Kercher and W. Tabakoff, "Heat Transfer by a Sparse Array of Round Air Jets Impinging Perpendicular to a Flat Surface Including the Effect of Spent Air," *J. Eng. Power*, vol. 22, no. 1, pp. 73–82, 1970.
- [119] A. I. Behbahani and R. J. Goldstein, "Local heat transfer to staggered arrays of impinging circular air jets," *J. Eng. Power*, vol. 105, no. 2, pp. 354–360, 1983.

- [120] C. Meola, "A new correlation of nusselt number for impinging jets," *Heat Transf. Eng.*, vol. 30, no. 3, pp. 221–228, 2009.
- [121] Y. Chung and K. H. Luo, "Unsteady Heat Transfer Analysis of an Impinging Jet," *J. Heat Transfer*, vol. 124, pp. 1039–1048, 2002.
- [122] Y. M. Chung, K. H. Luo, and N. D. Sandham, "Numerical study of momentum and heat transfer in unsteady impinging jets," *Int. J. Heat Fluid Flow*, vol. 23, no. 5, pp. 592–600, 2002.
- [123] H. Chattopadhyay, "Numerical investigations of heat transfer from impinging annular jet," *Int. J. Heat Mass Transf.*, vol. 47, pp. 3197–3201, 2004.
- [124] X. Jiang, H. Zhao, and K. H. Luo, "Direct computation of perturbed impinging hot jets," *Comput. Fluids*, vol. 36, pp. 259–272, 2007.
- [125] H. G. Lee, H. S. Yoon, and M. Y. Ha, "A numerical investigation on the fluid flow and heat transfer in the confined impinging slot jet in the low Reynolds number region for different channel heights," *Int. J. Heat Mass Transf.*, vol. 51, pp. 4055–4068, 2008.
- [126] M. HADŽIABDIĆ and K. HANJALIĆ, "Vortical structures and heat transfer in a round impinging jet," *J. Fluid Mech.*, vol. 596, no. January 2008, pp. 221–260, 2008.
- [127] N. Uddin, S. O. Neumann, and B. Weigand, "LES simulations of an impinging jet: On the origin of the second peak in the Nusselt number distribution," *Int. J. Heat Mass Transf.*, vol. 57, no. 1, pp. 356–368, 2013.
- [128] T. Dairay, V. Fortuné, E. Lamballais, and L. E. Brizzi, "LES of a turbulent jet impinging on a heated wall using high-order numerical schemes," *Int. J. Heat Fluid Flow*, vol. 50, pp. 177–187, 2014.
- [129] R. Dutta, A. Dewan, and B. Srinivasan, "Large Eddy Simulation of Turbulent Slot Jet Impingement Heat Transfer at Small Nozzle-to-Plate Spacing," *Heat Transf. Eng.*, vol. 37, no. 15, pp. 1242–1251, 2016.
- [130] P. S. Penumadu and A. G. Rao, "Numerical investigations of heat transfer and pressure drop characteristics in multiple jet impingement system," *Appl. Therm. Eng.*, vol. 110, pp. 1511–1524, 2017.
- [131] H. M. Hofmann, R. Kaiser, M. Kind, and H. Martin, "Calculations of steady and pulsating impinging jets - An assessment of 13 widely used turbulence models," *Numer. Heat Transf. Part B Fundam.*, vol. 51, no. 6, pp. 565–583, 2007.

- [132] F. R. Menter, "Two-equation eddy-viscosity turbulence models for engineering applications," *AIAA J.*, vol. 32, no. 8, pp. 1598–1605, 1994.
- [133] T. Zhou, D. Xu, J. Chen, C. Cao, and T. Ye, "Numerical analysis of turbulent round jet impingement heat transfer at high temperature difference," *Appl. Therm. Eng.*, vol. 100, pp. 55–61, 2016.
- [134] M. Hatami, F. Bazdidi-Tehrani, A. Abouata, and A. Mohammadi-Ahmar, "Investigation of geometry and dimensionless parameters effects on the flow field and heat transfer of impingement synthetic jets," *Int. J. Therm. Sci.*, vol. 127, no. January, pp. 41–52, 2018.
- [135] J. Issac, D. Singh, and S. Kango, "Experimental and numerical investigation of heat transfer characteristics of jet impingement on a flat plate," *Heat Mass Transf.*, vol. 56, pp. 531–546, 2020.
- [136] Y. Q. Zu, Y. Y. Yan, and J. D. Maltson, "CFD Prediction for Multi-Jet Impingement Heat Transfer," in *Proceedings of ASME Turbo Expo 2009: Power for Land, Sea and Air GT2009 June 8-12, 2009, Orlando, Florida, USA, 2009*, pp. GT2009-59488.
- [137] Z. Wen, Y. He, X. Cao, and C. Yan, "Numerical study of impinging jets heat transfer with different nozzle geometries and arrangements for a ground fast cooling simulation device," *Int. J. Heat Mass Transf.*, vol. 95, pp. 321–335, 2016.
- [138] J. Badra, A. R. Masri, and M. Behnia, "Enhanced Transient Heat Transfer From Arrays of Jets Impinging on a Moving Plate," *Heat Transf. Eng.*, vol. 34, no. 4, pp. 361–371, 2013.
- [139] P. Yu, K. Zhu, Q. Shi, N. Yuan, and J. Ding, "Transient heat transfer characteristics of small jet impingement on high-temperature flat plate.," *Int. J. Heat Mass Transf.*, vol. 114, pp. 981–991, 2017.
- [140] K. Zhu, P. Yu, N. Yuan, and J. Ding, "Transient heat transfer characteristics of array-jet impingement on high-temperature flat plate at low jet-to-plate distances.," *Int. J. Heat Mass Transf.*, vol. 127, pp. 413–425, 2018.
- [141] H. Huang, T. Sun, G. Zhang, D. Li, and H. Wei, "Evaluation of a developed SST k-w turbulence model for the prediction of turbulent slot jet impingement heat transfer," *Int. J. Heat Mass Transf.*, vol. 139, pp. 700–712, 2019.
- [142] R. Oguic, S. Poncet, and S. Viazzo, "High-order direct numerical simulations of a turbulent round impinging jet onto a rotating heated disk in a highly confined cavity," *Int. J. Heat Fluid Flow*, vol.

- 61, pp. 366–378, 2016.
- [143] H. Hattori and Y. Nagano, “Direct numerical simulation of turbulent heat transfer in plane impinging jet,” *Int. J. Heat Fluid Flow*, vol. 25, no. 5, pp. 749–758, 2004.
- [144] J. E. Jaramillo, F. X. Trias, A. Gorobets, C. D. Pérez-Segarra, and A. Oliva, “DNS and RANS modelling of a turbulent plane impinging jet,” *Int. J. Heat Mass Transf.*, vol. 55, no. 4, pp. 789–801, 2012.
- [145] T. Koide, K. Tsujimoto, T. Shakouchi, and T. Ando, “DNS analysis of multiple impinging jets,” *J. Fluid Sci. Technol.*, vol. 9, no. 3, pp. 1–12, 2014.
- [146] T. Dairay, V. Fortuné, E. Lamballais, and L. Brizzi, “Direct numerical simulation of a turbulent jet impinging on a heated wall,” *J. Fluid Mech.*, vol. 764, no. February, pp. 362–394, 2015.
- [147] G. Rabbani and D. Singh, “Large Eddy Simulation of Turbulent Slot Jet Impingement on Heated Flat Plate,” in *Recent Advances in Mechanical Engineering. Lectures Notes in Mechanical Engineering*, Springer., Singapore, 2021, pp. 795–806.
- [148] A. Javadi, “Numerical study of an impinging jet in cross-flow within and without influence of vortex generator structures on heat transfer,” *Heat Mass Transf. und Stoffuebertragung*, vol. 56, no. 3, pp. 797–810, 2020.
- [149] Q. Guo, Z. Wen, and R. Dou, “Experimental and numerical study on the transient heat-transfer characteristics of circular air-jet impingement on a flat plate,” *Int. J. Heat Mass Transf.*, vol. 104, pp. 1177–1188, 2017.
- [150] R. Leena, G. Syamkumar, and M. Jose Prakash, “Experimental and Numerical Analyses of Multiple Jets Impingement Cooling for High-Power Electronics,” *IEEE Trans. Components, Packag. Manuf. Technol.*, vol. 8, no. 2, pp. 210–215, 2018.
- [151] F. Afroz and M. Sharif, “Numerical investigation of heat transfer from a plane surface due to turbulent annular swirling jet impingement,” *Int. J. Therm. Sci.*, vol. 151, no. 106257, 2020.
- [152] S. H. Seyedein, M. Hasan, and A. S. Mujumdar, “Modelling of a single confined turbulent slot jet impingement using various  $k - \epsilon$  turbulence models,” *Appl. Math. Model.*, vol. 18, no. 10, pp. 526–537, 1994.
- [153] N. K. Chougule, G. V Parishwad, P. R. Gore, S. Pagnis, and S. N. Sapali, “CFD Analysis of Multi-jet Air Impingement on Flat Plate,” in *Proceedings of the World Congress on Engineering 2011*

*Vol III WCE 2011, July 6 - 8, 2011, London, U.K, 2011.*

- [154] H. Huang, T. Sun, G. Zhang, L. Sun, and Z. Zong, "Modeling and computation of turbulent slot jet impingement heat transfer using RANS method with special emphasis on the developed SST turbulence model," *Int. J. Heat Mass Transf.*, vol. 126, pp. 589–602, 2018.
- [155] A. Singh, B. Chakravarthy, and B. Prasad, "Numerical simulations and optimization of impinging jet configuration," *Int. J. Numer. Methods Heat Fluid Flow*, vol. 31, no. 1, pp. 1–25, 2021.
- [156] Y. A. Cengel and A. J. Ghajar, *Heat and Mass Transfer: Fundamentals and Applications*, Fifth Edit. New York: McGraw-Hill Education, 2011.
- [157] J. D. Wrbanek *et al.*, "Thin Film Heat Flux Sensor Development for Ceramic Matrix Composite (CMC) Systems," Cleveland, Ohio, USA, NASA, Tech. Rep. NASA TM -2010-216216, March 2010, 2009.
- [158] P. R. N. Childs, J. R. Greenwood, and C. A. Long, "Heat flux measurement techniques," *Proc. Inst. Mech. Eng. Part C J. Mech. Eng. Sci.*, vol. 213, no. 7, pp. 655–677, 1999.
- [159] N. Artmann, R. Vonbank, and R. L. Jensen, "Temperature measurements using type K thermocouples and the Fluke Helios Plus 2287A data logger," Department of Civil Engineering, Aalborg University. DCE Technical reports No. 52, 2008.
- [160] M. C. Assaad, B. Kimble, Y. Huang, and R. Burgan, "Thin Film Heat Flux Sensor for Measuring Film Coefficient of Rubber Components of a Rolling Tire," *Tire Sci. Technol.*, vol. 36, pp. 275–289, 2008.
- [161] E. Nathaniel and J. Hager, "Thin Foil Heat Meter," *Rev. Sci. Instrum.*, vol. 36, no. 1564, 1965.
- [162] R. Klopfenstein Jr., "Air velocity and flow measurement using a Pitot tube," *ISA Trans.*, vol. 37, pp. 257–263, 1998.
- [163] JGCM, *International vocabulary of metrology – Basic and general concepts and associated terms (VIM)*, 3rd ed. JCGM, 2012.
- [164] R. J. Moffat, "Describing the Uncertainties in Experimental Results," *Exp. Therm. Fluid Sci.*, vol. 1, no. 1, pp. 3–17, 1988.
- [165] ASME, *Test Uncertainty. Instruments and Apparatus*. New York, USA: The American Society of Mechanical Engineers, 1998.
- [166] M. Raffel, C. E. Willert, F. Scarano, and C. J. Kähler, *Particle Image Velocimetry, A Practical Guide*,

2nd ed. New York, USA: Springer Berlin Heidelberg, 2007.

- [167] W. Merzkirch, *Flow Visualization*, 2nd ed. London: Academic Press, Inc., 1987.
- [168] P. McInturff, M. Suzuki, P. Ligrani, C. Nakamata, and D. H. Lee, "Effects of hole shape on impingement jet array heat transfer with small-scale, target surface triangle roughness," *Int. J. Heat Mass Transf.*, vol. 127, pp. 585–597, 2018.
- [169] JCGM, *Evaluation of measurement data – Guide to the expression of uncertainty in measurement*, First edit. 2008.
- [170] M. M. Sorour, W. M. El-maghlany, M. A. Alnakeeb, and A. M. Abbass, "Experimental study of free single jet impingement utilizing high concentration SiO<sub>2</sub> nanoparticles water base nano fluid," *Appl. Therm. Eng.*, vol. 160, no. 114019, 2019.
- [171] D. Rumsey, *Statistics Essentials for Dummies*. Indianapolis: Wiley Publishing, Inc., 2010.
- [172] R. D. Keane and R. J. Adrian, "Theory of cross-correlation analysis of PIV images," *Appl. Sci. Res.*, vol. 49, no. 3, pp. 191–215, 1992.
- [173] T. O'Donovan, "Fluid Flow and Heat Transfer of an Impinging Air Jet," PhD Thesis, Department of Mechanical & Manufacturing Engineering, Trinity College, Dublin, 2005.
- [174] J. Westerweel, "Fundamentals of digital particle image velocimetry," *Meas. Sci. Technol.*, vol. 8, pp. 1379–1392, 1997.
- [175] A. Melling, "Tracer particles and seeding for particle image velocimetry," *Meas. Sci. Technol.*, vol. 8, no. 12, pp. 1406–1416, 1997.
- [176] L. F. G. Geers, M. J. Tummers, and K. Hanjalić, "Experimental investigation of impinging jet arrays," *Exp. Fluids*, vol. 36, no. 6, pp. 946–958, 2004.
- [177] A. Khayrullina, T. van Hooff, B. Blocken, and G. J. F. van Heijst, "PIV measurements of isothermal plane turbulent impinging jets at moderate Reynolds numbers," *Exp. Fluids*, vol. 58, no. 4, p. 0, 2017.
- [178] A. S. Nebuchinov, Y. A. Lozhkin, A. V Bilsky, and D. M. Markovich, "Combination of PIV and PLIF methods to study convective heat transfer in an impinging jet," *Exp. Therm. Fluid Sci.*, vol. 80, pp. 139–146, 2017.
- [179] E. P. Gnanamanickam, S. Bhatt, S. Artham, and Z. Zhang, "Large-scale motions in a plane wall jet," *J. Fluid Mech.*, vol. 877, pp. 239–281, 2019.

- [180] A. Singh and B. V. S. S. Prasad, "Heat transfer and flow visualization of equilaterally staggered jet arrangement on a flat surface," in *Proceedings of the ASME 2020 Turbomachinery Technical Conference and Exposition GT 2020 June 22-26, 2020, London, United Kingdom, 2020*, pp. GT2020-14196.
- [181] C. Zhang, S. Vasilevskis, and B. Kozlowski, "Particle Image Velocimetry - User Guide," Department of Civil Engineering, Aalborg University. DCE Technical reports No. 237, 2018.
- [182] X. Cao, J. Liu, N. Jiang, and Q. Chen, "Particle image velocimetry measurement of indoor airflow field : A review of the technologies and applications," *Energy Build.*, vol. 69, pp. 367–380, 2014.
- [183] R. Theunissen, F. Scarano, and M. L. Riethmuller, "Spatially adaptive PIV interrogation based on data ensemble," *Exp. Fluids*, vol. 48, pp. 875–887, 2010.
- [184] Dantec Dynamics, "Dynamic Studio, User's Guide." Skovlunde, Denmark, 2016.
- [185] G. Cao, M. Sivukari, J. Kurnitski, and M. Ruponen, "PIV measurement of the attached plane jet velocity field at a high turbulence intensity level in a room," *Int. J. Heat Fluid Flow*, vol. 31, pp. 897–908, 2010.
- [186] C. Tropea, A. L. Yarin, and J. F. Foss, *Springer Handbook of Experimental Fluid Mechanics*, 1st ed. Springer Berlin Heidelberg, 2007.
- [187] I. Grant, "Particle image velocimetry: a review," *Proc. Inst. Mech. Eng. Part C J. Mech. Eng. Sci.*, vol. 211, no. 55, pp. 55–76, 1997.
- [188] A. B. Basset, *A Treatise on Hydrodynamics*, 1st ed., vol. II. Cambridge, London: Deighton, Bell & Co, 1888.
- [189] J. O. Hinze, *Turbulence*, 2nd Ed. USA: McGraw-Hill Classic TextBook Reissue, 1975.
- [190] S. N. Sahasrabudhe *et al.*, "Density , viscosity , and surface tension of five vegetable oils at elevated temperatures : Measurement and modeling," *Int. J. Food Prop.*, vol. 20, no. 2, pp. 1965–1981, 2017.
- [191] G. Eshel, G. Levy, U. Mingelgrin, and M. Singer, "Critical evaluation of the use of laser diffraction for particle-size distribution analysis," *Soil Sci. Soc. Am. J.*, vol. 68, pp. 736–743, 2004.
- [192] S. B. Detwiler and K. S. Markley, "Smoke, Flash, and Fire Points of Soybean and Other Vegetable oils," *Oil Soap*, vol. 17, pp. 39–40, 1940.
- [193] P. B. Kowalczyk and J. Drzymala, "Physical meaning of the Sauter mean diameter of spherical

- particulate matter," *Part. Sci. Technol.*, vol. 34, no. 6, pp. 645–647, 2016.
- [194] C. Georgescu, U. Dunarea, D. J. Galati, and G. C. Cristea, "Flammability of Some Vegetal Oils on Hot Surface," *Rev. Chim. Ed.*, vol. 69, no. 3, pp. 668–673, 2018.
- [195] H. Liu, *SCIENCE AND ENGINEERING OF DROPLETS - Fundamentals and Applications*, 1st Ed. Norwich, New York: William Andrews, 1999.
- [196] M. Raffel, C. E. Willert, S. T. Wereley, and J. Kompenhans, *Particle Image Velocimetry, A Practical Guide*, 2nd Ed. New York, USA: Springer Berlin Heidelberg, 2007.
- [197] J. R. Harris, "Investigation of Relative Importance of Some Error Sources in Particle Image Velocimetry," M.S. Dissertation, Department of Mechanical Engineering, Utah State University, Utah, USA, 2012.
- [198] A. Sciacchitano, B. Wieneke, and F. Scarano, "PIV uncertainty quantification by image," *Meas. Sci. Technol.*, vol. 24, no. 4, p. 045302, 2013.
- [199] J. J. Charonko and P. P. Vlachos, "Estimation of uncertainty bounds for individual particle image velocimetry measurements from cross-correlation peak ratio," *Meas. Sci. Technol.*, vol. 24, no. 6, p. 065301, 2013.
- [200] A. Sciacchitano and B. Wieneke, "PIV uncertainty propagation," *Meas. Sci. Technol.*, vol. 27, no. 8, p. 084006, 2016.
- [201] B. Wieneke, "PIV uncertainty quantification from correlation statistics," *Meas. Sci. Technol.*, vol. 26, no. 7, p. 074002, 2015.
- [202] J. Westerweel, "Fundamentals of digital particle image velocimetry," *Meas. Sci. Technol.*, vol. 8, no. 12, pp. 1379–1392, 1997.
- [203] P. Sabharwall, T. Conder, R. Skifton, C. Stoots, and E. S. Kim, "PIV Uncertainty Methodologies for CFD Code Validation at the MIR Facility," Idaho National Laboratory, Idaho, USA, Tec. Rep. INL/EXT-12-27728, Dec., 2013.
- [204] D. J. White, W. A. Take, and M. D. Bolton, "Soil deformation measurement using particle image velocimetry ( PIV ) and photogrammetry," *Géotechnique*, vol. 53, no. 7, pp. 619–631, 2003.
- [205] E. Baydar, "Confined impinging air jet at low Reynolds numbers," *Exp. Therm. Fluid Sci.*, vol. 19, pp. 27–33, 1999.
- [206] D. W. Zhou and S. J. Lee, "Forced convective heat transfer with impinging rectangular jets," *Int.*

- J. Heat Mass Transf.*, vol. 50, no. 9–10, pp. 1916–1926, 2007.
- [207] B. Sagot, G. Antonini, A. Christgen, and F. Buron, “Jet impingement heat transfer on a flat plate at a constant wall temperature,” *Int. J. Therm. Sci.*, vol. 47, pp. 1610–1619, 2008.
- [208] G. E. Andrews, R. A. A. Hussain, and M. C. Mkpadi, “Enhanced Impingement Heat Transfer: The Influence of Impingement  $X/D$  for Interrupted Rib Obstacles (Rectangular Pin Fins),” *J. Turbomach.*, vol. 128, no. April 2006, pp. 321–331, 2006.
- [209] ANSYS, “ANSYS FLUENT Theory Guide,” ANSYS, Inc. Canonsburg, PA, USA, pp. 1–759, 2013.
- [210] J. H. Ferziger and M. Peric, *Computational Methods for Fluid Dynamics*, 3rd ed. New York, NY, USA: Springer, 1996.
- [211] F. R. Menter, J. C. Ferreira, and T. Esch, “The SST Turbulence Model with Improved Wall Treatment for Heat Transfer Predictions in Gas Turbines,” in *Proceedings of the International Gas Turbine Congress 2003 Tokyo, Nov. 2-7, 2003*, no. IGTC2003-TS-059, pp. 1–7.
- [212] R. F. Oliveira, “Study and development of a holding chamber for inhalation,” Ph.D. thesis, Department of Mechanical Engineering, Universidade do Minho, Guimarães, Portugal, 2016.
- [213] D. C. Wilcox, “Reassessment of the scale-determining equation for advanced turbulence models,” *AIAA J.*, vol. 26, no. 11, pp. 1299–1310, 1988.
- [214] D. C. Wilcox, “Comparison of two-equation turbulence models for boundary layers with pressure gradient,” *AIAA J.*, vol. 31, no. 8, pp. 1414–1421, 1993.
- [215] R. F. Oliveira, S. Teixeira, J. C. Teixeira, L. F. Silva, and H. Antunes, “pMDI Sprays: Theory, Experiment and Numerical Simulation,” in *Advances in Modeling of Fluid Dynamics*, no. Chapter 11, C. Liu, Ed. London, UK: InTech, 2012.
- [216] G. Rao, Y. Levy, and M. Kitron-Belinkov, “Heat Transfer Characteristics of a Multiple Jet Impingement System,” in *48th Israeli Aerospace Conference, March 5-7, Tel-Aviv, Israel, 2009*, pp. 1–15.
- [217] M. A. R. Sharif and K. K. Mothe, “Parametric study of turbulent slot-jet impingement heat transfer from concave cylindrical surfaces,” *Int. J. Therm. Sci.*, vol. 49, no. 2, pp. 428–442, 2010.
- [218] C. M. Rhie and W. L. Chow, “Numerical Study of the Turbulent Flow past an Airfoil with Trailing Edge Separation,” *AIAA J.*, vol. 21, pp. 1525–1532, 1983.
- [219] M. Ueckermann, J. Lin, S. Sroka, and P. Lermusiaux, “2.29 Finite Volume MATLAB Framework

- Documentation." MIT, Cambridge, MA, USA, p. 42, 2018.
- [220] M. Angioletti, E. Nino, and G. Ruocco, "CFD turbulent modelling of jet impingement and its validation by particle image velocimetry and mass transfer measurements," *Int. J. Therm. Sci.*, vol. 44, no. 4, pp. 349–356, 2005.
- [221] P. A. K. Lam and K. A. Prakash, "A numerical investigation and design optimization of impingement cooling system with an array of air jets," *Int. J. Heat Mass Transf.*, vol. 108, pp. 880–900, 2017.
- [222] E. V. Kartaev, V. A. Emelkin, M. G. Ktalkherman, S. M. Aulchenko, and S. P. Vashenko, "Upstream penetration behavior of the developed counter flow jet resulting from multiple jet impingement in the crossflow of cylindrical duct," *Int. J. Heat Mass Transf.*, vol. 116, pp. 1163–1178, 2018.
- [223] I. Celik, U. Ghia, C. Freitas, H. Coleman, and P. Raad, "Procedure for Estimation and Reporting of Uncertainty Due to Discretization in CFD Applications," *J. Fluids Eng.*, vol. 130, no. 7, p. 078001, 2008.
- [224] J. Lee and S. Lee, "STAGNATION REGION HEAT TRANSFER OF A TURBULENT AXISYMMETRIC JET IMPINGEMENT," *Exp. Heat Transf.*, vol. 12, no. 2, pp. 137–156, 2010.
- [225] K. Jambunathan, E. Lai, and M. A. Moss, "A review of heat transfer data for single circular jet impingement," *Int. J. Heat Fluid Flow*, vol. 13, no. 2, pp. 106–115, 1992.
- [226] S. Polat, "Heat and mass transfer in impingement drying," *Dry. Technol.*, vol. 11, no. 6, pp. 1147–1176, 1993.
- [227] F. T. M. Nieuwstadt, B. J. Boersma, and J. Westerweel, *Turbulence - Introduction to Theory and Applications of Turbulent Flows*, 1st ed. Switzerland: Springer Cham, 2016.
- [228] J. Kestin, P. F. Maeder, and H. E. Wang, "Influence of turbulence on the heat transfer of heat from plates with and without a pressure gradient," *Int. J. Heat Mass Transf.*, vol. 3, pp. 133–154, 1961.
- [229] S. A. Nada, "Buoyancy and cross flow effects on heat transfer of multiple impinging slot air jets cooling a flat plate at different orientations," *Heat Mass Transf.*, vol. 45, pp. 1083–1097, 2009.
- [230] A. Sexton, J. Punch, J. Stafford, and N. Jeffers, "The thermal and hydrodynamic behaviour of confined, normally impinging laminar slot jets," *Int. J. Heat Mass Transf.*, vol. 123, pp. 40–53, 2018.

- [231] H. H. Balla and R. Ch.Al-Zuhairy, "Heat Transfer of Single Jet Impingement at Low Reynolds Number," *Int. J. Innov. Res. Sci. Eng. Technol.*, vol. 6, no. 6, pp. 11082–11088, 2017.
- [232] E. M. Sparrow and T. C. Wong, "Impingement Transfer Coefficients due to Initially Laminar Slot Jets," *Int. J. Heat Mass Transf.*, vol. 18, pp. 597–605, 1975.
- [233] N. Didden and C.-M. Ho, "Unsteady separation in a boundary layer produced by an impinging jet," *J. Fluid Mech.*, vol. 160, pp. 235–256, 1985.
- [234] C. Shekhar and K. Nishino, "Oscillation and heat transfer in upward laminar impinging jet flows," *Int. J. Heat Fluid Flow*, vol. 50, pp. 316–329, 2014.
- [235] R. Gardon and C. Akfirat, "The role of turbulence in determining the heat-transfer characteristics of impinging jets," *Int. J. Heat Mass Transf.*, vol. 8, pp. 1261–1272, 1965.
- [236] C. Meola, L. Luca, and G. Carlomagno, "Influence of shear layer dynamics on impingement heat transfer," *Exp. Therm. Fluid Sci.*, vol. 13, pp. 29–37, 1996.
- [237] T. P. Sapsis, M. P. Ueckermann, and P. F. J. Lermusiaux, "Global analysis of Navier-Stokes and Boussinesq stochastic flows using dynamical orthogonality," *J. Fluid Mech.*, vol. 734, pp. 83–113, 2013.
- [238] M. P. Ueckermann and P. F. J. Lermusiaux, "Numerical schemes for dynamically orthogonal equations of stochastic fluid and ocean flows," *J. Comput. Phys.*, vol. 233, pp. 272–294, 2013.
- [239] F. Feppon and P. F. J. Lermusiaux, "A Geometric Approach to Dynamical Model-Order Reduction," *SIAM J. Matrix Anal. Appl.*, vol. 39, no. 1, pp. 510–538, 2018.
- [240] F. Feppon and P. F. J. Lermusiaux, "Dynamically Orthogonal numerical schemes for efficient stochastic advection and Lagrangian transport," *SIAM Rev.*, vol. 60, no. 3, pp. 595–625, 2018.
- [241] Y. Ozmen and E. Baydar, "Flow structure and heat transfer characteristics of an unconfined impinging air jet at high jet Reynolds numbers," *Heat Mass Transf.*, vol. 44, pp. 1315–1322, 2008.
- [242] R. A. Fisher, *The Design of Experiments*, 1st. Ed. Edinburgh, UK: Oliver and Boyd, 1935.
- [243] G. Taguchi, S. Chowdhury, and Y. Wu, *Taguchi's Quality Engineering Handbook*, 1st. Ed. New Jersey, USA: John Wiley & Sons, Inc., 2005.
- [244] C. Yuangyai and H. B. Nembhard, "Design of Experiments: A Key to Innovation in Nanotechnology," in *Emerging Nanotechnologies for Manufacturing*, 2nd Ed., PA, USA: Elsevier,

Inc, 2015, pp. 230–254.

- [245] R. K. Roy, *A Primer on The Taguchi Method*, 2nd Ed. Michigan, USA: Society of Manufacturing Engineers, 2010.
- [246] S. Chamoli, “A Taguchi approach for optimization of flow and geometrical parameters in a rectangular channel roughened with V down perforated baffles,” *Case Stud. Therm. Eng.*, vol. 5, pp. 59–69, 2015.
- [247] S. Athreya and Y. D. Venkatesh, “Application Of Taguchi Method For Optimization Of Process Parameters In Improving The Surface Roughness Of Lathe Facing Operation,” *Int. Ref. J. Eng. Sci.*, vol. 1, no. 3, pp. 13–19, 2012.
- [248] E. B. Dean and R. Unal, “Taguchi Approach To Design Optimization for Quality and Cost: an Overview,” in *1991 Annual Conference of the International Society of Parametric Analysts, Kansas City, USA, May 12-16, 1991*, pp. 1–10.
- [249] N. Semioshkina and G. Voigt, “An overview on Taguchi Method,” *J. Radiat. Res.*, vol. 47 Suppl A, no. 2, pp. A95–A100, 2006.
- [250] F. V Barbosa, S. D. T. Sousa, S. F. C. F. Teixeira, and C. F. José, “Application of DOE for the Study of a Multiple Jet Impingement System,” in *Lecture Notes in Computer Science, vol 11621.*, Misra S. e., Cham: Springer, 2019, pp. 1–9.
- [251] Y. Yamane, Y. Ichikawa, M. Yamamoto, and S. Honami, “Effect of injection parameters on jet array impingement heat transfer,” *Int. J. Gas Turbine, Propuls. Power Syst.*, vol. 4, no. 1, pp. 27–34, 2012.
- [252] W. Li, M. Xu, J. Ren, and H. Jiang, “Experimental Investigation of Local and Average Heat Transfer Coefficients Under an Inline Impinging Jet Array, Including Jets With Low Impingement Distance and Inclined Angle,” *J. Heat Transfer*, vol. 139, no. January, pp. 1–12, 2017.
- [253] Y. Ozmen and G. Ipek, “Investigation of flow structure and heat transfer characteristics in an array of impinging slot jets,” *Heat Mass Transf.*, vol. 52, no. 4, pp. 773–787, 2016.
- [254] Y. Li, B. Li, F. Qi, and S. C. P. Cheung, “Flow and heat transfer of parallel multiple jets obliquely impinging on a flat surface,” *Appl. Therm. Eng.*, vol. 133, no. March 2018, pp. 588–603, 2018.
- [255] F. V Barbosa, S. F. C. F. Teixeira, and J. C. F. Teixeira, “Influence of the nozzle-to-plate distance in a jet impinging a cold plate – a numerical approach,” in *PROCEEDINGS OF ECOS 2019 - THE*

32ND INTERNATIONAL CONFERENCE ON EFFICIENCY, COST, OPTIMIZATION, SIMULATION AND ENVIRONMENTAL IMPACT OF ENERGY SYSTEMS JUNE 23-28, 2019, WROCLAW, POLAND, 2019.

- [256] F. V Barbosa, S. F. C. F. Teixeira, and J. C. F. Teixeira, "Experimental and numerical analysis of the influence of the nozzle-to-plate distance in a jet impingement process," *Int. J. Thermodyn.*, vol. 23, no. 2, pp. 81–91, 2020.
- [257] M. M. Hassan, M. A. Teamah, and W. M. El-maghlany, "Numerical investigation for heat transfer enhancement using nanofluids over ribbed confined one-end closed flat-plate," *Alexandria Eng. J.*, vol. 56, no. 3, pp. 333–343, 2017.
- [258] W. El-maghlany and A. E. Kabeel, "PREMIUM JET COOLING WITH TWO RIBS OVER FLAT PLATE UTILIZING NANOFLUID MIXED CONVECTION," *Therm. Sci.*, vol. 21, no. 2, pp. 963–976, 2017.
- [259] A. Nozaki, Y. Igarashi, and K. Hishida, "Heat transfer mechanism of a swirling impinging jet in a stagnation region," *Heat Transf. - Asian Res.*, vol. 32, no. 8, pp. 663–673, 2003.
- [260] L. B. Y. Aldabbagh and A. A. Mohamad, "A three-dimensional numerical simulation of impinging jet arrays on a moving plate," *Int. J. Heat Mass Transf.*, vol. 52, pp. 4894–4900, 2009.
- [261] P. K. Kadiyala and H. Chattopadhyay, "Numerical Simulation of Transport Phenomena Due to Array of Round Jets Impinging on Hot Moving Surface," *Dry. Technol.*, vol. 35, no. 14, pp. 1742–1754, 2017.
- [262] A. Sciacchitano and B. Wieneke, "PIV uncertainty propagation," *Meas. Sci. Technol.*, no. August, p. 84006, 2016.